Hybrid Steel Frames

Ozgur Atlayan

Dissertation submitted to the faculty of the Virginia Polytechnic Institute and State University in partial fulfillment of the requirements for the degree of

Doctor of Philosophy

In

Civil Engineering

Finley A. Charney, Committee Chair

W. Samuel Easterling

Matthew R. Eatherton

Martin C. Chapman

April 5, 2013

Blacksburg, VA

Keywords: Seismic design, Structural steel, Buckling Restrained Braced Frames, Moment Resisting Steel Frames, Low Strength Steel

Hybrid Steel Frames

Ozgur Atlayan

ABSTRACT

The buildings that are designed according to the building codes generally perform well at severe performance objectives (like life safety) under high earthquake hazard levels. However, the building performance at low performance objectives (like immediate occupancy) under low earthquake hazards is uncertain. The motivation of this research is to modify the design and detailing rules to make the traditional systems perform better at multi-level hazards.

This research introduces two new structural steel systems: hybrid Buckling Restrained Braced Frames (BRBF) and hybrid steel Moment Frames (MF). The "hybrid" term for the BRBF system comes from the use of different steel material including carbon steel (A36), high-performance steel (HPS) and low yield point (LYP) steel. The hybridity of the moment frames is related to the sequence in the plastification of the system which is provided by using weaker and stronger girder sections. Alternative moment frame connections incorporating the use of LYP steel plates are also investigated.

The hybrid BRBF approach was evaluated on seventeen regular (standard) frames with different story heights, seismic design categories and building plans. By varying the steel areas and materials in the BRB cores, three hybrid BRBFs were developed for each regular (standard) frame and their behavior was compared against each other through pushover and incremental dynamic analyses. The benefits of the hybridity were presented using different damage measures such as story accelerations, interstory drifts, and residual displacements. Collapse performance evaluation was also provided.

The performance of hybrid moment frames was investigated on a design space including forty-two moment frame archetypes. Two different hybrid combinations were implemented in the designs with different column sections and different strong column-weak beam (SC/WB) ratios. The efficiency of the hybrid moment frame in which only the girder sizes were changed to control the plastification was compared with regular moment frame designs with higher SC/WB ratios. As side studies, the effect of shallow and deep column sections and SC/WB ratios on the moment frame behavior were also investigated.

In order to provide adequate ductility in the reduced capacity bays with special detailing, alternative hybrid moment frame connections adapting the use of low strength steel were also studied.

ACKNOWLEDGMENTS

I would like to express sincere gratitude to my advisor Dr. Finley Charney for giving me the opportunity to be a part of this research project. Dr. Charney's guidance and support were invaluable during all these years at Virginia Tech. His willingness to share his knowledge and experience with his positive attitude always inspired me and encouraged me to work harder.

I would like to express my appreciation to each of my committee members: Dr. Samuel Easterling, Dr. Matthew Eatherton and Dr. Martin Chapman. They all have contributed to my educational progress and I am impressed by the friendly approach of each one of them.

I would like to thank Dr. Charney and Dr. Easterling again for their sincere convincing conversation with me to stay at Virginia Tech and finish my Ph.D. degree.

I would also like to thank my parents, Baki and Nadide Atlayan, and my sister, Ozlem, for their love, support and patience. Thank you for introducing me to the field of civil engineering and encouraging me to pursue a higher education.

My research study has been financially supported by American Institute of Steel Construction (AISC). This support is gratefully appreciated and acknowledged.

TABLE OF CONTENTS

LIST OF FIGURES

LIST OF TABLES

LIST OF ABBREVIATIONS

ATC.....Applied Technology Council

BOB.....Business Office Building

BRB……...Buckling Restrained Brace

BRBF……...Buckling Restrained Braced Frame

CBF……...Concentrically Braced Frame

CMR……....Collapse Margin Ratio

DBE…….……Design Basis Earthquake

EBF……..Eccentrically Braced Frame

ELF.....Equivalent Lateral Force

FEMA.....Federal Emergency Management Agency

HPS……High Performance Steel

IDA.....Incremental Dynamic Analysis

IDR.....Interstory Drift Ratio

IMF ……Intermediate Moment Frame

LCF.....Low Cycle Fatigue

LYP……...Low Yield Point

MCE.....…...Maximum Considered Earthquake

MLE……Maximum Likelihood Estimation

MOB…….Medical Office Building

MR…….……Moment Resisting

MRI……Mean Return Interval

OMF……Ordinary Moment Frame

NSC……Non Simulated Collapse

PG……Performance Group

RBS……Reduced Beam Section

RS……Response Spectrum

SCBF……Special Concentrically Braced Frame

SC/WB……Strong Column-Weak Beam

SDC……Seismic Design Category

SEAOC……Structural Engineers Association of California

SMF……Special Moment Frame

SS……Stainless Steel

SST……Simpson Strong Tie

ULCF……Ultra Low Cycle Fatigue

CHAPTER 1: INTRODUCTION

Performance Based Earthquake Engineering requires various limit states to be satisfied at different seismic hazard levels. The optimum seismic structural performance depends directly on the ability of stable hysteretic energy dissipation of ductile systems. This research introduces two new structural steel systems: hybrid Buckling Restrained Braced Frames (BRBF) and hybrid steel Moment Frames (MF). The "hybrid" term for the BRBF system comes from the use of different steel material including carbon steel (A36), high-performance steel (HPS) and low yield point (LYP) steel. The "hybrid" term for the MF refers to a mixed moment frame system or a mixed material connection of the moment frame.

Hybrid BRBF includes a multi material brace core which is made of a combination of carbon steel, HPS, and LYP steel. In hybrid BRBF, the LYP component of the BRB core yields earlier than the carbon steel and the energy dissipation due to early yielding helps the hybrid BRBF to perform better than the regular (standard) BRBF under low to mid-level earthquakes. The HPS provides strength and counteracts the low post-yield stiffness of the regular BRBFs (with the help of high strain hardening of LYP steel), and thus increases the performance of the frame and reduces the likelihood of dynamic instability under high intensity ground motions.

A similar idea is implemented on steel moment frames. Girder sizes (including depth and reduced beam section properties) were changed across the stories to have a better control on the plastification of the moment frames. An alternative hybrid moment frame idea incorporates the use of LYP steel plate connections.

In this dissertation, the term "regular" is used to define the traditional or standard BRBF and MF systems which are designed and detailed according to the building code requirements.

1.1. Motivation and Objective

Structural systems available in *ASCE 7-10* (ASCE, 2010) are calibrated for good performance at Design Basis (DBE) or Maximum Considered Earthquake (MCE) level limit states, but performance at other (generally less severe shaking) limit states is uncertain. The motivation of this research is to modify the design and detailing rules to make the traditional systems perform better at multi-level limit hazards. Figure 1-1 shows a seismic performance comparison example of a regular and a hybrid system. In this figure, ground motion intensity is shown on the horizontal axis, and the expected damage state is shown on the vertical axis. The target performance is shown by the squares. The regular system, designed

according to *ASCE 7*, satisfies the life safety limit state under high intensity ground motions. However, the performance at other hazard levels is not guaranteed and could be unacceptable. The goal of the hybrid frame systems is to increase the performance at low intensity ground motions (See Figure 1-1) and, if at all possible, decrease the collapse probabilities of the regular frame systems.

The objectives of the hybrid systems can be listed as follows:

1. Obtain better performance at low-level ground motions.
2. Obtain better performance at DBE/MCE level limit states (reduce residual deformation).
3. Achieve more reliable performance across all limit states (reduce dispersion in computed behavior).
4. Reduce likelihood of dynamic instability and probability of collapse.
5. Keep the economic impact minimum while enhancing the performance.

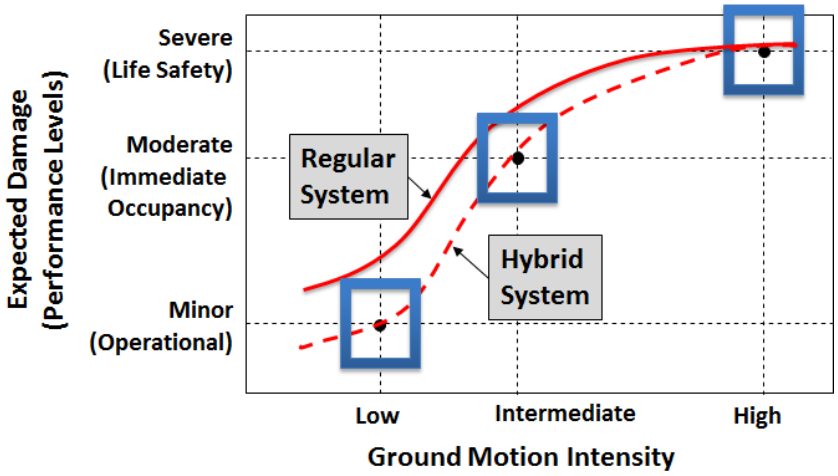

Figure 1-1. Regular and Expected Hybrid Frame Seismic Performance Comparison

The main objective of the hybrid frames is to have controlled yielding in the selected members of the structure. Figure 1-2 displays a regular frame and an expected hybrid frame pushover plot comparison. As may be seen in Figure 1-2, hybrid frames are expected to yield earlier than the regular frames and maintain positive global stiffness or delay negative post yield-slope at higher drift levels.

Hybrid behavior can be achieved using various strategies including mixed materials, mixed systems, and different gravity preloading patterns. In a hybrid material strategy, the hybrid behavior shown in Figure

1-2 can be achieved through the combination of LYP steel and HPS in a multi-core BRB. Likewise, LYP steel can be used in moment frame connections where early yielding is desired, and reinforcement can be added to the other specific connections in the moment frame to delay yielding. In a mixed system strategy, three different moment frames: special (SMF), intermediate (IMF), and ordinary (OMF) with different detailing requirements can be combined in a single hybrid moment frame.

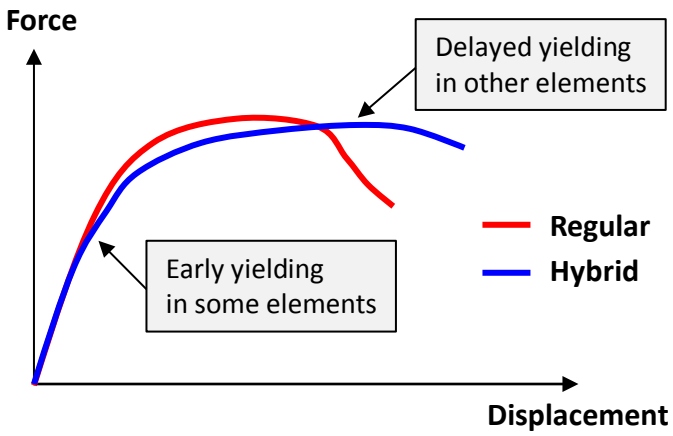

Figure 1-2. Pushover Plot Comparison between Hybrid and Regular Systems

Variations in gravity load distribution related to girder span lengths and beam orientations may help in achieving early yielding. Beams can be connected perpendicular to the girders when early yielding is targeted, and parallel to the girders when yielding is intended to be delayed. Thus, gravity preloading may also be used to influence the yielding sequence of moment frames.

1.2. Overview of Dissertation

The organization of this dissertation is as follows:

- Chapter 1 provides an introduction to hybrid systems with explanation of the objective and motivation of the research, and general hybrid strategies.
- Chapter 2 presents a summary of the literature survey focusing on BRBFs, use of low yield point steels, and previous research about hybrid moment frames.
- Chapter 3 provides a summary of *FEMA P-695* methodology, which is used for all the analyses and performance comparison in this dissertation.

- Chapter 4 discusses the development of hybrid BRBFs, analytical models, and the results obtained from numerical analyses.
- Chapter 5 discusses the development of hybrid MFs, analytical models, and the results obtained from numerical analyses.
- Chapter 6 presents two alternative approaches for hybrid strategy in moment frames through preliminary numerical models and analyses.
- Chapter 7 provides a summary of the research conducted and conclusions drawn. The suggestions for future research are also outlined.
- Appendix A includes the results of the BRBF archetypes included in the *ATC-76-1* (NIST, 2010) project. The performance comparison is made between regular and hybrid BRBFs.
- Appendix B discusses the effect of column depth (W14 vs W24) and strong column weak beam ratio (SC/WB) on moment frames. The sections of the design space (discussed in Chapter 5) are also provided.

CHAPTER 2: LITERATURE SURVEY SUMMARY

This chapter provides a summary of buckling restrained braced frames (BRBF) discussing design provisions, differences between BRBFs and other braced frames, low cycle fatigue (LCF) performance of BRBs, effect of connections on BRBF behavior, large permanent deformation problems of BRBFs and the previous research related to the lab tests of multi-core BRBs. Two different steel types: low yield point (LYP) and stainless steel (SS) that are useful in providing early yielding into the structural system are presented with the discussion of their mechanical properties, availability and cost. The previous study conducted on hybrid moment resisting steel frames is also summarized with its preliminary findings and limitations which prompted further investigation of hybrid moment resisting frames.

2.1. Buckling Restrained Braced Frames

In seismic regions, braced frames and moment frames are commonly used for steel construction. Braced frames have higher lateral stiffness for drift control compared to a moment frame. A braced frame can be generally classified as a concentrically braced frame (CBF) or an eccentrically braced frame (EBF). In a CBF, beams, columns and braces form a vertical truss system. The diagonal bracing members are designed to deform inelastically and they are expected to buckle and yield during a moderate or severe earthquake. In an EBF, links (the beam segments) are designed such that energy dissipation is concentrated in these elements, while the braces, columns and beams outside the link region are designed to remain elastic during a severe earthquake in accordance with capacity design principles (Uang and Nakashima, 2003, Uang et al., 2004).

The buckling restrained braced frame (BRBF) is a special type of CBF with a unique quality that the braces do not buckle when loaded in compression. Thus, BRBs yield in a ductile manner both in tension and compression. Figure 2-1 shows the difference in brace behavior between a conventional brace and a BRB when braces are subjected to cyclic axial load. A conventional brace buckles when loaded in compression, resulting in deterioration of strength and stiffness. It exhibits significantly different strengths in compression and tension. A buckling restrained brace yields both in tension and compression with very similar strengths and it exhibits a desirable behavior as an energy dissipating element. This avoids many of the difficulties that result from large unbalanced brace forces in concentrically braced frames, such as the difficulty in designing beams in V or chevron (inverted-V) braced CBFs.

Special concentrically braced frame (SCBF) is a type of CBF with additional detailing requirements to provide high energy dissipation capacity and ductility with which significant inelastic deformations are

resisted. SCBFs have larger brace areas than BRBFs due to local and global brace slenderness requirements, thus BRBFs have smaller elastic stiffness than SCBFs. After initial yielding, braces in the BRBFs dissipate energy and do not experience strength degradation. As a result, although BRBFs have smaller stiffness than SCBFs, the inelastic drift of the BRBF is comparable or lower than that corresponding to SCBFs (Sabelli et al., 2003).

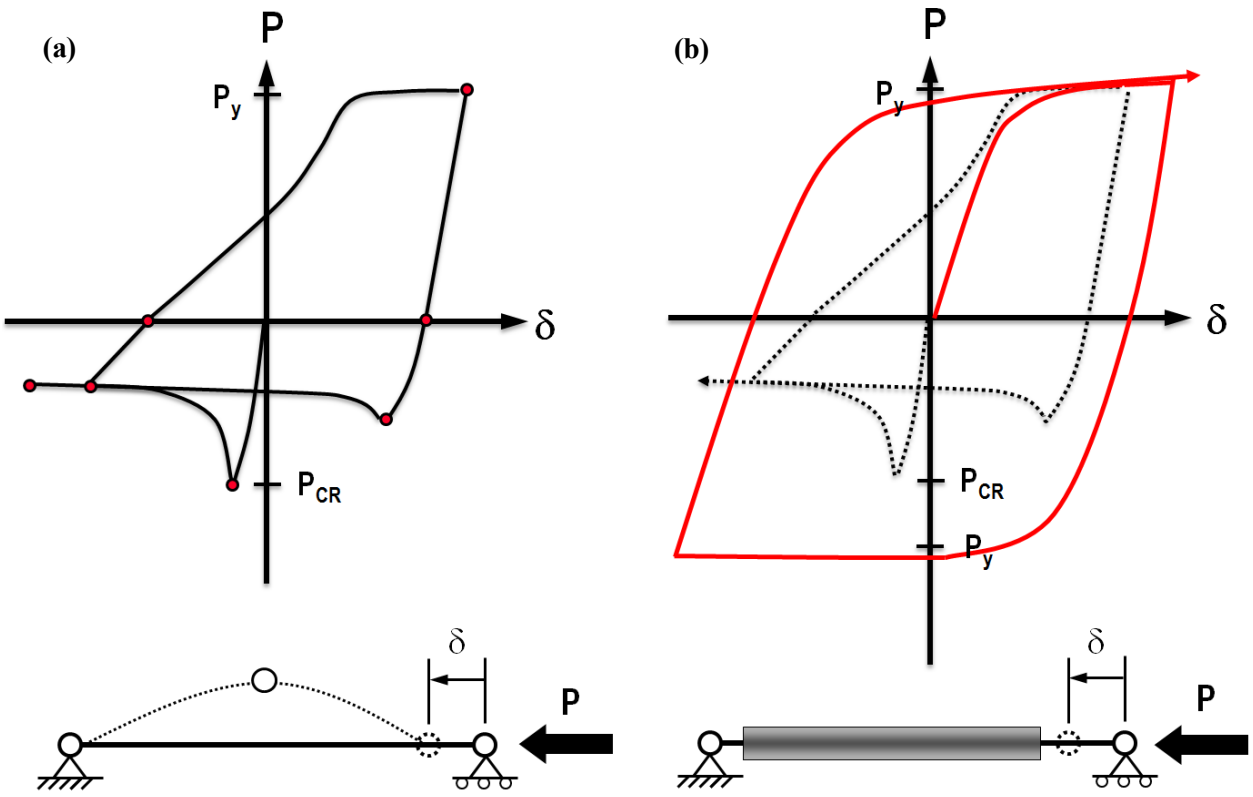

Figure 2-1. Behavior of (a) Conventional and (b) Buckling Restrained Brace (From Engelhardt, 2007: Used with Permission)

Similar to EBFs, BRBFs concentrate the majority of the energy dissipation in a system component intended for that role, i.e. links for EBFs and braces for BRBFs. BRBFs are different from EBFs because they possess an energy-dissipating element that does not resist gravity loads and is more easily repairable after an earthquake. In addition, while the BRBs can endure displacement protocols in excess of those associated with the design earthquake, the link beams of EBFs cannot (SEAOC Seismology Committee, 2008).

A BRB consists of a steel core and a casing. The casing, which restrains buckling of the core, is typically constructed of a mortar filled steel tube. The steel core is surrounded by a debonding material that decouples the steel core from the casing, for purposes of resisting axial force. That is, the debonding

material is intended to prevent transfer of axial stress from the steel core to the casing. Materials like rubber, polyethylene, silicon grease or mastic tape can be used as debonding material (Uang et al., 2004). Consequently, the casing essentially "floats" on the steel core. The maximum compression strength of a BRB may be about 5% greater than the maximum tension strength of the BRB. This higher measured compression strength may be due to partial engagement of the casing in resisting axial force, when the BRB is loaded in compression. This partial engagement of the casing may be due to imperfect debonding, resulting from expansion of the core in compression (Poisson's effect) and higher mode buckles in the core that cause the core to press against the casing.

In addition to rectangular plate steel cores (see Figure 2-2), cruciform shaped plates, or a pair of plates can also be used as BRB steel core. Because the steel core is designed to yield under cyclic loading, A36 or low strength steel that exhibits high ductility are the desirable materials.

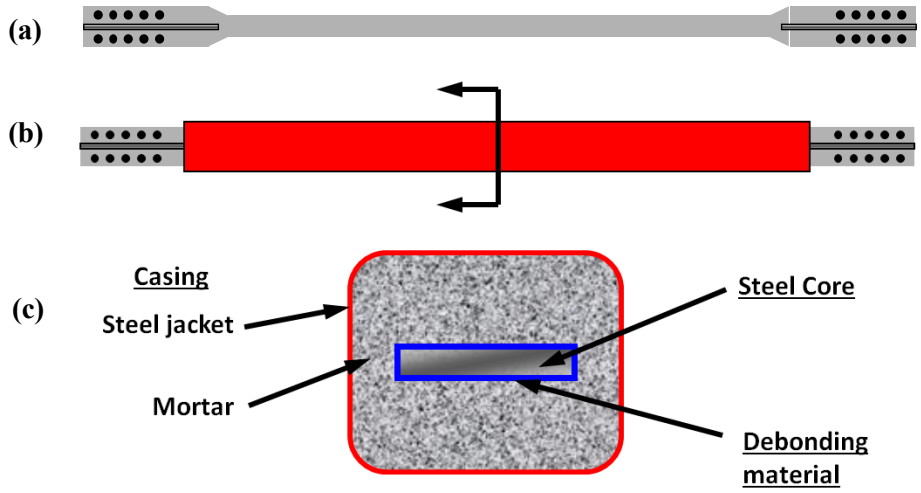

Figure 2-2. Buckling Restrained Brace (BRB) (a) Core (b) Core+Casing (c) Cross Section (From Engelhardt, 2007: Used with Permission)

In a properly designed and detailed BRB, the steel casing should not resist any significant axial load. The steel casing should have sufficient flexural stiffness to avoid global buckling of the BRB. Watanabe et al. (1988) suggested that the elastic buckling strength of the steel case be greater than the yield strength of the steel core. Assuming cyclic strain hardening would increase the compressive strength by 30%, and a resistance factor of 0.85, the elastic buckling strength of the steel case becomes 1.5 times the yield strength of the BRB core.

2.1.1. Low Cycle Fatigue (LCF) Properties of BRBs

Nakamura et al. (2000) tested numerous practical-scale unbonded braces investigating fatigue properties. Three steel grades were selected as BRB cores which were JIS SN400B, BT-LYP100 and BT-LYP235. LYP100 and LYP235 are low yield point steels with yield strengths of 100 MPa (14.5 ksi) and 235 MPa (34 ksi) respectively. SN400B is equivalent to ASTM A36. Tests showed that the number of cycles for causing fatigue failure was approximately 200 when the equivalent story drift angle was 1/100 and this proved that braces have good fatigue properties in consideration of accumulated plastic deformation.

Tests by Nakamura et al. (2000) also showed that the same fatigue properties could be obtained when different steel grades are used for the cores of the BRBs (See Figure 2-3). A formula was proposed for expressing a fatigue curve in consideration of strain concentration:

$$\Delta\varepsilon_a(\%) = \left(\frac{20.48}{\alpha}\right) N_f^{-0.49} \quad \text{(Nakamura et al., 2000)} \qquad \text{(Eq. 2-1)}$$

where; $\propto$ is the ratio of mean strain portion length of each BRB to the core length of BRB (See Figure 2-4), N_f is the number of cycles to failure, and $\Delta\varepsilon_a$ is the mean strain amplitude. Thus, fatigue life becomes shorter as the concentration ratio ($\propto$) increases (See Figure 2-3).

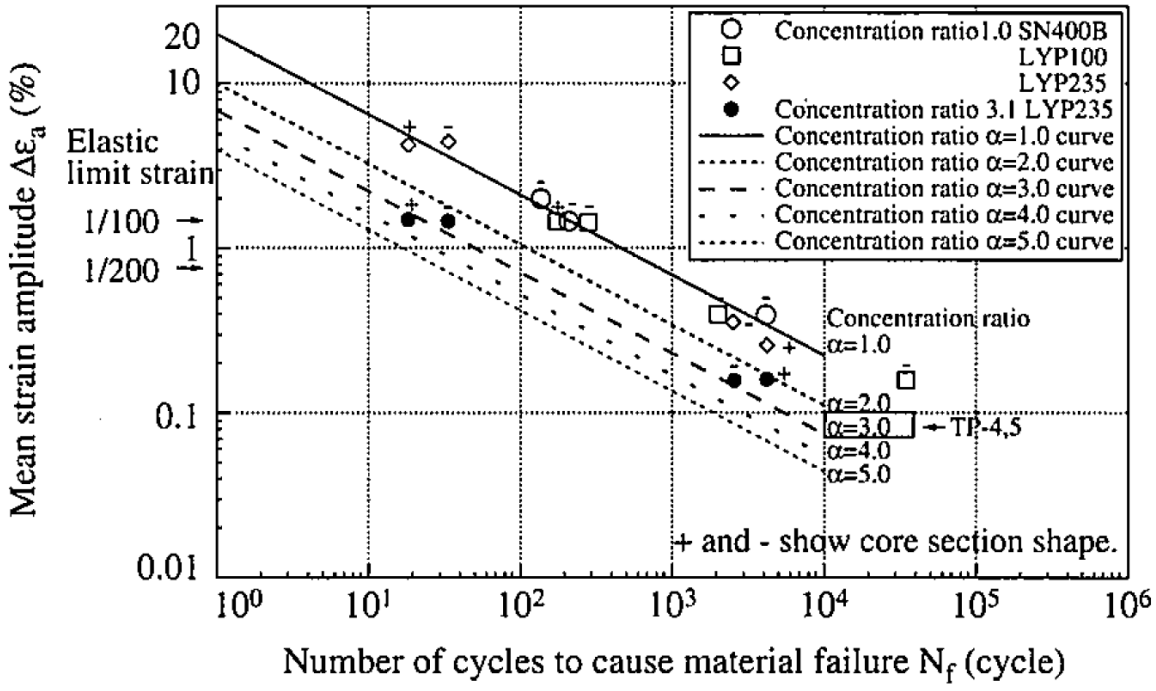

Figure 2-3. Fatigue Curves of Unbonded Braces Considering Strain Concentration (From Nakamura et al., 2000: Used with Permission)

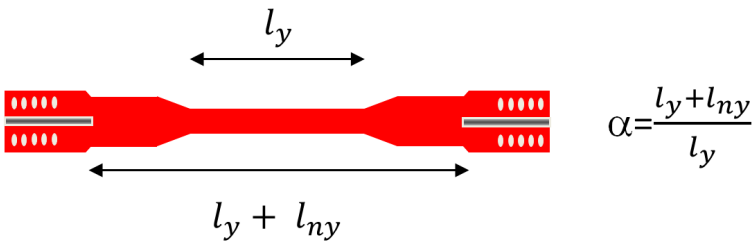

Figure 2-4. Definition of the concentration ratio ($\propto$)

Uriz and Mahin (2008) also tested a few BRB specimens to the point of failure of the brace and suggested values to use on Coffin-Manson relationship which assumes a linear relationship between the log of the number of constant amplitude cycles to failure, N_f, and the log of the strain amplitude, ε_i, experienced in each cycle. The formula of Coffin-Manson relationship is:

$$\varepsilon_i = \epsilon_0 (N_f)^m \qquad \text{(Eq. 2-2)}$$

where; ϵ_0 is the strain amplitude at which one complete cycle on a virgin material will cause failure, and m is the ratio of the log of the total strain amplitude to the log of the number of cycles to failure (slope of the low cycle fatigue log-log plots). Uriz and Mahin suggested using m of -0.458 and ϵ_0 of 0.12 for BRBs.

To compare the suggested BRB fatigue properties, the suggested values by Nakamura et al. (2000) and Uriz and Mahin (2008) are plotted together in Figure 2-5. As may be seen in Figure 2-5, the fatigue lines match well when the $\propto$ value in Eq.2-1 is 1.5.

Coffin-Manson relationship might not fit the experimental data well in the range of very low life cycles (up to 20 cycles). This very low cycle regime is called as extremely or Ultra Low Cycle Fatigue (ULCF) and distinguishes from the linear part of the life cycle curve (plotted in log axis). The failure modes in the ULCF range also differs from the LCF range. While the fatigue damage is dominated by ductility exhaustion at large plastic strain levels, crack propagation dominates at small plastic strain levels. Thus, the reduction in fatigue life for ULCF is due to the difference of the damage accumulation mechanisms (Kuroda, 2001).

The fundamental mechanisms for ULCF include a combination of void growth and cyclic damage processes similar to ductile fracture mechanisms. A new cyclic void growth model was proposed by Kanvinde and Deierlein (2007). This model operates at the continuum level to determine fracture initiation and investigate fracture over a wide range of structural details and components. This model has

not been tested on BRB components yet and large-scale component tests are necessary to validate the capabilities of the model.

Xue (2008) proposed a formula (exponential function) which combines the power law function of Coffin-Manson relationship in the LCF range with an exponential function that defines the fatigue behavior in the ULCF range. Thus, a unified expression is proposed for the entire LCF and ULCF ranges. In addition to the variables in the Coffin-Manson relationship (Eq. 2-2), a material constant, λ, is also defined in the formula proposed by Xue (2008). The slope of the proposed fatigue relationship, m, and the material constant, λ, are also found to be affected by temperature rises.

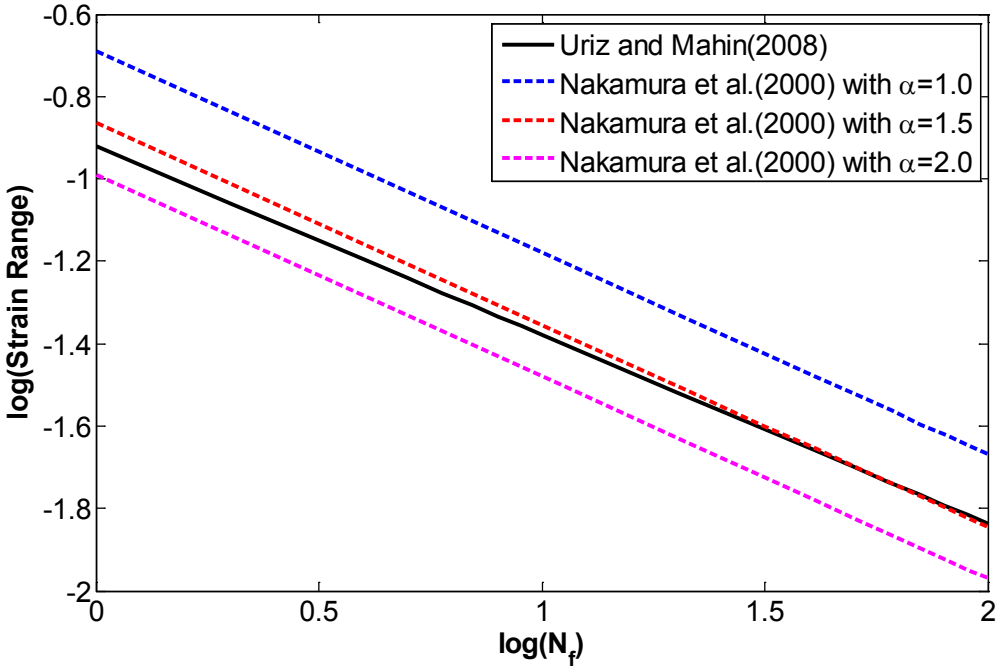

Figure 2-5. Comparison of BRB Fatigue Curves

2.1.2. Effect of Connections on BRBF Behavior

Although BRBFs show good overall seismic performance, they have limitations due to connection failure modes which do not allow the braces to reach their full ductility capacity. Both experimental and analytical research has been done investigating the connection performance of BRBFs. Both the beam-column connection and brace-gusset connection play an important role on BRBF performance. Figure 2-6 shows some example connection models.

Aiken et al. (2002) conducted three cyclic tests on a one-bay one-story BRBF with welded beam-column connections and bolted brace-gusset connections (See Figure 2-6(a)). In Test 1, the subassembly performed well up to 2% drift. In Test 2, cracks formed in a column-gusset weld at a story drift less than 2%, and at higher drifts, cracks propagated and gusset plate distortion was observed. Connections were modified by adding stiffener plates at the free edges of the gusset plates adjacent to the columns before Test 3. In Test 3, a crack initiated in the weld between the beam bottom flange and the column at a drift level of less than 2%. At 2.6% drift, a crack developed in the beam bottom flange at the end of the gusset plate and it propagated through the flange and into the web. As a result of this fracture, beam torsional rotations and BRB out-of-plane displacement occurred and the strength degraded significantly.

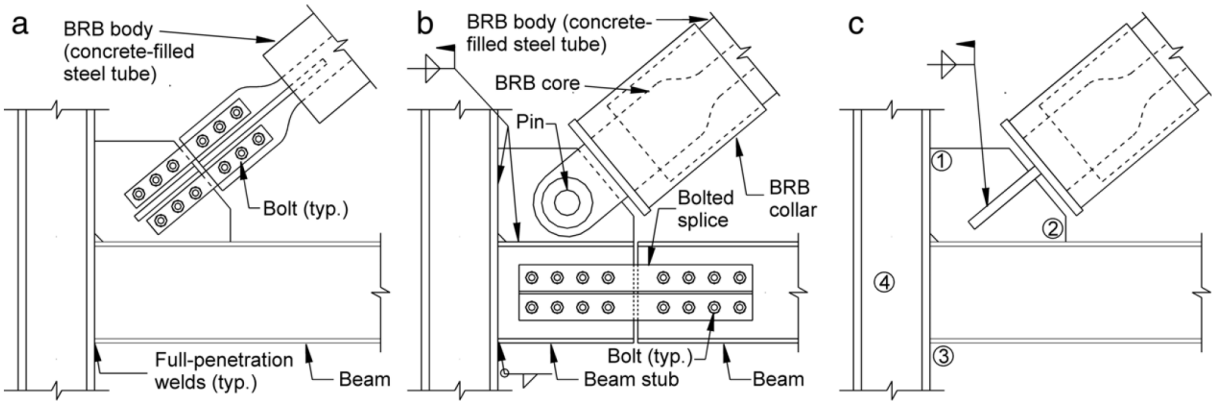

Figure 2-6. BRBF Connection Details (a) Continuous Beam, Bolted Brace; (b) Spliced Beam, Pinned Brace; (c) Continuous Beam, Welded Brace (From Wigle and Fahnestock, 2010: Used with Permission)

Tsai et al. (2003) tested a full-scale three story-three bay dual frame (BRBF+MF) using hybrid earthquake simulations. In these models, brace-gusset connections were bolted (Figure 2-6(a)), and bolted web splices were used for beam-column connections (Figure 2-6(b)). Tests showed acceptable BRB connection performance up to 2.5% story drift when stiffeners were added at the gusset plate free edges.

Christopulos (2005) tested five full-scale one-bay one-story BRBFs with bolted brace-gusset connections and single-plate shear tab connected beam-columns. As a result of these tests, four of the five BRBFs failed due to out-of-plane deformation of the BRB at story drifts between 2% and 2.5%.

Fahnestock et al. (2007) tested a four story BRBF using hybrid pseudo-dynamic earthquake simulations and quasi-static loading. The brace-gusset connections were pinned and bolted web splices were used for the beam-column connections (See Figure 2-6(b)). This beam column connection is referred as non-moment resisting connection. This connection type minimized the connection moment and allowed

rotation. The connection showed excellent performance and sustained only minor yielding at story drifts up to 4.8%. No distortion or damage of the gusset plates occurred. Although the bolted beam splices permitted significant relative rotations, the pinned connections and end collars of the BRBs, with the stocky gusset plates, played an important role in the good performance of the connection (Fahnestock et al., 2007).

It may be concluded from these studies that, depending on the beam-column-brace connection type, there might be large difference in story drift capacity of the BRBFs. The large difference in drift capacities (2.5% to 5%) shows that connection details have an important impact on global system performance.

Wigle and Fahnestock (2010) conducted nonlinear finite element analyses for various beam-column-brace connection configurations. Using three different brace-gusset connections (bolted, pinned, welded), two different beam column connections (continuous and spliced) and two different gusset plate thicknesses, twelve different cases were investigated. When spliced beam connections were used instead of continuous beams, significant reduction was obtained in connection region (column panel zone and gusset plate) stress and plastic strain demands. While equivalent plastic strain was zero for all regions in the spliced beam, plastic strain developed throughout the connection region for the continuous beam case. For bolted brace end connection, a small moment is transferred into the brace due to larger rotational restraint of the brace connection compared to pinned and welded cases. Regarding gusset plate thicknesses, it was concluded that gusset plates should be thick enough to prevent large distributed stresses, but the stiffness of the gusset should be proportioned to match the connected members to mitigate large strain concentrations at the interfaces (Wigle and Fahnestock, 2010).

2.1.3. BRBF Design Provisions

In *ASCE 7-05*, depending on the beam-column connection type, there were two different sets of design coefficients (response modification coefficient, R; system overstrength factor, Ω_0; and deflection amplification factor, C_d) for BRBFs. The coefficients for moment-resisting beam-column connections (continuous beams) were R=8, Ω_0=2.5, C_d=5, and for non-moment-resisting beam-column connections (spliced beams) R=7, Ω_0=2, C_d=5.5. The larger Ω_0 value for the moment-resisting beam-column connections can be explained with the reserve strength provided by continuous beams. The smaller C_d for BRBFs with moment-resisting beam-column connections means that the inelastic drift is expected to be smaller than the BRBFs with non-moment resisting beam-column connections due to reserve strength and stiffness provided by the moment-resisting connections (Wigle and Fahnestock, 2010).

When R is larger, the system can be designed for smaller forces but the system should have more ductility. As explained in the previous section, the expectation of larger ductility is not the case for BRBFs with moment-resisting beam-column connections due to poor connection performance. Thus, although the BRBFs with moment-resisting beam-column connections have greater redundancy and reserve strength, these connections are more likely to fail at smaller drift levels than the BRBFs with non-moment-resisting connections (Wigle and Fahnestock, 2010).

In addition, a numerical study by Sabelli (2001) showed that story drifts and ductility demands increased little when R was changed from 6 to 8, i.e. using a smaller R did not really offer significant benefit. Because of these reasons only one set of design coefficients (ignoring beam-column connection types) is tabulated in *ASCE 7-10* for BRBFs, which are R=8, Ω_0=2.5, C_d=5. This issue can further be investigated through *FEMA P-695* methodology (FEMA, 2009). Collapse margin ratios can be calculated for BRBF archetypes with moment-resisting and non-moment-resisting connections. In order to consider the effect of connection performance difference on system behavior, different non-simulated collapse (NSC) measures can be used for moment-resisting (MR) and non-moment resisting (NMR) beam-column connection models. The NSC values for MR and NMR connection models can be assumed as the maximum story drift ratios of 2.5% and 5% respectively considering the lab test results discussed in the previous section.

2.1.4. Large Permanent Deformation Problem of BRBFs

The most important problem of the BRBFs is the possible large residual deformations occurring at high levels of seismic input because BRBFs do not have a recentering mechanism and have low post-yield stiffness. Sabelli et al. (2003) conducted a numerical study and reported that the residual story drifts were about 40%-60% of the maximum drifts. Thus, although BRBFs exhibit excellent energy-dissipating characteristics, having high residual drifts can increase the repair costs after a major seismic event.

Kiggins and Uang (2006) studied the use of a backup moment frame system, which provides restoring force mechanism, in a dual frame system to minimize the residual deformations. In that study, three and six story BRBFs with and without a backup moment frame were analyzed. A chevron brace configuration was used and beam-column connections were modeled as rigid due to gusset connections. The addition of the backup moment frame proved to reduce the residual story drifts substantially. Figure 2-7 (a) and (b) show the comparison of the maximum and residual drift ratios between the braced frame and the dual frame respectively. The response comparison was made using twenty ground motions. As may be seen in

Figure 2-7, while the maximum drift ratios decreased about 10% when the dual system is used, the reduction in the residual drifts was more than 50% (Kiggins and Uang, 2006).

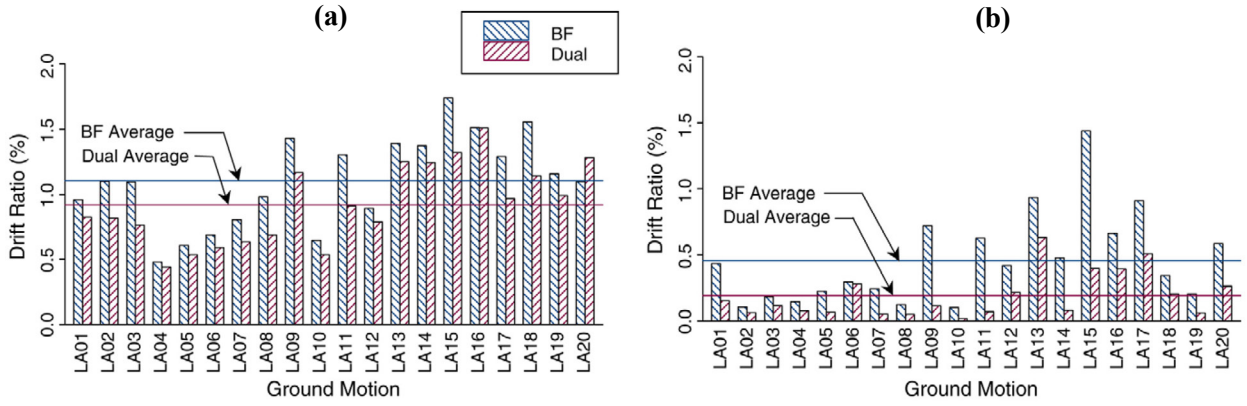

Figure 2-7. Change in (a) Maximum and (b) Residual Drift Ratios for a 6 Story BRBF Building when Backed Up by a Moment Frame (Dual Frame), (From Kiggins and Uang, 2006: Used with Permission)

Ariyaratana and Fahnestock (2011) investigated the reserve strength of BRBFs which can be provided by moment resisting connections (continuous beams) within the BRBF and/or a SMF in parallel with the BRBF to create a dual system. Four different configurations were studied on a seven-story building model: 1) BRBF with non-moment resisting beam-column connections (BRBF-NMR), 2) BRBF with moment resisting beam-column connections (BRBF-MR), 3) Dual system with non-moment resisting beam-column connections in the BRBF (DS-NMR), 4) Dual system with moment-resisting beam-column connections in the BRBF (DS-MR).

As a result of incremental dynamic analysis (IDA), the BRBF-NMR model experienced the largest maximum and residual story drifts, and the DS-MR model experienced the smallest drifts. However, no connection related failure modes (as explained in section 2.1.2) were considered in this study. It was judged that DS-NMR model would be the best configuration because it reduced the residual drift effectively and also connection related problems are not expected due to small flexural demands in the connection region (Ariyaratana and Fahnestock, 2011). Figure 2-8 shows the median maximum and residual drift IDA curves for the four configurations investigated in this study.

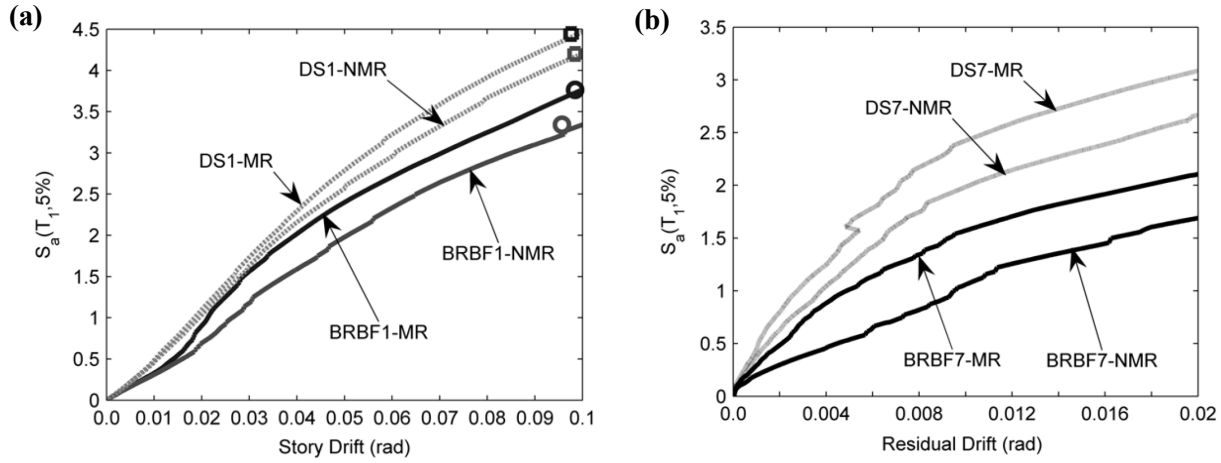

Figure 2-8. (a) Median Maximum Story Drift IDA Curves and Collapse Points (b) Median Residual Drift IDA Curves, (From Ariyaratana and Fahnestock, 2011: Used with Permission)

Tremblay et al. (2008) examined self-centering energy dissipative (SCED) bracing members. A numerical study was conducted to evaluate the seismic performance of steel frames built with a new type of SCED brace which consists of steel bracing elements interconnected by a friction energy dissipative mechanism and equipped with a simple self-centering mechanism including pretensioned fiber tendons. The brace is assembled in a way that the tendons are elongated when the brace is subjected to tension or compression forces, which results in a symmetrical flag-shaped hysteretic response with full recentering capability. Five steel frame buildings with different heights were designed with two types of bracing members: SCED braces and BRBs, and their seismic performance were compared through pushover and dynamic analyses by Tremblay et al. (2008). As a result of this study, when SCED bracing members were used; the peak story drifts were reduced, the residual deformations were eliminated under low and moderate hazard levels and were reduced significantly under 2% in 50-year ground motions. Figure 2-9 shows the pushover curve comparison for SCED and BRB systems and Figure 2-10 shows an example of residual drift elimination on a twelve story frame when SCED bracing members were used.

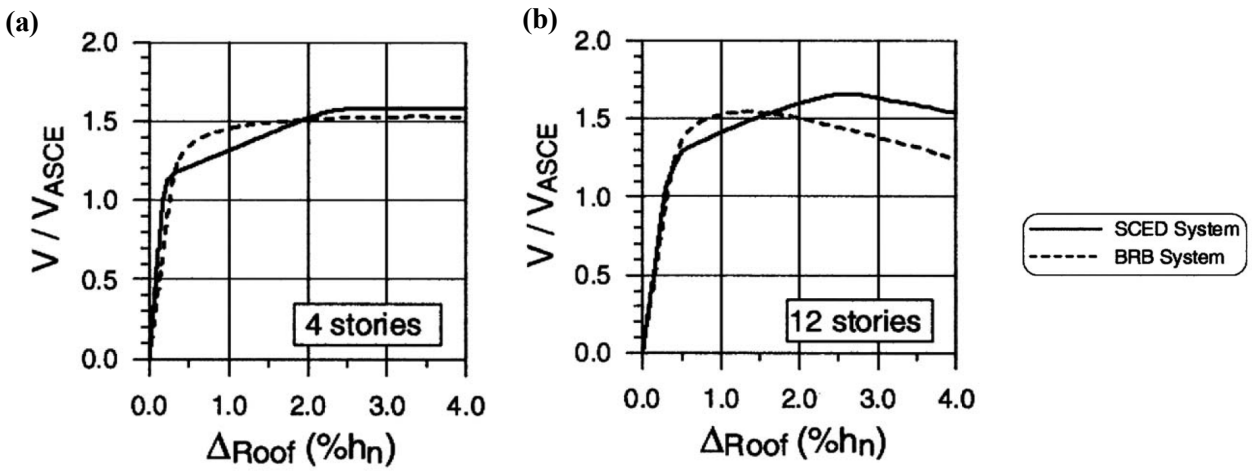

Figure 2-9. Pushover Curves for BRB System and SCED System for (a) 4 story and (b) 12 story Buildings, (From Tremblay et al., 2008: Used with Permission)

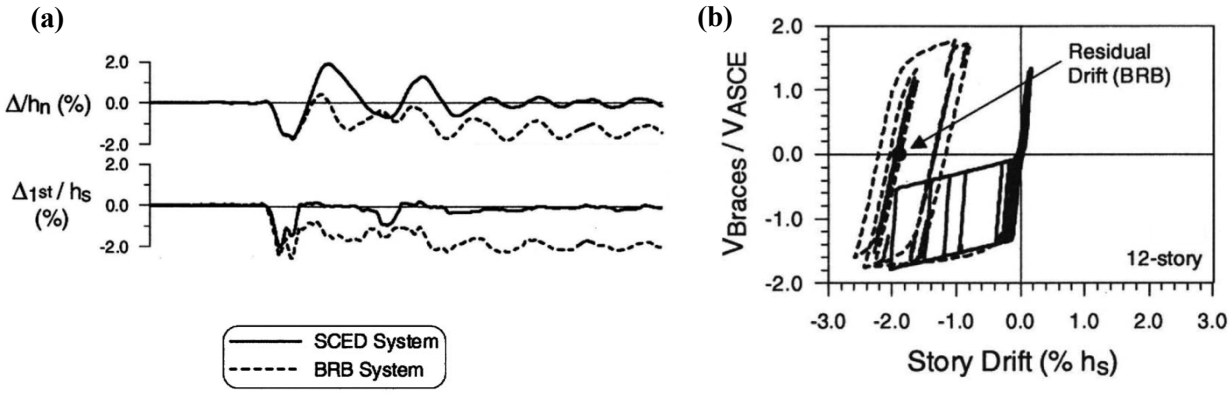

Figure 2-10. (a) Roof Drift and 1st Story Drift Response and (b) 1st Story Lateral Force-Lateral Deformation Response Comparison of BRB and SCED Systems when 12-Story Frames are Subjected to 2% in 50 Year Motion, (From Tremblay et al., 2008: Used with Permission)

2.1.5. Multi-core BRB

The possibility of a new type of buckling restrained brace (BRB) with a core made from the combination of high strength steel (WT780) and low strength steel (LYP100) was mentioned in a report by Sugisawa et al. (1995). The multi-core BRB specimens were tested on a 1,000 ton structure testing machine and the specimens provided stable hysteresis characteristics and uniform strain distribution when subjected to gradually increasing loading to achieve an axial strain of 1%. Figure 2-11 (a) to (c) shows the results of the tests for individual materials and the combined behavior. When the multi-core BRB was used, the increase in the energy absorption capacity due to low yield point steel was manifested and this confirmed

the feasibility of a new type of BRB featuring both earthquake resistance and vibration control (Sugisawa et al., 1995).

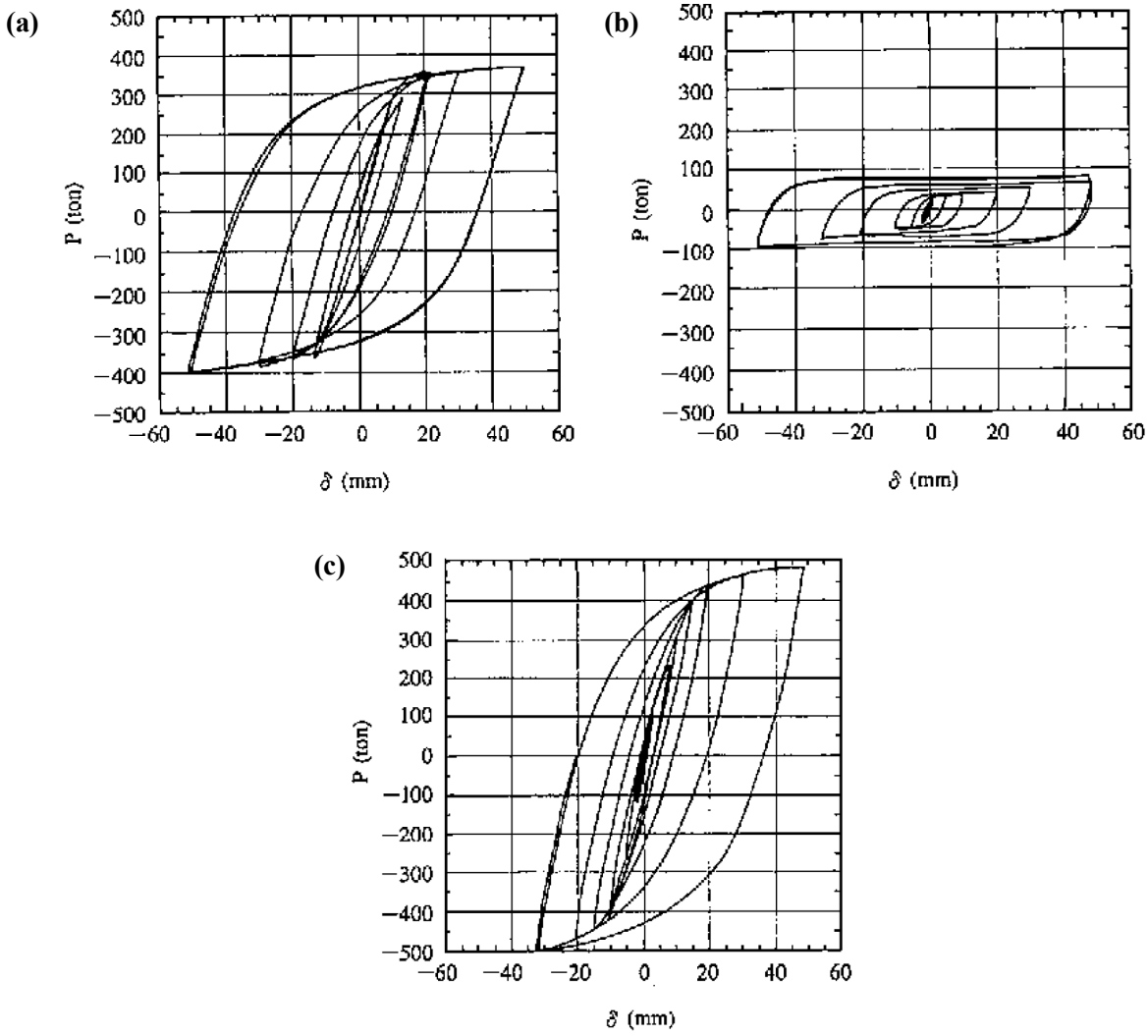

Figure 2-11. Load vs Axial Deformation for (a) WT780, (b) LYP100, and (c) WT780+LYP100, (From Sugisawa et al., 1995: Used with Permission)

2.2. Low Yield Point (LYP) Steels

Early yielding in members can be achieved by using materials having low yield point (LYP) compared to the standard structural steel grades of A36 or A572 . These materials with low yield strain will induce inelastic behavior and will start to dissipate energy under small drifts. It is necessary to have better ductility from these materials for seismic applications. This can be explained by the buckling restrained brace frame design (BRBF) requirements. The cyclic test provisions (AISC, 2010a) require every BRBF

design to have the capacity to undergo a certain number of cyclic loads corresponding to the design story drift. If the material has low yield strain, by the end of loading cycles, the cumulative inelastic deformation will be much greater than the cumulative inelastic deformation observed for standard structural steel grades. Thus, raising the energy absorbing capability should be without allowing fatigue failure due to repeated cycles of tension and compression.

2.2.1. Mechanical Properties of LYP Steels

The following methods may be utilized to decrease the yield strength of steels and to increase their elongation (Saeki, et al., 1998).

1) Reduce the alloy content as close as possible to that of pure iron.
2) Increase ferrite grain size.
3) Tie up carbon and nitrogen with other alloying elements.

Two low carbon steel alloys (carbon content: 0.01% - 0.1% or lower) have been identified that possess lower yield strength and higher ductility compared to the structural steel grade. The materials are called LYP and are available in two grades, LYP100 and LYP235, having 14.5 ksi and 32.5 ksi average yield stress respectively. The name LYP stands for 'Low Yield Point' and the numbers represent yield stresses in MPa unit. Plastic deformation-induced surface roughening and cracking suggest that the micro structural grain size of LYP100 is much greater than that of LYP235 (Saeki, et al., 1998).

In stress-strain relationship obtained from coupon tests, it was observed that LYP100 does not have a distinct yield point as usually observed for 36 ksi and 50 ksi grades (See Figure 2-12). On the other hand, LYP235 did show a definite point where material nonlinearity started (Saeki, et al., 1998). From 150 coupon tests, the average yield stress of LYP100 grade was found as 14.34 ksi with the standard deviation of 1.06 ksi. For LYP235 grade, the same numbers of tests were performed and the results showed the average stress of 36.6ksi with the standard deviation of 0.93 ksi (Yamaguchi, et al., 1998); implying that the materials are fairly predictable in terms of their mechanical properties.

When LYP100 is compared to mild carbon steels equivalent to ASTM A36 (See Figure 2-13), its Young's modulus is similar, the stress at initial yield is approximately one-third, no distinct plastic yield plateau appears, strain hardening is relatively larger, and the rupture strain is about 1.5-2 times larger (Nakashima, et al., 1994).

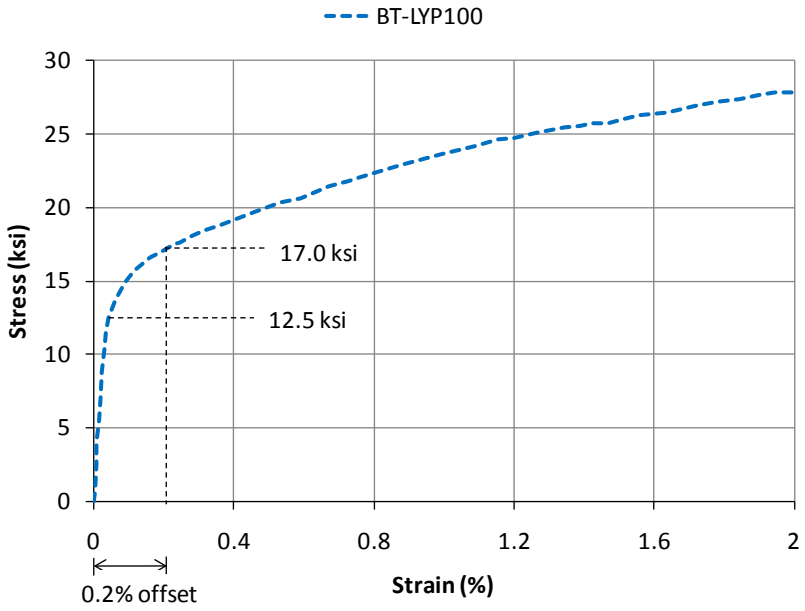

Figure 2-12. Yield Strength of LYP100 Steel (From Chen et al., 2001: Used with Permission)

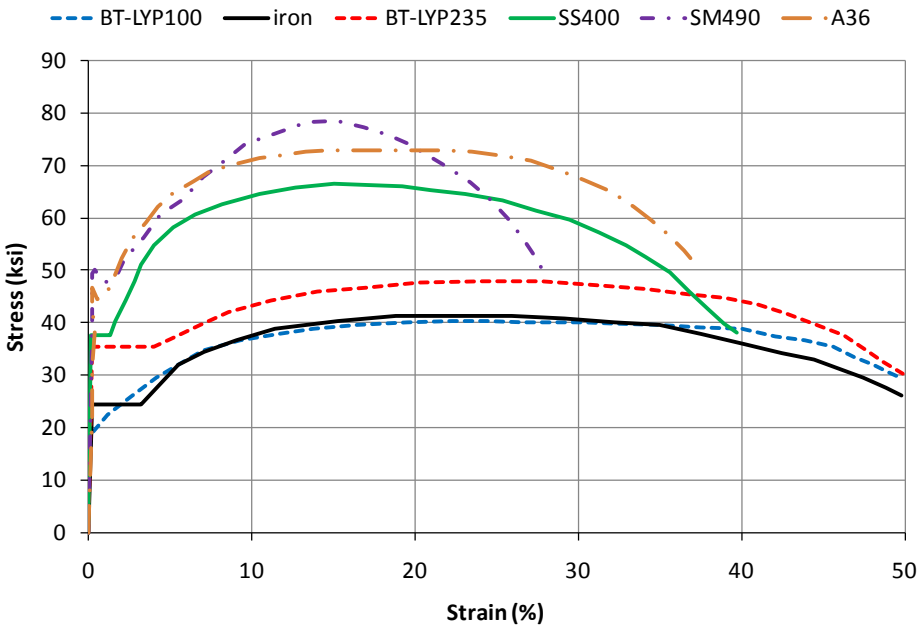

Figure 2-13. Stress-Strain Relationship for LYP Grade Steel (From Saeki et al., 1998: Used with Permission), (From Chen et al., 2001: Used with Permission), (From Nakashima et al., 1994: Used with Permission)

Figure 2-13 also displays two other steel types that are used in Japan market. These are named as SS400 and SM490. SS400 does not have any corresponding grade as per ASTM standard, but from yield stress and ultimate stress values, the material properties of SS400 are found close to the properties of A36 grade

steel. However, the SS400 seems to have better ductility compared to the A36 grade steel. SM490 is equivalent to A572 Grade 50 steel. The LYP grade steel is not explicitly covered in the ASTM standards. The Nippon Steel Corporation has classified the grades under code A1043, "Specification for structural steel with low yield to tensile ratio for use in buildings", of the ASTM standard.

Chemical composition of BT-LYP100 and BT-LYP225 provided by Nippon Steel Corporation (Nippon Steel, 2009) are as provided in the following table.

Table 2-1. Chemical Composition of Low Strength Steels

Brand Name	Chemical Composition (%)						
	C	Si	Mn	P	S	N	Ceq
BT-LYP100	≤ 0.01	≤ 0.03	≤ 0.20	≤ 0.025	≤ 0.015	≤ 0.006	≤ 0.36
BT-LYP225	≤ 0.10	≤ 0.05	≤ 0.50	≤ 0.025	≤ 0.015	≤ 0.006	≤ 0.36

General elongation properties of 50% or more are guaranteed for BT-LYP100 and 40% or more for BT-LYP225, thus offering large deformation capacity required of vibration dampers. Yield point of 30~36 ksi is provided for BT-LYP225 with tensile strength of 43.5~58 ksi. 0.2% proof stress of 11.6~17.5 ksi is given for BT-LYP100 with tensile strength of 29~43.5 ksi (Nippon Steel, 2009).

2.2.2. Low Cycle Fatigue and Energy Dissipation of Low Strength Steel

During an earthquake, members are repeatedly exposed to strain amplitude beyond yield point; thus a lot of importance is given in testing the low-cycle fatigue properties of the materials used for seismic applications (Yamaguchi, et al., 1998). Low cycle fatigue tests are characterized by repeatedly straining the specimen beyond the yield point at certain strain amplitudes until failure is observed. This is what typically happens with structural components under seismic loads. When a ground motion hits a structure, these components undergo large strain during high intensity vibrations. Using low cycle fatigue tests, materials are tested for ability to avoid sudden fracture under large strains.

In moderate to strong seismic events, strain rates on structural components can go as high as 2-4%/sec. The strain rate for cyclic loading is usually determined considering the member size and the inter-story drift angle. However, experimental data shows that the strain rate at which cyclic load is applied does not significantly affect the cyclic stress-strain behavior (Dusicka, et al., 2007). According to Saeki et al. (1998), the effect of strain rate is 20-30% in initial cycles, and diminishes in half of the number of cycles to failure.

The overall fatigue life is similar for the plate steels with different yield strength (Dusicka et al., 2007; Saeki et al., 1998; Nakamura et al., 2000). See Figure 2-3 and Figure 2-14 for the low cycle fatigue comparison of different steel material obtained from BRB specimen tests and coupon tests respectively.

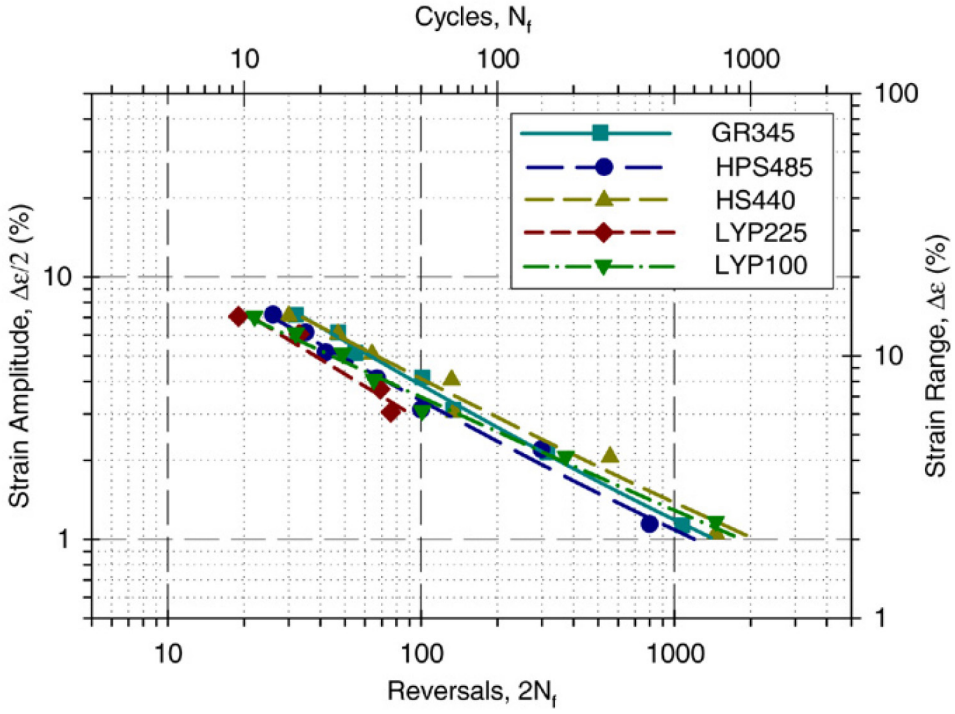

Figure 2-14. Low Cycle Fatigue for Five Different Steel Types Obtained from Coupon Tests (From Dusicka et al., 2007: Used with Permission)

Figure 2-15 shows the cumulative hysteresis energy-total strain range curves for pure iron (P), LYP100 (L), LYP235 (H), and SS400 (S). The energy absorption capacity of low yield steels is not superior to that of mild steels when total strain amplitude is more than 0.8%, but it is extremely good when total strain amplitude is less than 0.7%. Especially between 0.1% to 0.3% strain amplitude, where mild steels are elastic and have no energy absorption capacity, low yield point steels have a great absorption capacity (Saeki et al., 1998).

2.2.3. Material Availability and Application

LYP grades are available in plates in Japan market, but currently not available in US market. BT-LYP100 and BT-LYP225 are provided in the category of "Steel for Elasto-plastic Hysteretic type Dampers for Building Structures" by Nippon Steel Corporation (Nippon Steel, 2009). Standard available sizes for LYP grades are as given in Table 2-2. The cost of LYP100 steel is about twice the cost of A36 steel.

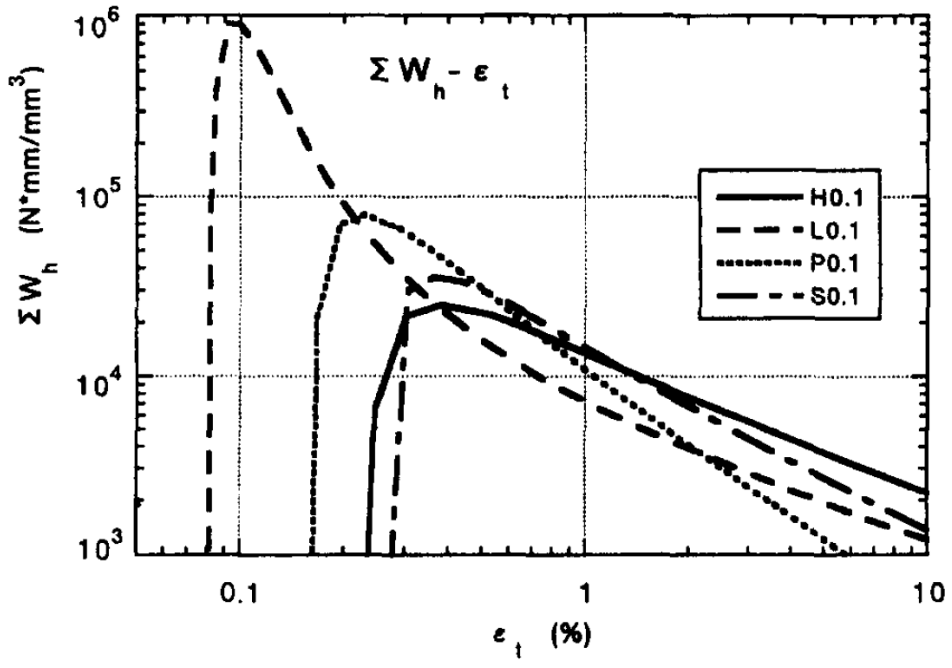

Figure 2-15. Cumulative Hysteresis Energy ($\sum W_h$) -Total Strain Amplitude (ε_t) Relationship (log scale), (From Saeki et al., 1998: Used with Permission)

Table 2-2. Standard Available Sizes of LYP Steels

Thickness	0.24 ~ 1.97 in. (6 ~ 50 mm)
Length	118.11 ~ 314.96 in. (3000 ~ 8000 mm)
Width	39.37 ~ 98.43 in. (1000 ~ 2500 mm)

Types of seismic control devices developed using LYP steel are shown in Figure 2-16. Types of devices can be classified as axial yield, as shown in (a) in the figure, and shear yield as shown in (b) to (e) in the figure (Yamaguchi, et al., 1998).

Due to the low yield point and high ductility, the LYP grades have been specifically developed and studied extensively for the development of the axial-yield type hysteretic dampers. One of the most common techniques for damage control is to provide BRB specimens that use LYP grade steels as load carrying elements. A study conducted by Chen et al. (2001) on a simple three story frame with BRB specimens including LYP100 steel as load carrying elements has been reported to have shown excellent performance by assigning higher strength ratio (required strength divided by provided strength) to braces and a lower strength ratio to the beams and columns. This approach ensures that yielding occurs in brace members keeping the other members elastic during major earthquakes.

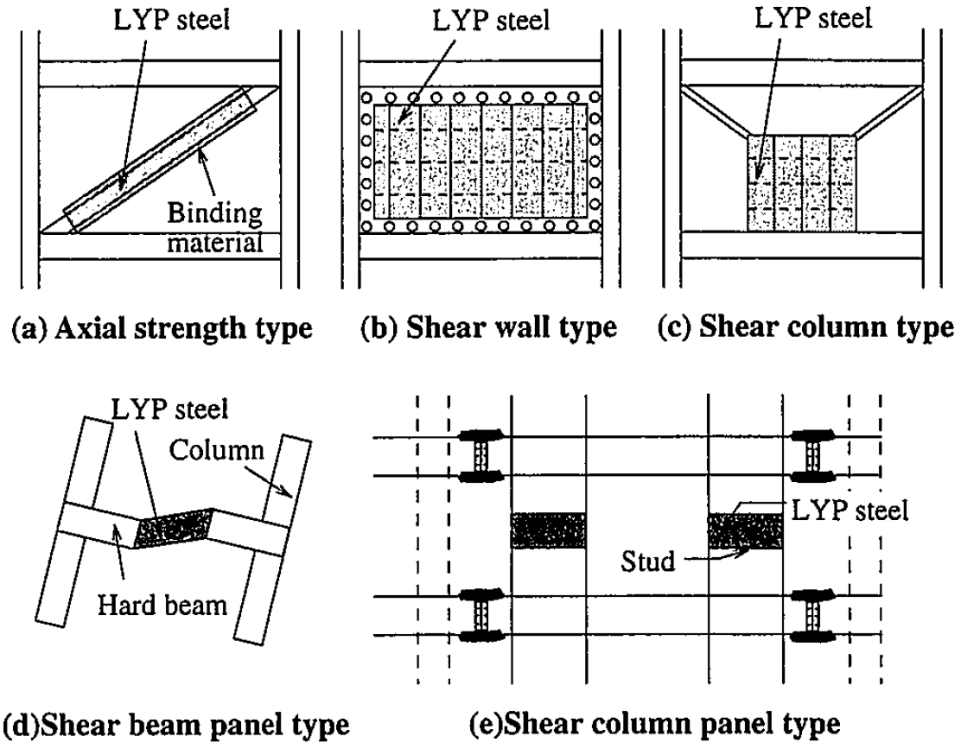

Figure 2-16. Types of Seismic Control Devices using LYP Steel (From Yamaguchi, et al., 1998: Used with Permission)

Shear yield type devices with LYP have also been studied before. In one of these studies by Nakashima et al. (1994), LYP100 type steel was used as shear panels. The tested shear panels yielded at a shear force that is approximately 1/3 of the yield shear force of equivalent shear panels made of common mild steel. Shear panels exhibited stable hysteresis ensuring large energy dissipation capacity. Sufficient strain hardening was observed in the shear panels tested and energy dissipation capacity of about 1.5 times larger than that of an equivalent linear elastic-perfectly plastic system was obtained (Nakashima, et al., 1994).

De Matteis et al. (2003) examined the seismic response of moment resisting steel frames enhanced with low yield shear panels made of LYP100. Carrying out a parametric analysis varying several parameters as strength, stiffness, hysteretic behavior and ductility of shear panels, it was found that beneficial effect of low yield shear panels appears to be significantly dependent on both yield strength ratio and secondary stiffness ratio. Acting as hysteretic dampers, low yield shear panels supplied a large source of energy dissipation resulting in a limitation of plastic deformation demand to the primary structure (De Matteis et al., 2003).

Similarly, Vian and Bruneau (2004) tested specimens utilized with LYS steel plates having yield stress of 24 ksi and ultimate strength of 43 ksi. The lower yield strength and thickness of the tested panels resulted in a reduced stiffness and earlier onset of energy dissipation by the panel as compared to currently available hot-rolled plate.

2.3. Stainless Steel

Another alternative for highly ductile low strength steel is stainless steel (SS). SS is about four times the cost of carbon steel and is not a popular or a common choice of material in building construction (Di Sarno et al., 2006). Most common type of stainless steel (SS) grades used in structural purpose is austenitic and ferric type. However, the ferric SS alloys do not possess required ductility. The mechanical properties and the chemical composition of austenitic SS grade are provided in section A276 of ASTM. The austenitic stainless steel alloys have low yield stress and relatively high ultimate tensile stress compared to standard carbon steel. Moreover SS is durable and has excellent corrosion resistance characteristics. Table 2-3 provides the list of austenitic SS grades and their mechanical properties as per ASTM A276 standard (ASTM, 2009).

Table 2-3. Austenitic SS Grade Properties (ASTM A276)

Grade	Type	Yield Stress (ksi)	Tensile Stress (ksi)	Elongation (%)	Elastic Modulus, E (ksi)	Finish	Diameter or Thickness
Austenitic SS Grades	304L, 316L	25	70	40	≈ 28,000	Hot/cold finish	All
	304N, 316N	35	80	30			
	302, 302B, 304	25-30	70-75	40			
	304LN, 305, 308						
	309 , 309S						
	309Cb, 310, 310S						
	317, 321, 347, 348						

Typically these austenitic type grades have yield stress around 25-35ksi. The material does not have a defined yield point hence yield stress is defined by taking the values corresponding to 0.2% proof stress.

Tests have suggested that the yield strength of stainless steel varies with the thickness of a member (Di Sarno et al., 2006). A general stress strain plot for stainless steel looks as given in Figure 2-17. The ultimate strain for common austenitic stainless steel grades is approximately 40-60% compared to 20-30% for carbon steel (Gardner, 2005). SS exhibits significant strain hardening region which could be helpful under cyclic loading in terms of energy dissipation. The fatigue characteristic of stainless steel is similar to that of carbon steel (European Commision, 2001).

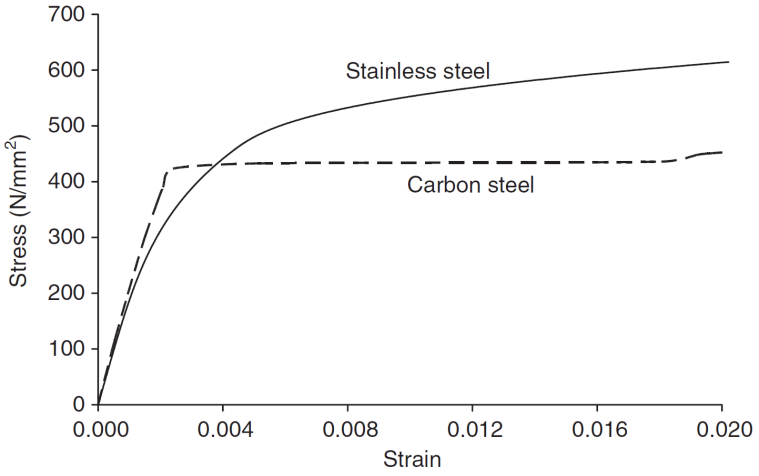

Figure 2-17. Comparison of Stress-Strain Relationship between Stainless Steel and Carbon Steel (From Gardner, 2005: Used with Permission)

As mentioned earlier, the cost of SS is about four times the cost of carbon steel. However, this cost comparison between SS and carbon steel is based on the initial material expense. The Steel Construction Institute compared life-cycle costs of offshore structures made from stainless steel, carbon steel and aluminum. While making the comparison, in addition to the initial material costs, corrosion, fire resistance, and potential losses during maintenance were also considered. According to this study, stainless steel and aluminum provided significant life-cycle cost savings as compared to carbon steel (Gardner, 2005 and Shuttleworth, 1989). Another life cycle cost study is made by Gardner et al. (2007) on an office building by using stainless steel, carbon steel and aluminum materials. Assuming a design life of 50 years, and different scenarios for inspection, maintenance and end-of-life costs of the buildings, the life cycle cost of the office building was estimated. Although the durability and residual value of aluminum and stainless steel offered cost savings, the carbon steel building remained the most economical solution for all the scenarios considered. In the same study by Gardner et al. (2007), a similar comparison was made on a bridge, and the life-cycle-cost of the bridge with stainless steel gave the most

economical solution. Thus, the savings with stainless steel over carbon steel depends on the amount of exposed areas of the building structure that these materials are used.

Stainless steel is available in a wide variety of sizes and sections. In terms of wide flange sections, it is available up to 24 in. deep beams, W24s.

DiSarno et al. (2008) studied the influence of stainless steel members on global structural behavior. The study consisted of modeling a five story building with three different structural systems to resist lateral load: concentrically, eccentrically braced frames and moment frame. Further, each system was modeled multiple times, using stainless steel on different members. For example, the CBF system was modeled with SS braces, SS braces and columns, SS columns only, and so on. Models were analyzed using pushover and nonlinear response history analysis. The results demonstrated excellent energy dissipation capacity from SS members.

The performance was evaluated using SEAOC provisions. Observations showed better performance from structural systems with SS braces and SS braces and columns compared to the same system consisting of all carbon steel members. Increase in the over-strength was observed about 33%. Also, with SS braces, systems showed higher energy dissipation capacity, resulting into smaller roof drifts.

Prior to comparing CBF and EBF, DiSarno, et al. (2006) studied the performance of a moment frame and a CBF using SS members. Comparison was done considering similar performance based criteria. Results indicated that the frames with SS members show better overall ductility and overstrength compared to the identical frames when modeled with carbon steel members.

Thus, SS can be considered as an alternative to the LYP steels discussed in the previous section. Although LYP steels are more ductile and have lower yield strengths than SS, SS is easier to obtain and it is available in a wide range of sections. The use of stainless steel is particularly attractive for moment frames because SS is available as wide flange sections (I beams) up to 24 in. depth (W24s).

2.4. Past Research on Hybrid Moment Frames

The hybrid moment frame concept was investigated by Atlayan (2008) and Charney and Atlayan (2011) through preliminary analysis. A summary of that work is provided herein.

The Hybrid Moment Frame concept was demonstrated by the analysis of a five-bay nine-story frame building, located near Seattle, Washington. The geometry of this building is identical to that studied in the

SAC Steel Project (FEMA, 2000a). Four different frame configurations were used in this study. The first configuration, Hybrid-0, is closest to the regular frame design, because the same girder sizes were used for each bay in a given story. The other three configurations are the real hybrid designs, referred to Hybrid-1, Hybrid-2, and Hybrid-3 frames, as the girder sizes for these frames are different in different bays. The Hybrid-0 frame is the least hybrid (closest in design to the traditional frame), and Hybrid-3 frame is the most hybrid (furthest in design concept from the traditional frame). Figure 2-18 shows the member sizes used for the different frames. Member sizes for the girders are shown above each girder, with the Hybrid-0 frame at the bottom and the Hybrid-3 frame at the top. The column sizes were the same for all of the designs.

The two exterior girders of the hybrid frames (bays 1 and 5) were designed and detailed as special moment frames (SMF), the two interior girders (bays 2 and 4) were designed and detailed as intermediate moment frames (IMF) and the middle girder (bay 3) was designed and detailed as an ordinary moment frame (OMF). Because of this reason, a new response reduction factor, R, and deflection amplification factor, C_d, were assumed as 6 and 5, respectively, for hybrid frame design. Note that these values were close to the weighted average R and C_d values of the SMF (2 bays), IMF (2 bays), and OMF (1 bay). After the sections of the Hybrid-0 were found by using R = 6 and C_d = 5, the plastic capacities were changed throughout the story for the other real hybrid frames. The plastic capacities of the exterior girders were decreased by 25%, 37.5% and 50% for the Hybrid-1, Hybrid-2 and Hybrid-3 frames, respectively. Since the main idea of the hybrid frame concept is to keep the total strength of the story the same, the plastic capacity of the middle girder was increased by 50%, 75% and 100% for the Hybrid-1, Hybrid-2 and Hybrid-3 frames, respectively. Bay-2 and Bay-4 girder capacities were kept the same for all the frames. In summary, as the frame identification number gets bigger, the frames become more hybrid with a greater variation in beam sizes at each story. The column sections were kept the same for all the designs but the panel zone doubler plate thicknesses were changed as necessary. Reduced beam sections were used for all the girders except for the girder in the middle bay, which was designed according to the rules for an OMF. The strong column - weak beam requirement was satisfied at the joints of the columns on column lines 1, 2, 5, and 6.

Material nonlinearity was considered through assigning a bilinear moment-rotation relationship to beams and columns. Two percent strain hardening was used in the development of moment-rotation relationships. Panel zones were explicitly represented by use of Krawinkler model (Charney and Marshall, 2006). P-Delta effects were included in all analysis, using a special linear "leaner column," which captures the entire gravity load tributary to the leaning columns. The inherent damping was determined by setting the critical damping ratio to 2% at the natural period of the structure and at a period

of 0.2 sec, as it was done in the SAC Report (FEMA, 2000a). A more detailed description of beam-column, and panel zone design and modeling information can be found in Atlayan (2008).

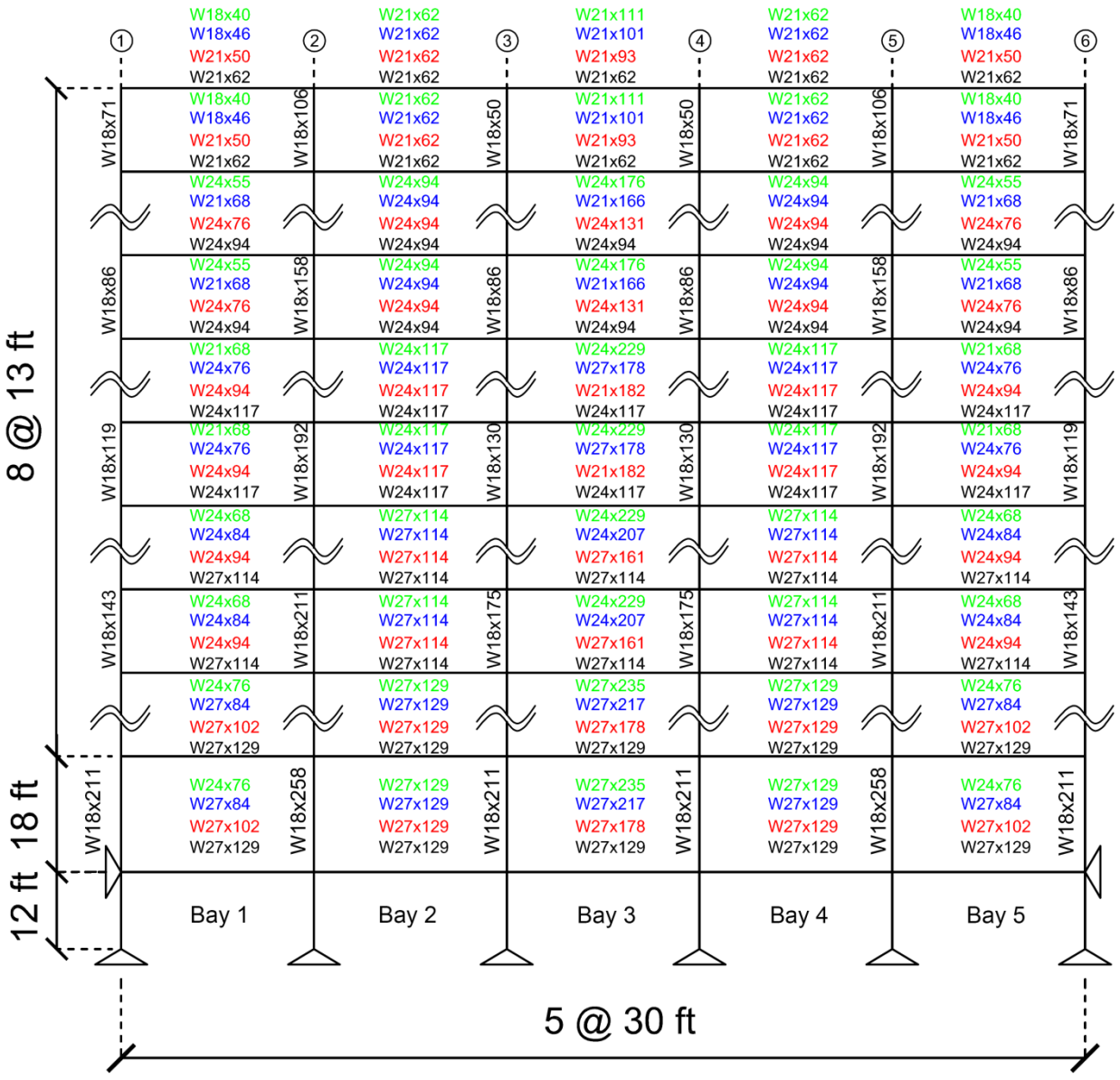

Figure 2-18. Member Sizes used for Hybrid-0 to Hybrid-3 Frames (bottom to top) (From Charney and Atlayan, 2011: Used with Permission)

All structural analyses were conducted using Perform-3D (CSI, 2006), using a planar model consisting of one of the two perimeter frames that are parallel to the design ground motion. Two types of analysis were performed for each frame: nonlinear static pushover analysis and incremental dynamic analysis (IDA).

2.4.1. Nonlinear Static Pushover Analysis

Nonlinear static pushover curves for the four different Hybrid frames are illustrated in Figure 2-19. Note that the point of the first significant yield and the point at which the post-yield curve becomes negative are shown on the figure. As expected, Hybrid-3 frame starts yielding first, and Hybrid-0 frame yields last. The more reduction in the plastic capacity of the exterior bays, the earlier the structure starts yielding. In addition, the negative post yield stiffness of the pushover curves is reached later as the frames become more hybrid. It is foreseen that the early yielding of the pushover curve will provide hysteretic energy dissipation to the frame, which will result in a better dynamic behavior under gentle ground motions. Furthermore, negative post yield stiffness has a significant effect on structures and is a significant contributor to dynamic instability. Although the frames were pushed until they reached 4% roof drift, it is predicted that the Hybrid-0 (normal frame) will reach a steeper negative stiffness than the real hybrid frames if the frames are pushed more than 4% reference drift. This behavior may be observed in the last portion of Figure 2-19.

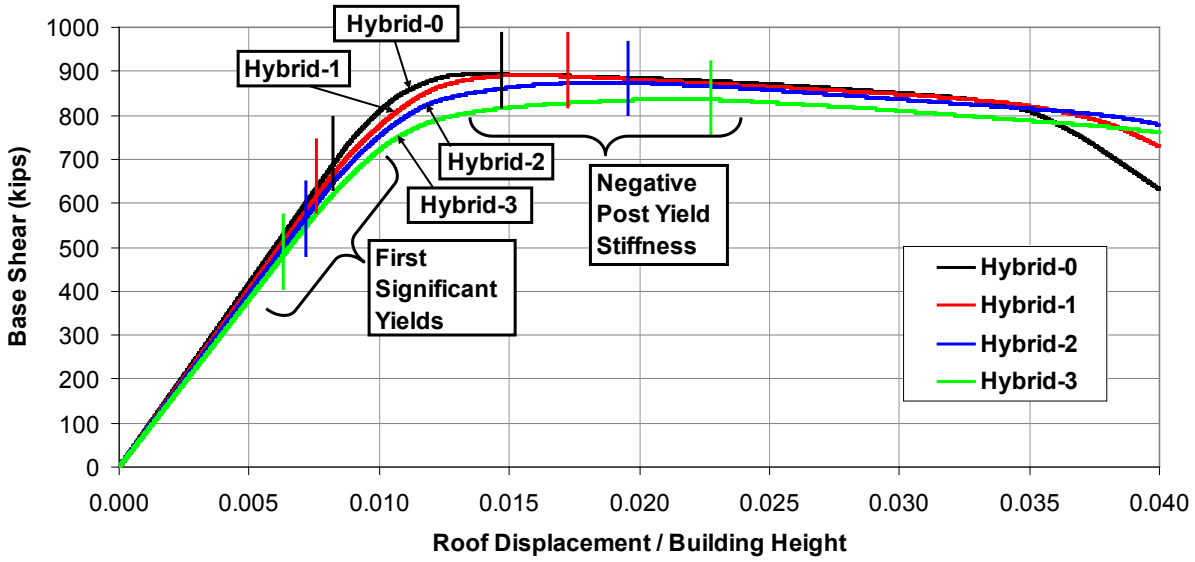

Figure 2-19. Static Pushover Curves for Hybrid Frames (From Charney and Atlayan, 2011: Used with Permission)

2.4.2. Incremental Dynamic Analysis (IDA)

IDA was conducted using ten different earthquake records at intensities of 0.2 to 2.0 times the ground motion scaled to match the design basis earthquake. The ground motions were selected from *FEMA 355-C* (FEMA, 2000a). Figure 2-20 and Figure 2-21 illustrate the roof displacement response histories of

hybrid frames subjected to Miyagi Oki and Valparaiso-2 earthquakes with scale factors of 2.0 and 1.6 times the anchored design spectrum scaling, respectively. These two earthquakes are the most severe ones out of all the earthquakes used in this study. As can be seen from Figure 2-20, Hybrid-0, Hybrid-1, and Hybrid-2 frames reach dynamic instability whereas the Hybrid-3 frame, the most hybrid frame, resists the collapse with 60 in. residual displacement at the roof level. Similarly, all of the real hybrid frames (except the normal frame, Hybrid-0) resist the collapse under 1.6 times DBE scaled Valparaiso-2 motion (See Figure 2-21). Note that Hybrid-2 frame results in the smallest residual displacement in Figure 2-21.

Figure 2-22 shows the roof displacement response histories when the frames are subjected to Shallow Interpolate-2 earthquake with IDA scaling of 2.0. Although none of the frames collapse, the residual displacement is the most for the Hybrid-0 frame, which is actually the regular frame. Similar to the behavior in Figure 2-21, the Hybrid-2 instead of the Hybrid-3 frame gives better results in terms of residual displacements.

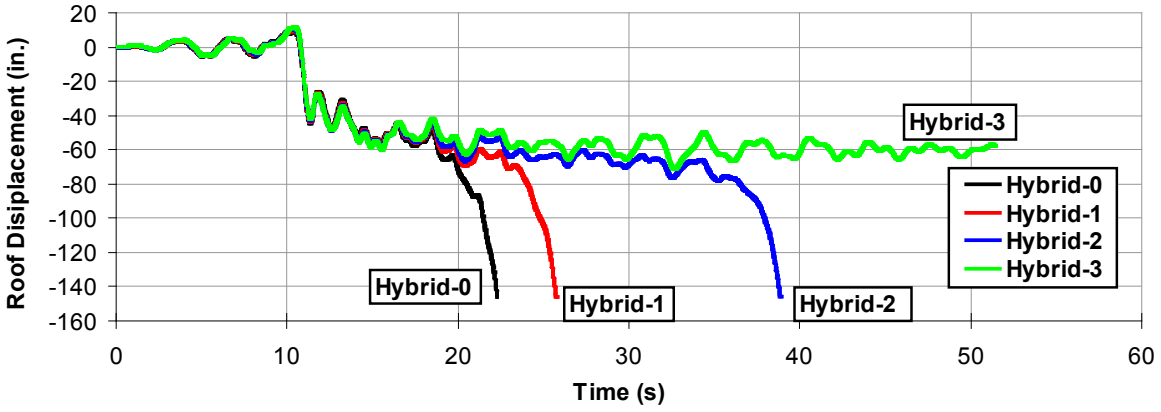

Figure 2-20. Roof Displacement Response History of Hybrid Frames subject to Miyagi Oki Earthquake with Scale of 2.0 Times the Anchored Design Spectrum Scale (From Charney and Atlayan, 2011: Used with Permission)

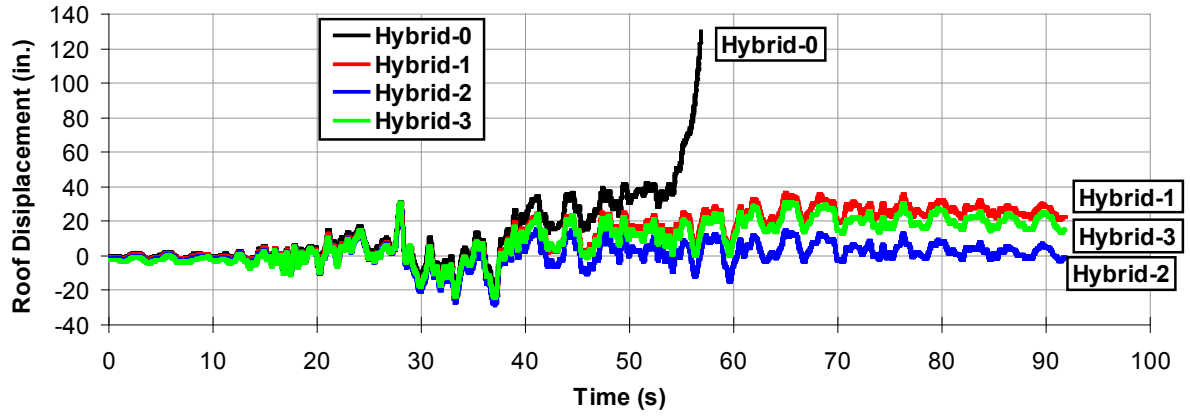

Figure 2-21. Roof Displacement Response History of Hybrid Frames subject to Valparaiso-2 Earthquake with Scale of 1.6 Times the Anchored Design Spectrum Scale (From Charney and Atlayan, 2011: Used with Permission)

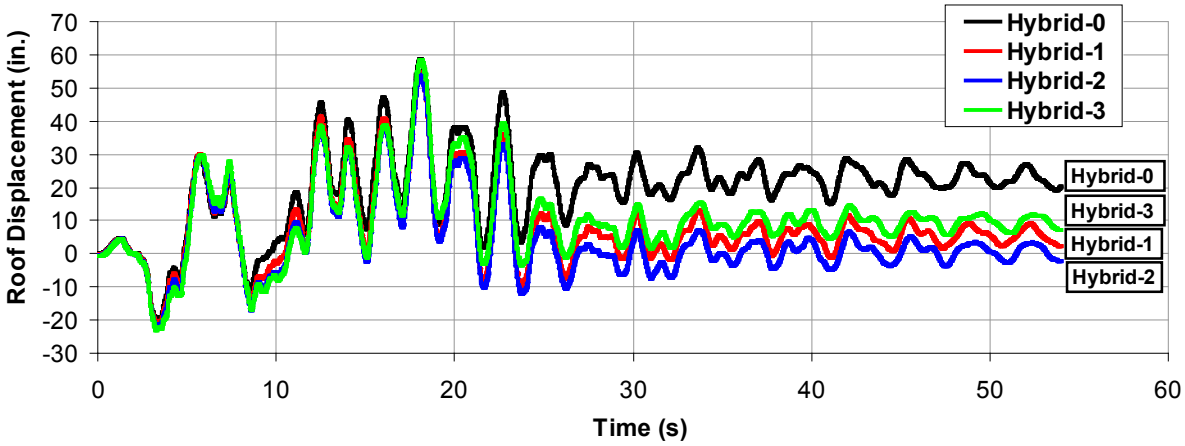

Figure 2-22. Roof Displacement Response History of Hybrid Frames subject to Shallow Interpolate-2 with Scale of 2.0 Times the Anchored Design Spectrum Scale (From Charney and Atlayan, 2011: Used with Permission)

The effect of early yielding of hybrid frames on pushover curves is observed at low scaled earthquakes. Figure 2-23 shows an example of this behavior when the frames are subjected to Mendocino earthquake. As the frames become more hybrid, the maximum displacements decrease due to hysteretic energy dissipation, which is a predicted result of early yielding.

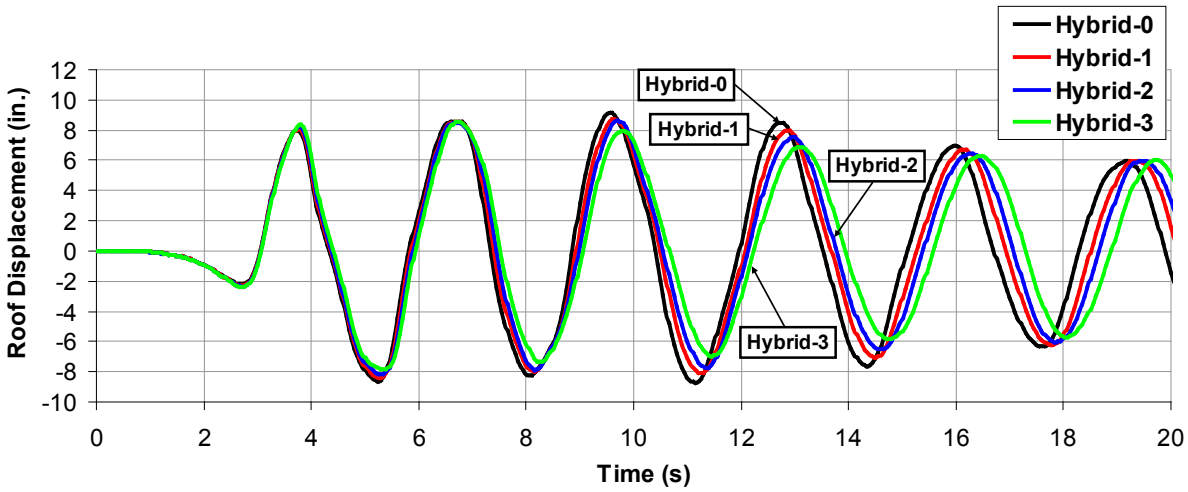

Figure 2-23. Roof Displacement Response History of Hybrid Frames subject to Mendocino Earthquake with Scale of 0.4 times the Anchored Design Spectrum Scale (From Charney and Atlayan, 2011: Used with Permission)

Figures 24(a) and 24(b) illustrate the residual displacement IDA plots when the hybrid frames are subjected to Shallow Interplate-2 and Valparaiso-1 ground motions respectively. The real hybrid frames (Hybrid-1, 2, and 3) result in better results (less residual displacements) for Shallow Interplate-2. The results of Valparaiso-1 are close, however, hybrid frames (especially Hybrid-2 and 3) result in more residual displacements than the normal frame.

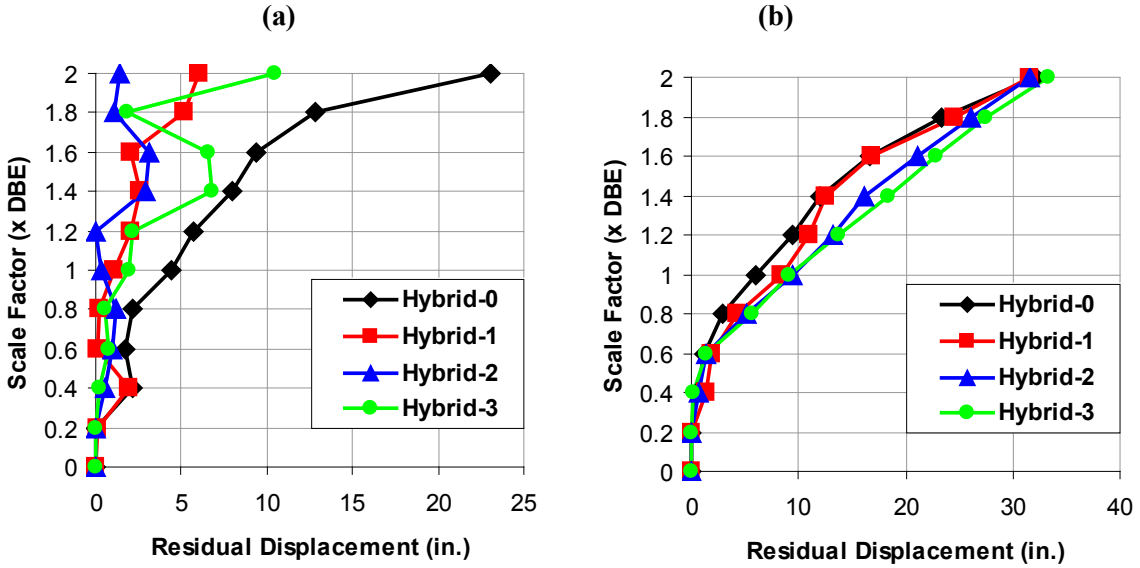

Figure 2-24. IDA Plots for Residual Roof Displacement using (a) Shallow Interplate-2 and (b) Valparaiso-1 Ground Motions (From Charney and Atlayan, 2011: Used with Permission)

In hybrid frames, there is an increase in ductility demand for the elements that are expected to yield early. Figure 2-25 illustrates the ductility demand IDA plots for the entire hybrid frames subjected to Seattle earthquake. Plastic hinge rotations of the 1st story bays were used to calculate the ductility demands.

As may be seen in Figure 2-25, Bay-1, the weakest bay referring to SMF, has higher ductility than Bay-2 and Bay-3, which correspond to IMF and OMF systems, respectively. While Bay-1 has the highest ductility demand, Bay-3 has the lowest ductility demand for all of the hybrid designs. As the frames become more hybrid (from Hybrid-0 to Hybrid-3), the ductility demand difference between the bays increases at the same level of ground motion intensity. Since the Hybrid-0 frame has the same girder sizes across the same level (story), the ductility demands of different bays are very close to each other (See Figure 2-25(a)).

As a result of this preliminary moment frame study, real hybrid frames (Hyrid-1, 2 and 3) always gave better results than Hybrid-0 (normal) frame when the structures were subjected to severe earthquakes that caused collapses or significant residual displacements, i.e., hybrid frames are useful in terms of collapse prevention. This structural behavior can be explained with the effect of the relatively late occurrence of negative post yield stiffness in Hybrid frames (See Figure 2-19). Although hybrid frames could not improve the structural performance for three out of ten ground motions, if the overall performance is considered, Hybrid frames resulted in better dynamic responses of the system.

Hewitt, et al. (2009) compared the cost of an ordinary moment frame with a special moment frame supposing that material and labor represent 30% and 70% of the total cost of the frame respectively, and 50% of the labor cost is due to special connections, and additional special inspection requirements for the connections. As a result of this scenario, the cost premium for a SMF over an OMF is about 22%. Even though this is a very rough estimate as the foundation costs were ignored and moment frames were assumed as strength controlled, labor cost associated with fabrication and inspection of the connections is significant. Since hybrid moment frame limits the number of special connections and elements, it is expected to be more economical than a special moment frame.

Due to the increase in the ductility demand of the low-strength bays of the hybrid moment frames, alternative ways were suggested to provide hybridity into the systems. In order to provide high ductility in the early yielding components of the hybrid frame, the use of low-strength steel and stainless steel was mentioned as alternative ways for hybrid moment frames.

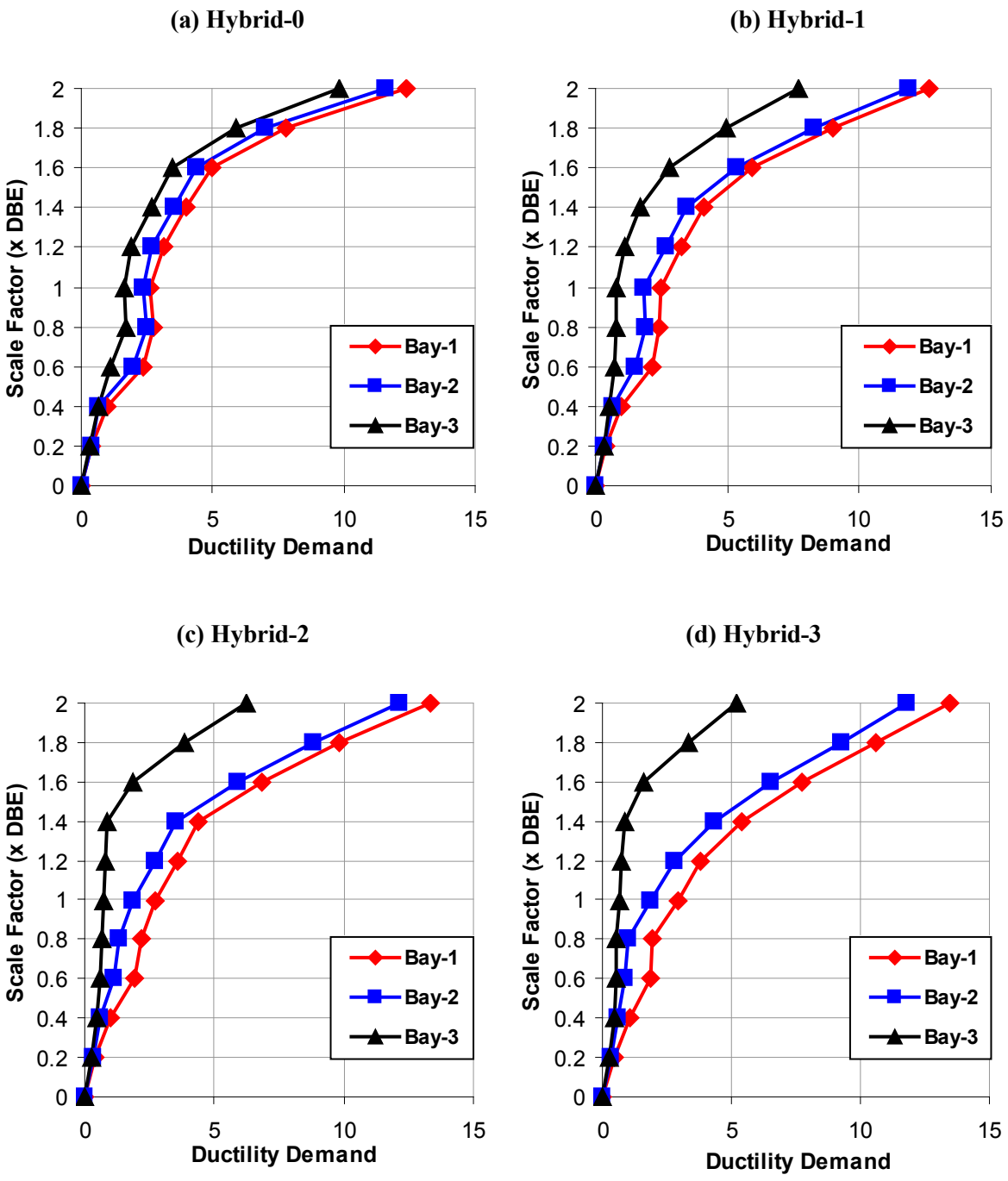

Figure 2-25. Rotational Ductility Demand IDA Plots for the 1st Story Bays of Hybrid Frames (Ground Motion: Seattle) (From Charney and Atlayan, 2011: Used with Permission)

2.4.3. Limitations of Previous Research on Hybrid Steel Moment Frames and Additional Background Information for Moment Frames

The previous work by Atlayan (2008) had certain limitations. The work was conducted prior to the availability of *FEMA P-695* methodology and only a nine-story building frame was investigated with ten ground motions. Cyclic deterioration in strength and stiffness of the steel components of the analyzed buildings was neglected. These limitations prompted further investigation of hybrid moment resisting steel frames which is discussed in Chapter 5 of this dissertation.

A different hybrid moment frame study similar to the work of Atlayan (2008) is not available in the literature. However, the effects of member size, model geometry and steel yield strength on plastic rotation capacities are discussed in a report by SAC Steel Program: *FEMA-355D, State of the Art Report on Connection Performance* (FEMA, 2000b). This report evaluates the pre and post Northridge connections and provides rotational capacities to various moment frame connections. The rotational capacities suggested in this report are still used in practice through *ASCE 41-06, Seismic Rehabilitation of Existing Buildings* (ASCE, 2006b).

Regarding the beam depth, less ductility is expected from deep beams than from shallow beams. This is expected for all connection types, and the amount of reduction depends on the connection type. For example, the reduction in ductility or plastic rotation capacity is not significant for reduced beam section connections (FEMA, 2000b). If two beams with different depths but with the same material and flange geometry are compared, the maximum plastic curvature of the deep beam will be smaller than that of the shallow beam. Plastic rotations are calculated by integrating the plastic curvature over the yield length. Thus, for the same beam lengths, smaller plastic rotations are achieved for deeper beams. Also, deeper beams are more susceptible to low-cycle fatigue (El Tawil et al., 1998). The dependency of rotation capacities on the beam depth are explained in details in *FEMA-355D* and are also tabulated in *ASCE 41-06*. Modified Ibarra-Krawinkler model which is calibrated with 350 steel component tests are used in the analyses conducted in Chapter 5 of this dissertation. The plastic capacity and deterioration parameters of this model are related to various section parameters including the depth of the beam. While the girder sections of hybrid moment frames were selected, the change in plastic capacities was checked and possible reductions in plastic capacities were tried to be kept minimum. This is further discussed in Chapter 5.

Short-span beams have less inelastic rotational capacity than longer span beams (FEMA, 2000b). The length of the beam does not change the maximum strain level capacity or maximum curvature that can be

achieved with a given beam section. The plastic rotation depends on the length of the beam if the depth is constant. For a shorter length beam, the plastic curvature is accumulated over a proportionally shorter length and thus the achievable plastic rotation by that beam is reduced. When the regular moment frames were made hybrid in Chapter 5 and 6 of this dissertation, the span lengths were kept the same. Thus, the change in span length was not considered as an alternative to change the yielding sequence or the plastic behavior of the hybrid moment frames. The change in plastic rotation capacities and deterioration parameters with respect to span length is reflected in Modified Ibarra Krawinkler model multi-regression formulas within shear span to depth ratios.

Coons (1999) checked the yield strength of mild steel from 1940 to 1990 and showed that there is a steady increase in the average yield stress of steel and this contributed to the reduced ductility of the pre-Northridge connections. Analyses were conducted by Chi et al. (1997) and El Tawil et al. (1998) showed that the reduced yield stress of the beam results in larger plastic strains, and early yielding in the beam, which is caused by reduced yield stress, delayed the high hydrostatic and principle stress development which would otherwise cause brittle fracture of the connection (FEMA, 2000b). The results of the analysis conducted by Chi et al. (1997) and El Tawil et al. (1998) match with the findings of stainless steel usage as wide flange members which is discussed in Section 2.3 of this dissertation. In the hybrid moment frame study conducted in Chapter 5 of this dissertation, the expected yield strength of wide flange steel members were assumed as 55 ksi for all the steel components of both regular and hybrid frames. Thus, the possibility of low yield strength steel usage as wide flange steel sections is not investigated in this dissertation. However, low yield point steel (LYP100), which is available in plates, is investigated on new connection types, where yielding is occurring in the plates, through preliminary analyses in Chapter 6.

CHAPTER 3: SUMMARY OF *FEMA P-695* METHODOLOGY

This chapter provides a summary of *ATC-63* project report, *Quantification of Building Seismic Performance Factors* (FEMA, 2009), also known as *FEMA P-695* methodology. All of the nonlinear analyses discussed in the following chapters were performed according to this methodology.

FEMA P-695 methodology is used to evaluate the seismic performance factors, including the response modification coefficient (R), the system overstrength factor (Ω_0), and the deflection amplification factor (C_d), of new building structural systems. The primary objective of this methodology is to determine these seismic performance factors so that when they are implemented in the design process, they will result in equivalent earthquake performance of buildings having different lateral-force resisting systems.

3.1. Basis of *FEMA P-695* Methodology

The principles of the methodology can be summarized as follows (FEMA, 2009):

- It is applicable to the evaluation of lateral force resisting systems of new building structures.
- It is compatible and intended for use with *NEHRP Recommended Provisions* (FEMA, 2004a) and seismic provisions of *ASCE 7-05* (ASCE, 2006a).
- It is only based on life safety performance objective and does not address damage protection and functionality issues. Seismic importance factor, I_e, of 1.0 is assumed which stands for occupancy (risk) categories of I and II in *ASCE 7*.
- It achieves the life safety performance objective by providing uniform protection against partial or global instability of the seismic system for Maximum Considered Earthquake (MCE) level ground motions.
- It evaluates collapse under MCE level ground motions which are based on spectral response parameters of *ASCE 7*, including site class effects.
- It is consistent with the seismic performance factor definitions of *ASCE 7*, and the nonlinear static analysis concepts of *NEHRP Provisions* (FEMA, 2004b).
- It does not explicitly address gravity system and nonstructural components as it assumes that deformation compatibility and related *ASCE 7* requirements protect such components against premature failure.

Figure 3-1 defines the seismic performance factors on a pushover curve. The seismic design procedure requires the elastic design force, V_E, to be divided by the R factor to find the design base shear, V.

Assumed drift levels, δ, for inelastic design are calculated by multiplying the roof drift, δ_E/R, (design base shear drift level) with the C_d factor. Thus, buildings are designed at a force level of V and a displacement level of δ as shown in Figure 3-1. Ω_0 is the ratio of the maximum strength, V_{max}, of the yielded system, to the design base shear, V. The methodology develops seismic performance factors consistent with the concepts and definitions described herein.

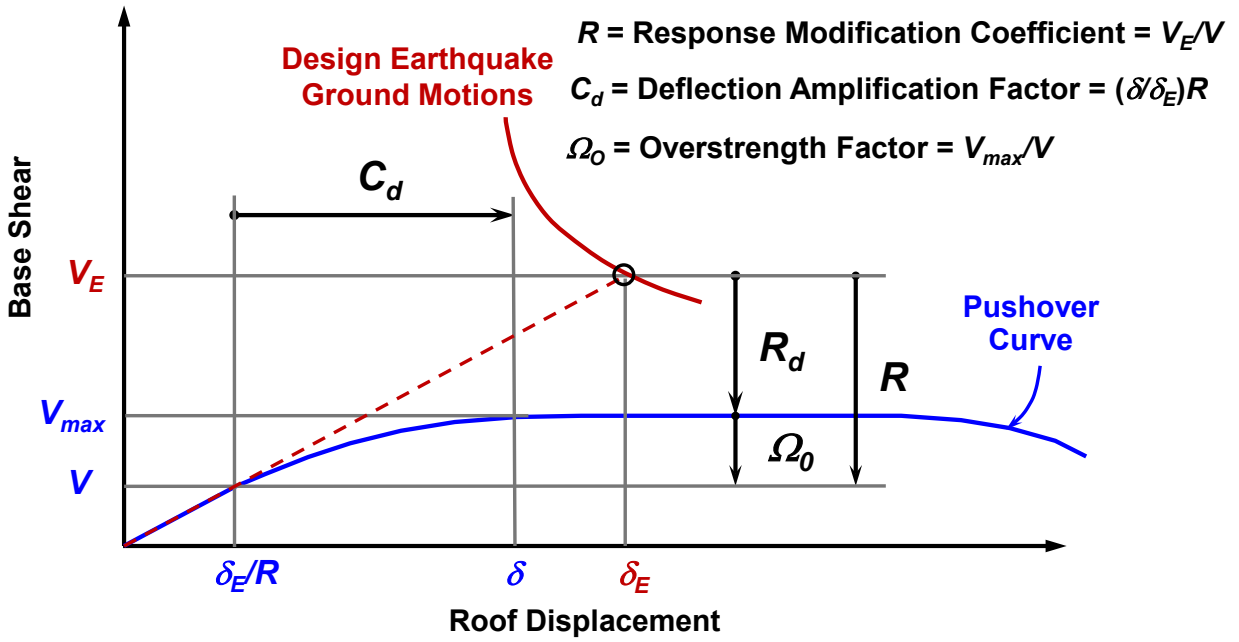

Figure 3-1. Definition of Seismic Performance Factors as Defined in *NEHRP Recommended Provisions* (From FEMA, 2009: Used under Fair Use)

Figure 3-2 illustrates the seismic performance factors as defined by the methodology. Figure 3-2 matches the pushover curve in Figure 3-1 using spectral coordinates rather than force displacement coordinates. While converting the coordinates, it is assumed that the whole seismic weight of the structure participates in the fundamental period, T (FEMA, 2009).

In Figure 3-2, the term S_{MT} is the MCE level spectral acceleration at the fundamental period of the system, T, the term S_{max} is the maximum strength of the fully yielded system normalized by the effective seismic weight, W, and C_s is the seismic response coefficient which is defined as the ratio of design base shear, V, to the effective seismic weight of the structure, W. The ratio of the S_{MT} to the C_s is 1.5 times the R factor because design basis earthquakes of *ASCE 7* are two-thirds of MCE level earthquakes.

The methodology requires the overstrength factor to be calculated from the nonlinear pushover analysis. The overstrength parameter, Ω, is defined as the ratio of S_{max} to the C_s in Figure 3-2, which is essentially

the same as the ratio of V_{max} to the V in Figure 3-1.

As may be seen in Figure 3-2, the methodology defines the inelastic system displacement at the MCE level, SD_{MT}, as $1.5C_d$ times the spectral displacement corresponding to C_s. This is based on the Newmark equal displacement concept which defines the C_d factor to be equal to the R factor.

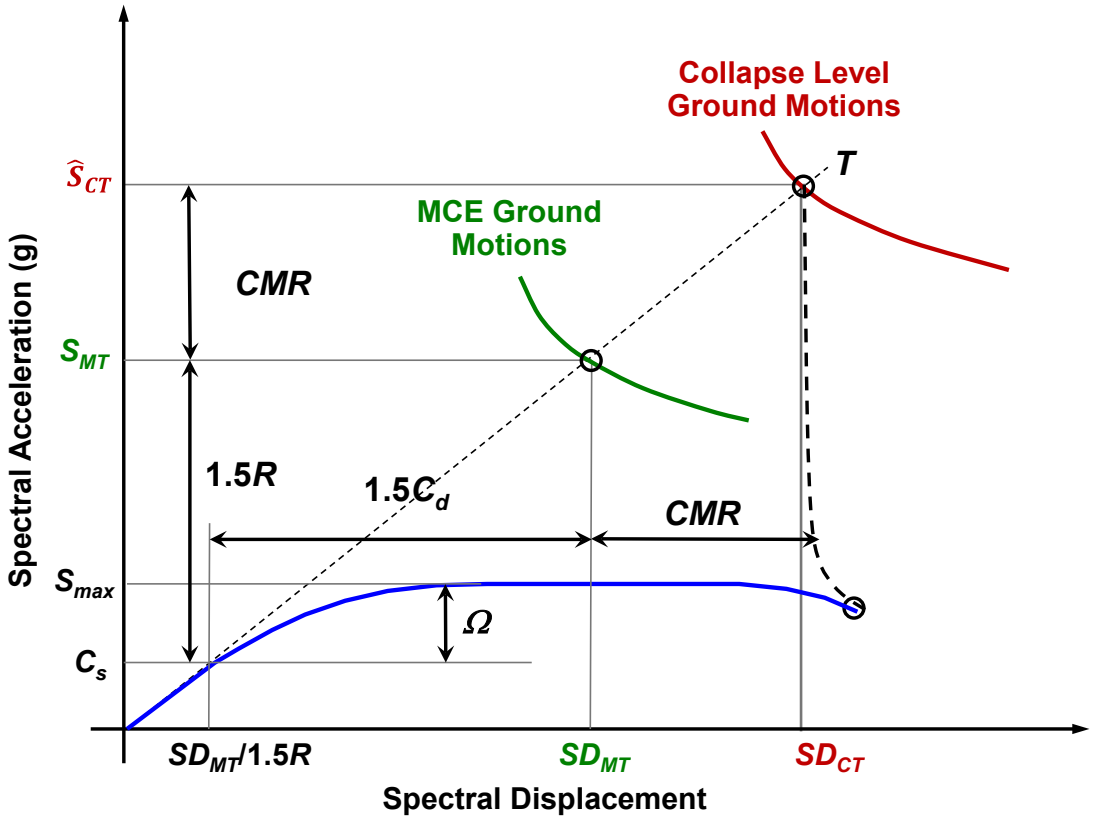

Figure 3-2. Seismic Performance Factors as Defined by the *FEMA P-695* Methodology (From FEMA, 2009: Used under Fair Use)

The methodology defines collapse margin ratios (*CMRs*) as the ratio of median collapse intensity, $\hat{S}_{CT}$, to the MCE level earthquake spectral demand, S_{MT}. *CMRs* can also be explained as the amount that S_{MT} must be increased so that 50% of the ground motions will cause collapse of the building system.

3.2. Overview of *FEMA P-695* Methodology

Figure 3-3 shows the flowchart of the *FEMA P-695* process. The process starts with the development of a concept for the decision of seismic force resisting system, system configuration, construction materials and inelastic dissipation mechanisms. Then, the required system information, such as material, component

test data and detailed design requirements, is obtained. Next step is to characterize the system behavior through structural system archetype development. While defining archetypes, various characteristics such as seismic design category, building height (fundamental period), bay sizes, framing configurations, and magnitude of gravity loads are considered. Later, nonlinear models are developed. Models should explicitly simulate collapse modes, if not; non-simulated collapse modes should be defined. Models also need to be calibrated using material or component test data. The next step is to perform nonlinear static and dynamic analyses.

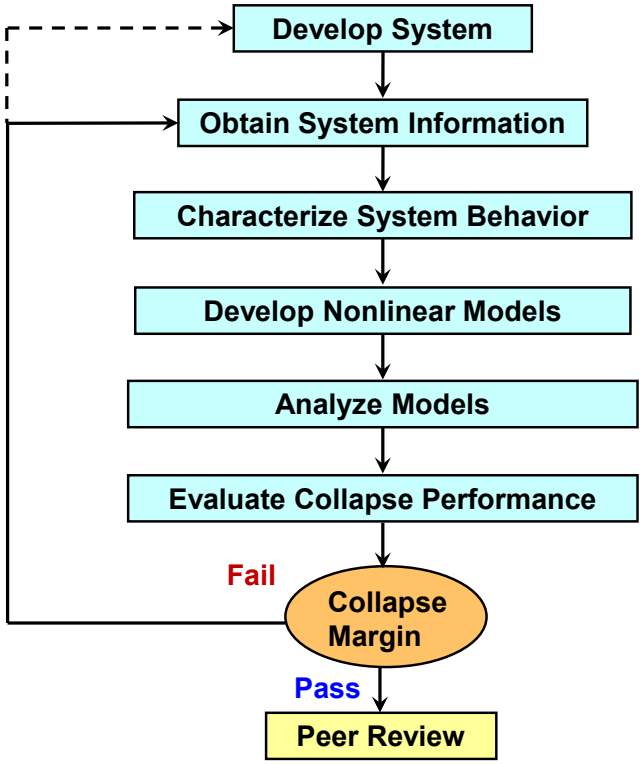

Figure 3-3. *FEMA P-695* Methodology Flow Chart

Performance evaluation is done by using collapse margin ratios (*CMRs*). After the *CMRs* are found, they are adjusted to account for unique characteristics of extreme ground motions that lead to building collapse. This adjustment is a function of period based ductility and structural period and it is based on the shape of the spectrum of rare ground motions. Adjusted *CMRs* are compared against the acceptable *CMRs* which are defined in terms of an acceptably low collapse probability for MCE ground motions. Acceptable *CMRs* are a function of total system uncertainty which is based on the test data-related uncertainty, design requirements-related uncertainty, record-to record uncertainty and analytical model uncertainty. The probability of collapse due to MCE ground motions applied to a population of archetypes (performance group) is limited to 10%. In order to eliminate potential outliers within a performance

group, 20% collapse probability is acceptable for individual archetypes.

If the adjusted collapse margin ratio is greater than the acceptable collapse margin ratio, then the trial value of *R* for the building system is acceptable and the results are documented for peer review. If not, the system must be redefined by adjusting the design requirements such as using a lower *R* factor for the building system.

3.3. Performance Evaluation Procedure of *FEMA P-695* Methodology

As explained in the previous section, performance evaluation is done through the calculation of collapse margin ratios (*CMRs*), which is defined as the amount that MCE spectral demand must be increased so that half of the ground motions will cause collapse of the building. Figure 3-4 illustrates the calculation of *CMR* of a 4 story BRBF archetype. As may be seen in the figure, *CMR* is the ratio of $\hat{S}_{CT}$ to S_{MT}. If the ground motions are anchored at MCE level, then they are basically normalized by S_{MT}, and further scaling of the ground motions through incremental dynamic analysis will directly give the *CMR* (see the secondary Y axis in Figure 3-4).

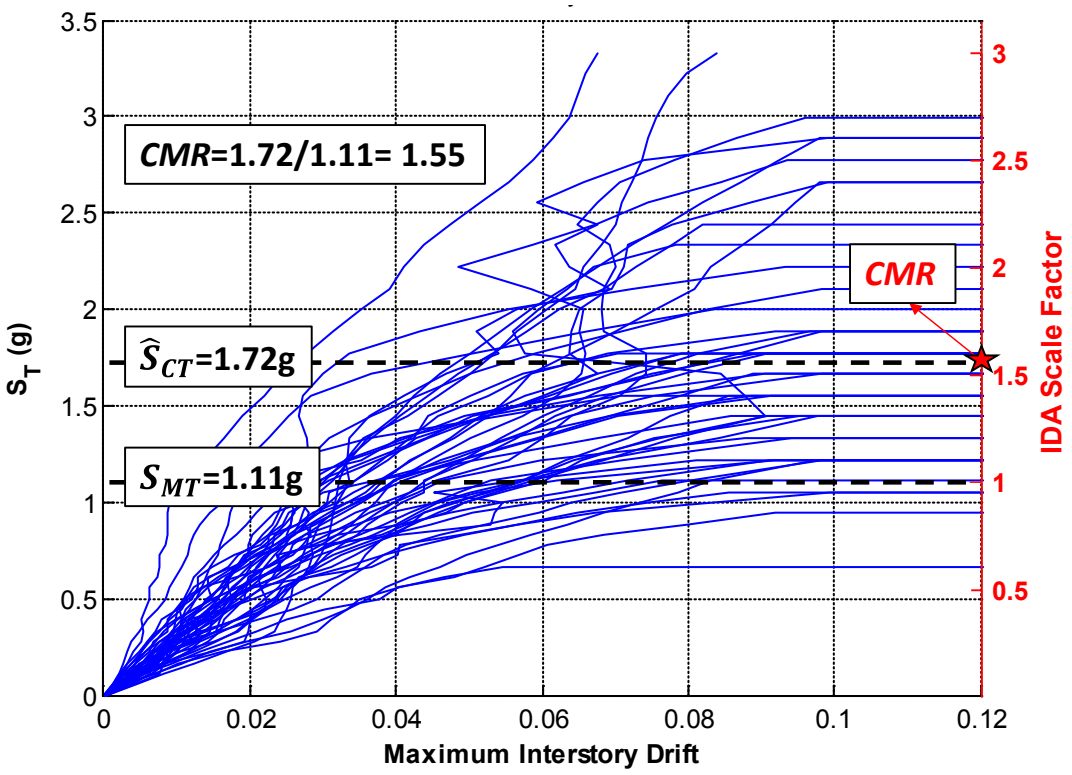

Figure 3-4. Incremental Response History Analyses of a 4 story BRBF Archetype Displaying *CMR* Calculation

According to the *FEMA P-695* methodology, *CMRs* should be adjusted with respect to the spectral shape factors (*SSF*). *SSF* is a function of fundamental period, *T*, seismic design category, and period based ductility, μ_T. Eq. 3-1 shows the calculation of *SSF*. *SSF* depends on three factors: β_1, $\bar{\varepsilon}_o(T)$, and $\bar{\varepsilon}(T)_{,records}$. The β_1 factor indicates the sensitivity of the collapse capacity to the changes in the spectral shape, ε. Buildings with large inelastic deformation capacity have dramatic period elongation which makes long period response more important in collapse evaluation. This causes the spectral shape, ε, to become more important. The β_1 factor is used to quantify this kind of spectral shape effects on collapse capacity. Eq. 3-2, which relates β_1 to the period based ductility, μ_T, was derived from 5 building data sets and a total of 118 buildings (FEMA, 2009). $\bar{\varepsilon}_o(T)$ is the expected or target ground motion spectral shape which depends on site and hazard level of interest. In the methodology, target $\bar{\varepsilon}_o(T)$ value of 1.5 is used for seismic design category (SDC) D, and 1.0 is used for SDCs B and C. These values were determined from the mean of up to more than 20,000 data points for different zip codes in the USA. $\bar{\varepsilon}(T)_{,records}$ is a factor for spectral shape adjustment and it depends on the fundamental period, *T* (see Eq. 3-3). Eq. 3-3 is computed using Abrahamson and Silva attenuation model (FEMA, 2009).

$$SSF = exp\left[\beta_1\left(\bar{\varepsilon}_o(T) - \bar{\varepsilon}(T)_{,records}\right)\right] \quad \text{(Eq. 3-1)}$$

$$\beta_1 = (0.14)(\mu_T - 1)^{0.42} \quad \text{(Eq. 3-2)}$$

$$\bar{\varepsilon}(T)_{,records} = (0.6)(1.5 - T) \quad \text{(Eq. 3-3)}$$

Period based ductility, μ_T, is the ratio of ultimate roof displacement, δ_u, to the effective yield roof displacement, $\delta_{y,eff}$(see Eq. 3-4). Ultimate displacement, δ_u, is found through nonlinear pushover analysis. It is assumed as the displacement where there is 20% strength loss (see Figure 3-5). Note that if a non-simulated collapse (NSC) occurs before 20% strength loss, then the roof displacement that corresponds to NSC governs δ_u. Effective roof displacement is found by a formula (see Eq. 3-5) provided in *ASCE 41-06* (ASCE, 2006b) and is a function of maximum period (T=$C_u T_a$ or T_1 = computed fundamental period from eigenvalue analysis), maximum base shear normalized by building weight (*W*), and C_0. C_0 accounts for the difference between the roof displacement of a multi degree of freedom system and the displacement of an equivalent single-degree of freedom system. Eq. 3-6 is also provided in *ASCE 41-06* (ASCE, 2006b) and first mode shape ordinates, $\emptyset_{1,x}$, are used for the calculation of C_0 in the methodology.

$$\mu_T = \frac{\delta_u}{\delta_{y,eff}} \quad \text{(Eq. 3-4)}$$

$$\delta_{y,eff} = C_0 \frac{V_{max}}{W} \left[\frac{g}{4\pi^2}\right] \left(max(T, T_1)\right)^2 \quad \text{(Eq. 3-5)}$$

$$C_0 = \emptyset_{1,r} \frac{\sum_1^N m_x \emptyset_{1,x}}{\sum_1^N m_x \emptyset_{1,x}^2} \quad \text{(Eq. 3-6)}$$

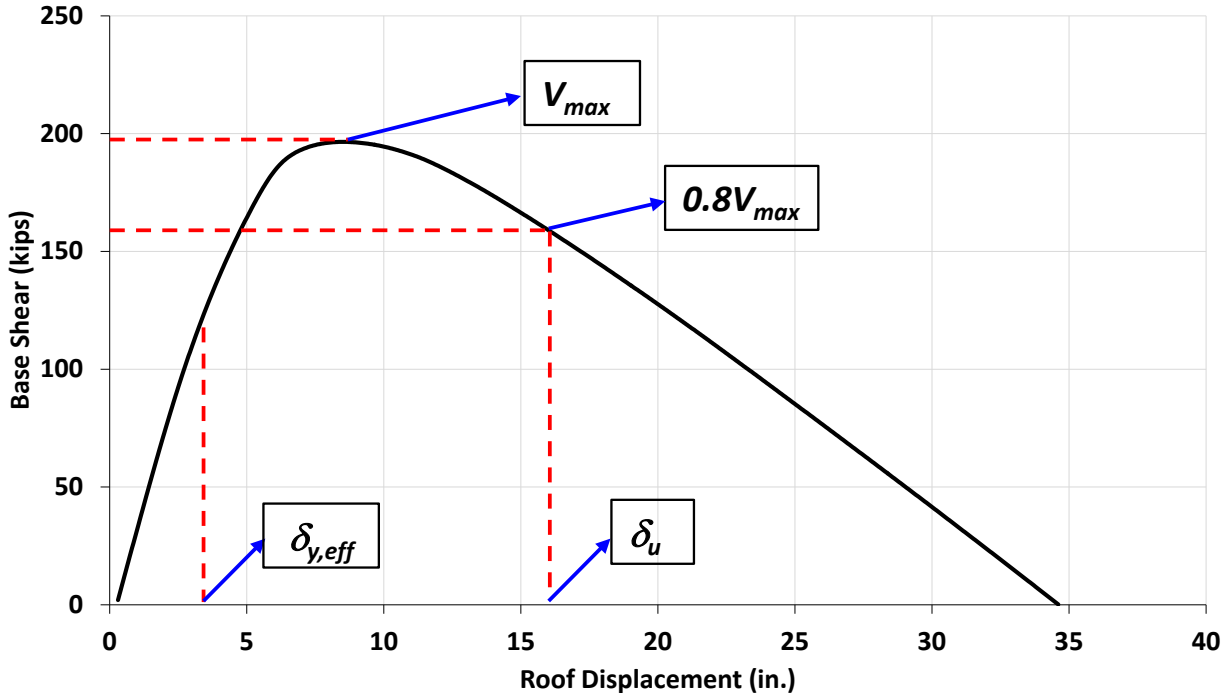

Figure 3-5. Calculation of Period Based Ductility on a 6 story BRBF Archetype Pushover Curve

Adjusted collapse margin ratios (*ACMR*) are calculated by multiplying the *CMRs* by the *SSF*.

$$ACMR = CMR \times SSF \quad \text{(Eq. 3-7)}$$

The acceptable value of *ACMR* for individual archetypes is denoted by $ACMR_{20\%}$ and the acceptable value for a performance group is denoted by $ACMR_{10\%}$. As explained before, higher collapse probability is allowed for single archetypes to eliminate the potential outliers. $ACMR_{10\%}$ and $ACMR_{20\%}$ are based on total system collapse uncertainty, β_{TOT}. Total system uncertainty is a function of β_{RTR}, β_{DR}, β_{TD}, and β_{MDL} which are record to record collapse uncertainty, design requirements-related collapse uncertainty, test-data related collapse uncertainty, and modeling-related collapse uncertainty respectively (see Eq. 3-8). Higher uncertainties result in higher acceptable *AMCRs* and it becomes more difficult for building models to pass the methodology collapse margin requirements.

$$\beta_{TOT} = \sqrt{\beta_{RTR}^2 + \beta_{DR}^2 + \beta_{TD}^2 + \beta_{MDL}^2} \quad \text{(Eq. 3-8)}$$

Finally, *ACMRs* are compared against $ACMR_{10\%}$ and $ACMR_{20\%}$. If *ACMRs* are greater than the acceptable $ACMR_{20\%}$ or $ACMR_{10\%}$, then the archetype or the performance group passes the criteria, if not, they fail.

$ACMR \geq Acceptable\ ACMR_{10\%}$ ➔Requirement for performance group to pass *FEMA P-695* criteria

$ACMR \geq Acceptable\ ACMR_{20\%}$ ➔Requirement for building archetype to pass *FEMA P-695* criteria

3.4. Nonlinear Analyses

The methodology requires both nonlinear static and dynamic analyses to be performed. Expected dead and live loads with load combination of 1.05*D*+0.25*L* are used in the analyses. The vertical distribution of the lateral force used in the pushover analyses should be in proportion to the fundamental mode of the building.

3.4.1. *FEMA P-695* Methodology Ground Motions

Nonlinear response history analyses are conducted by using the Far-Field and the Near-Field record set provided in Appendix A of *FEMA P-695* (FEMA, 2009). The Far-Field record set of *FEMA P-695* includes twenty-two horizontal ground motion pairs (44 individual components) selected from PEER NGA database. The Far-Field set includes ground motions that are recorded at sites located greater than 10km from the fault rupture. Table 3-1 tabulates the summary of the Far-Field record set. The Near-Field record set includes twenty-eight horizontal ground motion pairs which are from sites located less than 10 km from fault rupture. The Near-Field record set is divided into two subsets according to the presence of strong pulses in these records. Table 3-2 and Table 3-3 tabulate the pulse and the non-pulse record subsets of the Near-Field record set respectively. Figure 3-6 shows the response spectra of both Far-Field and Near-Field ground motion set and comparison of the median spectra. As may be seen in Figure 3-6 (d), seismic demand at long periods increases significantly for Near-Field pulse subset.

Record selection procedure of *FEMA P-695* methodology does not differentiate ground motion records according to site condition or source mechanism. The distance to fault rupture was used to develop separate Far-Field and Near-Field record sets. The methodology uses the Far-Field record set to establish the seismic performance factors of new seismic force resisting systems. The Near-Field record set is recommended for the verification of life safety performance of an individual building located near an active fault and it is useful in examining the change in collapse fragilities due to near-fault directivity and pulse effects.

In P-695 methodology, "Near-Field" and "Far-Field" terms are used to distinguish the motions with respect to their distance to fault rupture. These terms are actually used differently in engineering seismology. In elastic wave radiation, the displacement is calculated with the help of Green's function. There are three main terms inside the Green's function of displacement calculation. These terms represent "Near-Field" displacement, "Far-Field" S-wave displacement, and "Far-Field" P-wave displacement (Aki and Richards, 2009). These displacements are named according to their dependencies to the source-receiver distance, *r*. The seismic data used in geophysics are mostly collected in the Far-Field (distances at which Far-Field terms in the displacement equation are dominant), and the seismic data used in earthquake engineering is occasionally collected in the Near-Field. When one takes up in more detail the question of where the Near-Field ends and where the Far-Field begins, it becomes apparent that Far-Field terms can be big enough to cause earthquake damage to engineering structures. To summarize, in the displacement calculation of elastic wave radiation, "Far-Field" terms dominate in the Far-Field, but "Near-Field" and "Far-Field" terms are of equal importance in the Near-Field after they have been convolved with a source time function (Aki and Richards, 2009).

A method proposed by Baker (2007) was used to classify the near field ground motions as pulse or non-pulse records. This method uses wavelet-based signal processing to identify and extract the largest velocity pulse from a ground motion, and if the extracted signal is large relative to the remaining (residual) signal, the ground motion is considered as pulse-type motion. The ratios of peak ground velocity (PGV) and energy between the original and residual motions are effective predictors for this classification. Velocity pulses are mainly caused by directivity effects. A pulse may also be created, if a site is located near an asperity in the fault rupture. In addition, constructive interference of seismic waves passing through a complicated earth structure (like the edge of a geologic basin) might also result in velocity pulses. The classification method of Baker (2007) does not distinguish between the potential causal mechanisms of velocity pulses; however, they are mainly due to directivity effects. It is mentioned that ground motions can be used without further classification for structural response calculations (Baker, 2007).

The methodology specifies the use of Far-Field record set for collapse evaluation of buildings designed at Seismic Design Category (SDC) B, C, and D. The Near-Field record set is suggested for use for individual buildings that are located near an active fault and are designed at SDC E.

FEMA P-695 methodology does not require the vertical component of the ground motions for nonlinear dynamic analyses as this direction of shaking is not considered of primary importance for collapse evaluation.

Table 3-1. *FEMA P-695* Far-Field Earthquake Record Summary

ID No.	Earthquake				Site Data		Source (Fault Type)
	M	Year	Name	Recording Station	*NEHRP* Class	Vs_30 (m/sec)	
1-2	6.7	1994	Northridge	Beverly Hills - Mulhol	D	356	Thrust
3-4	6.7	1994	Northridge	Canyon Country-WLC	D	309	Thrust
5-6	7.1	1999	Duzce, Turkey	Bolu	D	326	Strike-slip
7-8	7.1	1999	Hector Mine	Hector	C	685	Strike-slip
9-10	6.5	1979	Imperial Valley	Delta	D	275	Strike-slip
11-12	6.5	1979	Imperial Valley	El Centro Array #11	D	196	Strike-slip
13-14	6.9	1995	Kobe, Japan	Nishi-Akashi	C	609	Strike-slip
15-16	6.9	1995	Kobe, Japan	Shin-Osaka	D	256	Strike-slip
17-18	7.5	1999	Kocaeli, Turkey	Duzce	D	276	Strike-slip
19-20	7.5	1999	Kocaeli, Turkey	Arcelik	C	523	Strike-slip
21-22	7.3	1992	Landers	Yermo Fire Station	D	354	Strike-slip
23-24	7.3	1992	Landers	Coolwater	D	271	Strike-slip
25-26	6.9	1989	Loma Prieta	Capitola	D	289	Strike-slip
27-28	6.9	1989	Loma Prieta	Gilroy Array #3	D	350	Strike-slip
29-30	7.4	1990	Manjil, Iran	Abbar	C	724	Strike-slip
31-32	6.5	1987	Superstition Hills	El Centro Imp. Co.	D	192	Strike-slip
33-34	6.5	1987	Superstition Hills	Poe Road (temp)	D	208	Strike-slip
35-36	7	1992	Cape Mendocino	Rio Dell Overpass	D	312	Thrust
37-38	7.6	1999	Chi-Chi, Taiwan	CHY101	D	259	Thrust
39-40	7.6	1999	Chi-Chi, Taiwan	TCU045	C	705	Thrust
41-42	6.6	1971	San Fernando	LA-Hollywood Star	D	316	Thrust
43-44	6.5	1976	Friuli, Italy	Tolmezzo	C	425	Thrust

Table 3-2. *FEMA P-695* Near-Field Earthquake Record Summary (Pulse Record Subset)

ID No.	Earthquake				Site Data		Source (Fault Type)
	M	Year	Name	Recording Station	*NEHRP* Class	Vs_30 (m/sec)	
1-2	6.5	1979	Imperial Valley-06	El Centro Array #6	D	203	Strike-slip
3-4	6.5	1979	Imperial Valley-06	El Centro Array #7	D	211	Strike-slip
5-6	6.9	1980	Irpinia, Italy-01	Sturno	B	1000	Normal
7-8	6.5	1987	Superstition Hills-02	Parachute Test Site	D	349	Strike-slip
9-10	6.9	1989	Loma Prieta	Saragota – Aloha	C	371	Strike-slip
11-12	6.7	1992	Erzincan, Turkey	Erzincan	D	275	Strike-slip
13-14	7.0	1992	Cape Mendocino	Petrolia	C	713	Thrust
15-16	7.3	1992	Landers	Lucerne	C	685	Strike-slip
17-18	6.7	1994	Northridge-01	Rinaldi Rec. Stn.	D	282	Thrust
19-20	6.7	1994	Northridge-01	Sylmar- Olive View	C	441	Thrust
21-22	7.5	1999	Kocaeli, Turkey	Izmit	B	811	Strike-slip
23-24	7.6	1999	Chi-Chi, Taiwan	TCU065	D	306	Thrust
25-26	7.6	1999	Chi-Chi, Taiwan	TCU102	C	714	Thrust
27-28	7.1	1999	Duzce, Turkey	Duzce	D	276	Strike-slip

Table 3-3. *FEMA P-695* Near-Field Earthquake Record Summary (No Pulse Record Subset)

ID No.	Earthquake				Site Data		Source (Fault Type)
	M	Year	Name	Recording Station	*NEHRP* Class	Vs_30 (m/sec)	
1-2	6.8	1976	Gazli, USSR	Karakyr	C	660	Thrust
3-4	6.5	1979	Imperial Valley-06	Bonds Corner	D	223	Strike-slip
5-6	6.5	1979	Imperial Valley-06	Chihuahua	D	275	Strike-slip
7-8	6.8	1985	Nahanni, Canada	Site 1	C	660	Thrust
9-10	6.8	1985	Nahanni, Canada	Site 2	C	660	Thrust
11-12	6.9	1989	Loma Prieta	BRAN	C	376	Strike-slip
13-14	6.9	1989	Loma Prieta	Corralitos	C	462	Strike-slip
15-16	7.0	1992	Cape Mendocino	Cape Mendocino	C	514	Thrust
17-18	6.7	1994	Northridge-01	LA- Sepulveda VA	C	380	Thrust
19-20	6.7	1994	Northridge-01	Northridge – Saticoy	D	281	Thrust
21-22	7.5	1999	Kocaeli, Turkey	Yarimca	D	297	Strike-slip
23-24	7.6	1999	Chi-Chi, Taiwan	TCU067	C	434	Thrust
25-26	7.6	1999	Chi-Chi, Taiwan	TCU084	C	553	Thrust
27-28	7.9	2002	Denali, Alaska	TAPS Pump Sta. #10	C	553	Strike-slip

3.4.2. Scaling of Ground Motions

Ground motions are scaled according to *FEMA P-695* scaling procedure which has two steps:

1) Normalization of records: Normalization is done with respect to peak ground velocity (PGV) defined in PEER NGA database, which is the geomean of two horizontal components. Ground motion pairs are rotated by one quadrant in small degree increments to find the median PGV at different record orientations (See Figure 3-7 (a)). Each ground motion pair is assigned one scale factor; thus 22 different normalization factors for Far-Field set and 14 different normalization factors were used for each Near-Field Pulse and Non-Pulse subsets.

2) Scaling of record sets: Scaling is done by anchoring the median spectra of the 44 Far-Field, or 28 Near-Field (separately for Pulse and Non-Pulse subsets) ground motions to the *ASCE 7* MCE level spectrum at $T=C_u T_a$. Thus, only one scale factor is calculated for each ground motion set and this same scale factor is applied to all the ground motions of that record set.

The product of these two scales (normalization+ anchoring) becomes the scale factor of the ground motion. Figure 3-7 shows the scaled 44 Far-Field ground motions with their median spectrum matching the *ASCE 7* MCE level spectrum at a period of 1.0 sec.

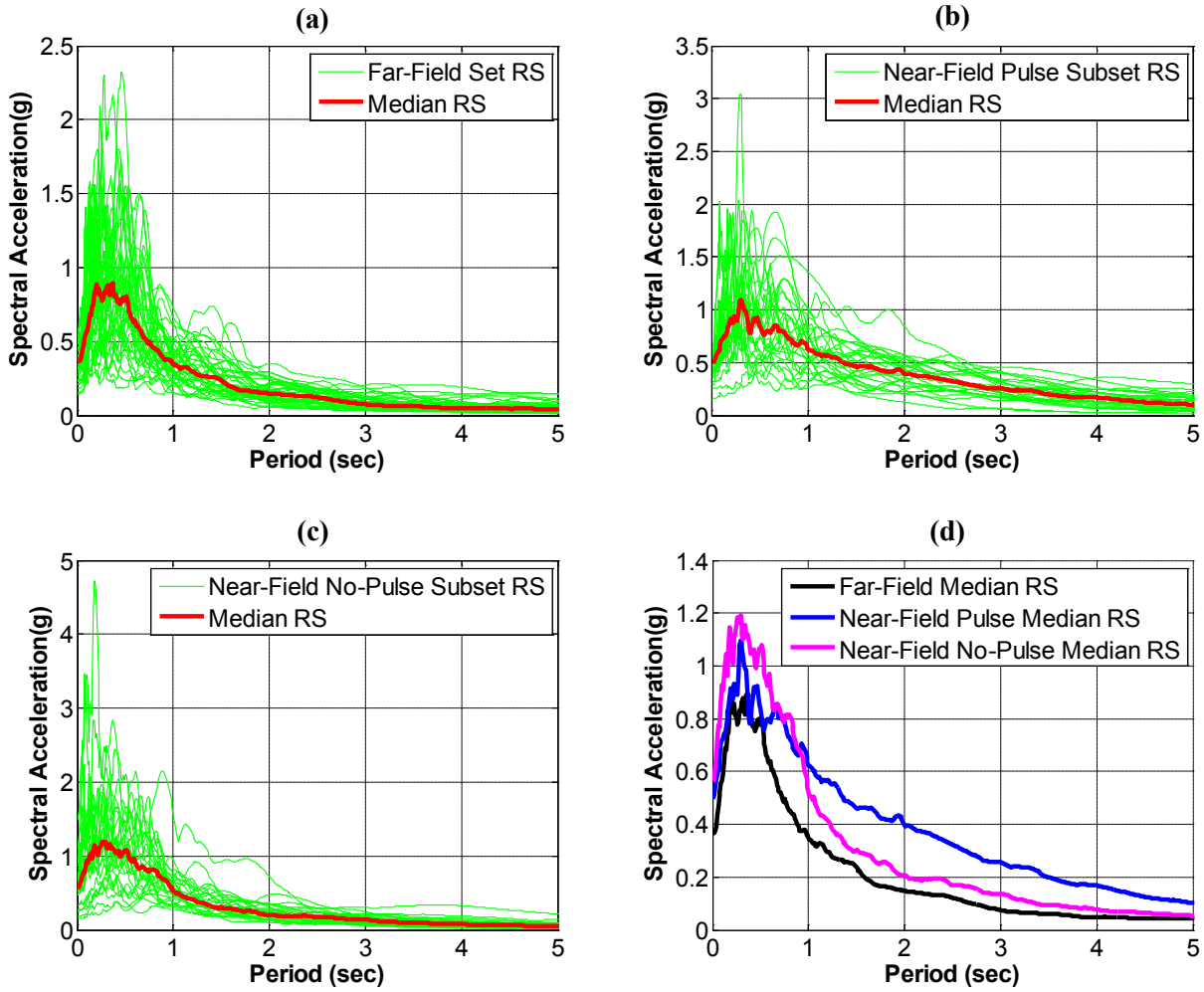

Figure 3-6. (a) Response Spectra for Far-Field Set (b) Response Spectra for Near-Field Pulse Subset (c) Response Spectra for Near-Field No-Pulse Subset (d) Comparison of Median Response Spectra

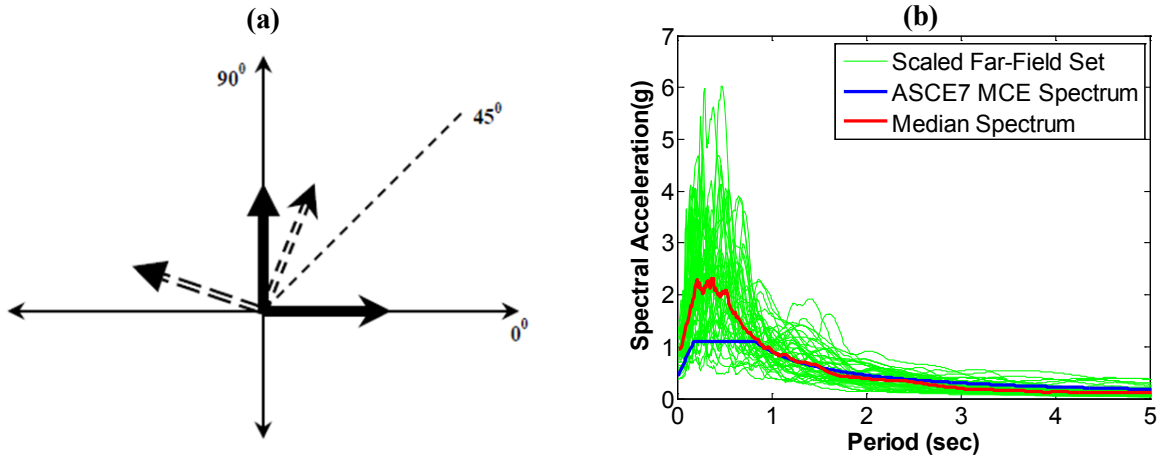

Figure 3-7. Ground Motion Scaling (a) Normalization (b) Anchoring at *T=CuTa*

3.5. Collapse Evaluation of Individual Buildings

Although the methodology is developed through structural archetype development to be able to evaluate the performance for various building characteristics, it can be adapted for individual buildings.

To assess if an individual building could pass *FEMA P-695* criteria or not, the methodology can be evaluated backwards, and collapse check intensity can be found. If half of the ground motions (22 out of 44) cause collapse at this level, then the building fails the criteria, if not it passes. Note that *CMR* cannot be calculated with this method, i.e, this method is only useful to check if the methodology passing criteria is satisfied for a single building. Eq. 3-9 shows the calculation of the collapse check level scale factor. As may be seen in the equation, acceptable *ACMR* corresponding to 10% collapse probability is used for individual buildings, similar to the evaluation of a performance group. In Eq. 3-9, C_{3D} is a three-dimensional analysis coefficient and it is taken as 1.2 for 3-D analysis, and 1.0 for 2-D analysis. S_{NRT} is the median spectral acceleration of the normalized record set. Thus, (S_{MT}/S_{NRT}) in Eq. 3.9 is basically the anchoring scale factor of the ground motions at the fundamental period of the building.

$$SF = \frac{ACMR_{10\%}}{C_{3D}SSF}\left(\frac{S_{MT}}{S_{NRT}}\right) \quad \text{(Eq. 3-9)}$$

3.6. Fragility Curves

FEMA P-695 methodology requires the analyses to be run up to a ground motion intensity at which half of the ground motions cause collapse, i.e. median collapse intensity is required to find the collapse margin ratios. For most of the analytical models discussed in the next chapters, analyses were stopped at the ground motion intensity which caused collapse for 50% of the records. Although it could be interesting to find the collapse level intensity for each earthquake, this is computationally very expensive and also not required by the methodology. The collapse probabilities that are greater than 50% are calculated with the help of fragility functions.

The Maximum Likelihood Estimation (MLE) technique, which is described by Baker (2011), was used to estimate collapse fragility functions from structural analysis data. The MLE function fits a lognormal cumulative distribution function to observed probability of collapse data using optimization on the likelihood function for the data. The MLE technique is more general than the popular fragility fitting functions derived from IDA. This method can be used with different ground motions for different intensity levels and the analysis does not have to be performed up to an intensity level at which all ground motions cause collapse. See Baker (2011) for the detailed explanation of this method.

Figure 3-8 shows an example of MLE technique on a BRBF model that is discussed in the next chapter. For this building model, nonlinear dynamic analyses were run up to ground motion intensities at which 37 out of 44 Far-Field ground motions caused collapse, which is much more than the needed 22 collapses. While fitting the fragility curve in Figure 3-8, only the collapse data up to 50% collapse probability was used. As may be seen, the fragility curve matches the real collapse data at the high intensities well.

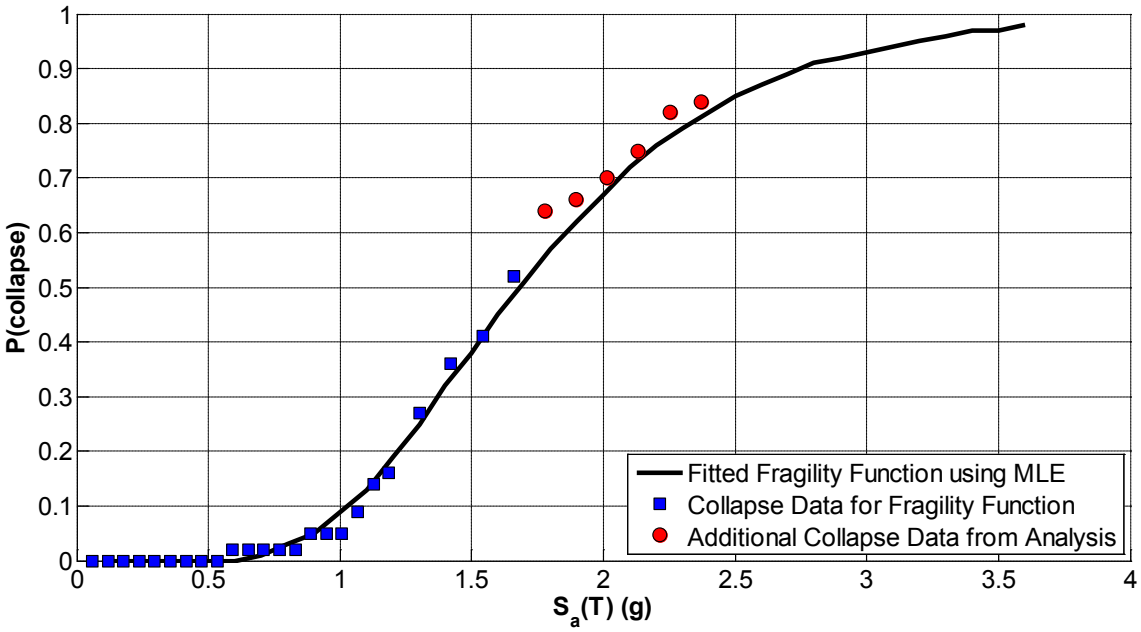

Figure 3-8. Collapse Fragility Example with MLE Technique

In the next chapters, fragility curves will be used to show the difference in collapse probability between the regular and the hybrid frames. Real collapse probability that is obtained from the empirical data is not as smooth as how it appears on the fragility curves. The difference is shown in Figure 3-9 and Figure 3-10. Figure 3-9 shows the real collapse probability which is obtained from the analysis data. Real collapse curves have variability in them, and are incomplete as the analyses are generally stopped after the median collapse intensity. However, as may be seen in Figure 3-10, fragility curves are smooth and can be extended to intensity levels that cause collapse for all ground motions.

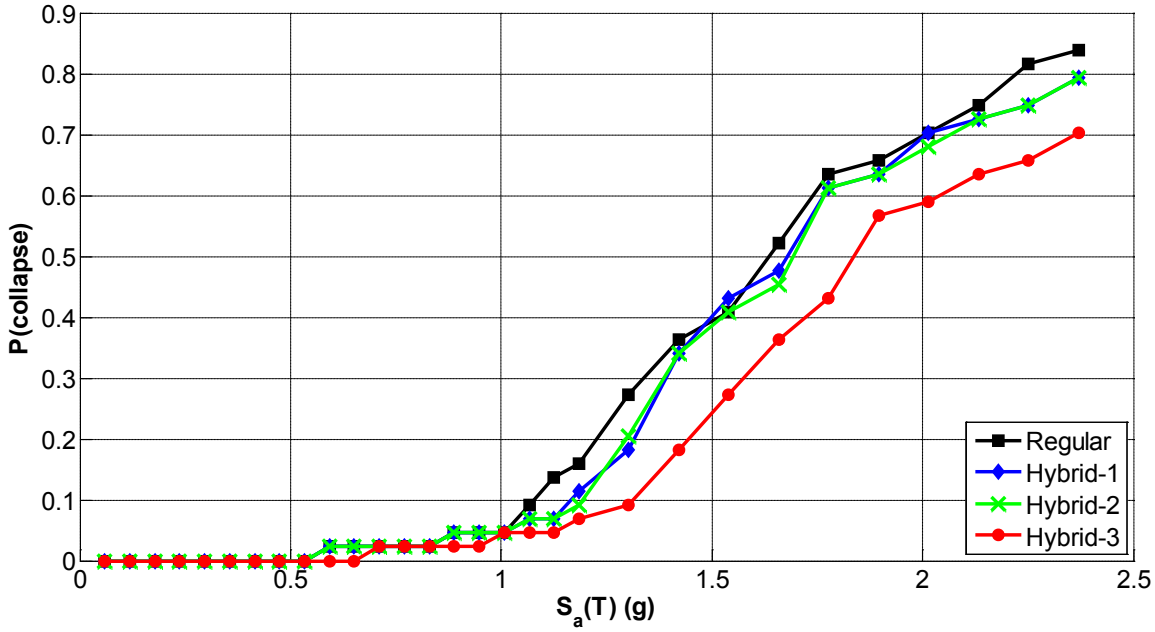

Figure 3-9. Collapse Probability Comparison Example from Real Analysis Data

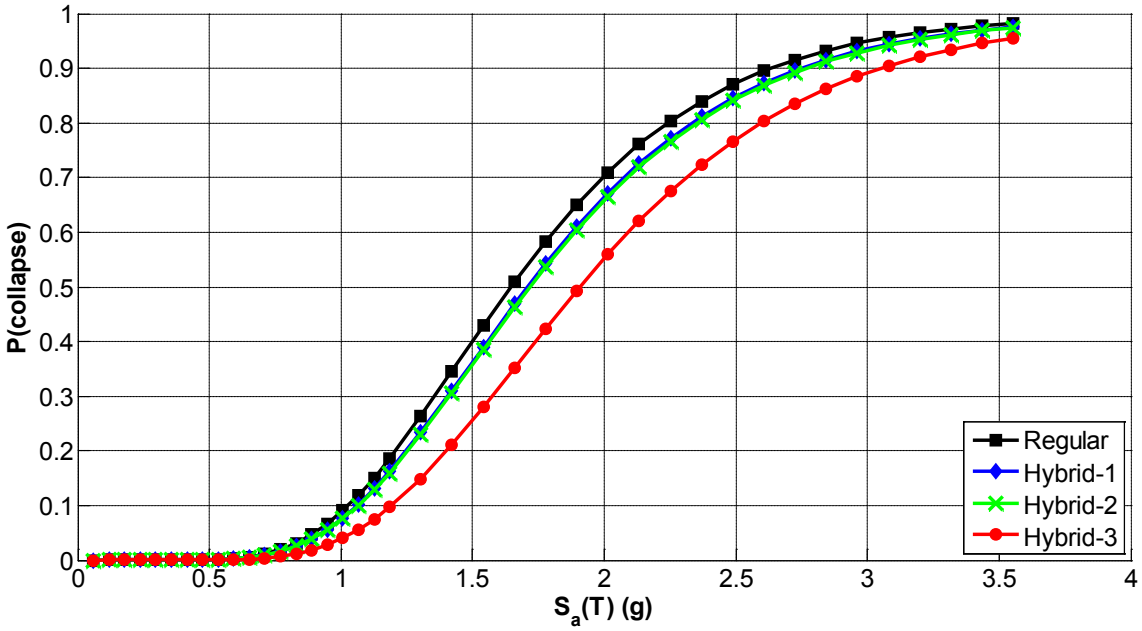

Figure 3-10. Collapse Probability Example Obtained by Fragility Fitting with MLE Technique

CHAPTER 4: HYBRID BUCKLING RESTRAINED BRACED FRAMES

This chapter compares and discusses the performance of Hybrid BRBFs and regular (nonhybrid) BRBFs. Two different case studies were investigated by comparing seismic performance at various seismic intensities including *FEMA P-695* collapse evaluation. All the concepts of *FEMA P-695* methodology summarized in the previous chapter were adapted in the modeling and analyses of the buildings. Two case studies investigated in this chapter are:

1. Five story Business Office Building (BOB) located in an area of moderate to high seismicity (close to seismic design category Dmax) with diagonal brace configuration.

2. Five story Medical Office Building (MOB) located in area of high seismicity (seismic design category E) with V-bracing configuration.

In addition, the BRBF performance groups (PG) included in Chapter 7 of *ATC-76-1* project (NIST, 2010) are also investigated their results are discussed in Appendix A of this dissertation. The summary of these performance groups are as follows:

1. Long period Performance Group including four, six, nine, twelve, and eighteen story archetypes designed at seismic design category Dmax.

2. Long period Performance Group including two, three, four, six, nine, twelve, and eighteen story archetypes designed at seismic design category Dmin.

3. Short period Performance Group including one, two, and three story archetypes designed at seismic design category Dmax.

The modeling techniques of the BRBF models are explained on the BOB model, which is a five story office building. For all the other BRBFs investigated in this dissertation, similar modeling assumptions were used.

4.1. Case Study 1: Five Story Business Office Building (BOB)

The performance of hybrid BRBs was investigated on a five story three bay BRBF office building. The building model is provided as an example in the book by Bruneau et al. (2011). Figure 4-1 shows the (a) plan and (b) elevation views of the building model. As may be seen in Figure 4-1(a), there are two braced frames located at the perimeter of the building for each direction. The analyses were conducted on one of the perimeter braced frames as highlighted in Figure 4-1(a).

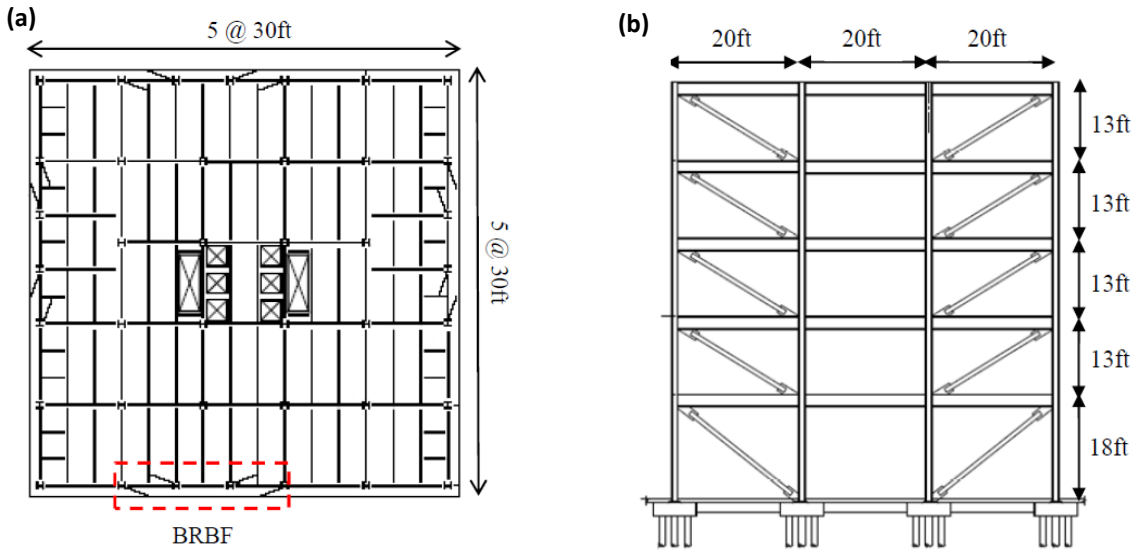

Figure 4-1. (a) Plan and (b) Elevation Views of BRBF Used for Hybrid Frame Analyses

The requirements of *ASCE 7* (ASCE, 2006a) and *AISC 341* (AISC, 2010a) were applied in the design of this model. Table 4-1 tabulates the seismic design data and the gravity loads of the BOB. As may be seen in the seismic design data, this building is located in an area of moderate to high seismicity. The design spectral acceleration at 1.0 sec, S_{D1}, is the same as SDC Dmax level design spectral acceleration at 1.0 sec. Table 4-2 displays the member sizes of this BRBF building.

Table 4-1. Seismic Design Data and Gravity Loads for the BOB Model

S_S	1.0g	I	1.0
S_1	0.60g	**Code based period, T**	1.02 sec
Site Class	D	**Seismic weight**	12512 kips
S_{DS}	0.733g	**Base shear**	$0.074W$
S_{D1}	0.60g	**Floor / Roof dead load**	100 psf
R	8	**Floor live load**	50 psf
C_d	5	**Roof live load**	20 psf
Ω_o	2.5	**Cladding load**	20 psf

Table 4-2. Member Sizes of BRBF

Level / story	Brace Area (in.^{2})	Beams	Columns	
			Exterior	Interior
Roof	-	W18x50	-	-
5	3.0	W18x60	W14x74	W14x68
4	4.5	W21x73	W14x74	W14x68
3	6.0	W21x73	W14x74	W14x68
2	7.0	W21x83	W14x145	W14x132
Ground	8.0	-	W14x145	W14x132

4.1.1. Nonlinear Model Details

Two dimensional analyses were conducted on the model shown in Figure 4-1 using OpenSees (Mazzoni et al. 2006). Columns were fixed at the base and were oriented to resist lateral forces through strong axis bending. Nonlinear beam-column elements with fiber sections were used to model beams and columns. Rigid offsets were used at the beam column connections and brace to frame connections to model the gusset plates. BRBs were modeled with a corotational truss element with yielding steel core area. Since a single truss element was used for the whole brace, equivalent elastic modulus was used to model the yielding and the nonyielding core (tapered ends) of the brace. Consistent with the design, the total brace stiffness was calibrated to be 1.5 times the single truss element stiffness (with yielding core area) that would extend from work-point to work-point. Both moment resisting (MR) and non-moment resisting (NMR) beam-column connections were used for the braced bay connections (1st and 3rd bays). NMR beam-column connections were used for the middle bay. Inherent damping was modeled as Rayleigh damping by setting the critical damping ratio to 2% at the fundamental (T_1=1.37 sec.) and third modes (T_3=0.27 sec.) of the structure. A leaning column was used to model second order effects. The effect of the gravity framing system was neglected in the models. Figure 4-2 shows the summary of model details.

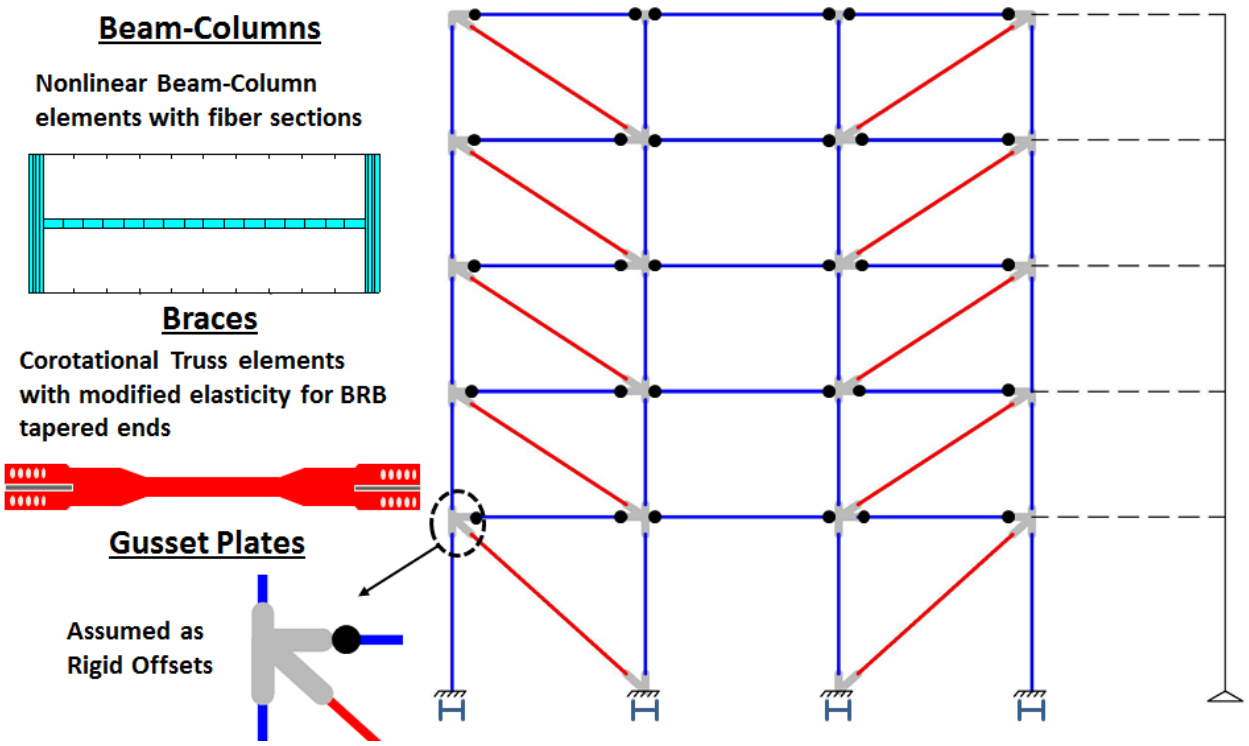

Figure 4-2. Summary of Model Details

4.1.2. Low Cycle Fatigue Modeling

The fatigue material of OpenSeeS, which uses Coffin-Manson (Coffin (1954) and Manson (1953)) log-log relationship to describe fatigue failure, was applied to model low cycle fatigue failure of BRBs and beam-column elements. This material covers the parent material and does not influence the stress-strain relationship of it. Damage at each strain amplitude is estimated by dividing the number of cycles at that amplitude by the number of constant amplitude cycles necessary to cause failure, and overall damage due to low-cycle fatigue is estimated by linearly summing the damage for all of the amplitudes of deformation cycles considered (Uriz and Mahin, 2008). This is known as Minor's rule (damage accumulation rule). Recommended Coffin-Manson curve slope and strain (at which one cycle causes failure) values by Uriz and Mahin (2008) were used for low cycle fatigue parameters. Figure 4-3(a) shows the fatigue material properties assigned on BRBs and wide flange sections. Figure 4-3(b) shows an example of this material when assigned on a truss element with BRB low cycle fatigue properties. As may be seen in Figure 4-3(b), when the element is applied ten cycles of 0.00418 strain (range) value, the damage index reached 1.0. Once the damage index reaches 1.0, the force in the element becomes zero. Note that the dashed lines in Figure 4-3(a) display the corresponding loading shown in Figure 4-3(b), i.e. $\log(N_f=10)=1$, and $\log(\varepsilon_t=0.0418)=-1.37$.

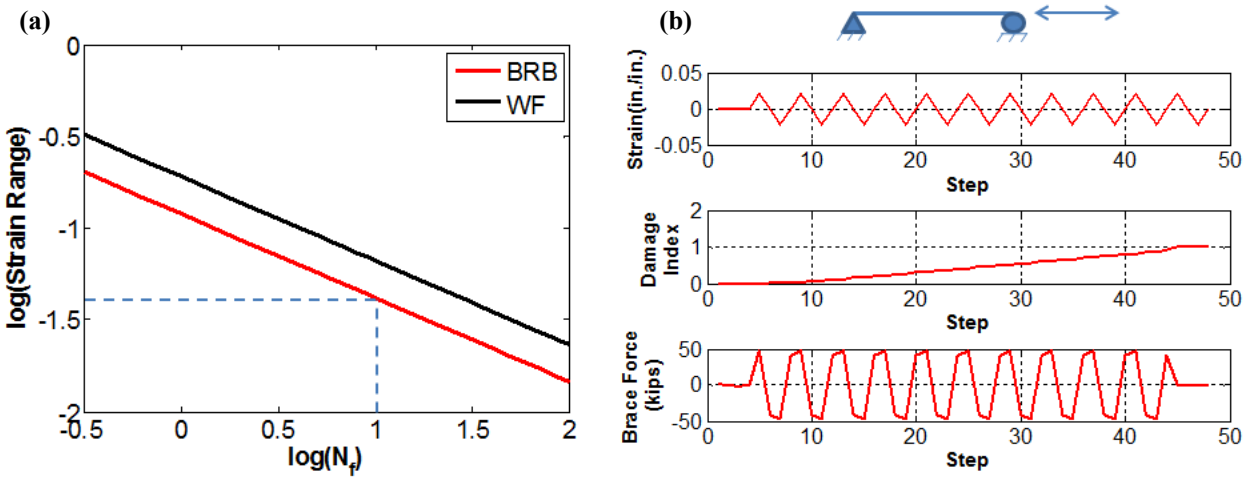

Figure 4-3. (a) Fatigue Material Properties for BRB and WF Sections (b) Fatigue Material Test on a Truss Element with Unit Length and Area

Figure 4-4 shows a low cycle fatigue failure example on a BRBF. Figure 4-4 (a) shows brace damage histories of the five story BRBF building. As may be seen in Figure 4-1 and Figure 4-2, there are ten braces in the building. Thus, ten brace damage histories are displayed in Figure 4-4(a). Continuous lines are for the braces at the left side, and dashed lines are for the braces at the right side of the frame. As may be seen, the first story brace (at the right) fails due to fatigue, and at about the same time, the drift of the first story bumps up (See Figure 4-4(b)), as well as the roof displacement (See Figure 4-4(c)). Eventually, BRBF fails due to the loss of first story brace.

Note that since fatigue material of OpenSees uses Coffin-Manson relationship for all strain amplitudes, it has the limitation of modeling the Ultra Low Cycle Fatigue (ULCF). The possible change of fatigue lines with ULCF is explained in Section 2.1.1 of this dissertation.

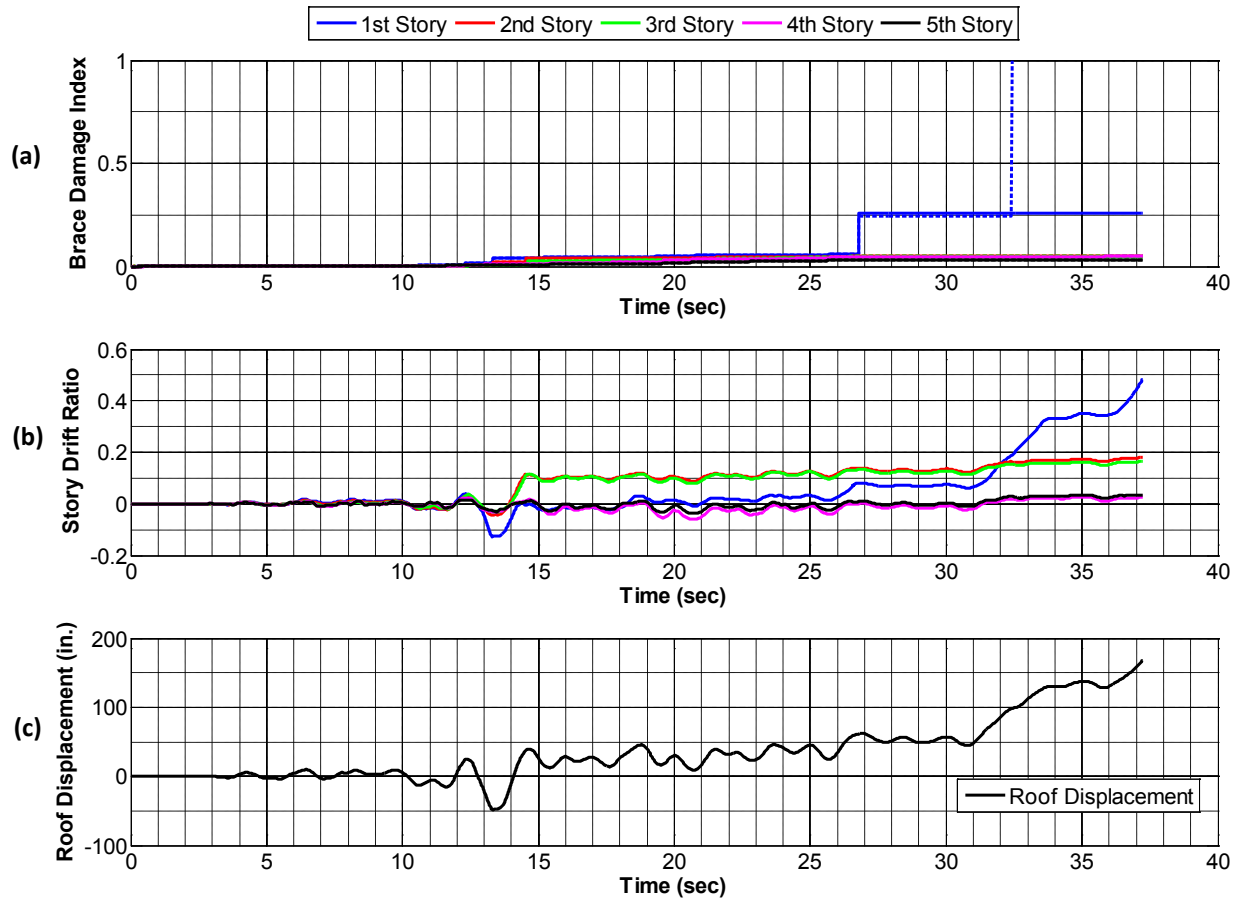

Figure 4-4. Brace Damage Example from the BRBF (a) Brace Damage Index, (b) Story Drift Ratio, (c) Roof Displacement histories

4.1.3. Material Calibration

Material calibration for beam and column elements (A992 steel wide flange sections) was made using the test data from ATLSS Report (Kauffmann et al., 2001). Tests were conducted at four different strain range levels of 2%, 4%, 6% and 8%. Each test consisted of ten tension-compression cycles at a single strain range. Giuffre-Menegotto-Pinto steel material (STEEL02) with isotropic strain hardening was used for the calibration. Stress-strain and energy dissipation (for unit length and area) comparisons between the test data and calibrated material is shown in Figure 4-5.

BRB test results (Romero et al., 2007) were used for the calibration of A36 material for BRB cores. The testing protocol used by Romero et al. (2007) exceeded the criteria provided by AISC Seismic Provisions to ensure greater severity in terms of inelastic deformation. The braces were pulled out of plumb by displacing them 4 inches at the bottom to simulate the rotation of the brace in a frame. The steel core of

the BRB was modeled in OpenSees using 1-D bar elements and STEEL02 material. Three elements in series were used to model the yielding and two transition zones of the core which have different lengths and areas. See Figure 4-6 for the comparison of calibrated STEEL02 of OpenSees and tested A36 BRB steel core.

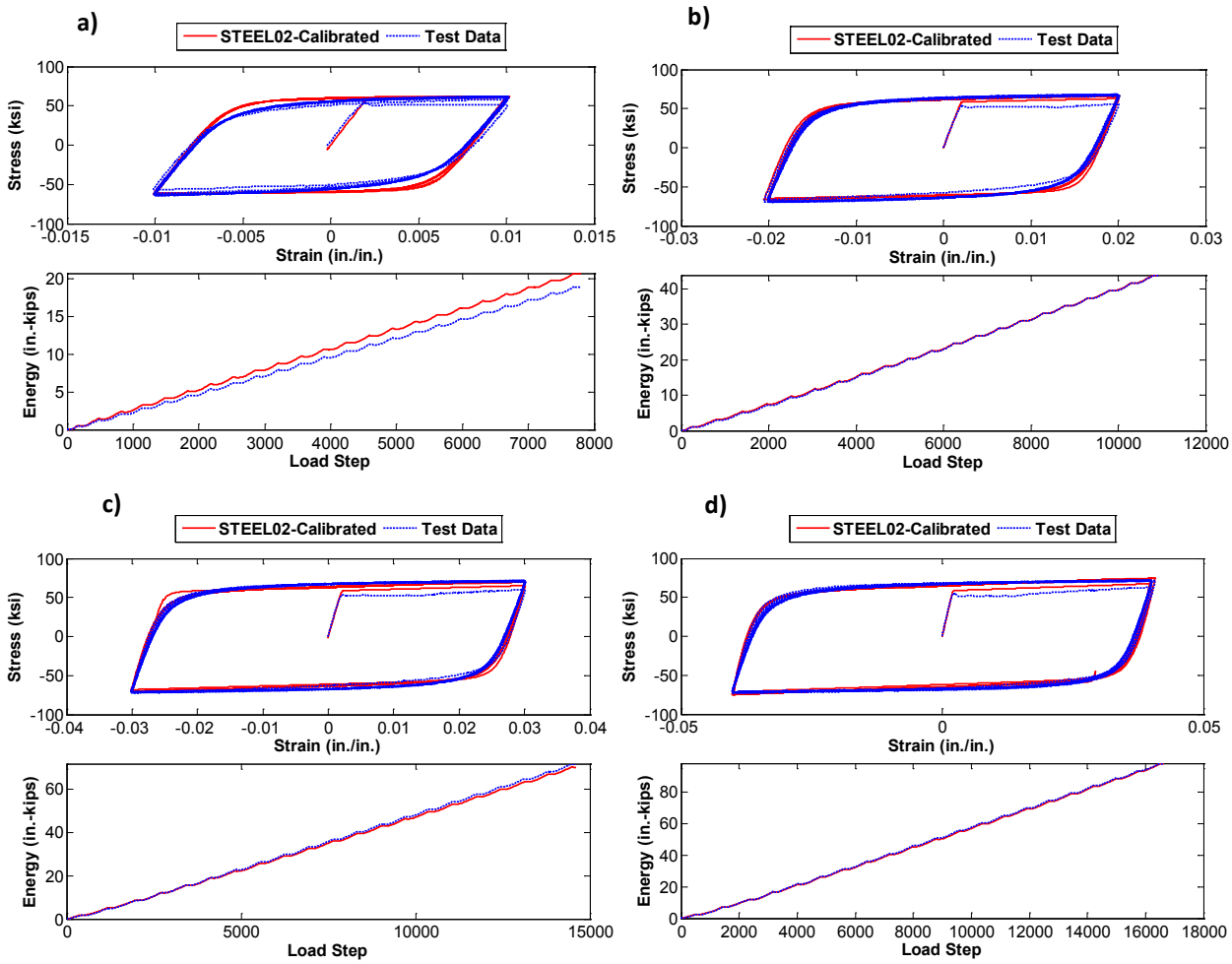

Figure 4-5. Material Calibration for A992 Steel for a) 2%, b) 4%, c) 6% and d) 8% Strain Ranges Note: Energy Plots are for Unit Length and Area.

Material calibration for high strength steel (HPS70W) was made using the test data from Dusicka et al. (2007). Axial coupons were tested for HPS70W steel to investigate the response under repeated inelastic demands of constant strain amplitude between 1% and 7% strain. See Figure 4-7 for the calibrated OpenSees STEEL02 material and HPS70W cyclic test data comparison.. Cyclic test data for HPS100W couldn't be found in the literature. Thus, the same material coefficients of HPS70W were used for HPS100W except the yield strength, which was estimated as 108 ksi according to tensile property data of ArcelorMittal (2011).

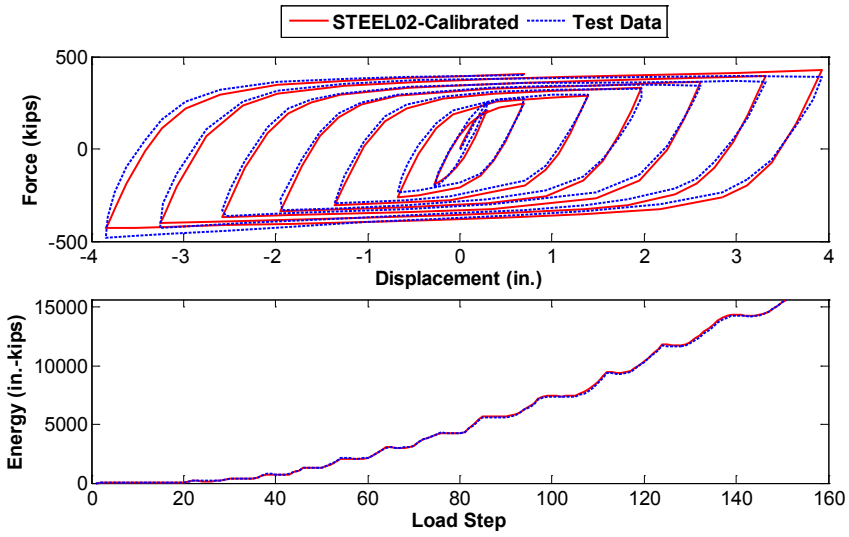

Figure 4-6. Material Calibration for A36 Steel Using BRB Test Data

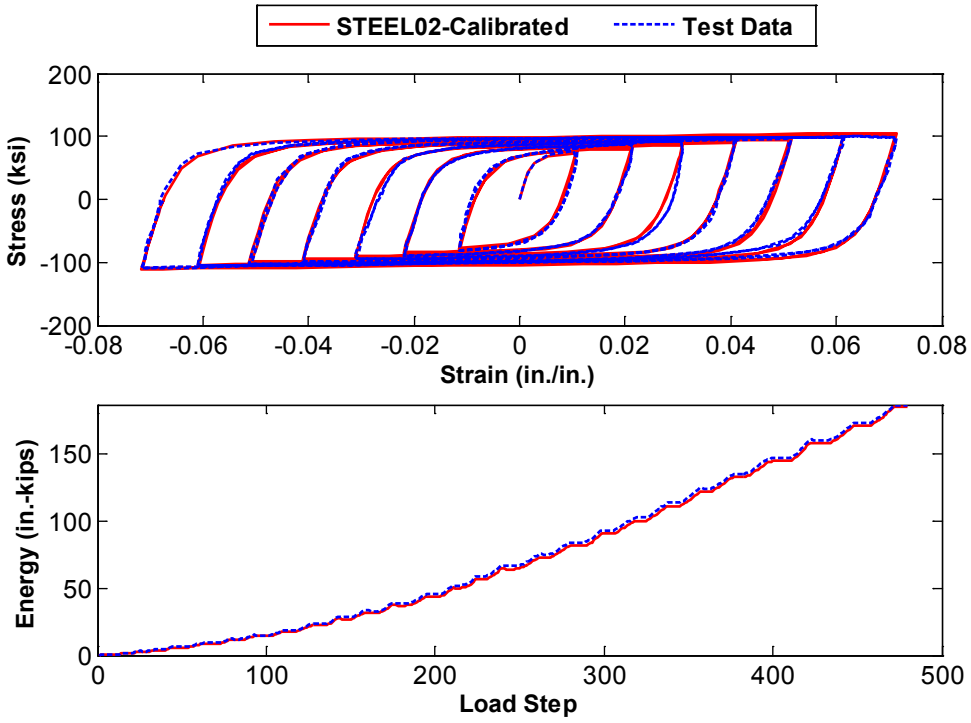

Figure 4-7. Material Calibration for HPS70W Note: Energy Plot is for Unit Length and Area.

Chen et al. (2001) tested a large scale BRB specimen with low strength steel (LYP100) used as brace core. A572 stiffeners were attached to the end portions of the core and the specimen was tested under cyclic loading to investigate the hysteretic behavior. To calibrate the material, three bar elements in series

were used in OpenSees. The parallel material of OpenSees (made of two STEEL02 materials) was assigned at the edge elements representing the LYP100 and A572 steels. Figure 4-8 shows the calibrated OpenSees STEEL02 material and the test results by Chen et al. (2001). The monotonic stress-strain comparison between LYP100 and calibrated STEEL02 material may be seen in Figure 4-9. Test data for the monotonic stress-strain plot is also obtained from Chen et al. (2001).

Once LYP100 and A36 were calibrated, it was found that LYP100 has more significant strain hardening than A36 which is consistent with the previous studies (Nakashima et al., 1994; De Matteis et al., 2003).

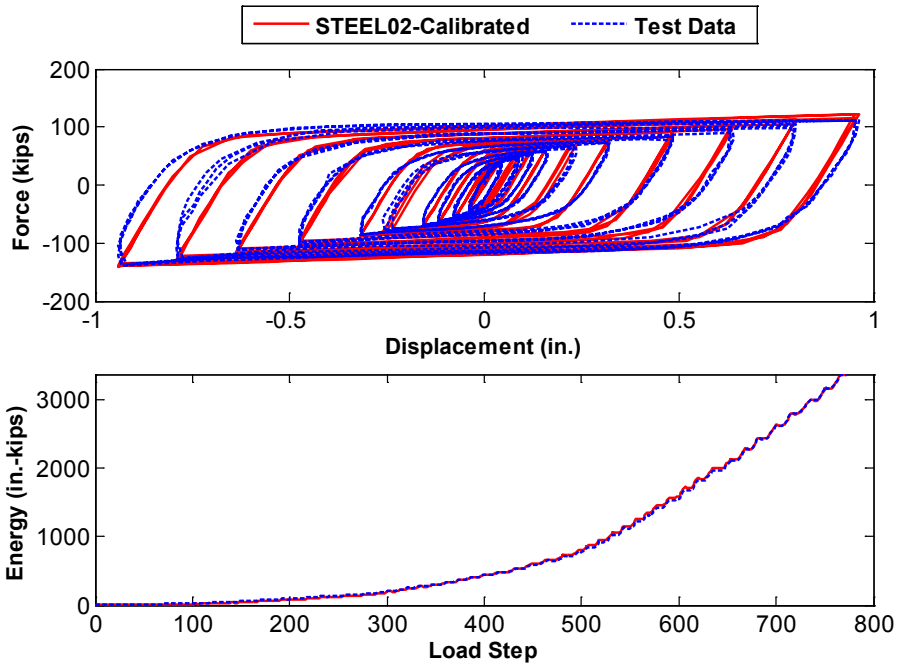

Figure 4-8. Material Calibration for LYP100

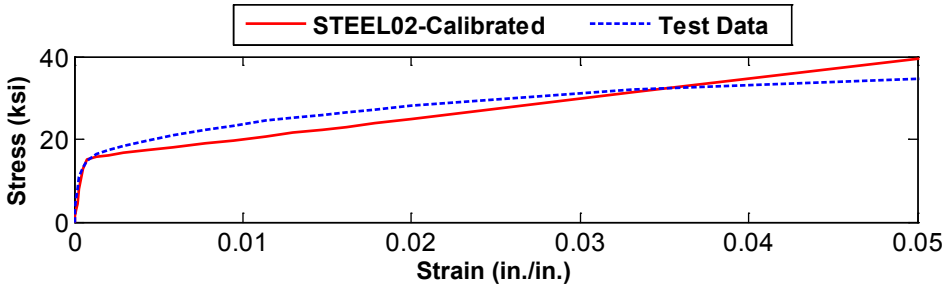

Figure 4-9. Monotonic Stress-Strain for LYP100

Table 4-3 shows the yield strength and modulus of elasticity of different steel materials obtained as a result of calibration with respect to the test results. In addition to the test results by Chen et al. (2001), the lab tests by Chou and Tsai (2002) were also considered for the modulus of elasticity value of LYP100 steel. The tabulated values in Table 4-3 provided good matches with respect to the cyclic test data used for the calibration as may be seen in Figures 4-5 to 4-8. Note that the tabulated values of yield strength and elastic modulus might change in different tests.

Table 4-3. Yield Strength and Modulus of Elasticity of Different Materials

Material	F_y(ksi)	E_0(ksi)
A992	58	29,000
A36	42	29,000
LYP100	15.5	27,000
HPS70W	73	29,000
HPS100W	108	29,000

4.1.4. Hybrid BRBF Design

Hybrid BRBs were built by combining various steel materials with different yield strengths in a single hybrid brace. It was assumed that different steel cores are connected in parallel, thus, in the numerical model; two or three brace elements were assigned on top of each other. Figure 4-10 shows the multi-material core BRB used in the models.

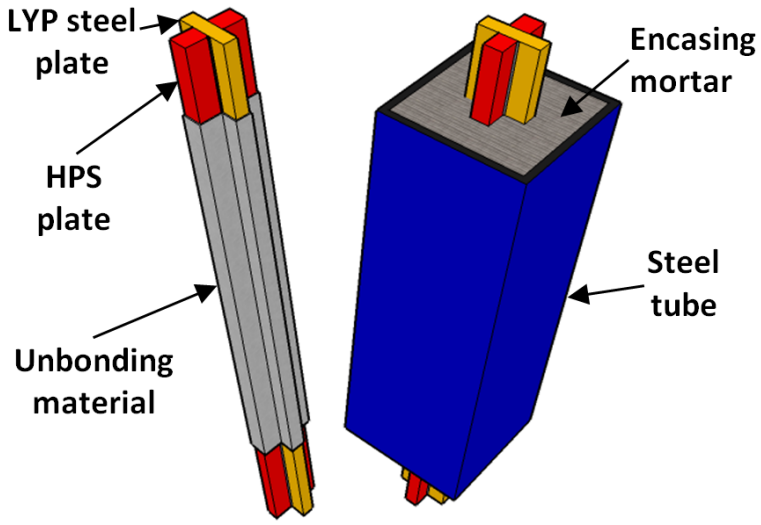

Figure 4-10. Hybrid BRB with Multi-Material Yield Core

Note that the multi-material BRB tested by Nippon Steel also had similar configuration as shown in Figure 4-10. See Section 2.1.5 for the details of the test.

When a multi-material BRB was modeled, the total brace stiffness and strength were kept the same as the regular BRB. The stiffness was not changed because in order to make a comparison between regular and hybrid frames, they need to attract the same level of seismic force. Also, since the beam and column design in BRBFs depend on the adjusted brace strengths, the total strength of the brace was unchanged so that the same beam and column sections could be used (capacity design principle). These are not requirements and a hybrid BRB can also be modeled with different total brace stiffness and strength. However, in the hybrid BRB models and analyses presented in this dissertation, total brace stiffness and strength of the hybrid BRBF were kept the same as the regular BRBF.

In the regular BRBF, only structural steel (A36) with F_y=42 ksi was used. In hybrid BRBs, LYP100, HPS100W and HPS70W were also used as additional core materials. Table 4-4 provides the three different hybrid BRB configurations that were used in the models. Areas, total stiffness and total strength are shown as ratios. As may be seen in Table 4-4, steel core areas are assigned in a way that total stiffness and strength of the BRBs will be the same.

Table 4-4. Hybrid BRB Combinations

		Regular BRB	Hybrid BRB-1	Hybrid BRB-2	Hybrid BRB-3
Area Ratios	**A36**	1.00	0.167	-	-
	LYP100	-	0.493	0.591	0.776
	HPS70W	-	0.375	0.450	-
	HPS100W	-	-	-	0.278
Total Stiffness (*A/L)		29,000	29,019	29,007	29,009
Total Strength (*A)		42.00	42.00	42.01	42.03

The same low cycle fatigue parameters were used for A36, LYP100 and HPS to model the fatigue material of OpenSees (Dusicka et al. 2007, Saeki et al. 1998).

When the original BRBF was modified as hybrid, only the brace elements were modified with respect to the multi-core material and section properties provided in Table 4-3 and Table 4-4. Thus, in the analytical model, there became three braces (for Hybrid BRB-1 model) or two braces (for Hybrid BRB-2 and Hybrid BRB-3 models) connected in parallel instead of only one brace. All the other model properties except brace material and brace sections are the same in the regular and hybrid BRBFs discussed herein.

4.1.5. Yield Interstory Drift Ratio of BRBFs

One of the parameters that is useful for the design of concentric braced frame structures is the yield interstory drift ratio which is only a function of material properties, model geometry, brace configuration, gusset plate size, and the ratio of the yield core length of the brace to the total length of the brace. Beam-column connection types and base column fixity also have a minor effect on the yield IDR. For a single diagonal braced bay, the story stiffness and strength can be calculated as follows:

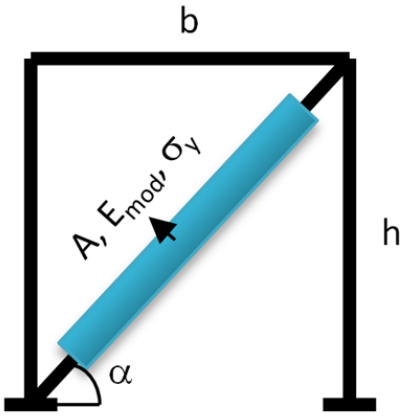

$$k_s = \frac{E_{mod}A}{\sqrt{b^2+h^2}}(\cos\propto)^2 = \frac{E_{mod}Ab^2}{(b^2+h^2)^{\frac{3}{2}}}$$

$$V_y = \sigma_y A\cos\alpha = \frac{A\sigma_y b}{\sqrt{(b^2+h^2)}}$$

$$d_y = \frac{V_y}{k_s} \quad , \quad IDR_y = \frac{d_y}{h} = \frac{\sigma_y(b^2+h^2)}{E_{mod}bh}$$

Figure 4-11. Calculation of Yield Interstory Drift Ratio for a Single Diagonal Braced Frame

where A is the brace core area, E_{mod} is modulus of elasticity of brace core material with modification for tapered ends and gusset plates, σ_y is expected yield strength of brace core, b is the span length, h is the story height, d_y is yield displacement and IDR_y is yield interstory drift.

Assuming a model geometry of b=20ft, h=13ft, and brace material properties of σ_y= 42 ksi, E_{mod}=43,500 ksi, yield interstory drift ratio (IDR_y) is 0.211%. When a low strength steel (LYP100) is used as the brace material for the same geometry, IDR_y decreases to 0.084% and when a high strength steel (HPS100W) is used, IDR_y increases to 0.543%. Thus, low strength steel (LYP100) of a hybrid frame yields at about 40% of the yield interstory drift ratio of A36 steel of a regular frame, and high strength steel (HPS100W) of a hybrid frame yields at about 2.5 times the yield interstory drift ratio of A36 of a regular frame.

4.1.6. Nonlinear Pushover Analysis

Figure 4-12 (a) and Figure 4-12(b) display the pushover curves of regular and three hybrid BRBFs for NMR and MR beam-column connections respectively. As seen in the figures, hybrid BRBFs start

yielding early due to LYP100 material and have higher post-yield stiffness than the regular BRBFs. Note that all the frames have the same initial stiffness. As mentioned earlier, total brace strengths were also kept the same for the models discussed herein. HPS70W and HPS100W help hybrid BRBs with LYP100 to have the same strength as the regular frames.

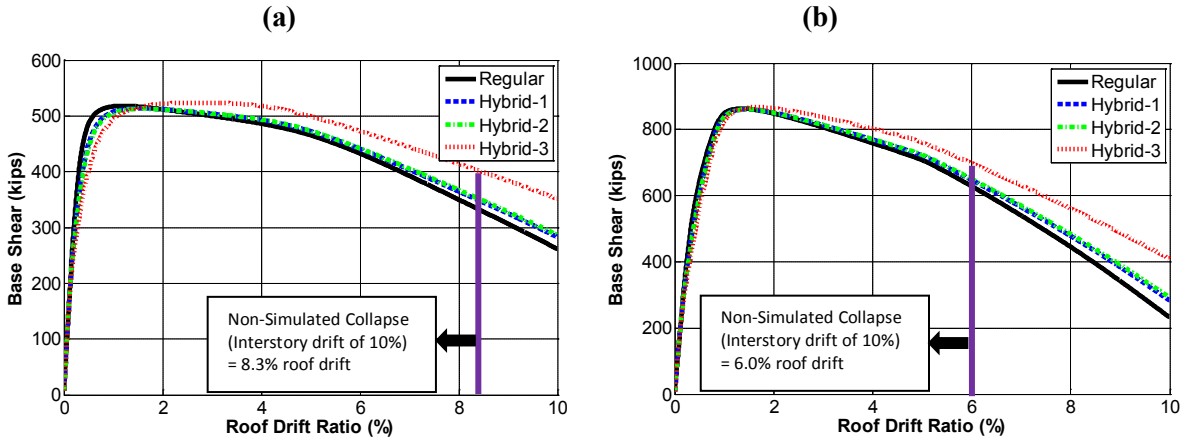

Figure 4-12. Pushover Curves of Regular and Hybrid BRBFs for (a) Non-Moment Resisting (NMR) and (b) Moment Resisting (MR) Beam-Column Connections

Early yielding of the hybrid BRBs will minimize the response by dissipating energy under low-mid intensity earthquakes. Also, as a result of early yielding period elongation will occur. Figure 4-13(a) shows example pushover curves for regular and hybrid frames and Figure 4-13(b) shows the change in period with respect to pushover drift ratio. The period calculation is based on the secant stiffness of the pushover curves. As may be seen in Figure 4-13(b), early yielding of the hybrid frame increases the period at low drift ratios. This can be beneficial in reducing the effect of the seismic excitation because spectral accelerations of the earthquakes tend to decrease with increasing period. Figure 4-13(c) and Figure 4-13(d) display the spectral acceleration and spectral displacement response spectra of the 44 ground motions used in this study beginning from the fundamental period of the structure which is 1.37 sec. It is hard to conclude if period elongation helps or not. As may be seen from the change of spectral curves of different ground motions, period elongation will decrease the response for some ground motions at certain building periods, and increase the response at some other ones. The effect of period elongation on hybrid frames should be further investigated in the frequency domain.

High strain hardening of the LYP100 material increases the post yield stiffness and strength of the hybrid BRB pushover curves. High post yield stiffness will control residual displacements and collapses under MCE level motions.

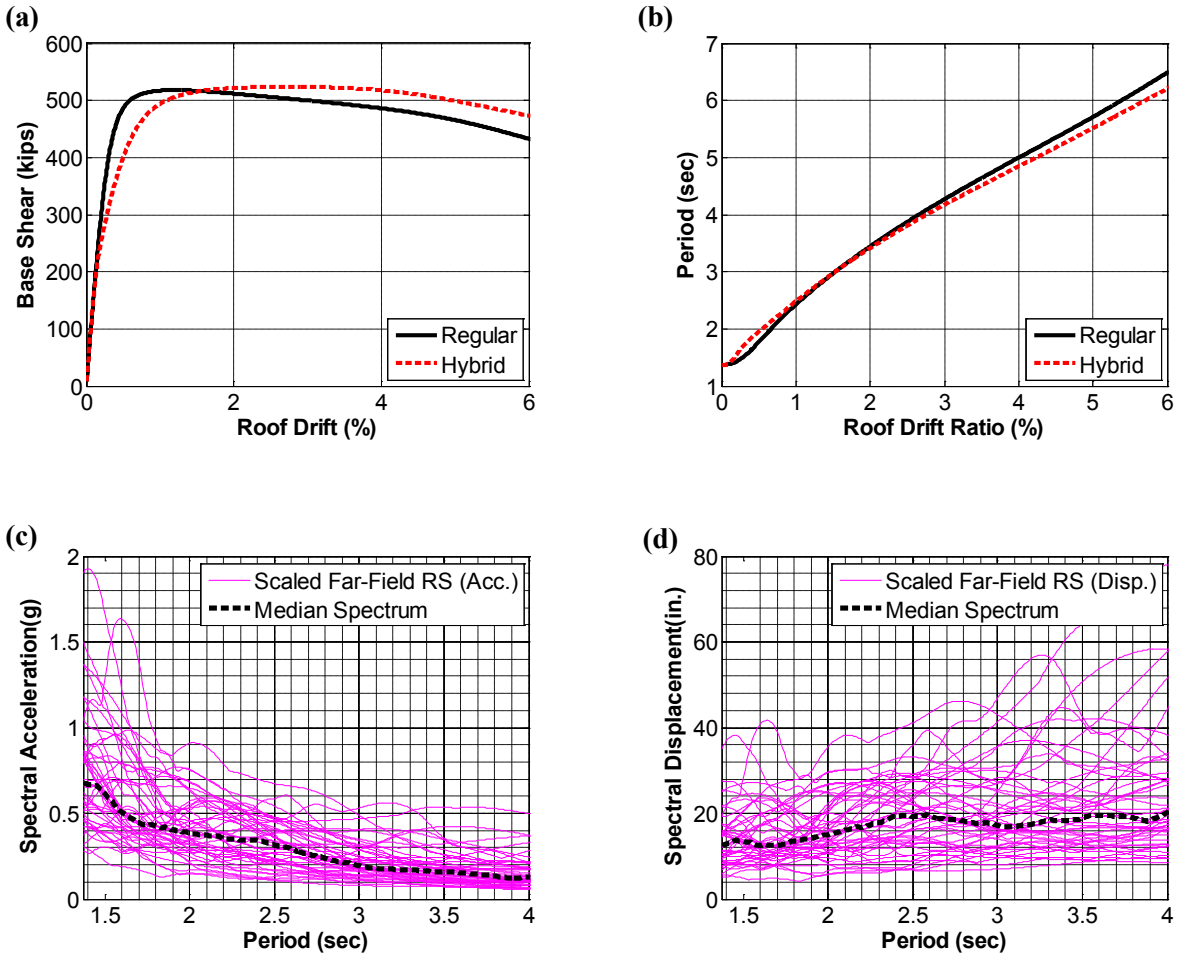

Figure 4-13. (a) Pushover Results for Positive Stiffness (b) Period Elongation from Pushover Analysis (c) Spectral Acceleration Response of Scaled Far-Field Set (d) Spectral Displacement Response of Scaled Far-Field Set

4.1.7. Effect of Beam-Column Connections

As may be seen in the pushover curves of Figure 4-12, moment resisting (MR) beam-column connections provide reserve strength to the structure. Hybrid frames with both NMR and MR beam-column connections yielded earlier than the regular frame and the post yield-stiffness is higher for the hybrid frames. However, the change in the pushover curves (from regular to hybrid) is observed to be more beneficial when NMR beam-column connections are used (See Figure 4-12). The early yielding of the hybrid frames is more distinct for the NMR connection model than the MR connection model. Post-yield stiffness of the hybrid frames becomes negative at higher drift ratios than the regular frame for the NMR connection models, while hybrid frames and regular frame reach negative post-yield stiffness at virtually the same drift levels for the MR connection models. Note that the only modification was made on the

braces when regular BRBFs made hybrid. Thus, the effect of hybridity is more evident when NMR connections are used because possible yielding of beam-column elements in MR connection models results in closer structural behavior between regular and hybrid frames.

When dynamic analyses were performed, it was seen that the performance improvement of the hybrid frames was much more significant when NMR beam-column connections were used. In order to investigate this issue, the effect of beam-column connections on the drift profiles was studied at different roof drift ratio levels. Table 4-5 shows the effect of beam-column connections on drift profiles at different roof drift ratios (1%, 2%, 4%, 6%, 8%, and 10%) for the model studied. In a straight line displacement profile, the bottom story accounts for 25.7% of the roof drift, while the other stories accounts for 18.6% of roof drift. When NMR connections were used, the drift distribution is very uniform, i.e. the maximum contribution of any story is at most 25% at all roof drift levels. However, when MR connections were used, the damage accumulates at the 1st story especially after 4% drift. Indeed, for the MR connection model, 1st story interstory drift reaches 10% at 6% roof drift ratio. An interstory drift of 10% is reached at 8.3% roof drift for NMR connection model (See Figure 4-12).

Table 4-5. Effect of Beam Column Connection on Drift Profiles (Maximum Story Contributions are Highlighted)

Story	H_{story} / $H_{building}$	1%		2%		4%		6%		8%		10%	
		Non-MR	MR	Non-MR	MR	Non-MR	MR	Non-MR	MR	Non-MR	MR	Non-MR	MR
5	18.6	12.9	14.0	18.2	8.5	22.5	5.7	20.3	5.6	16.0	5.7	13.2	5.4
4	18.6	20.8	18.5	23.0	11.1	24.5	7.0	22.4	6.4	19.1	6.3	16.7	5.9
3	18.6	25.6	19.5	24.5	19.2	23.1	20.8	22.7	18.0	22.2	15.0	21.9	12.9
2	18.6	23.7	20.5	20.7	26.0	18.3	28.4	19.8	24.7	22.3	20.1	24.0	17.0
1	25.7	17.0	27.5	13.6	35.2	11.5	38.1	14.8	45.3	20.4	52.9	24.2	58.8

In this study, 10% interstory drift is used as a non-simulated collapse (NSC) criterion for BRBFs. This is consistent with *ATC-76-1* project and determined from the lab tests by Newell and Uang (2008). Stocky W14 columns which were representative of those in bottom stories of multistory braced frames were tested by Newell and Uang (2008). As a result of these lab tests, columns began to lose capacity after 7%-9% story drift under cyclic axial and lateral loads.

As may be seen in Figure 4-12 and Table 4-5, the NMR connection model is more ductile than the MR connection model due to damage concentration of the MR connection model. Figure 4-14 displays the drift profiles of Non-MR and MR beam column connection models at 10% roof drift ratios which is the NSC value used in this study.

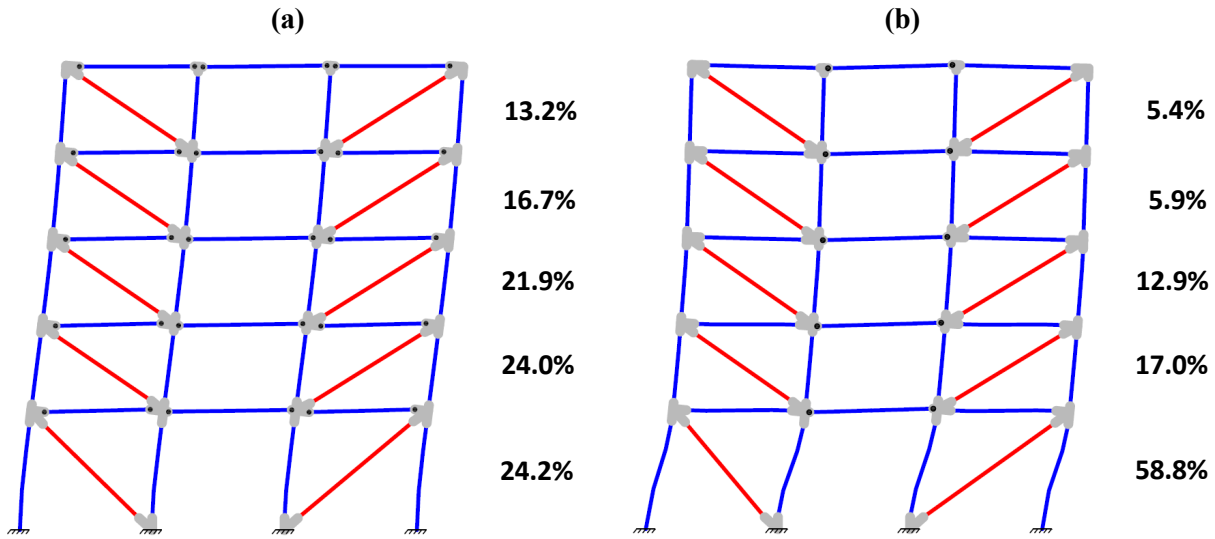

Figure 4-14. Deformed Shape Comparison at 10% Roof Drift Ratio for (a) Non-MR and (b) MR Beam-Column Connection Models

4.1.8. Incremental Dynamic Analysis (IDA)

As explained in Chapter 3 of this dissertation, Appendix F of *FEMA P-695* provides a collapse level ground motion scale for individual archetypes. If 22 out of 44 ground motions causes collapse at this level, then the building fails *FEMA P-695* methodology criteria, if not it passes. The collapse level ground motion for this building model is 1.33xMCE. See Section 3.5 of this dissertation for the details of collapse level ground motion scale calculation for individual buildings. Twenty IDA increments were used up to this level and the performance at each level was compared between the regular and hybrid BRBFs.

Figures 4-15 through 4-18 show the maximum interstory drift ratio comparison of four different BRBFs (one regular and three hybrid) under 44 ground motions at different seismic intensity levels. Only the results of non-moment-resisting beam column connection models are presented. In these plots, the 'x' axis is completely random and the order of the ground motions on the 'x' axis is the same as *FEMA P-695* far field ground motion set order. This kind of plot was chosen instead of bar charts for better visibility.

Figures 4-15 through 4-18 compare the response at four different intensity levels which are: serviceability (assumed as 10% of collapse level or 13% of MCE), DBE (2/3 of MCE), MCE, and collapse level (133% of MCE). To decide on the serviceability level, 50 yr MRI was assumed. Since this BRBF building is presented as a design example in Bruneau et al. (2011), the seismic design data was provided without the location of the building. To estimate for the 50 yr MRI ground motion scale, the 0.2 sec and 1.0 sec

spectral shaking of 2,500 yr MRI (MCE) and 50 yr MRI were compared throughout the United States. The ratios were about 10% to 20% of MCE level. It was decided to use 13% of MCE level as the serviceability level for this building model. This level is equal to 10% of the collapse level intensity.

As may be seen in the figures, hybrid frames generally performed better than the regular frame, and as the frames became more hybrid, the response got better, i.e. decreased. The number of collapses reduced for hybrid frames. As may be seen in Figure 4-18, four of the collapses that occurred on regular frame could be resisted by the Hybrid-3 frame. The ground motions that caused collapse for the regular frame but not for Hybrid-3 frame are highlighted in Figure 4-18.

Figures 4-19 through 4-22 compare the residual roof displacement of the four different BRBFs under 44 ground motions at different seismic intensity levels. As may be seen in the figures, residual displacements decreased with the hybrid frames, and the response got better as the hybridity increased. It was expected to obtain larger residual displacements from hybrid frames at low intensity ground motions assuming that only LYP steel of the hybrid brace would yield but not the A36 of the regular brace. This wasn't the case though as seen in Figure 4-19. When the brace force-deformation histories were checked, yielding was observed in both the regular and the hybrid braces. Note that residual displacements at low intensity motions are negligible and the comparison at high intensities are more reasonable.

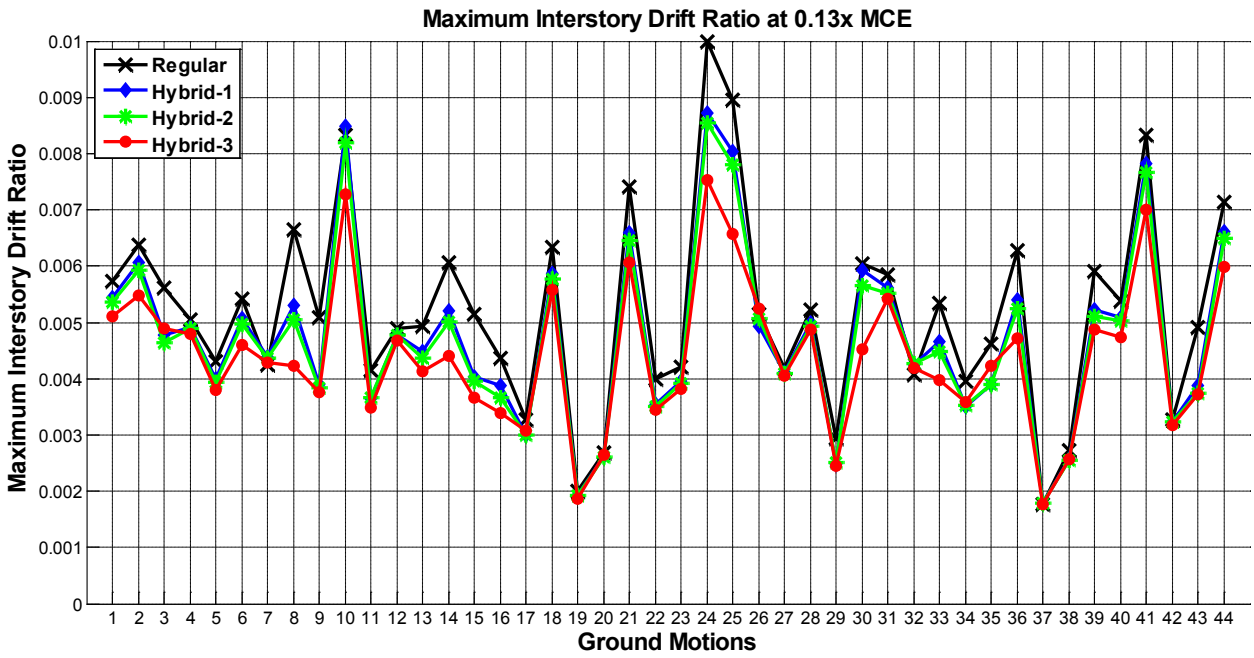

Figure 4-15. BRBF Maximum Interstory Drift Ratio Performance Comparison at Serviceability Level

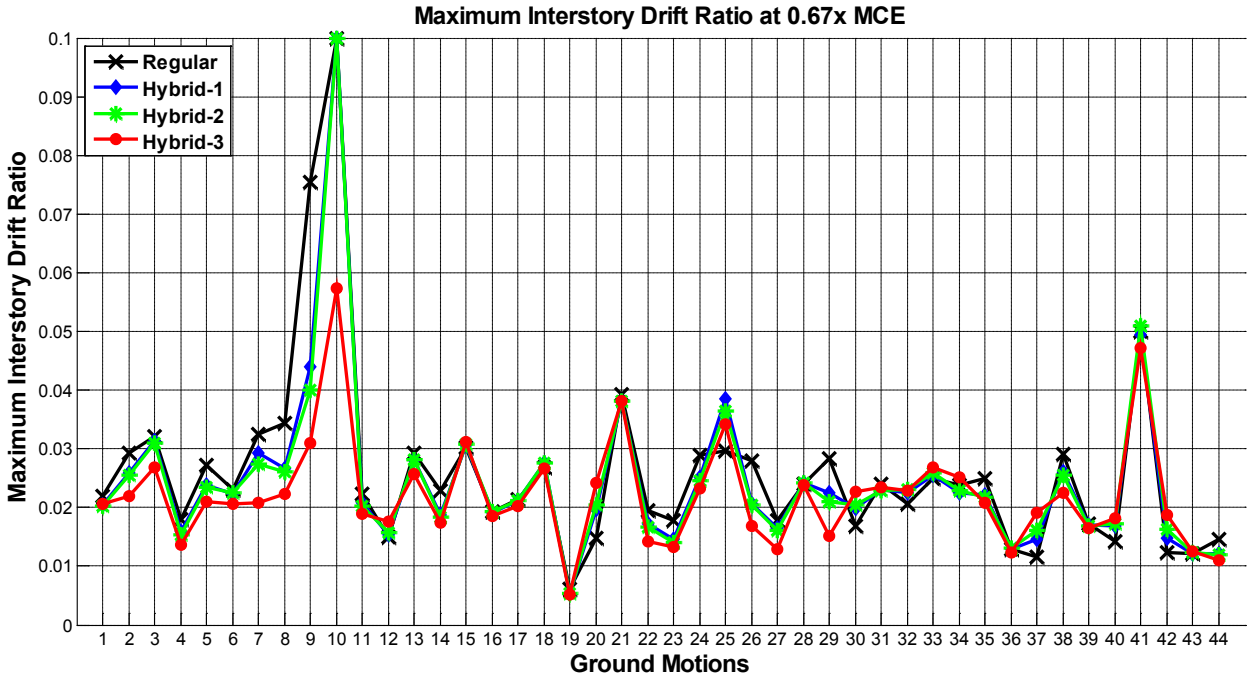

Figure 4-16. BRBF Maximum Interstory Drift Ratio Performance Comparison at DBE Level

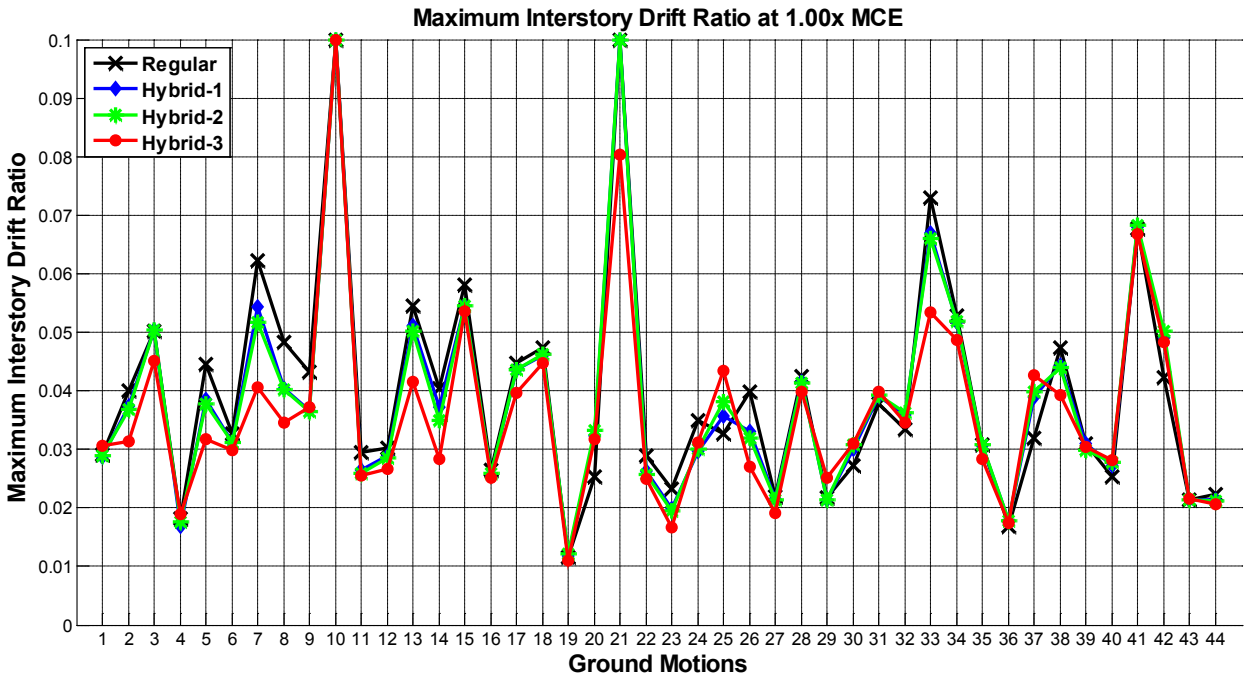

Figure 4-17. BRBF Maximum Interstory Drift Ratio Performance Comparison at MCE Level

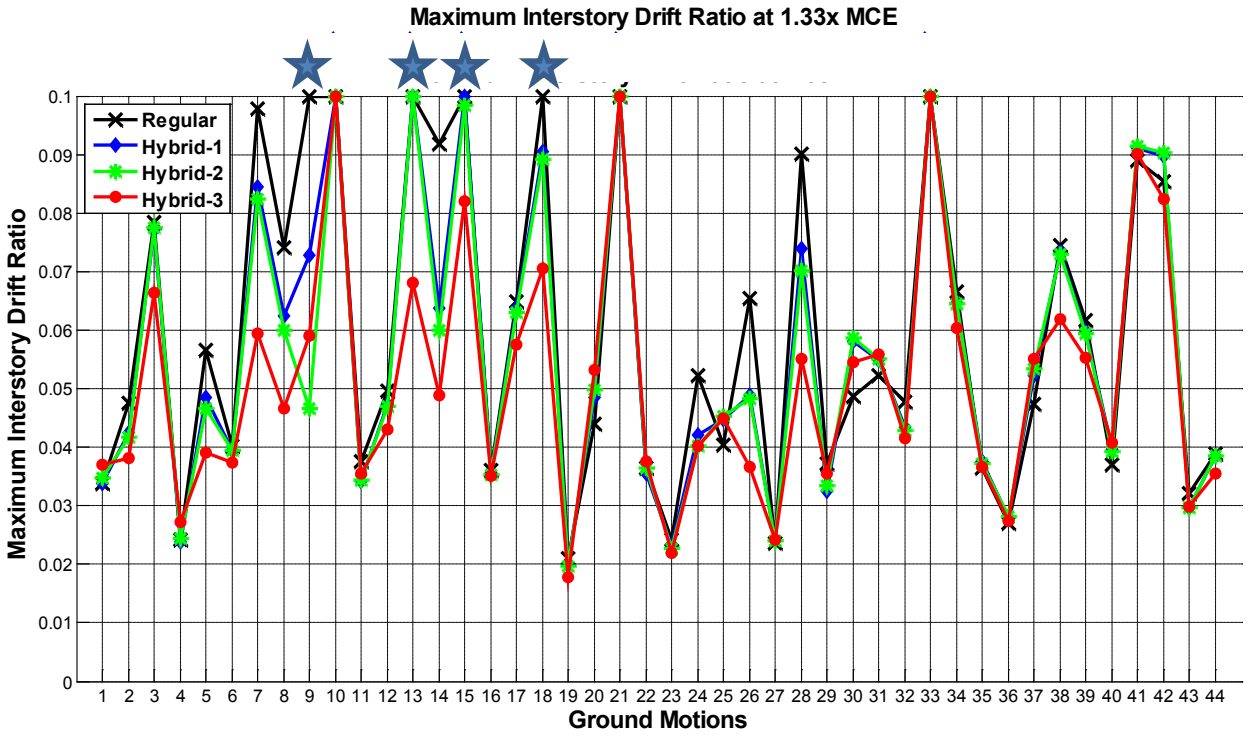

Figure 4-18. BRBF Maximum Interstory Drift Ratio Performance Comparison at Collapse Level (Stars at top of figure show the eliminated collapses from Regular frame to Hybrid-3 frame)

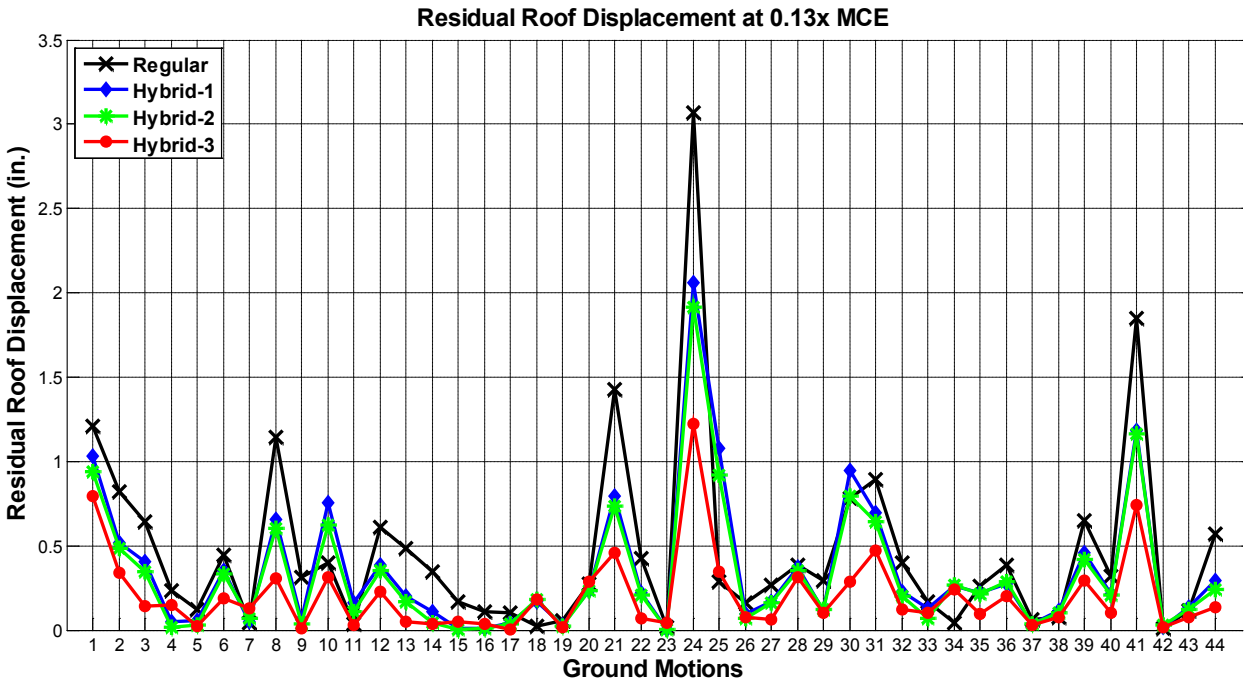

Figure 4-19. BRBF Residual Roof Displacement Performance Comparison at Serviceability Level

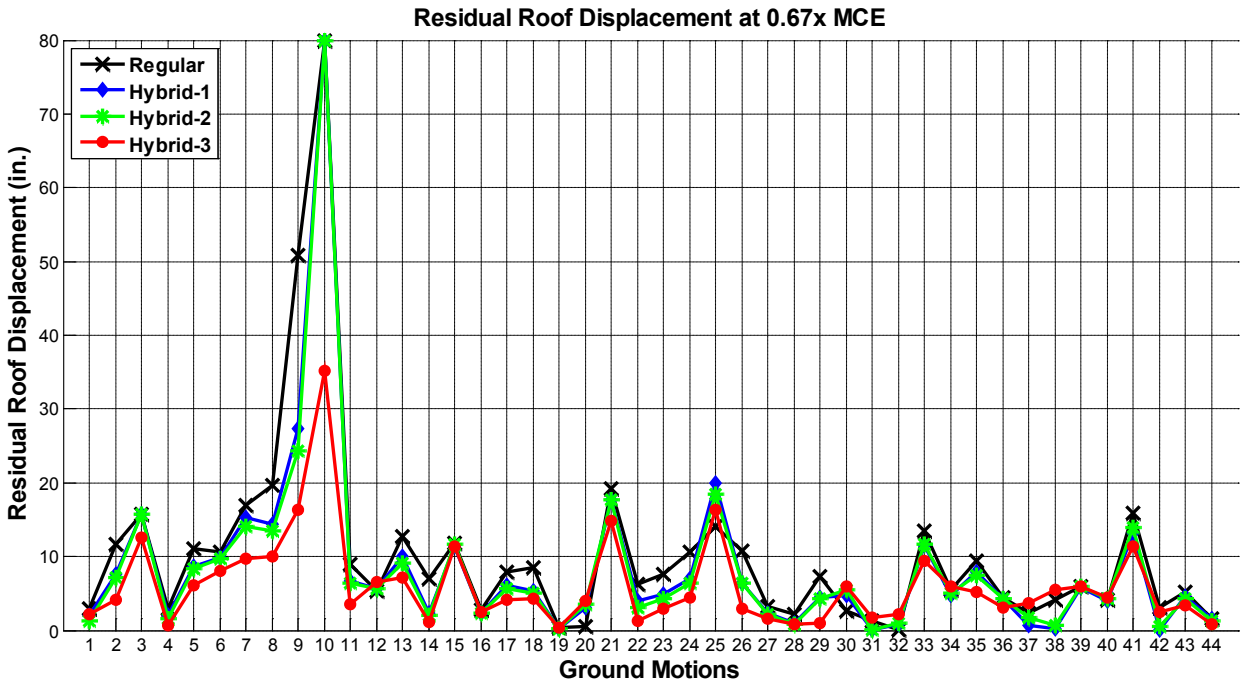

Figure 4-20. BRBF Residual Roof Displacement Performance Comparison at DBE Level

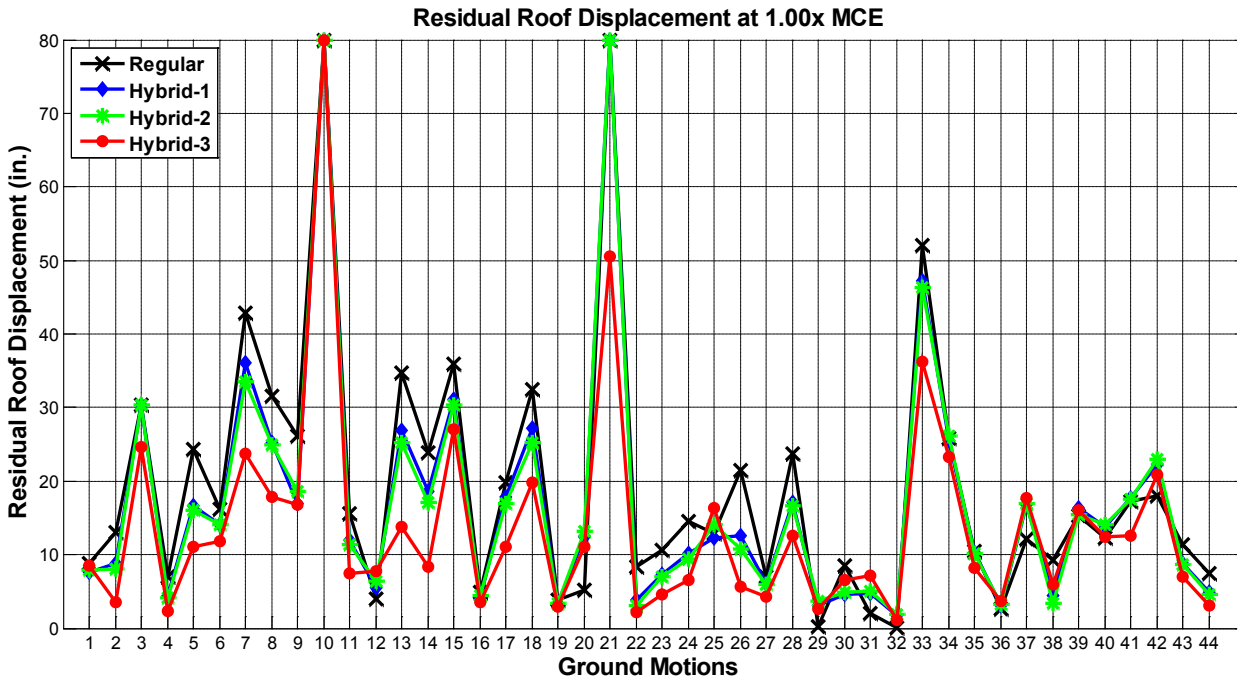

Figure 4-21. BRBF Residual Roof Displacement Performance Comparison at MCE Level

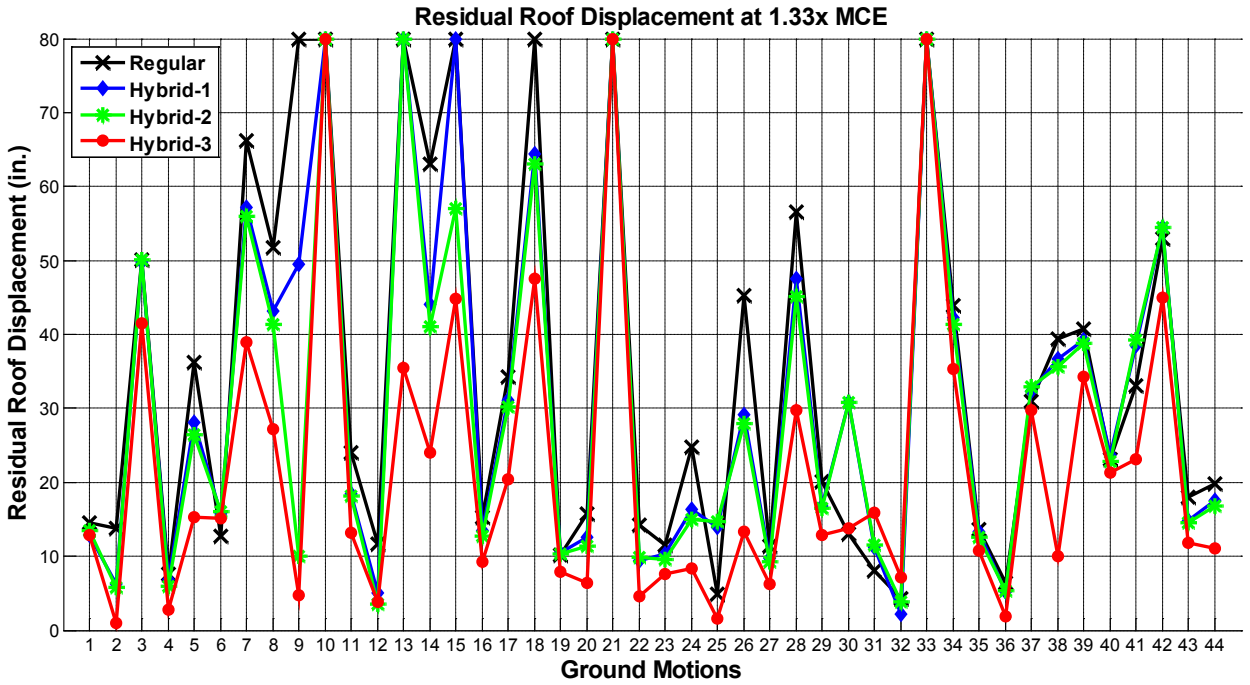

Figure 4-22. BRBF Residual Roof Displacement Performance Comparison at Collapse Level

To calculate the residual displacements, analyses were run 10 sec. more to allow for free vibration decay and residual displacements were determined by calculating the running average of this additional 10 sec. response. Figure 4-23 shows the roof displacement time histories of four BRBFs for three different ground motions which are scaled at MCE. Hybrid frames performed better as a result of higher post-yield stiffness shown in the pushover curves (See Figure 4-12).

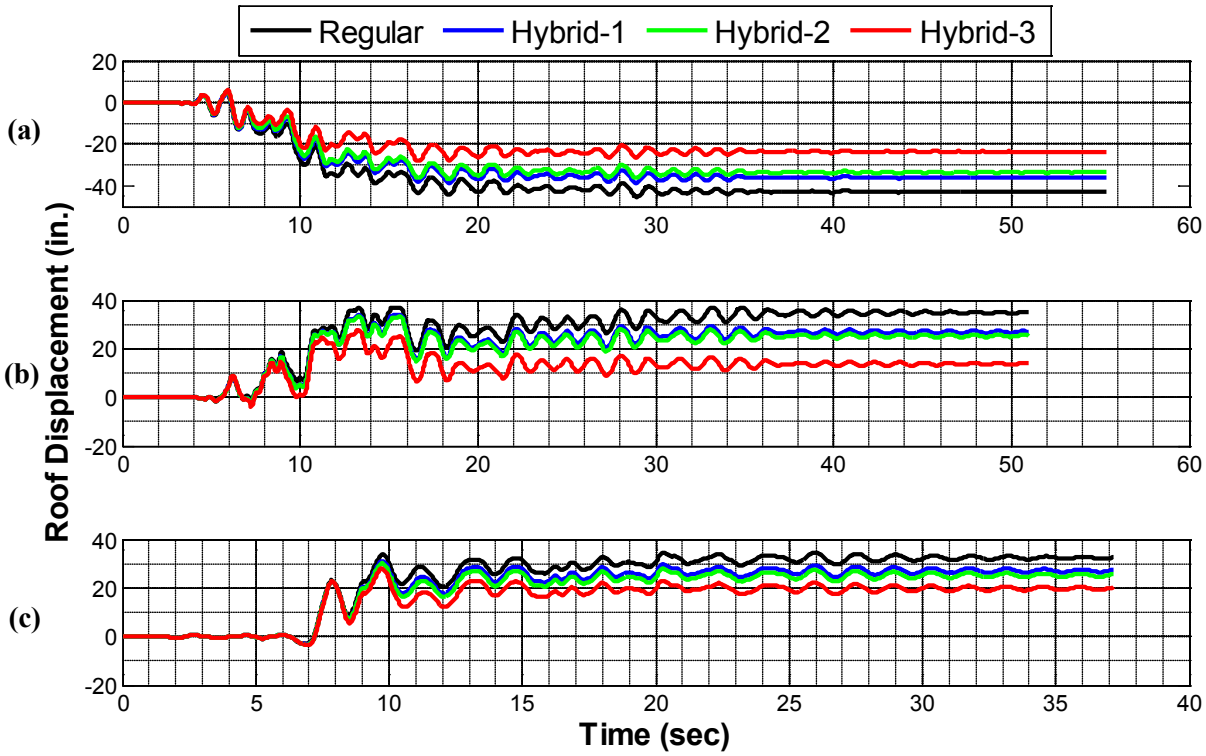

Figure 4-23. Residual Displacement Response Comparison at MCE Levels of (a) Hector Mine EQ, (b) Kobe, Japan EQ, and (c) Kocaeli, Turkey EQ

Figure 4-24 shows the median performance improvement for three hybrid frame configurations with respect to the regular frame. In Figure 4-24, three damage measures (maximum story acceleration, maximum interstory drift ratio (IDR), and residual roof displacement) were used for comparison. Only the result of NMR connection model is provided. As may be seen in the figure, hybrid frames did not produce significant benefits in terms of story accelerations. Hybrid frames reduced the interstory drifts by about 10% at all ground motion intensities up to collapse level. The benefit of the hybridity is most evident in residual roof displacements. The reduction in residual displacements was about 40% at all intensities up to collapse level. Figure 4-25 shows similar set of plots as Figure 4-24, however, instead of median response comparison, 84th percentile comparison is made. As may be seen in Figure 4-25, similar or even better improvement was achieved with the 84th percentile response than the median response.

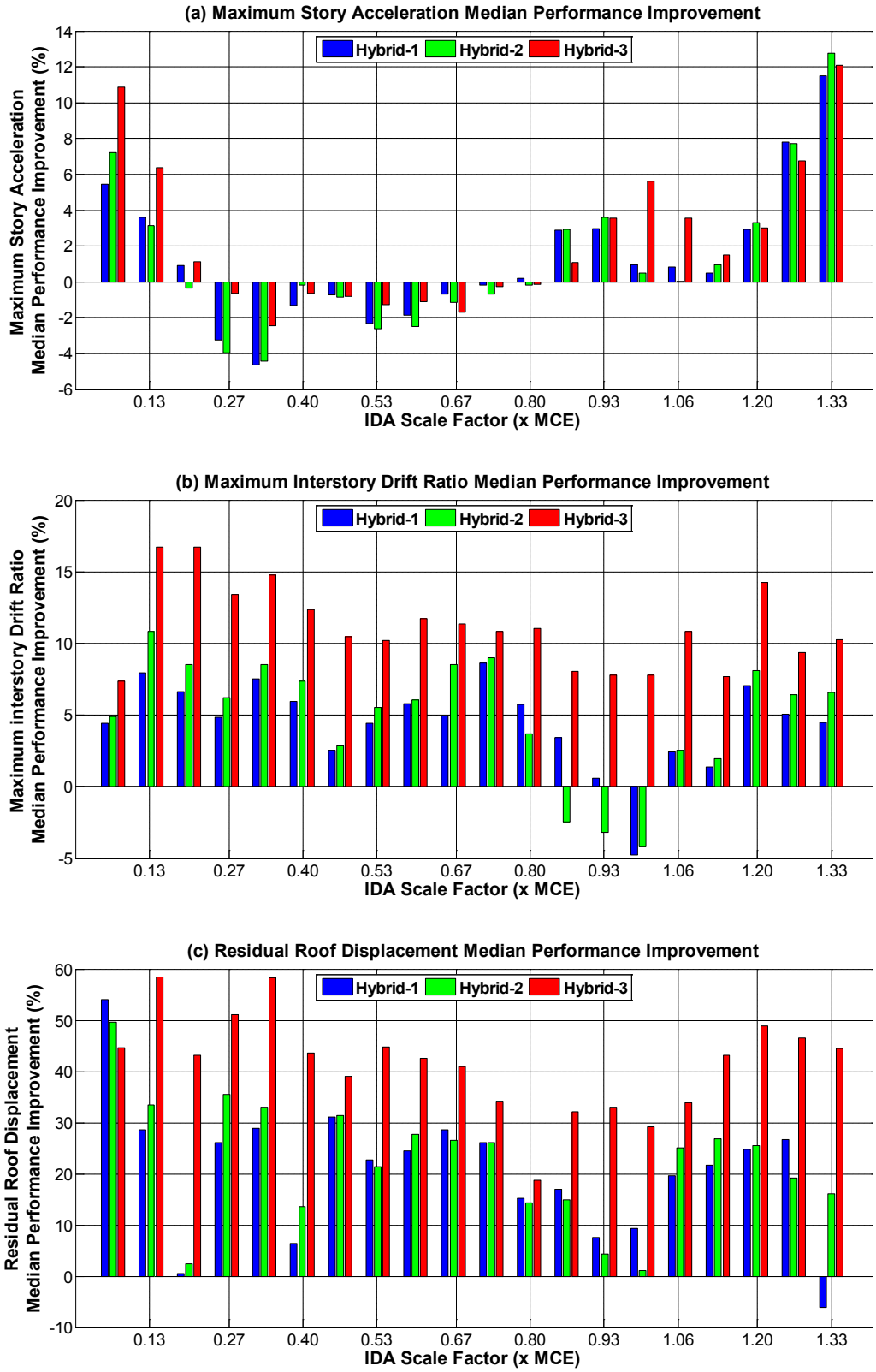

Figure 4-24. Median Performance Improvements for (a) Maximum Story Acceleration (b) Maximum Interstory Drift Ratio (c) Residual Roof Displacement

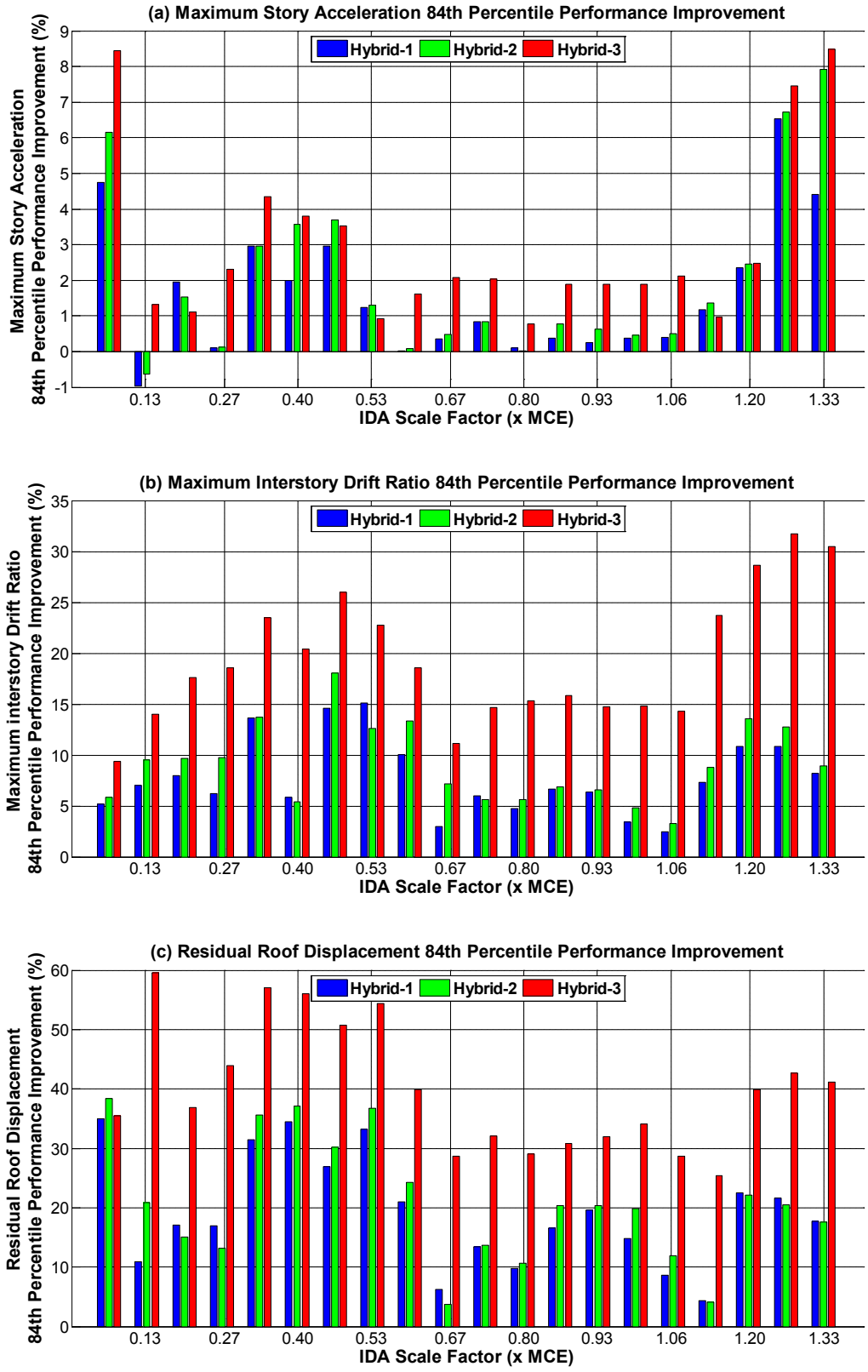

Figure 4-25. 84th Percentile Performance Improvements for (a) Maximum Story Acceleration (b) Maximum Interstory Drift Ratio (c) Residual Roof Displacement

4.1.9. IDA Dispersion

The dispersion of the IDA curves can be used to see the effect of hybridity in terms of giving a reliable estimate of the performance of the buildings. To measure the IDA dispersion, the standard deviation of the responses, produced at each intensity level of 44 different earthquakes, was calculated for each structure with different level of hybridity.

Figure 4-26 (a) and (b) illustrate the IDA dispersion for maximum IDR and residual roof displacement. When a collapse occurred at high scale factors, collapse measures of 10% IDR and 80 in. roof displacement, which is about $1/10^{th}$ of building height, were used for IDR and residual roof displacement dispersion respectively. As may be seen in Figure 4-26, standard deviation decreases with the hybrid frames and as the hybridity increases, the results get better. Hybrid-3 frame, the most hybrid frame, gave the best results in IDA dispersion study.

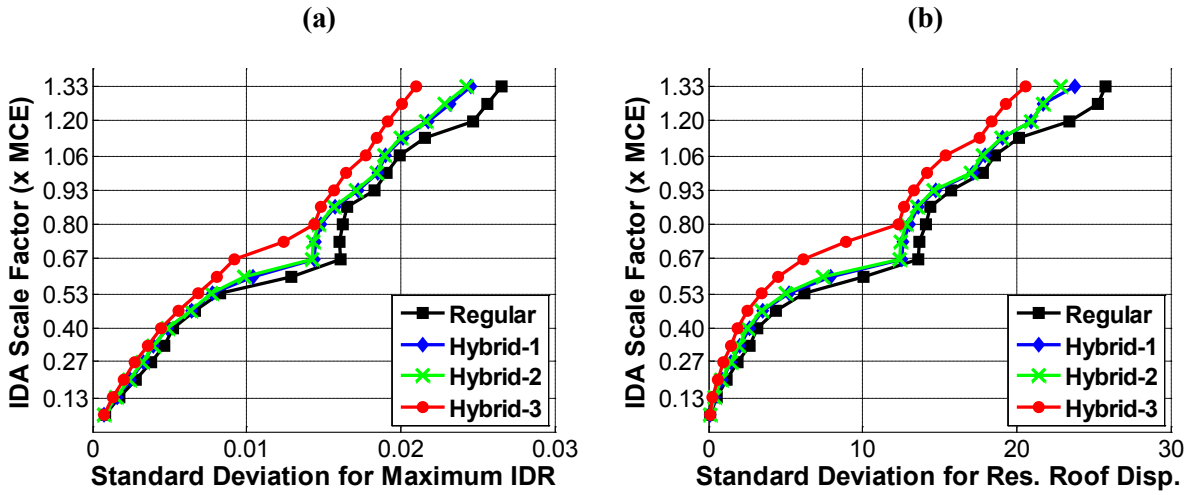

Figure 4-26. IDA Dispersion for (a) Maximum Interstory Drift Ratio (IDR) and (b) Residual Roof Displacement

4.1.10. *FEMA P-695* Performance Evaluation

Table 4-6 shows the collapse performance evaluation of BRBF models for both NMR and MR beam-column connections. When beam-column connections were changed from NMR to MR, the static overstrength increased as expected (See Figure 4-12). The MR connection model resulted in higher collapse margin ratios (CMR) than NMR connection model and period based ductility is higher for the NMR connection model.

To calculate the acceptable adjusted collapse margin ratios (Accept. *ACMR*), the total system uncertainty,

β_{TOT}, needs to be calculated (See Section 3.3 of this dissertation). Total system uncertainty depends on the quality of design requirements, test data, and nonlinear modeling. Consistent with *ATC-76-1* project BRBF study, the quality rating of "B", which stands for "Good" in *FEMA P-695* methodology, was used for BRBF buildings investigated in this dissertation.

Both regular NMR and MR connection models passed the criteria with MR connection model having a lower probability of collapse. Hybrid frames performed better than regular frames for both NMR and MR connection types. For NMR connection models, while the probability of collapse is 3.24% for the regular frame, it is reduced to 1.73% in Hybrid-3. For MR connection models, while the probability of collapse is 2.18% for the regular frame, it is reduced to 1.27% in Hybrid-3. Indeed, the NMR connection Hybrid-3 model (1.73% collapse probability) performed better than MR connection regular frame (2.18% collapse probability).

In terms of number of collapses, at collapse check level (1.33xMCE), 7 earthquakes (out of 44) caused collapse on regular frame with NMR connection. The number of collapses reduced to 5, 4, and 3 for Hybrid-1, Hybrid-2 and Hybrid-3 frames respectively.

Note that connection performance was neglected in collapse evaluation of presented in Table 4-6. Consistent with NIST (2010), 10% maximum interstory drift ratio (IDR) was used as non-simulated collapse measure in addition to low-cycle fatigue deterioration mode of braces.

Table 4-6. BRBF Model I Collapse Performance Evaluation Using 10% Interstory Drift + Low Cycle Fatigue Failure of Braces as Collapse Criteria

Beam-Column Connection	BRBF Model	Computed Overstrength and Collapse Margin Parameters					Acceptance Check		
		Static Ω	*CMR*	μ_T	*SSF*	*ACMR*	Accept. *ACMR 10%*	Pass / Fail	Collapse Probability (%)
Non-MR	Regular	1.12	1.80	26.0	1.46	2.63	1.96	Pass	3.27
	Hybrid-1	1.11	1.90	27.5	1.46	2.79	1.96	Pass	2.55
	Hybrid-2	1.11	1.92	27.9	1.46	2.81	1.96	Pass	2.44
	Hybrid-3	1.13	2.07	31.2	1.46	3.04	1.96	Pass	1.71
MR	Regular	1.91	1.97	12.4	1.46	2.88	1.96	Pass	2.18
	Hybrid-1	1.90	2.03	12.9	1.46	2.98	1.96	Pass	1.87
	Hybrid-2	1.90	2.05	13.1	1.46	3.00	1.96	Pass	1.82
	Hybrid-3	1.91	2.21	14.7	1.46	3.23	1.96	Pass	1.27

Recalculation of *CMRs* by assuming 5% IDR instead of 10% IDR was done followed by modified collapse performance evaluation (see Table 4-7). When Tables 4-5 and 4-6 are compared, period based

ductility, μ_T, dropped with the use of 5% IDR as non-simulated collapse (NSC) criteria. This is because non-simulated collapse of 5% IDR governed the ultimate displacement, δ_u, that is used in the period based ductility calculation (see Equation 3.4).

With the reduced collapse measure for the NSC criteria, *CMRs* reduced and collapse probabilities increased as expected. All the models except the Regular BRBF with Non-MR beam-column connection model passed *FEMA P-695* methodology collapse criteria. Regular BRBF with Non-MR beam-column connection failed the criteria as the collapse probability was slightly more than 10%. All the Hybrid combinations for Non-MR beam-column connection models gave collapse probabilities less than 10%, and the most Hybrid combination (Hybrid-3) gave the best results, with a collapse probability of 7.32%. Regarding MR beam-column connection models, Regular, Hybrid-1, and Hybrid-2 models resulted in identical response (7.32% collapse probability). However, in consistent with the Non-MR beam-column connection model, Hybrid-3 model gave the best response with 6.02% collapse probability.

Table 4-7. BRBF Model I Collapse Performance Evaluation Using 5% Interstory Drift + Low Cycle Fatigue Failure of Braces as Collapse Criteria

Beam-Column Connection	BRBF Model	Computed Overstrength and Collapse Margin Parameters					Acceptance Check		
		Static Ω	*CMR*	μ_T	*SSF*	*ACMR*	Accept. *ACMR 10%*	Pass / Fail	Collapse Probability (%)
Non-MR	Regular	1.12	1.30	15.2	1.46	1.91	1.96	Fail	10.90
	Hybrid-1	1.11	1.36	15.5	1.46	1.99	1.96	Pass	9.54
	Hybrid-2	1.11	1.38	15.6	1.46	2.03	1.96	Pass	8.93
	Hybrid-3	1.13	1.46	15.9	1.46	2.14	1.96	Pass	7.32
MR	Regular	1.91	1.46	8.5	1.46	2.14	1.96	Pass	7.32
	Hybrid-1	1.90	1.46	8.6	1.46	2.14	1.96	Pass	7.32
	Hybrid-2	1.90	1.46	8.6	1.46	2.14	1.96	Pass	7.32
	Hybrid-3	1.91	1.54	8.7	1.46	2.26	1.96	Pass	6.02

4.1.11. Collapse Probability

The probabilities of collapse were calculated by fitting the fragility curves to the data obtained from IDA. The Maximum Likelihood Estimation (MLE) based approach as explained in the previous chapter was used for the fragility function fitting.

Figure 4-27 and Figure 4-28 show the comparison of collapse probabilities for Non-MR and MR beam-column connection models. Both 10% and 5% interstory drift collapse criterion results are provided for both beam-column connection models. As may be seen from the figures, the probability of collapses is

lower for the hybrid frames than the regular frames at all ground motion intensities. The reduction in the collapse probabilities is more significant when 10% IDR was used as the collapse criteria rather than 5% IDR. For both beam column connection types, the most hybrid frame (Hybrid-3) performed the best, and the performance improvement is more significant for the Non-MR beam-column connection models.

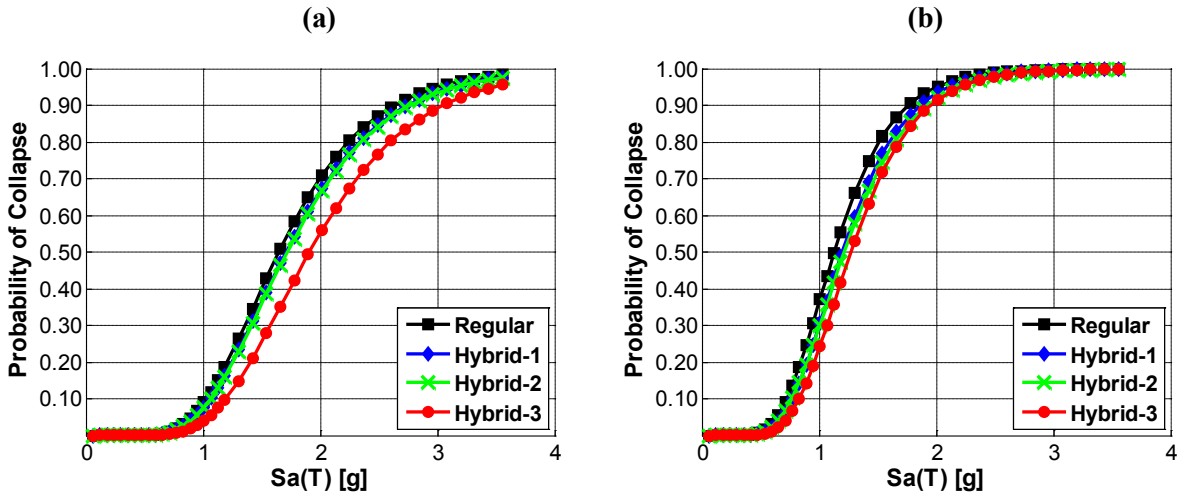

Figure 4-27. Collapse Probability Comparison between Hybrid and Regular Frames with Non-MR Beam Column Connections (a) Using 10% Interstory Drift + Low Cycle Fatigue Failure of Braces as Collapse Criteria and (b) Using 5% Interstory Drift + Low Cycle Fatigue Failure of Braces as Collapse Criteria

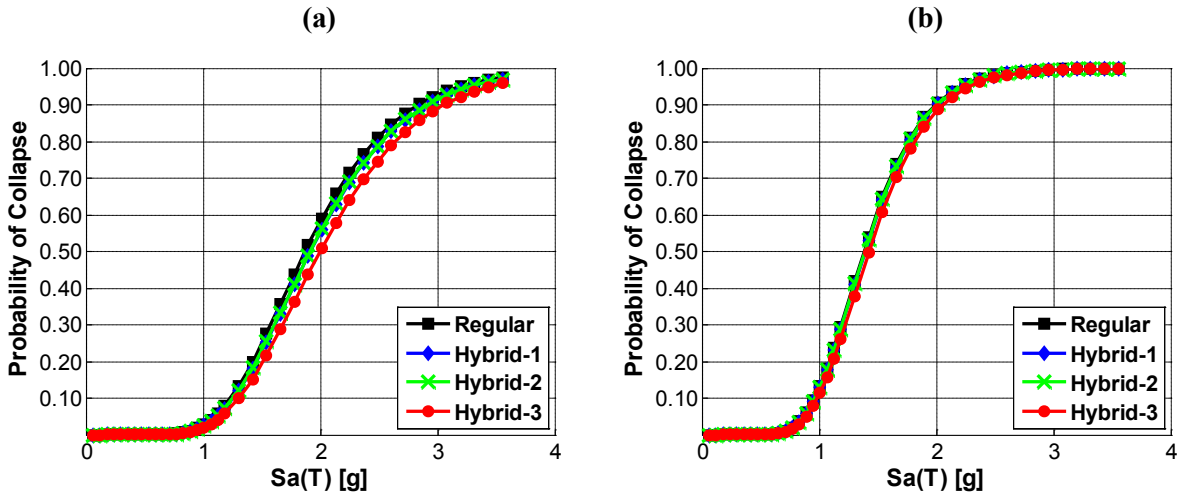

Figure 4-28. Collapse Probability Comparison between Hybrid and Regular Frames with MR Beam Column Connections (a) Using 10% Interstory Drift + Low Cycle Fatigue Failure of Braces as Collapse Criteria and (b) Using 5% Interstory Drift + Low Cycle Fatigue Failure of Braces as Collapse Criteria

4.2. Case Study 2: Five Story Medical Office Building (MOB)

Degenkolb Engineers provided a five story BRBF building model with V bracing configuration. This building, located in Oakland, CA, is a medical office building and is designed according to 2001 California Building Code (CBC-2001). Table 4-8 shows the member sizes and Figure 4-29 shows the plan and elevation view of the model. The building has uniform bay width and story height of 28ft 4 in. and 14 ft respectively (see Figure 4-29).

Table 4-8. Member Sizes of BRBF

Level / story	Brace Area (in.^{2})	Beams	Columns	
			Exterior	Interior
Roof	-	W24x131	-	-
5	5.29	W24x104	W14x109	W14x61
4	9.54	W24x104	W14x233	W14x82
3	11.37	W24x104	W14x233	W14x82
2	13.26	W24x104	W14x311	W14x109
Ground	15.87	-	W14x311	W14x109

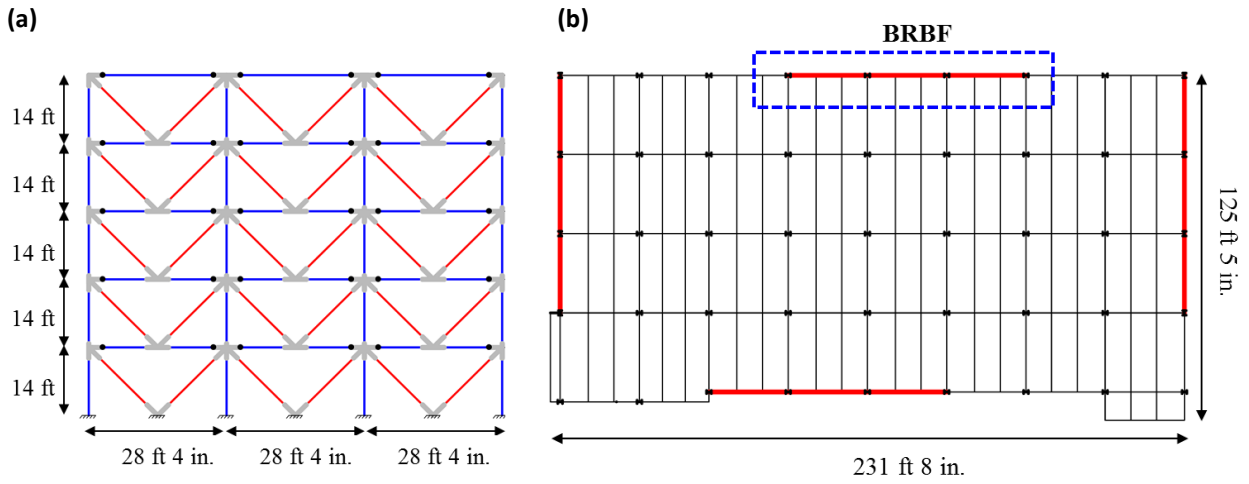

Figure 4-29. Elevation and Plan View of BRBF Model with V Brace Configuration

Note that since this building is designed according to a building code other than *ASCE 7*, it is not really compatible with *FEMA P-695* methodology. Indeed, the code based period calculated from *ASCE 7* and *UBC 97* (which uses the same coefficients as CBC-2001) differ by 50% because of the difference in building period coefficient, C_t. Thus, the design base shears that are calculated according to *UBC 97* and *ASCE 7* are different. Figure 4-30 compares three design spectra which are the *UBC 97* design spectrum found from the seismic coefficients of building data, *ASCE 7* design spectrum obtained from USGS maps

by using exact coordinates of the building, and Dmax design spectrum which is the maximum allowable spectrum level for *FEMA P-695* compatibility. As may be seen in Figure 4-30, this building is designed at a much higher design level than *ASCE 7* spectrum, the difference is even more when the comparison is made with the Dmax spectrum. Although this building model is not compatible with the methodology due to the reasons mentioned, analyses were still run through the methodology. Note that the main goal of this project is to understand the effect of hybrid BRBs and compare the performance of hybrid frames against regular frames. Thus, even though this building is stronger than it should be according to *ASCE 7*, it is still used to see the effect of hybridity on a real design project.

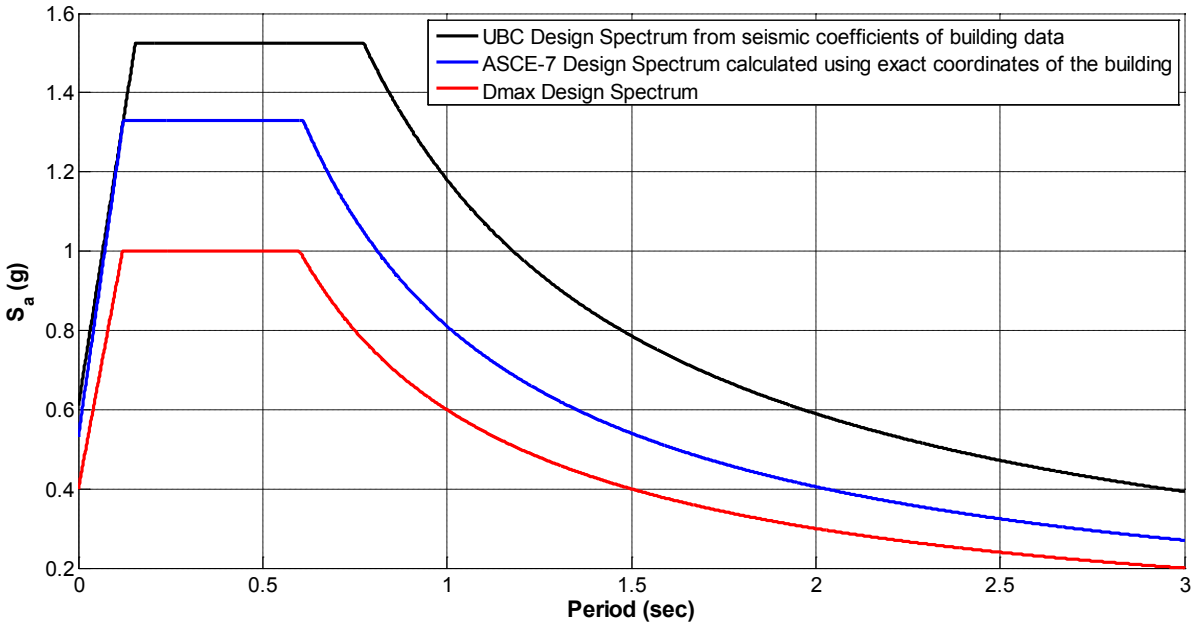

Figure 4-30. Design Spectra Comparison

Table 4-9 tabulates the seismic design data of this building according to CBC-2001 or *UBC 97*. Since there are two identical perimeter braced frames in each direction, base shear values in the table should be divided by two for compatibility with two-dimensional analysis. Dead loads were based on actual building and equipment operating weights. The seismic weights of the typical stories and roof were calculated about 3,000 kips, and 3,400 kips respectively. Floor live load of 80 psf and roof live load of 20 psf were used for this building model.

Table 4-9. Seismic Data for the Building Model

Seismic zone	4	**Seismic coefficient, C_a**	0.61
Importance factor, I	1.0	**Seismic coefficient, C_v**	1.18
Soil profile type	S_D	**Base shear**	$0.190W$
Seismic source type	A	**Code base period, T**	0.56 sec
Near source factor, N_a	1.38	**R for BRBF**	8
Near source factor, N_v	1.84	**Design base shear, V**	4003 kips

4.2.1. Nonlinear Model Details and Pushover Analysis

Using similar techniques as discussed earlier in the previous case study, the building was modeled in OpenSees. The fundamental period was calculated as 0.66 sec. and was confirmed with Degenkolb Engineers. Non-moment-resisting (NMR) beam-column connections were used at the braced bays. Figure 4-31 displays the pushover curves of the model. Similar to the results of the 1st case study discussed in this chapter, early yielding could be achieved with the help of LYP steel in the hybrid configurations and the post yield stiffness of the pushover curves are greater for the hybrid systems than the regular system. As may be seen in pushover plots, the strength of the pushover curves is high and actually negative post-yield stiffness couldn't be achieved for this building. This can be explained with the high seismic design category (E) and high design base shear of the building.

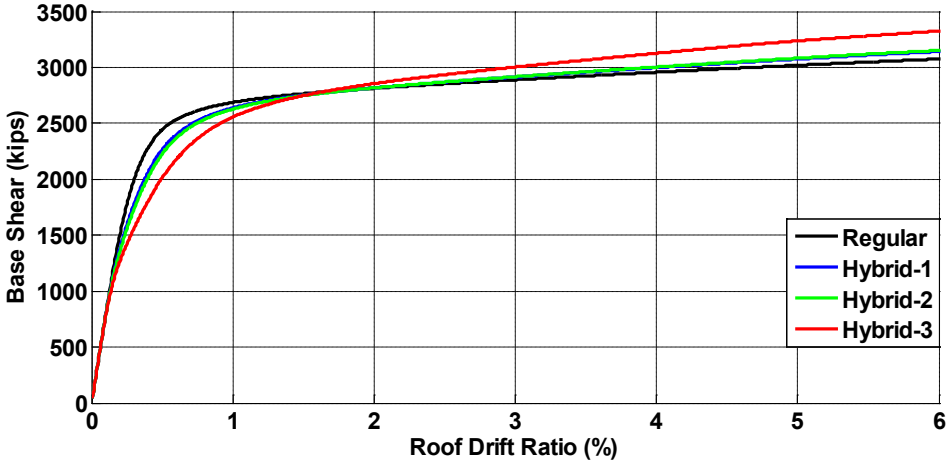

Figure 4-31. Pushover Analyses Results for Medical Office Building (MOB)

4.2.2. Incremental Dynamic Analysis

Nonlinear dynamic analyses were conducted by using both the far-field and near-field set of *FEMA P-695* methodology. Note that the building is at a high seismic zone (about 3 km away from Hayward Fault),

and seismic design category (SDC) is E according to *ASCE 7*. Due to this reason, near-field set of *FEMA P-695* is recommended for the analyses. Even though both far and near field motions are anchored to the MCE spectrum at the fundamental period, near field motions cause much more damage. The level of damage especially increases for the pulse type near-field motions. The analyses were run for both far-field (44 motions) and near-field (56 motions) for the MOB discussed in this section.

Figure 4-32 and Figure 4-33 show the median and 84th percentile performance comparison of Hybrid frames with respect to the regular frame under far-field motions, and Figure 4-34 show the median performance comparison under near-field motions. Similar to the previous case study, maximum story acceleration, maximum interstory drift ratio (IDR), and residual roof displacement performance comparisons are displayed in the figures. In these bar charts, if the bars are in positive y axis, then the performance increases, i.e. story acceleration, maximum IDR and residual roof displacement decreases. Hybrid-3 frame, which is the most or the real hybrid frame, gave the best performance for this building model similar to the previous model. When Hybrid-3 frame performance is compared with the regular frame performance, Hybrid-3 increased performance by about 20% to 30% for residual displacements. Maximum interstory drifts decreased by about 5% to 10% with Hybrid-3 frame, and maximum story accelerations slightly decreased. Note that 1.60 x MCE is the collapse check level for this building.

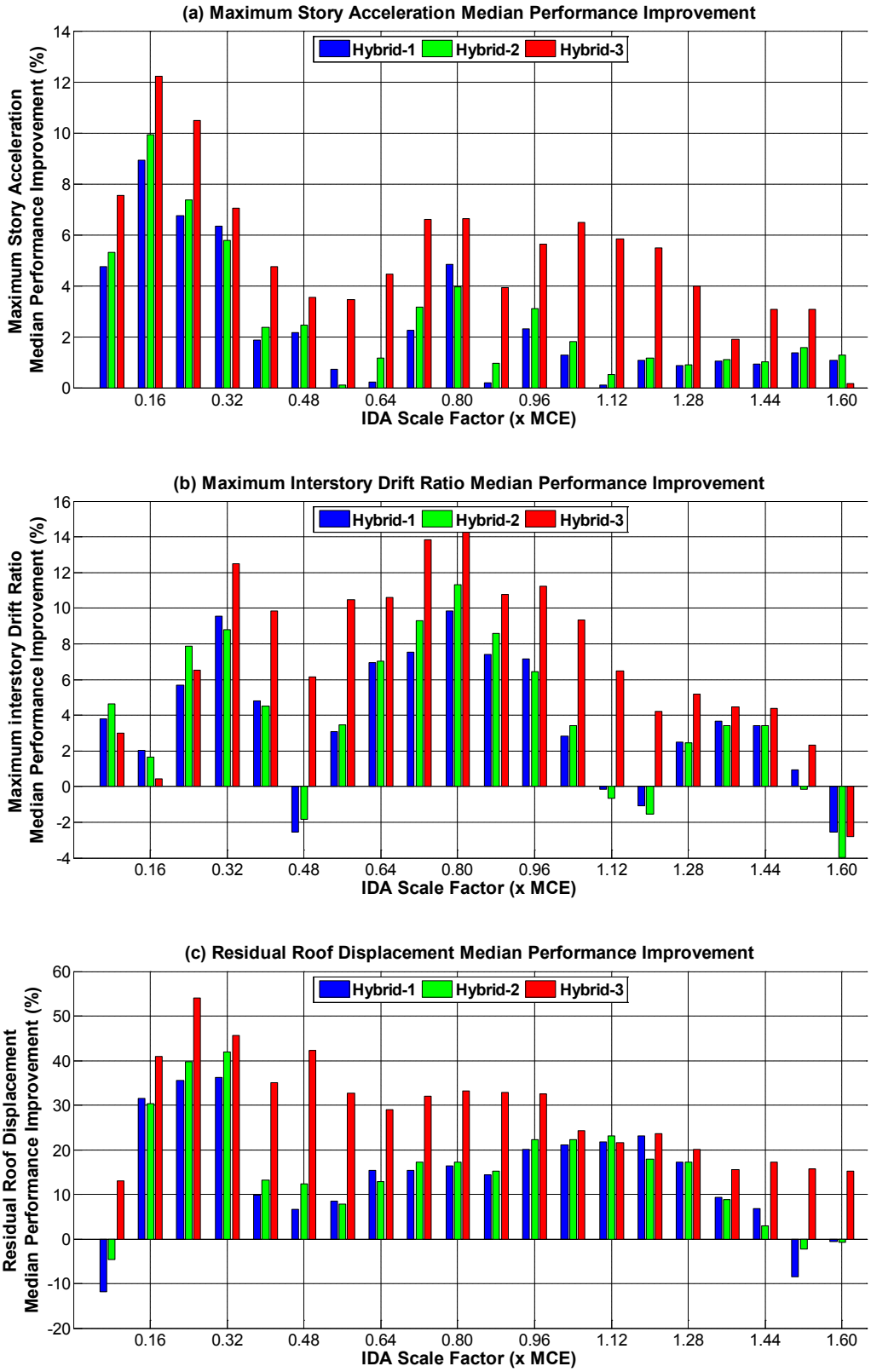

Figure 4-32. MOB Model Median Performance Improvements of 44 Far-Field Motions for (a) Max. Story Acceleration (b) Max. Interstory Drift Ratio (c) Residual Roof Displacement

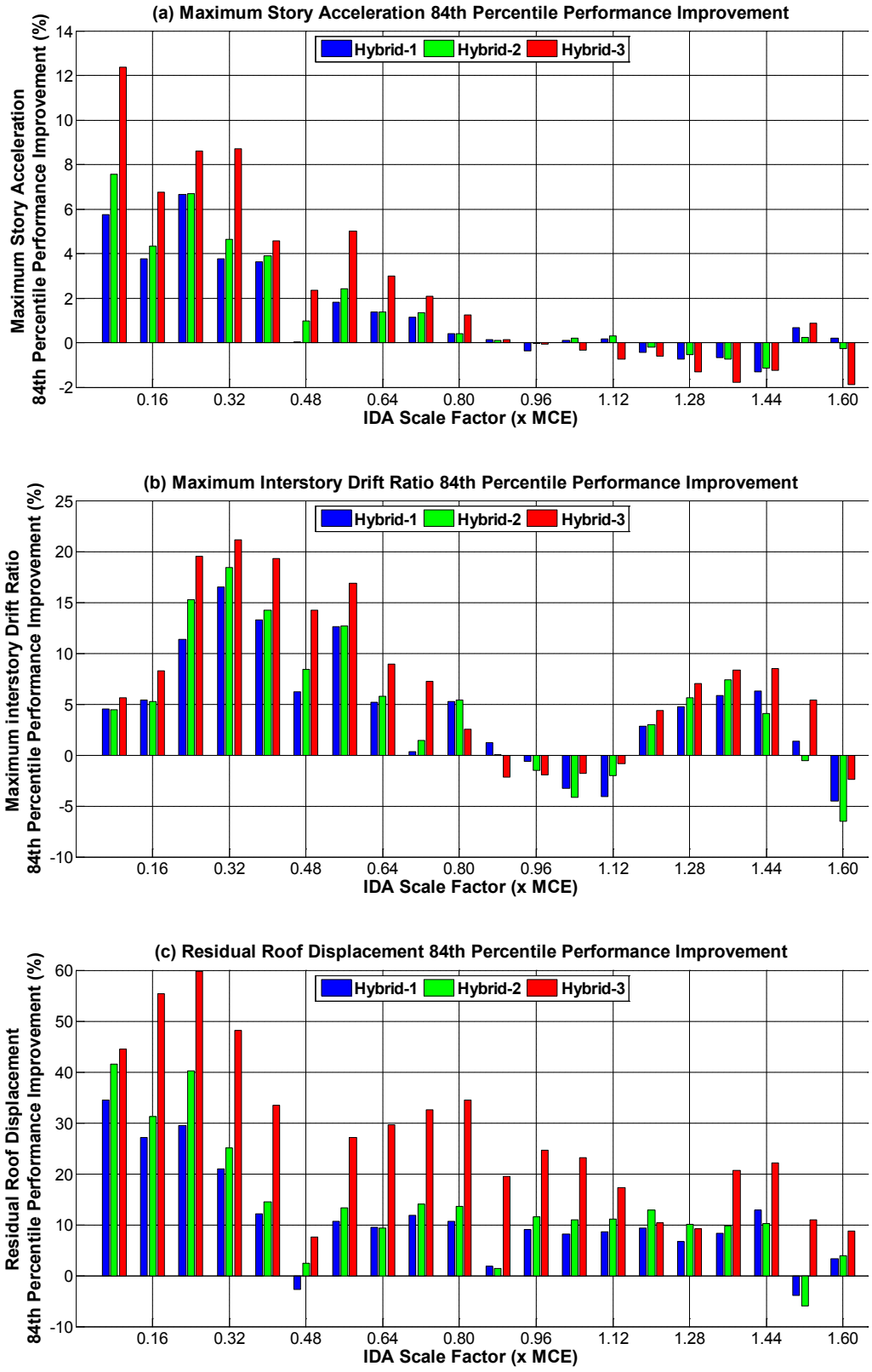

Figure 4-33. MOB Model 84th Percentile Performance Improvements of 44 Far-Field Motions for (a) Max. Story Acceleration (b) Max. Interstory Drift Ratio (c) Residual Roof Displacement

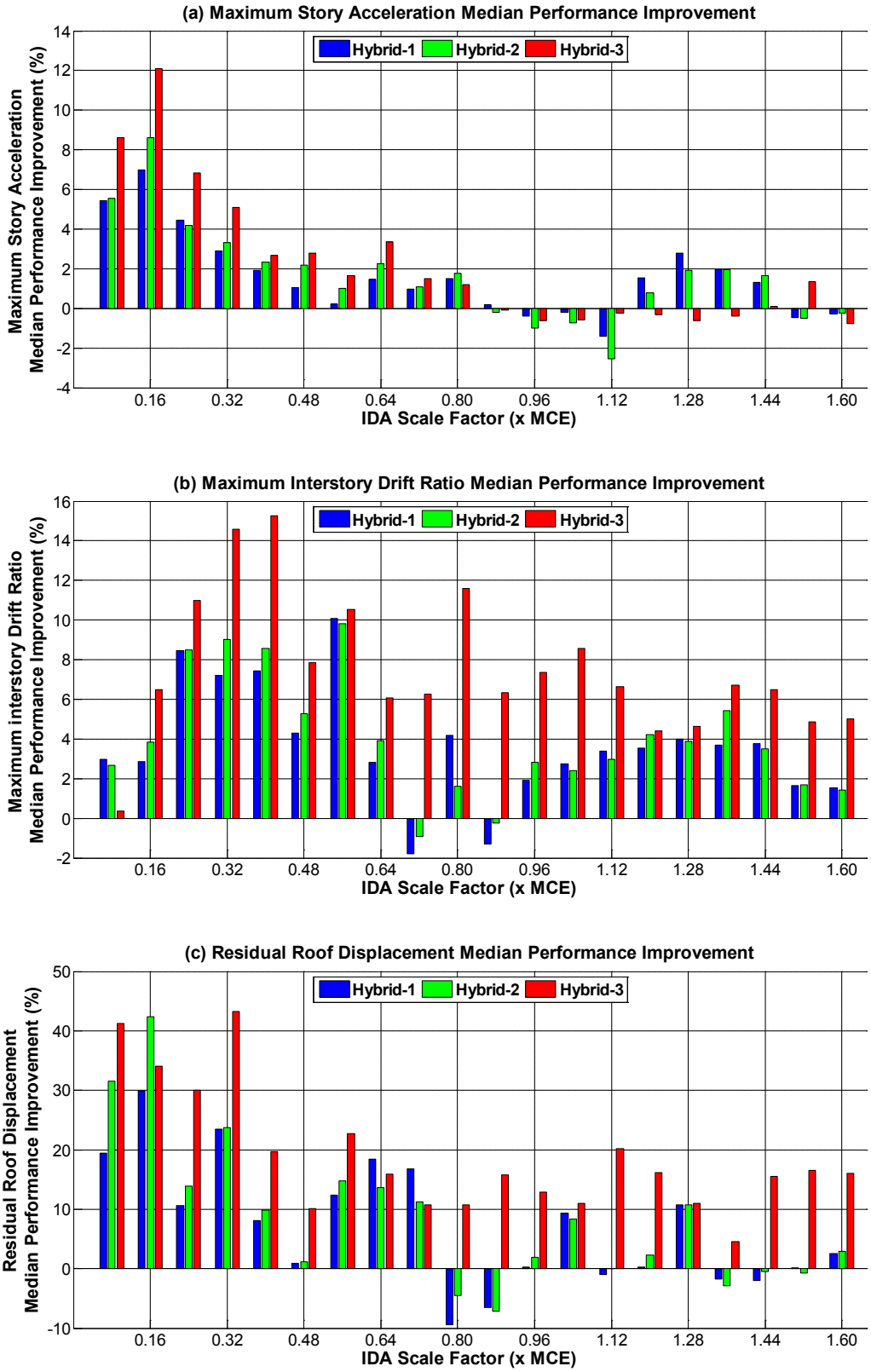

Figure 4-34. MOB Model Median Performance Improvements of 56 Near-Field Motions for (a) Max. Story Acceleration (b) Max. Interstory Drift Ratio (c) Residual Roof Displacements

4.2.3. IDA Dispersion

Figure 4-35 shows the IDA dispersion comparison of hybrid and regular BRBFs when they are subjected to 44 far-field ground motions. The dispersion in terms of maximum IDR is similar for regular and hybrid frames. Hybrid-3 combination gave less dispersion in terms of residual roof displacements after MCE level.

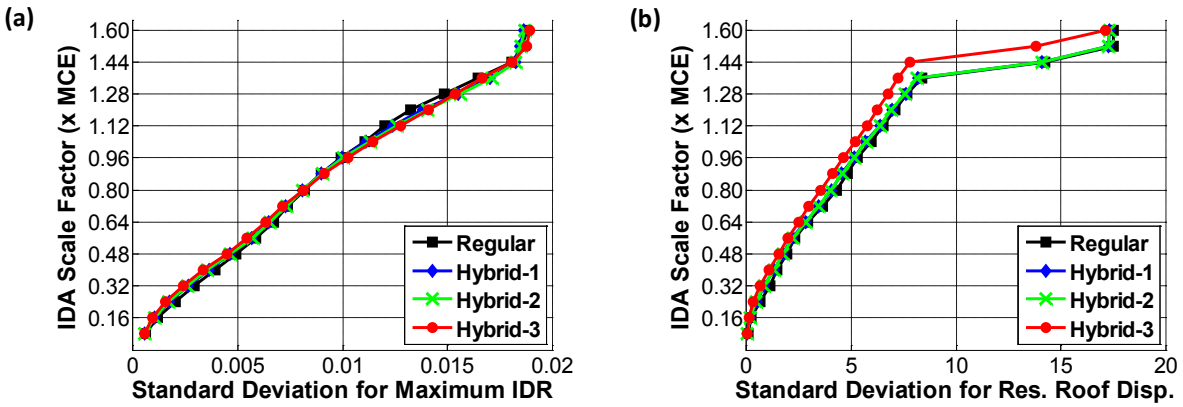

Figure 4-35. IDA Dispersion Calculated from 44 Far-Field Motions for (a) Maximum Interstory Drift Ratio (IDR) and (b) Residual Roof Displacement

Figure 4-36 shows the IDA dispersion comparison of hybrid and regular BRBFs when they are subjected to 56 near-field ground motions. Similar to far-field ground motion results, the dispersion in terms of maximum IDR is negligible, while hybrid frames resulted in smaller dispersion in terms of residual displacements.

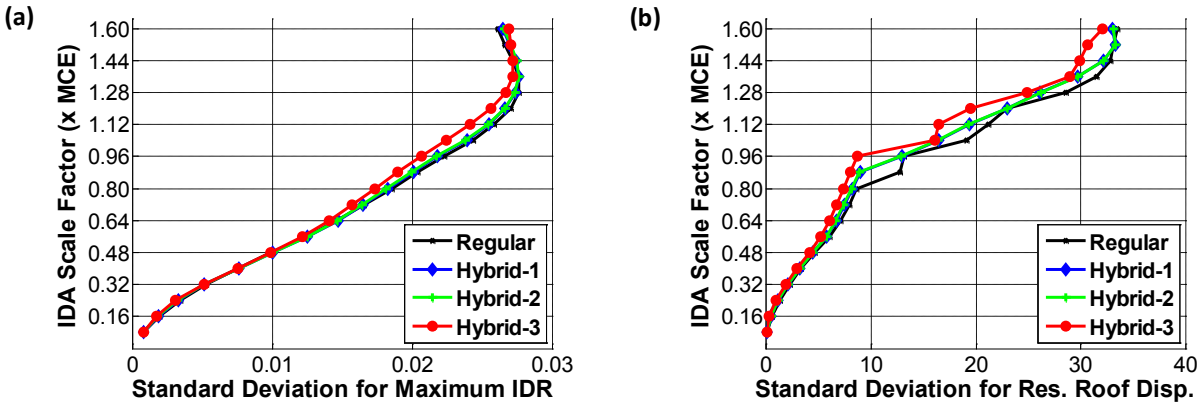

Figure 4-36. IDA Dispersion Calculated from 56 Near-Field Motions for (a) Maximum Interstory Drift Ratio (IDR) and (b) Residual Roof Displacement

4.2.4. *FEMA P-695* Performance Evaluation

FEMA P-695 evaluation is performed using 10% maximum interstory drifts as non-simulated collapse criteria in addition to the low cycle fatigue failure of braces. Table 4-10 and Table 4-11 tabulate the performance comparison between hybrid and regular BRBFs subjected to Far-Field and Near-Field ground motion sets respectively. All the building models passed the *FEMA P-695* methodology acceptance check. As explained before, the collapse performance evaluation may not reflect the correct behavior for this system due to the use of different building code. Also, as discussed in the previous title, residual displacements decreased consistently with hybrid systems. Due to these facts, it can be concluded that hybrid systems could improve the structural behavior for this 2nd case study building.

Table 4-10. MOB BRBF Model Collapse Performance Evaluation Using Far-Field Motions and 10% Interstory Drift + Low Cycle Fatigue Failure of Braces as Collapse Criteria

Beam Column Connection	BRBF Model	Computed Overstrength and Collapse Margin Parameters					Acceptance Check		
		Static Ω	*CMR*	μ_T	*SSF*	*ACMR*	Accept. *ACMR 10%*	Pass / Fail	Collapse Probability (%)
Non-MR	Regular	1.58	2.65	27.4	1.22	3.23	1.96	Pass	1.27
	Hybrid-1	1.62	2.71	27.5	1.22	3.30	1.96	Pass	1.14
	Hybrid-2	1.63	2.74	27.5	1.22	3.34	1.96	Pass	1.08
	Hybrid-3	1.76	3.02	26.3	1.22	3.69	1.96	Pass	0.64

Table 4-11. MOB BRBF Model Collapse Performance Evaluation Using Near-Field Motions and 10% Interstory Drift + Low Cycle Fatigue Failure of Braces as Collapse Criteria

Beam Column Connection	BRBF Model	Computed Overstrength and Collapse Margin Parameters					Acceptance Check		
		Static Ω	*CMR*	μ_T	*SSF*	*ACMR*	Accept. *ACMR 10%*	Pass / Fail	Collapse Probability (%)
Non-MR	Regular	1.58	2.32	27.4	1.22	2.83	1.96	Pass	2.38
	Hybrid-1	1.62	2.34	27.5	1.22	2.85	1.96	Pass	2.30
	Hybrid-2	1.63	2.34	27.5	1.22	2.85	1.96	Pass	2.30
	Hybrid-3	1.76	2.43	26.3	1.22	2.97	1.96	Pass	1.92

4.2.5. Collapse Probability

Figure 4-37 and Figure 4-38 show the collapse fragility curves obtained from the IDA using Far-Field and Near-Field ground motion sets respectively. Note that since this building is designed at a location which is about 5kms away from Hayward Fault in California, its performance is excellent under far-field

motions. This may be seen from the ground motion intensity levels that cause collapses in Figure 4-37. Although ground motion intensities decrease with Near-Field motions, the values are still high. Thus, the performance of this BRBF building is excellent and the performance is further increased with the implementation of hybrid braces.

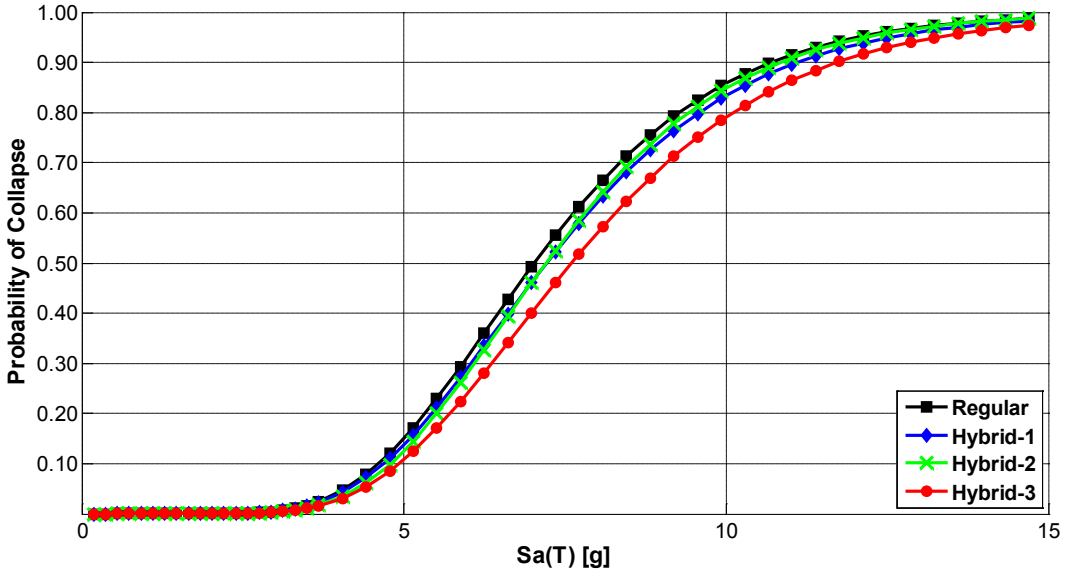

Figure 4-37. Far-Field Motions Collapse Probability Comparison Between Hybrid and Regular Frames using 10% Interstory Drift + Low Cycle Fatigue Failure of Braces as Collapse Criteria

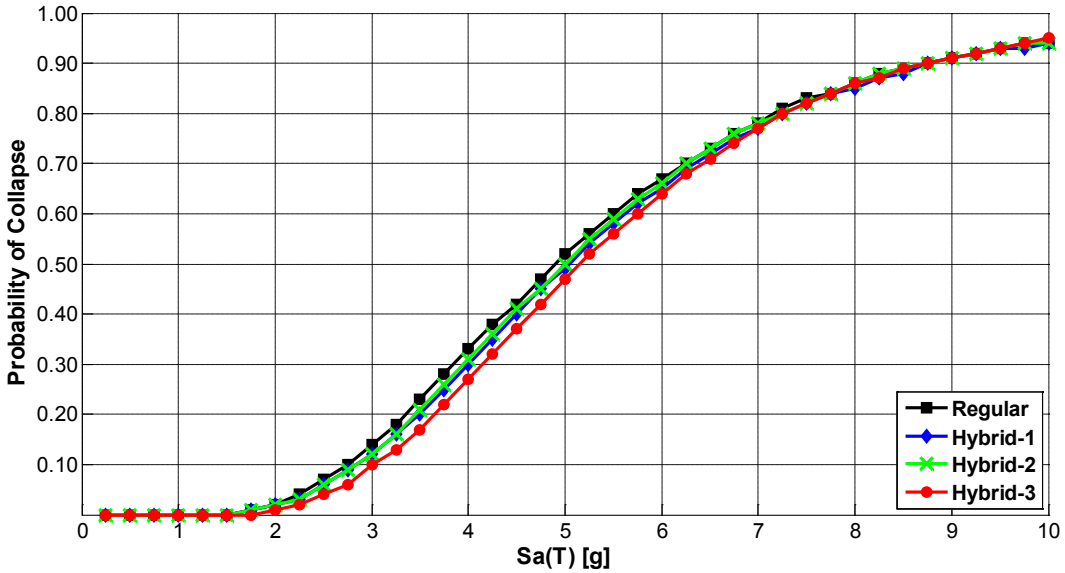

Figure 4-38. Near-Field Motions Collapse Probability Comparison between Hybrid and Regular Frames (a) Using 10% Interstory Drift + Low Cycle Fatigue Failure of Braces as Collapse Criteria

4.3. Summary of *ATC-76-1* Project Buckling Restrained Braced Frame Archetypes Performance Evaluation

The BRBF archetypes that are included in Chapter 7 of *ATC-76-1* project were analyzed and included in Appendix A of this dissertation. Three performance groups: 1) Long period BRBF archetypes designed at seismic design category (SDC) Dmax, 2) Long period BRBF archetypes designed at SDC Dmin, and 3) Short period archetypes designed at SDC Dmax. These performance groups involve five, seven and three different story heights respectively making a total of fifteen archetypes. The building height varies from two to eighteen stories. In addition to the regular (non-hybrid) systems, three hybrid BRBF combinations were also analyzed for each of these archetypes making a total of sixty models. Because there are 44 ground motions and the total number of scale factors for each ground motion is about 35 (20 scaling increments up to MCE, and then about 15 to find the CMR) the number of nonlinear dynamic analyses conducted on these archetypes is about 100,000.

The same modeling techniques explained in this chapter were also implemented on the archetypes of *ATC-76-1* project. The results obtained from these archetypes are similar to the two case studies explained in this chapter. The pushover curves were similar, with hybrid frames yielding earlier and also maintaining the positive post-yield stiffness at higher drift ratios than the regular frames. Hybrid BRBFs improved the performance especially by reducing the residual displacements. The benefit of hybrid frames was more on the archetypes where P-Delta effects are more critical. Since P-Delta effects are more critical on tall buildings designed at low SDCs, the performance of hybrid BRBFs reduced for especially one and two story short period archetypes designed at SDC Dmax. Collapse margin ratios increased and probability of collapses at the MCE levels decreased with hybrid BRBFs.

See Appendix A of this dissertation for the detailed summary of the results of *ATC-76-1* project archetypes.

4.4. Implementation of Hybrid BRBFs and Design Recommendations

Hybrid BRBs can be implemented in redundant core systems used in practice. Redundant core BRBs have multiple cores in multiple tubes and are used to reach high capacities. In hybrid BRBs, different steel materials will be used in these tubes. Figure 4-39 displays an example redundant core BRB and its cross-section. In these systems, a collar is used to connect to all braces for equal elongation at the brace ends. This matches well with the analytical model where hybrid BRB is created by connecting the braces in parallel. The collar also increases the overall stability of the brace by preventing core section extension

from out of plane buckling (Uang et al. 2004). Pin connections are used at the brace ends for these systems. The use of pin and collar assembly also allows the use of grouping multiple braces together to make large capacity braces. In the multi-core hybrid BRBs, different yielding levels can create an eccentricity and an internal moment problem might occur. This problem can be solved by sandwiching the HPS core in LYP core (or vice versa) using a similar section as in Figure 4-39(b). In addition, this problem could actually occur if different steel materials were used in the same tube. In redundant core system, different steel materials will be placed in different tubes, each having their own steel cases. Thus, if these cases are designed properly providing sufficient flexural stiffness, the interaction between different steel materials can be minimized.

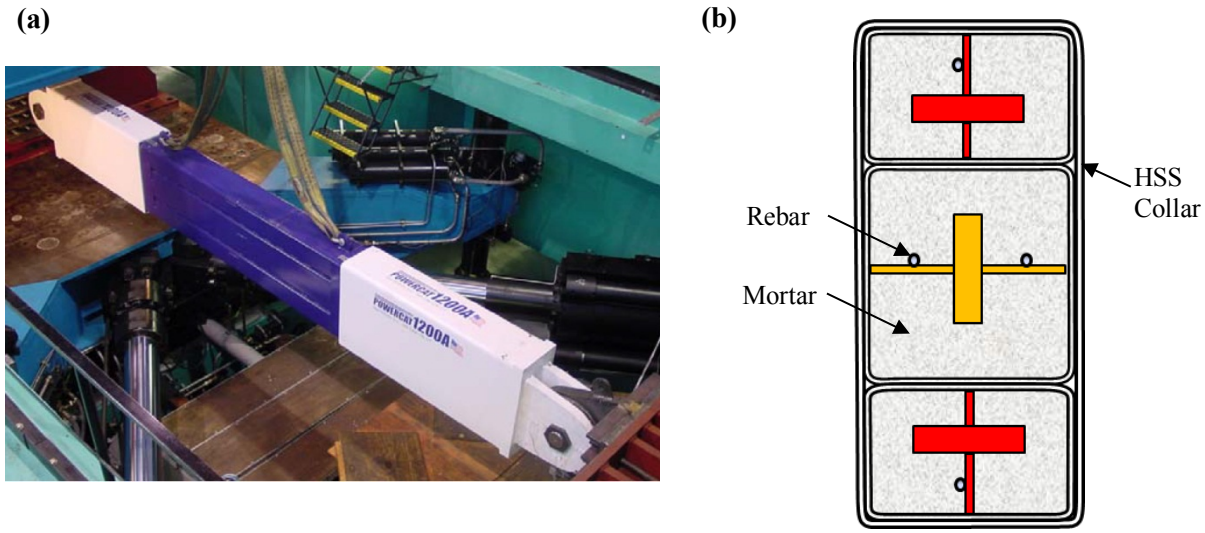

Figure 4-39. Multi core BRB (a) Overview (Merritt et al., 2003: Used under Fair Use) (b) Cross Sectional View at the End of Brace

Redundant core BRBs are supplied by the brace manufacturer, Star Seismic. It can contain up to eight independent cores. Figure 4-40 shows two photos of redundant core BRBs used in two different projects: Figure 4-40(a) is from the San Joaquin County Administration Building (3 independent cores), and Figure 4-40(b) is from the LA Live Hotel & Residences Building (4 independent cores).

(a) (b)

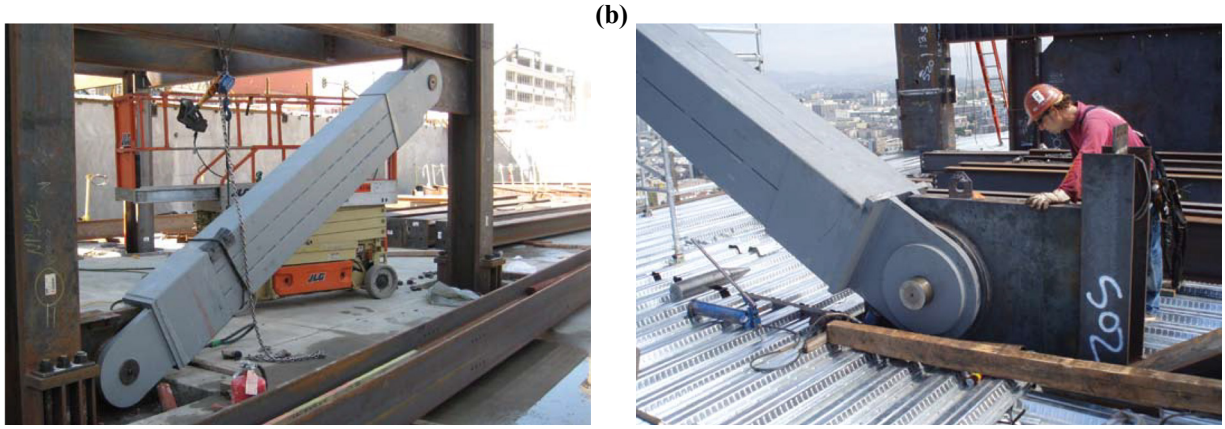

Figure 4-40. Redundant Core BRB Examples from Star Seismic Brace Manufacturer (http://www.starseismic.net/projects.html)

Although the redundant core BRB is a good alternative for hybrid BRBs, it provides some eccentricity between the cores. In order to keep the eccentricity small, a configuration shown in Figure 4-10 is more appropriate. Note that, the brace tested by Nippon Steel also had a similar configuration like the one shown in Figure 4-10.

As explained earlier in this chapter, there are two constraints while designing the hybrid BRBs. As a preliminary design concept, the stiffness and the strength of the brace should be kept the same as the regular brace. Thus, while designing the hybrid brace, first the design can be made as a regular BRB design in which the core is made of only A36 steel. Then, A36 yield core can be replaced with LYP100 and HP100W with the area ratios shown in Table 4-4.

Regarding the area ratios provided in Table 4-4, the strength of the hybrid BRB was kept the same as the regular BRB due to capacity design principles. In the hybrid brace area assignment of Table 4-4, the strain hardening of LYP100 and HPS100W was not considered. Another way to replace A36 with LYP100 and HPS100W might be to keep the strength the same at twice the design story drift. Twice the design story drift is generally used to validate the capacity design with the brace manufacturer. In other words, the brace manufacturer provides the overstrength, β, and strain hardening factors, ω, at twice the design story drift and the designer should check the assumed values at the design stage with the brace manufacturer data. The adjusted brace strengths used for capacity based design are verified with the brace manufacturer in this way.

For the BOB model (1st case study) explained in this chapter, a unit A36 area (1.0xA36) was replaced with 0.776xLYP100 and 0.278xHPS100W for Hybrid-3 combination. For that specific model, the brace

core strain that corresponds to twice the design story drift is 1.7%. If the strength of Hybrid-3 BRB at 1.7% brace strain is kept the same as the strength of regular A36 BRB, then the area assignment of the hybrid BRB becomes 0.800xLYP100 and 0.254xHPS100W. Thus, the area of LYP100 increases slightly while the area of HPS100W decreases from the original material combination. The effects of this change on the global pushover behavior are the slight increase in ductility and the slight decrease in the overstrength.

Note that this difference in area assignment is happening because A36, LYP100, and HPS100W have different strain hardening values. As the yield strength of steel increases, strain hardening decreases.

The design of the steel casing of hybrid BRB can be similar to the current design practice in which the elastic buckling strength of the casing should be 1.5 times the yield strength of the BRB core. Note that the yield strength of the hybrid BRB core can be assumed as the same as the yield strength of the regular brace A36 yield core for this calculation. Or, the strength at which both LYP100 and HPS100W yield can be used which will be more or less the same as the yield strength of the regular brace with A36 yield core.

4.5. Summary of Hybrid Buckling Restrained Braced Frames

The hybrid BRBF approach was tested on various buildings with different story heights, seismic design categories and building plans in this Chapter and in Appendix A. Hybrid BRBs were developed through the use of different yield strength steel as the brace core material. Especially, the use of LYP100 type low strength steel in combination with HPS100W type high strength steel enhanced the performance of the BRBFs. The use of low strength steel results in early yielding of the system and provides high ductility capacity.

The overall seismic performance could be improved with hybrid BRBF systems. The most significant improvement was in the residual displacements which decreased about 30% to 40% at all ground motion intensities. Maximum interstory drifts decreased up to 10% at most of the intensities and story accelerations remained the same.

Collapse margin ratios increased and probability of collapse decreased for hybrid BRBFs. The dispersion of the IDA obtained from hybrid BRBFs are less than that of regular (non-hybrid) BRBFs. This proves that the reliability of the hybrid BRBF systems is more than the regular BRBFs.

The preliminary design concept of hybrid BRBs requires the initial stiffness and strength of the hybrid BRBs to be the same as the regular (non-hybrid) BRBs. This method satisfies the capacity design

principles of braced frames automatically.

The cost of hybrid BRBFs is very close to the cost of non-hybrid BRBFs. The only cost increase for hybrid BRBs is due to the higher material costs of low strength steel and high strength steel compared to the cost of carbon steel. This minor impact on cost makes hybrid BRBFs more attractive.

In this dissertation, the performance of the hybrid BRBFs were compared with non-hybrid BRBFs using *FEMA P-695* methodology. Although the initial intent was to derive seismic performance factors (R, C_d, and Ω_0) for hybrid BRBFs, it was decided that this would be premature before conducting lab tests on hybrid BRBs. As explained in Chapter 3 of this dissertation, the quality of the lab testing is necessary to make a true calculation of the acceptable collapse margin ratios which is necessary for *FEMA P-695* evaluation. However, the increased collapse margin ratios or reduced collapse probabilities of hybrid BRBFs indicate that a higher response modification factor (R) than 8, which is used for non-hybrid BRBFs, could be used for hybrid BRBF systems.

The increase in the R factor of hybrid BRBFs will make the hybrid BRBFs perform similar to non-hybrid BRBFs, but will result in a cheaper system than the regular BRBFs. If the same R factor of regular BRBFs, which is 8, is also used for hybrid BRBFs, then the cost will be similar but the performance will be enhanced.

The challenging aspect of the hybrid BRB is the availability of low strength steel. LYP steel is available in Japan through Nippon Steel but currently not available in the US market. Due to the difficulty in procurement of LYP steel, Nippon Steel Corporation in Japan is only willing to supply LYP plates to Nippon Steel Engineering USA depending on the required quantity of the plates. The research team is working with BRB manufacturers to clarify the issues in obtaining LYP steel and building a multi-core BRB for lab testing.

CHAPTER 5: HYBRID MOMENT RESISTING STEEL FRAMES

A hybrid moment frame containing members and connections associated with ordinary (OMF), intermediate (IMF), and special moment frames (SMF) was proposed by Charney and Atlayan (2011). In that study, special detailed elements were designed to yield at force levels well below the DBE and provide inelastic energy dissipation that helps to control dynamic amplification. In addition, elements with ordinary detailing were designed to remain elastic during the DBE and provide post-yield stiffness to counteract P-Delta effects. The hinges that form first had the highest ductility demand and were detailed according to the rules for SMF. The hinges that form last have the lowest ductility demand and were detailed according to the rules for IMF or OMF.

The previous work by Charney and Atlayan (2011) had certain limitations. Only a nine-story building frame was investigated with ten ground motions and cyclic deterioration in strength and stiffness of the steel components of the analyzed buildings was neglected. This chapter investigates similar hybrid moment frame approach as studied before on a design space made of 42 SMF archetypes.

5.1. Design Space

SMF archetypes were designed in accordance with the design requirements specified in *AISC 341-10*, *Seismic Provisions for Structural Steel Buildings* (AISC, 2010a), *AISC 358-10*, *Prequalified Connections for Special and Intermediate Steel Moment Frames for Seismic Applications* (AISC, 2010b), *AISC 360-10*, Specification for Structural Steel Buildings (AISC, 2010c), and *ASCE 7-10*, *Minimum Design Loads for Buildings and Other Structures* (ASCE, 2010).

A square plan configuration (see Figure 5-1) consisting of a five-bay perimeter frame on each side of the building was selected for investigation. In Figure 5-1, the dark grey shaded area shows the penthouse, and the light grey shaded area shows the mass associated with the highlighted 2-D frame that was used for the analysis. The bay width of the models is 30 feet. Three different building heights were used in the design space: three, six and ten story SMF buildings. Typical story height of 13 feet was used on top of the 15 foot bottom story (See Figure 5-2).

Table 5-1 tabulates the 42 SMF archetypes investigated. In addition to three building heights, two different column sizes (W14 and W24) and three different strong column weak beam ratios (1.0, 1.5 and 2.0) were used. SDC of Dmax was chosen for all the designs. In addition to regular frames, two levels of Hybrid frames were also designed for each regular design with different column sizes and SC/WB ratios.

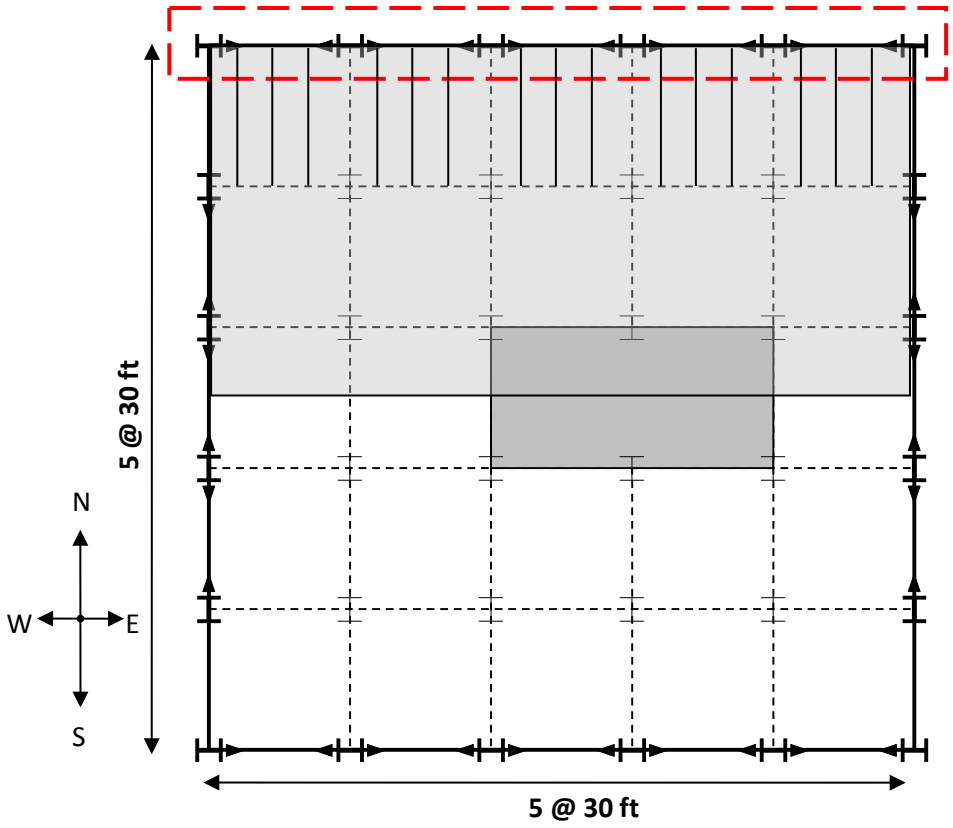

Figure 5-1. Typical Plan Configuration for SMF Archetypes

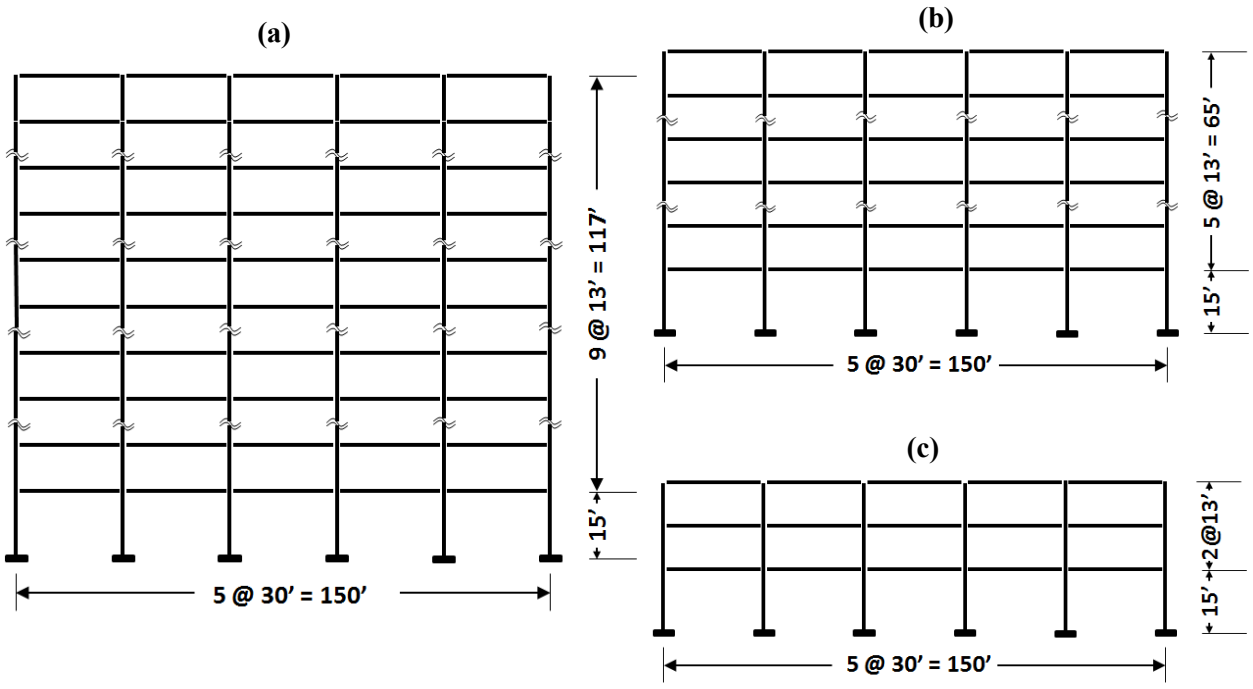

Figure 5-2. Elevations of (a) 10 story (b) 6 story and (c) 3 Story Models

Table 5-1. Design Space for Moment Frames

Archetype ID	No. of Stories	SDC	Columns	SC/WB Ratio	Frame Type	T_1 (sec)
1-3St-Dmax-W14-SC/WB=1.0-REG	3	Dmax	W14	1.0	Regular	1.32
2-3St-Dmax-W14-SC/WB=1.0-HYB1				1.0	Hybrid-1	1.33
3-3St-Dmax-W14-SC/WB=1.0-HYB2				1.0	Hybrid-2	1.34
4-3St-Dmax-W14-SC/WB=1.5-REG				1.5	Regular	1.29
5-3St-Dmax-W14-SC/WB=1.5-HYB1				1.5	Hybrid-1	1.29
6-3St-Dmax-W14-SC/WB=1.5-HYB2				1.5	Hybrid-2	1.30
7-3St-Dmax-W14-SC/WB=2.0-REG				2.0	Regular	1.25
8-3St-Dmax-W24-SC/WB=1.0-REG			W24	1.0	Regular	1.23
9-3St-Dmax-W24-SC/WB=1.0-HYB1				1.0	Hybrid-1	1.23
10-3St-Dmax-W24-SC/WB=1.0-HYB2				1.0	Hybrid-2	1.23
11-3St-Dmax-W24-SC/WB=1.5-REG				1.5	Regular	1.20
12-3St-Dmax-W24-SC/WB=1.5-HYB1				1.5	Hybrid-1	1.20
13-3St-Dmax-W24-SC/WB=1.5-HYB2				1.5	Hybrid-2	1.20
14-3St-Dmax-W24-SC/WB=2.0-REG				2.0	Regular	1.15
1-6St-Dmax-W14-SC/WB=1.0-REG	6	Dmax	W14	1.0	Regular	2.00
2-6St-Dmax-W14-SC/WB=1.0-HYB1				1.0	Hybrid-1	2.02
3-6St-Dmax-W14-SC/WB=1.0-HYB2				1.0	Hybrid-2	2.01
4-6St-Dmax-W14-SC/WB=1.5-REG				1.5	Regular	2.00
5-6St-Dmax-W14-SC/WB=1.5-HYB1				1.5	Hybrid-1	2.02
6-6St-Dmax-W14-SC/WB=1.5-HYB2				1.5	Hybrid-2	2.02
7-6St-Dmax-W14-SC/WB=2.0-REG				2.0	Regular	2.03
8-6St-Dmax-W24-SC/WB=1.0-REG			W24	1.0	Regular	1.94
9-6St-Dmax-W24-SC/WB=1.0-HYB1				1.0	Hybrid-1	1.95
10-6St-Dmax-W24-SC/WB=1.0-HYB2				1.0	Hybrid-2	1.96
11-6St-Dmax-W24-SC/WB=1.5-REG				1.5	Regular	1.95
12-6St-Dmax-W24-SC/WB=1.5-HYB1				1.5	Hybrid-1	1.97
13-6St-Dmax-W24-SC/WB=1.5-HYB2				1.5	Hybrid-2	1.97
14-6St-Dmax-W24-SC/WB=2.0-REG				2.0	Regular	1.97
1-10St-Dmax-W14-SC/WB=1.0-REG	10	Dmax	W14	1.0	Regular	2.46
2-10St-Dmax-W14-SC/WB=1.0-HYB1				1.0	Hybrid-1	2.48
3-10St-Dmax-W14-SC/WB=1.0-HYB2				1.0	Hybrid-2	2.50
4-10St-Dmax-W14-SC/WB=1.5-REG				1.5	Regular	2.50
5-10St-Dmax-W14-SC/WB=1.5-HYB1				1.5	Hybrid-1	2.52
6-10St-Dmax-W14-SC/WB=1.5-HYB2				1.5	Hybrid-2	2.53
7-10St-Dmax-W14-SC/WB=2.0-REG				2.0	Regular	2.51
8-10St-Dmax-W24-SC/WB=1.0-REG			W24	1.0	Regular	2.40
9-10St-Dmax-W24-SC/WB=1.0-HYB1				1.0	Hybrid-1	2.43
10-10St-Dmax-W24-SC/WB=1.0-HYB2				1.0	Hybrid-2	2.45
11-10St-Dmax-W24-SC/WB=1.5-REG				1.5	Regular	2.42
12-10St-Dmax-W24-SC/WB=1.5-HYB1				1.5	Hybrid-1	2.45
13-10St-Dmax-W24-SC/WB=1.5-HYB2				1.5	Hybrid-2	2.45
14-10St-Dmax-W24-SC/WB=2.0-REG				2.0	Regular	2.44

In the original hybrid moment frame study explained in Chapter 2, when the regular frames were made hybrid, only the girder sizes were changed by keeping the total plastic capacity and the structural weight of the story the same. The column sizes were unchanged. The change in girder sizes by keeping the story wise total girder capacity and weight the same resulted in a reduction in the stiffness. This can actually be observed in the pushover curve of the preliminary hybrid moment frame study (see Figure 2-19). When the building in the original study was reanalyzed with better modeling techniques and more ground motions, it was observed that the response of the building at low level ground motions was affected by this stiffness change. While implementing hybridity, in order to keep the story stiffness the same (in addition to total plastic capacity), the total weight of the girders has to be increased.

The reason for varying the column sizes and the SC/WB ratios in the new design space was to investigate the performance of hybrid frames for different design scenarios and also to evaluate the effectiveness of hybrid frames versus regular frames with stronger columns. In other words, if the weight of the hybrid frames is more than the regular frames then would it be a better idea to increase the column sizes of the regular frame instead of making them hybrid by changing the girder sizes? Hybrid frame design and performance evaluation is explained later in this chapter.

In addition to hybrid moment frame performance investigation, two explicit side studies were also made to compare the performance of regular designs with different column sizes (W14 and W24) and different SC/WB ratios. The results of this study are discussed in Appendix B.

Archetype IDs shown in Table 5-1 will be used in the legends of the figures in this chapter and in Appendix B. Computed first mode periods, T_1, of the design space are also tabulated in Table 5-1. Appendix B provides the sections of the moment frame archetypes that are tabulated in Table 5-1.

Table 5-2 tabulates the weight and doubler plate use comparison of the moment frames which gives some insight on the cost calculations. The tabulated girder and column weights were calculated by multiplying the length of the sections with their weights. Calculated weights are only for the 2-D SMF frame used for the analysis, not for the whole structure or whole lateral load resisting system. Doubler plate comparison was made by using the vertical edge areas of the plates which were calculated as the beam clear depth multiplied by the thickness of the doubler plate. The reason for using only the vertical edges is that the full strength of the doubler plates can be developed by only welding the doubler plates along their vertical edges (Shirsat, 2011). Similar to the weight calculation, doubler plate edge areas were also calculated by only using the single 2-D SMF frame. The number of joints that needed doubler plate supply is also shown in parenthesis in Table 5-2.

Table 5-2. Weight and Doubler Plate Use Comparison for Moment Frames

Archetype ID	Weight (lbs)			Doubler Plate Vertical Edge Area (in^2)
	Column	Girder	Total	
1-3St-Dmax-W14-SC/WB=1.0-REG	36900	32700	69600	656 (16)
2-3St-Dmax-W14-SC/WB=1.0-HYB1	36900	36420	73320	705 (16)
3-3St-Dmax-W14-SC/WB=1.0-HYB2	36900	36480	73380	726 (12)
4-3St-Dmax-W14-SC/WB=1.5-REG	45428	31500	76928	349 (12)
5-3St-Dmax-W14-SC/WB=1.5-HYB1	45428	34500	79928	371 (14)
6-3St-Dmax-W14-SC/WB=1.5-HYB2	45428	36030	81458	409 (12)
7-3St-Dmax-W14-SC/WB=2.0-REG	55186	30300	85486	117 (10)
8-3St-Dmax-W24-SC/WB=1.0-REG	23124	30300	53424	332 (18)
9-3St-Dmax-W24-SC/WB=1.0-HYB1	23124	33330	56454	439 (16)
10-3St-Dmax-W24-SC/WB=1.0-HYB2	23124	34290	57414	379 (16)
11-3St-Dmax-W24-SC/WB=1.5-REG	27716	29100	56816	240 (18)
12-3St-Dmax-W24-SC/WB=1.5-HYB1	27716	31050	58766	276 (16)
13-3St-Dmax-W24-SC/WB=1.5-HYB2	27716	32760	60476	310 (16)
14-3St-Dmax-W24-SC/WB=2.0-REG	34276	29100	63376	156 (12)
1-6St-Dmax-W14-SC/WB=1.0-REG	91992	87600	179592	1748 (36)
2-6St-Dmax-W14-SC/WB=1.0-HYB1	91992	99930	191922	1873 (34)
3-6St-Dmax-W14-SC/WB=1.0-HYB2	91992	99750	191742	1879 (32)
4-6St-Dmax-W14-SC/WB=1.5-REG	112052	80850	192902	843 (30)
5-6St-Dmax-W14-SC/WB=1.5-HYB1	112052	95220	207272	1027 (32)
6-6St-Dmax-W14-SC/WB=1.5-HYB2	112052	93570	205622	1078 (24)
7-6St-Dmax-W14-SC/WB=2.0-REG	132748	74400	207148	65 (8)
8-6St-Dmax-W24-SC/WB=1.0-REG	59236	77850	137086	973 (36)
9-6St-Dmax-W24-SC/WB=1.0-HYB1	59236	89640	148876	1101 (34)
10-6St-Dmax-W24-SC/WB=1.0-HYB2	59236	87810	147046	1111 (34)
11-6St-Dmax-W24-SC/WB=1.5-REG	67892	72900	140792	705 (36)
12-6St-Dmax-W24-SC/WB=1.5-HYB1	67892	83910	151802	811 (30)
13-6St-Dmax-W24-SC/WB=1.5-HYB2	67892	82650	150542	831 (28)
14-6St-Dmax-W24-SC/WB=2.0-REG	82028	70200	152228	350 (30)
1-10St-Dmax-W14-SC/WB=1.0-REG	222176	188550	410726	3050 (58)
2-10St-Dmax-W14-SC/WB=1.0-HYB1	222716	210000	432716	3391 (52)
3-10St-Dmax-W14-SC/WB=1.0-HYB2	222716	208230	430946	3555 (50)
4-10St-Dmax-W14-SC/WB=1.5-REG	267396	171750	439146	631 (34)
5-10St-Dmax-W14-SC/WB=1.5-HYB1	267396	191400	458796	1067 (36)
6-10St-Dmax-W14-SC/WB=1.5-HYB2	267396	192690	460086	1234 (36)
7-10St-Dmax-W14-SC/WB=2.0-REG	307056	159450	466506	64 (6)
8-10St-Dmax-W24-SC/WB=1.0-REG	135472	174600	310072	2646 (60)
9-10St-Dmax-W24-SC/WB=1.0-HYB1	135472	199020	334492	2876 (56)
10-10St-Dmax-W24-SC/WB=1.0-HYB2	135472	195330	330802	2913 (52)
11-10St-Dmax-W24-SC/WB=1.5-REG	178864	164400	343264	1110 (52)
12-10St-Dmax-W24-SC/WB=1.5-HYB1	178864	184260	363124	1508 (44)
13-10St-Dmax-W24-SC/WB=1.5-HYB2	178864	182910	361774	1528 (42)
14-10St-Dmax-W24-SC/WB=2.0-REG	211440	161400	372840	359 (36)

The designs made with W14 columns are heavier than the designs made with W24 columns. Although W14 columns have thicker webs, doubler plate vertical edge areas are greater for the W14 column designs. This is not only due to the deep column sections, but also due to the possible deeper girders that are used with the W14 column designs. The number of joints that needs doubler plate supply is less for W14 column designs than W24 column designs. The girder sections used for W14 column designs were sometimes deeper than the W24 column designs for the drift controlled buildings (6 and 10 story models).

When the SC/WB is increased, column sections get bigger and thus the requirement for doubler plates decreases. Column weights increased with higher SC/WB ratio designs. Girder weights reduced for the drift controlled designs as the SC/WB increased.

As explained earlier, the weight of the Hybrid frames had to be increased in order to keep the story stiffnesses the same as the regular frames. The increase was on average of 10% both for the structural weight and for the doubler plate edge areas.

5.2. Design Details

- The Equivalent Lateral Force (ELF) procedure was used for the design. The design period, $C_u T_a$, for the three, six and ten story designs are 0.76 sec., 1.31 sec., and 1.95 sec. respectively. The computed periods, which are longer than the design periods, were used while checking the drift. The period was recalculated each time a section was changed, and new set of lateral forces were used to check the drift of the updated design.

- Six and ten story models were drift controlled, while three story model was strength controlled. While modifying the sections to satisfy drift requirements, displacement participation factors were considered (Charney, 1991 and Charney, 1993). Virtual work option of SAP2000 (CSI, 2012) computer program was used for this purpose.

- Unlike the design spaces that are created for *FEMA P-695* methodology, archetype designs were based on the code required SMF displacement participation factor, C_d, of 5.5.

- ASTM A992 steel with 50 ksi yield strength was used for member designs.

- The floor dead load is 96 psf on all floors and 83 psf on the roof. Unreduced live load is 50 psf on all floors and 20 psf on the roof. Cladding and parapet loads are 25 psf and are applied as perimeter loads. 5 feet tall parapet was used at the roof.

- Three beams were connected perpendicular to the girder with unbraced length of girder as 7.5 ft.

- In the regular frame designs, all girders at a floor level are of the same section.

- All sections were designed as reduced beam section (RBS) connections using a=0.625b_f, b=0.75d_b, and c=0.175 b_f where d_b is the beam depth and b_f is the beam flange width. See Figure 5-3 for the definition of a, b, and c. Note that these are the middle values of the limits specified in *AISC 358-10* (AISC, 2010b). For the hybrid frames, reduction in flange areas was changed. This is explained later in this chapter.

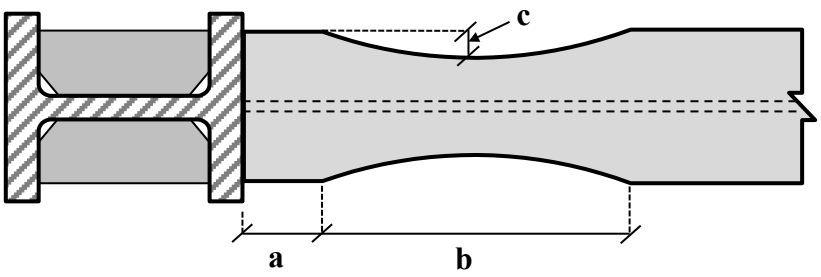

Figure 5-3. RBS Connection Details

- Direct analysis method was used for the column stability design. The analyses were done with SAP2000 (CSI, 2012) software which is capable of including flexural, shear and axial deformations. Benchmark problems of *AISC 360-10* (AISC, 2010b) were solved with SAP2000 to verify the software capability. A factor of 0.8 was applied to modify the member stiffnesses and notional loads with a factor of 0.003 times the gravity loads were assigned for initial imperfections. Note that stiffness reduction was not made when calculating the period or drifts as this would be too conservative. Recommendations by Nair et al. (2011) were followed while applying direct analysis method with ELF seismic design procedure.

- Sometimes seismic compactness criteria caused jumps in column sizes.

- Girder sizes at the 2nd level are mostly smaller than the 3rd and 4th story girders on 10 story model. Column sizes were not increased progressing upwards.

- Clear story height was used as unbraced column length.

- All columns were fixed at the base and were oriented to resist strong axis bending.

- Two exterior columns and four interior columns are of different sizes. Same sections were used for all four interior columns. Interior column sizes were mostly controlled by girder sizes due to SC/WB requirement.

- Panel zone shear strength was determined from *AISC 360-10* (AISC, 2010c) and doubler plate thicknesses were modified by 1/16 in. increments.

- Column splices were provided at every two stories and located at 4 ft above the floor level. At the joints that are close to column splices, SC/WB calculation was based on the column size that occurs at the joint. There are no splices in the three story model.

- Amplified seismic load was used in the SC/WB formulation when calculating the column axial load to reduce the column plastic capacity. This is required by *AISC 341-10* (AISC, 2010a).

- Complete new designs were made when SC/WB was increased from the code required value of 1.0 to 1.5 and 2.0. When the frames are drift controlled (six and ten story designs), the girder sizes of the higher SC/WB ratio designs were mostly smaller than the lower SC/WB designs. Thus, increasing the SC/WB ratio does not have a significant impact on the overstrength of the drift controlled designs.

5.3. Nonlinear Model Details

The inelastic behavior was modeled through concentrated plasticity where inelastic rotational springs with hysteretic properties are used at the ends of elastic beam-column elements and panel zones. Figure 5-4 shows the details of the analytical model used for the moment frames. Reduced beam section (RBS) connections were used for the beams and rigid parallelograms incorporating Krawinkler model were used for the panel zones. Nonlinear models were created and run on OpenSees.

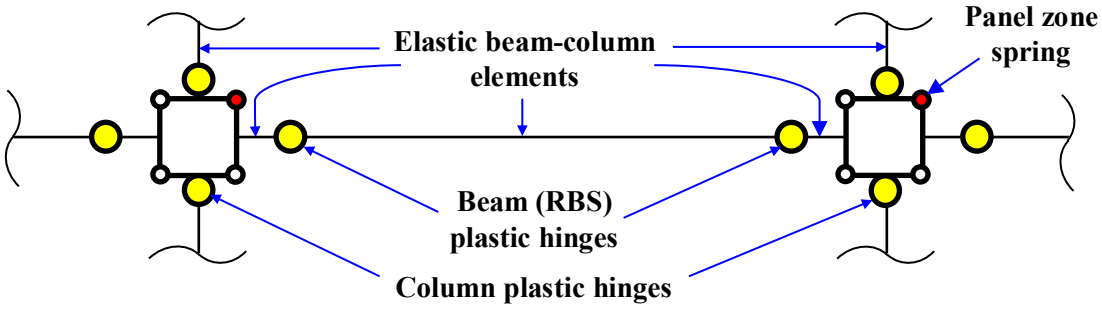

Figure 5-4. Moment Frame Analytical Model Details

5.3.1. Plastic Hinge Model for Beams

The modified Ibarra-Krawinkler deterioration model with bilinear hysteretic response was used to model girder plastic hinges. The hysteretic response of this material is calibrated with more than 350 experimental data of steel beam-column connections. The modified Ibarra Krawinkler model is capable of modeling basic strength, post capping strength, unloading stiffness, and accelerated stiffness cyclic deterioration modes. Figure 5-5 shows an example cyclic force deformation test on a cantilever W24x103 beam section. The deterioration modes can be seen in Figure 5-5 (d). The important parameters of this model are shown on the backbone curve in Figure 5-5 (c). Pre-capping plastic rotation, θ_p, is the difference in yield rotation and the rotation at maximum moment. Post-capping rotation, θ_{pc}, is the difference in rotation at maximum and zero moment. The other parameters are ultimate rotation capacity, θ_u, effective yield moment, M_y, capping moment strength, M_c, and residual moment, M_r. Another important parameter of this model is reference cumulative rotation capacity; Λ, which is reference hysteretic energy dissipation capacity, E_t, divided by M_y (Lignos and Krawinkler, 2011).

Lignos and Krawinkler (2011) provided multivariate regression formulas to estimate the deterioration parameters (pre-capping plastic rotation, θ_p, post-capping plastic rotation, θ_{pc}, and cyclic deterioration, Λ) for different connection types. Different formulas are proposed for beams with RBS and beams other than RBS. In the regression formulas, the main contributor of the deterioration parameters is the beam web depth over thickness ratio (h/t_w). This is because beams with large h/t_w are more prone to web local buckling. Flange width to thickness ratio ($b_f/2t_f$) and shear span over depth ratio (L/d), unbraced length divided by radius of gyration about the y-axis of the beam, (L_b/r_y) also have minor effect on deterioration parameters.

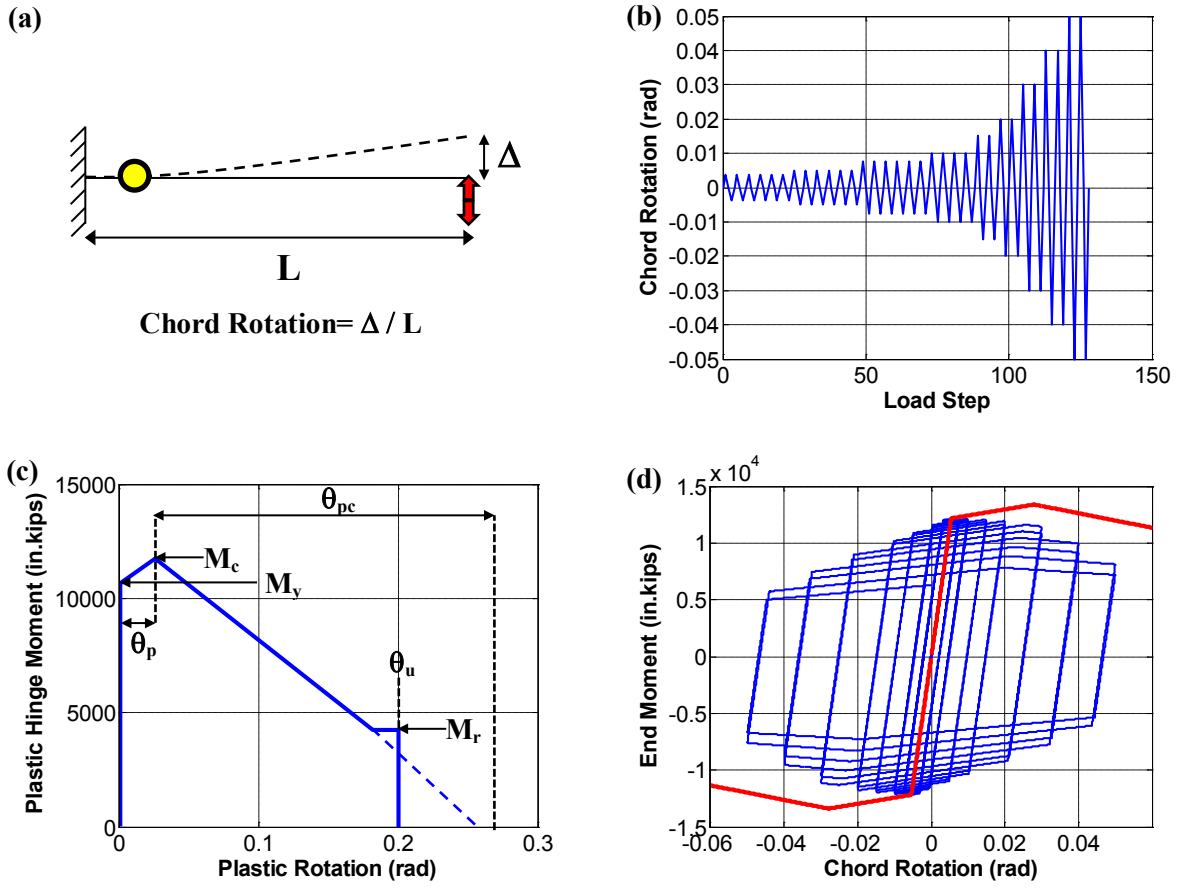

Figure 5-5. (a) Definition of Chord Rotation (b) *AISC 341* Cyclic Load Test up to 0.05 rad. (c) Moment Rotation Backbone Curve for W24x103 (RBS) (d) *AISC 341* Cyclic Load Test on W24x103 (RBS) Modeled with Ibarra-Krawinkler Concentrated Plasticity Model

Figure 5-6 shows the effect of deterioration parameters on the hysteretic response of the base model shown in Figure 5-5 (d). As mentioned before, θ_p, θ_{pc}, and Λ were found from the regression formulas. Residual strength ratio, κ, in Figure 5-6 (d) is the ratio of M_r and M_y. Residual strength ratio of 0.4 and ultimate rotation, θ_u, of 0.2 radians were used for the moment frame models. The effective yield strength, M_y, is 10% greater than the plastic moment capacity, M_p, which is plastic section modulus, Z_x, multiplied by the expected material yield strength, F_{ye}. The reason for the 10% increase is to take care of cyclic hardening which is not directly captured in the modified Ibarra-Krawinkler model. The ratio of capping moment strength and effective yield moment, M_c/M_y, was used as 1.10 in the numerical model. Note that these values are suggested by Lignos and Krawinkler (2011) and also used in *ATC-76-1* project (NIST, 2010).

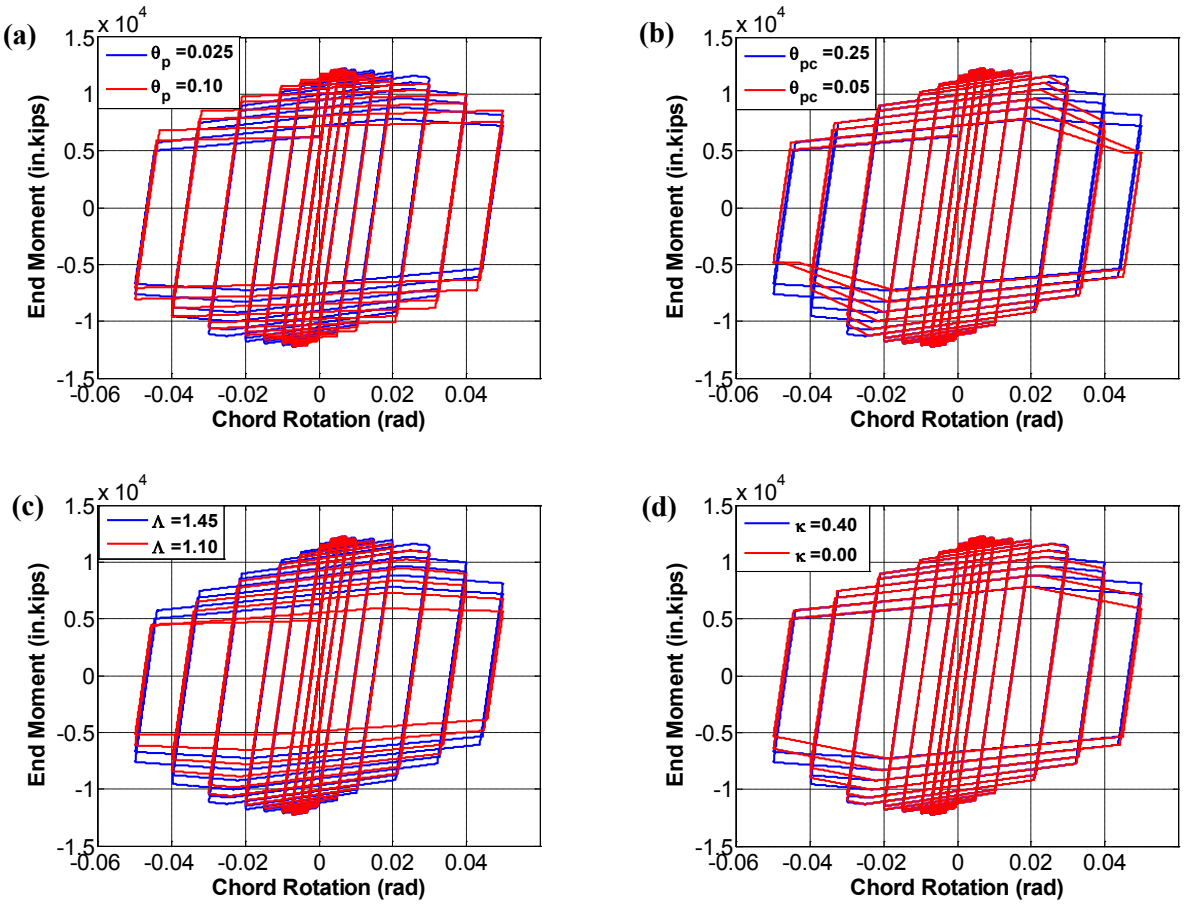

Figure 5-6. Effect of Cyclic Deterioration Parameters on Hysteretic Response (a) Plastic Rotation Capacity (θ_p), (b) Post-capping Rotational Capacity (θ_{pc}), (c) Strength-Stiffness Deterioration (Λ) (d) Residual Strength Ratio (κ)

5.3.2. Plastic Hinge Model for Columns

Due to the lack of experimental data on wide flange column sections, the regression formulas for "other than RBS beams" were used to determine the deterioration parameters of column hinges. This is consistent with *ATC-76-1* (NIST, 2010) project moment frame study which was investigated by Dimitrios Lignos. Note that the hysteretic behavior of large wide flange sections is currently being investigated by a new ATC project, *NIST GCR 11-917-13: Research Plan for the Study of Seismic Behavior and Design of Deep, Slender Wide Flange Structural Steel Beam-Column Members* (NIST, 2011). The findings of that research will propose strength and stiffness degradation parameters for wide flange columns as a function of axial force (NIST, 2011).

The concentrated hinge elements in OpenSees do not capture axial force-moment (P-M) interaction. The

moment-rotation response of column hinges was defined based on average column axial loads that are estimated from pushover analysis. Half of the maximum axial load that occurred in the columns (due to lateral loads) was added to the column gravity loads. This final force was used with *AISC 360* P-M interaction equations and the reduced bending strength was calculated. This same method is also used in *ATC-76-1* project (NIST, 2010). The column bending strengths were reduced about 10% as a result of this method, and this reduced strength was used in the response history analyses. The reduction was the most for the exterior columns and also the deeper columns. Figure 5-7 shows how the pushover curves of 10 story model changed with the effect of axial load calculated with the method described herein. As may be seen in the figure, the effect of axial load on the system behavior is much more significant on the model in which W24 columns were used.

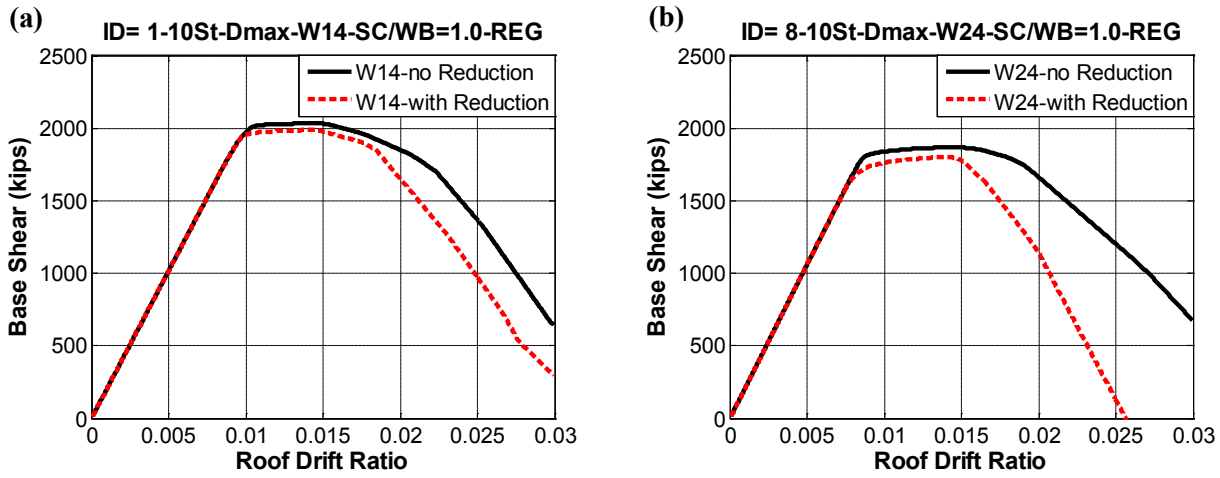

Figure 5-7. Pushover Curves for 10 Story Models (SC/WB=1.0) with and without Bending Strength Reduction in Column Hinges (a) Model with W14 columns (b)Model with W24 Columns

5.3.3. Beam-Column Joint Region Modeling

The beam-column joint regions (panel zones) are modeled using a trilinear shear force shear distortion relationship developed by Krawinkler (1978). This model considers the shear resistance of the web of the column and the flexural resistance of the flanges of the column. Strain hardening stiffness was assumed as 3% of the initial stiffness of the joint. Details of this model including strength and stiffness properties are explained in PEER/ATC (2010) and Charney et al. (2010). Deterioration in the panel zone properties was not considered.

Figure 5-8 shows the Krawinkler type panel zone and the panel zone shear force-deformation example tested with *AISC 341* cyclic test loading protocol up to 4% story drift ratio. In this example a W24x84 girder was connected to W14x159 column and a doubler plate thickness of 1-5/16 in. was used.

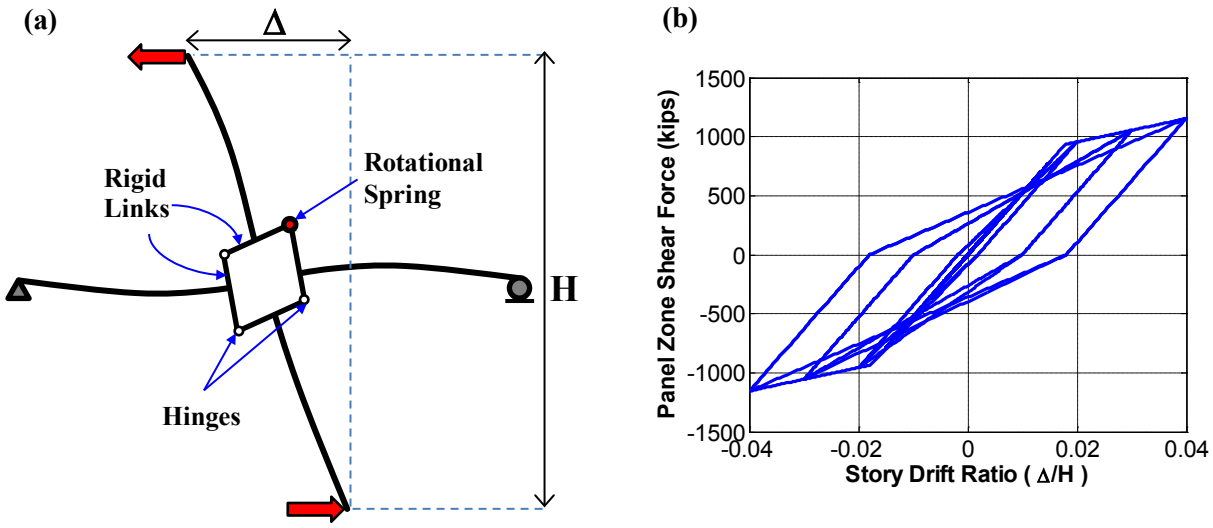

Figure 5-8. (a) Interior Beam-Column Subassemblage (b) Panel Zone Shear Force – Story Drift Ratio

5.4. Hybrid Moment Frame Design

Regular SMF designs with SC/WB of 1.0 and 1.5 were modified by changing the plastic hinging sequence of the girders. The strength decrease was made on the 1st, 3rd and the 5th bays, while strength increase was made on the 2nd and 4th bays. The plastic capacities of the 1st, 3rd and the 5th bays were decreased by about 30% and 40% for the Hybrid-1 and Hybrid-2 designs respectively. The plastic capacities of the 2nd and 4th bays were increased about 45% and 60% for the for the Hybrid-1 and Hybrid-2 frames respectively. Thus, the total story plastic capacities of the stories were kept the same. While the exterior (1st and 5th) and middle (3rd) bay girders yielded early, the interior (2nd and 4th) girders yielded late for the Hybrid frames. In addition to the flexural strengths, the stiffness of the Hybrid frames was also kept the same as regular frames. These two constraints resulted in an increase in the weight of the Hybrid moment frame girders. The same column sections were used for the regular and the Hybrid moment frames.

The following approaches were used to change the yield sequence of the moment frames:

- To provide early yielding, the RBS properties were modified. As explained earlier, the medium

values of the *AISC 358* limits with 35% flange cut were used for the RBS of the regular designs. For the hybrid frames, the flange cut of the 1st, 3rd and 5th bay girders were increased to provide early yielding and the cut of the 2nd and 4th bays were decreased to delay the yielding. The maximum flange cut of 50%, which is the limit specified in *AISC 341-10*, was used as necessary for the reduced capacity hybrid frame girders. While decreasing the flange cut to increase the capacity, it was made sure that the hinging would still occur at the RBS region, but not at the column face. The location of the RBS was also attempted to change. However, the effect of change in "a" and "b" values shown in Figure 5-3 was minimum in changing the yield sequence. Thus, the same "a" and "b" values of the regular systems were also used for the Hybrid frames.

- Girder sizes were increased at the 2nd and 4th hybrid frame bays, and decreased at the 1st, 3rd and 5th bays. The change in depth of the girders at the same level was at most one level (3in.), i.e. (from W33 to W30 or from W30 to W27).

- The beams are connected to the girders perpendicularly in the regular frame design. In hybrid frames, the load path of the interior bays (2nd and 4th bays) was changed by connecting the beams parallel to the girders to delay the yielding at these bays (See Figure 5-9). Note that changing the direction of the beams at the interior bays not only reduces the moment at the ends of the girders, but also helps to decrease the cut of the RBS by reducing the shear. The cut of the RBS could be decreased further with the smaller shear force, because the probable moment at the column face was minimized when beams were connected parallel to the girders. Thus, change in beam directions helped to delay the hinging sequence in two ways.

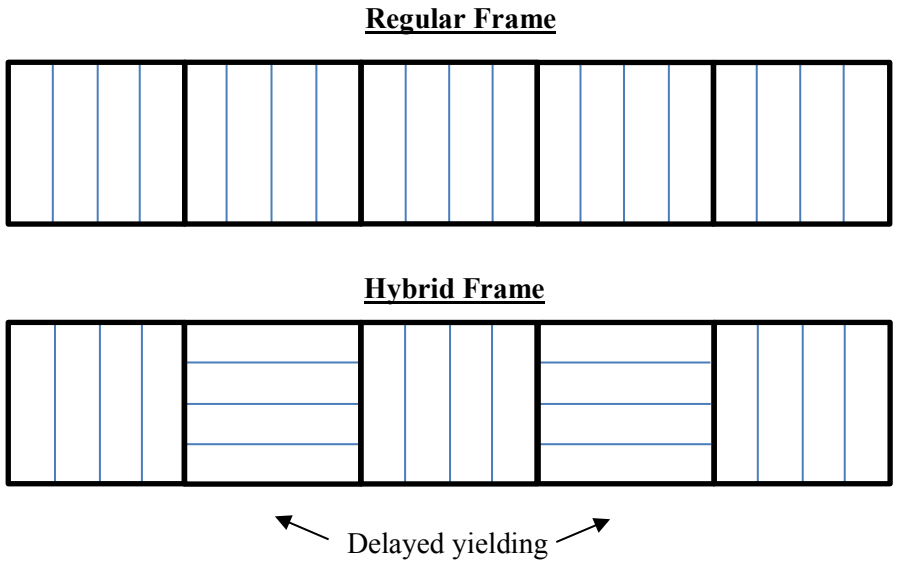

Figure 5-9. Change in Beam Directions for Hybrid Moment Frames

Table 5-3 shows an example for the change in girder sections and doubler plate thicknesses for hybrid moment frames. The sections in the table are for the ten story models with IDs: 1-10St-Dmax-W14-SC/WB=1.0-REG and 2-10St-Dmax-W14-SC/WB=1.0-HYB1. As may be seen in the table, the interior bay capacities were increased by increasing the girder size and minimizing the RBS cut (if possible). The exterior and middle bay capacities were decreased by increasing the RBS cut and using smaller girder sizes. The effect of this change in the doubler plates is also shown in the table. The doubler plate thicknesses of the exterior joints decrease as a result of the capacity decrease in the exterior bay, and the thicknesses of the interior and middle joint doubler plates increase as a result of the capacity increase in the interior bays.

The sections shown in Table 5-3 are for the first hybrid combination (Hybrid-1), where the capacities are decreased by 30% at the exterior and middle bays while the capacities increased by 45% at the interior bays. The weight of the frame and the doubler plate thicknesses increased by 11% for this 10 story building hybrid frame scenario. The total plastic capacities and inertias of the stories are the same.

Table 5-3. Comparison of 10 Story Regular and Hybrid Moment Frames (IDs 1 vs 2)

Level / story	Girders with RBS flange cut				Doubler Plate Thickness (in.)					
	Bays 1-3-5		Bays 2-4		Exterior Col.		Interior Col.		Middle Col.	
	Regular	Hybrid	Regular	Hybrid	Regular	Hybrid	Regular	Hybrid	Regular	Hybrid
Roof	W21x44 (38%)	W18x40 (50%)	W21x44 (38%)	W18x71 (36%)	-	-	3/16	6/16	3/16	7/16
10	W24x94 (35%)	W24x76 (48%)	W24x94 (35%)	W21x147 (32%)	9/16	3/16	1-9/16	2-1/16	1-9/16	1-13/16
9	W30x116 (35%)	W27x102 (48%)	W30x116 (35%)	W27x178 (34%)	11/16	6/16	1-2/16	1-9/16	1-2/16	1-10/16
8	W33x118 (38%)	W30x108 (47%)	W33x118 (38%)	W33x152 (34%)	12/16	7/16	1-2/16	1-4/16	1-2/16	1-9/16
7	W33x130 (37%)	W30x116 (50%)	W33x130 (37%)	W30x191 (32%)	5/16	-	11/16	1-2/16	11/16	1-3/16
6	W33x141 (36%)	W30x132 (50%)	W33x141 (36%)	W30x211 (36%)	8/16	2/16	15/16	1-7/16	15/16	1-8/16
5	W33x152 (35%)	W33x118 (45%)	W33x152 (35%)	W30x235 (35%)	10/16	1/16	1-4/16	1-13/16	1-4/16	1-9/16
4	W33x152 (35%)	W33x118 (45%)	W33x152 (35%)	W30x235 (35%)	10/16	1/16	1-4/16	1-13/16	1-4/16	1-9/16
3	W33x169 (35%)	W33x130 (45%)	W33x169 (35%)	W30x261 (35%)	7/16	-	1-6/16	1-15/16	1-6/16	1-11/16
2	W33x141 (36%)	W30x132 (50%)	W33x141 (36%)	W30x211 (36%)	2/16	-	11/16	1-2/16	11/16	1-3/16

Figure 5-10 shows the change in plastic section modulus, Z_x, inertia, I_x, girder weight, and doubler plate vertical edge areas for the same hybrid frame being discussed. Note that the comparison is made at each level and bay in Figure 5-10. For the doubler plate comparison, the exterior joints and the middle joints

were values were displayed. Interior joints are not shown as the interior and middle joints usually had similar thick doubler plates.

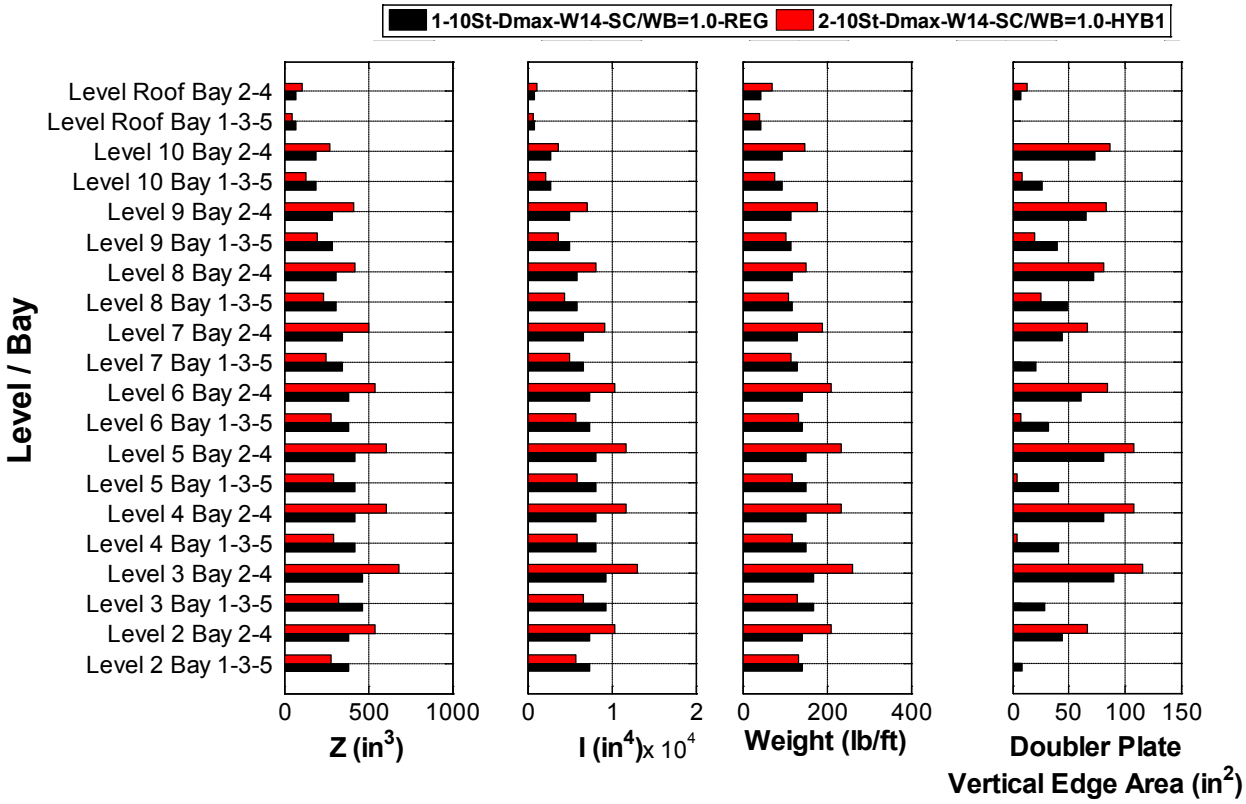

Figure 5-10. Change of Section Properties, Weight and Doubler Plates for 10 Story Hybrid Frame Example

The changes in deterioration parameters for the same ten story hybrid scenario are shown in Figure 5-11. While the girder sections for the hybrid frames were selected, these parameters were checked and the sections with the better deterioration parameters were attempted to be selected for the hybrid frames. In general, the deterioration parameters get worse for the reduced capacity girders and get better for the increased capacity girders. When the sections of the regular frames are modified for hybrid frames, the change in deterioration parameters are affected positively if a smaller depth girder is picked for the hybrid system. This is due to the better (smaller) h/t_w values of the shallow depth sections.

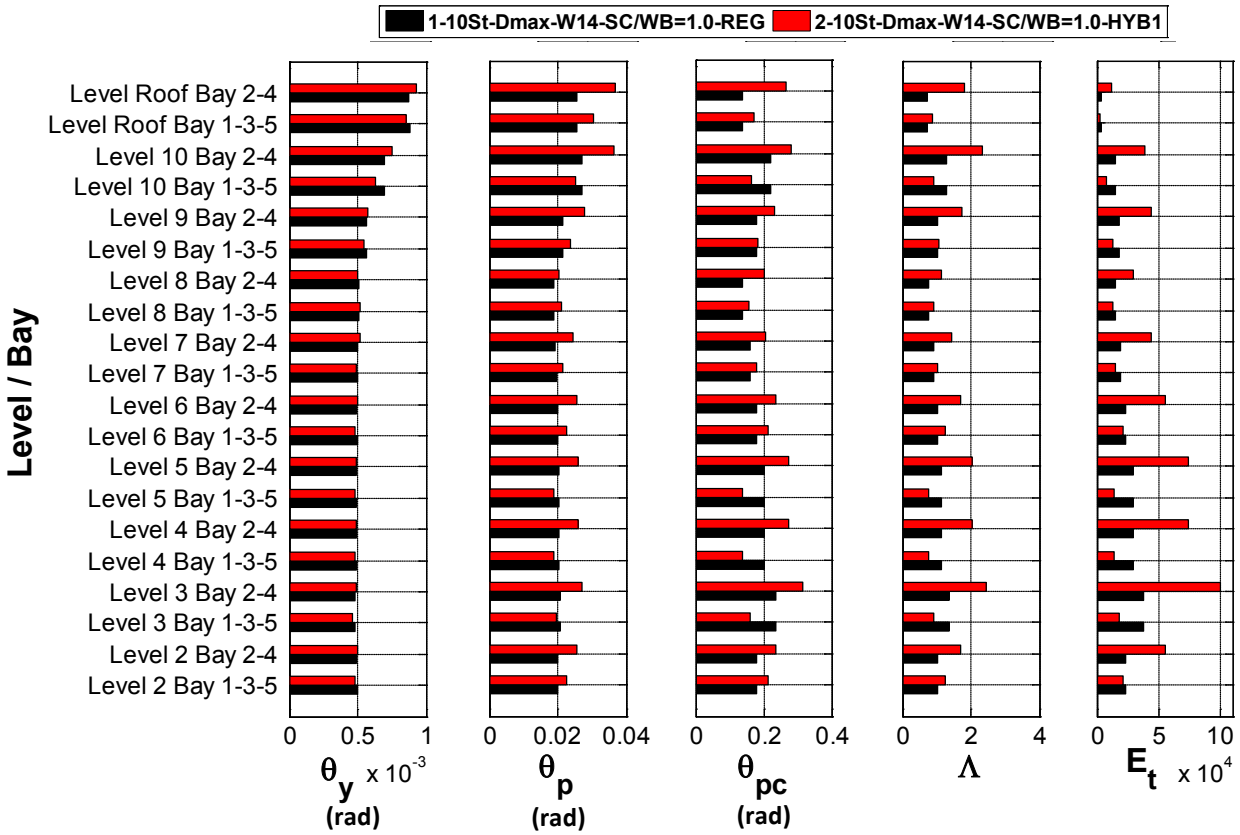

Figure 5-11. Change of Deterioration Parameters for 10 Story Hybrid Frame Example

5.5. Nonlinear Analysis

In the nonlinear analytical models, P-Delta effects were included with the help of a leaning column. Consistent with *FEMA P-695* methodology, a gravity load combination of 1.05D+0.25L was used for the nonlinear analysis. Load assignment of the displacement controlled static pushover analysis was determined from the 1st mode shape of the frames. Nonlinear dynamic analyses were performed by using the Far-Field ground motion set with the scaling method explained in Chapter 3. Rayleigh damping of 2.5% was used at the 1st and 3rd fundamental periods. Full *FEMA P-695* type analyses were not performed on the moment frames. Ground motions scaled at 0.1, 0.2, 0.67, 1.00 and 1.50 times the MCE level were used. Since there are 42 models in the design space, 42x44x5=9,240 nonlinear dynamic analyses were performed for the discussion in this chapter.

5.6. Collapse Definition for Moment Frames

In *FEMA P-695* special moment frame (SMF) supporting study, a non-simulated collapse (NSC) value of 0.063 radians was used for SMF. This value which is about an interstory drift ratio (IDR) of 6.3% was

related to the ductile fracture of the RBS. In *ATC-76-1* project, the only collapse mode that was considered was the sidesway collapse which might occur in a single story or in a series of stories. Sidesway collapse occurs as structure loses its lateral load carrying capacity due to P-Delta effects and cyclic deterioration in strength and stiffness of the steel components.

In this study, full *FEMA P-695* type analyses were not performed on moment frames. However, collapse fragilities were developed by using the results of the runs up to 1.5xMCE level. In terms of non-simulated collapse criteria, 10% IDR was used. This was because the plots that are obtained from incremental dynamic analyses (IDA) usually flatten about 10% IDR. Note that since the dynamic analyses conducted on the moment frames were limited, full IDA curves could not be developed to verify the flattening at 10% IDR, but, nevertheless 10% IDR was used as NSC measure.

An example for sidesway collapse is illustrated in Figure 5-12 where a 10 story moment frame (ID=8-10St-Dmax-W24-SC/WB=1.0-REG) was subjected to MCE level Kocaeli earthquake (Arcelik station). Figure 5-12 (a) and Figure 5-12 (b) show the roof displacement and interstory drift ratio (IDR) response histories. Note that the response histories are almost flat up to 12 seconds into the response. This is because the real shaking for this ground motion starts after 12 seconds, thus actually the early time of this earthquake can be considered inside the 'bracketed duration'. Indeed, the velocity history of this earthquake is almost entirely flat up to 12 seconds. As may be seen in Figure 5-12(b), the IDR of the bottom two stories reach about 20%. When the reason of collapse was investigated, it was observed that the entire column hinges at the bottom of 1st story (base) yielded as well as the column hinges at the top of the 2nd story. Thus, the reason of the collapse was the story mechanism that formed at the bottom two stories. Figure 5-12 (c) and Figure 5-12 (d) show the column moment-rotation histories for two of the hinges that played role in the collapse mechanism. All the column hinges at these levels had similar hysteresis, i.e. they all yielded and reached the ultimate rotation capacity of 0.2 radians. In addition, all the girder hinges at the 2nd level (top of 1st story) also reached the ultimate rotation capacity of 0.2 radians.

Note that although very high drift values could be achieved for this specific model and ground motion, it was very difficult to get the analyses converged at high ground motion intensities. About 10% to 15% of the analyses at MCE and 1.5xMCE levels did not converge initially and the amount of time spent to solve the convergence problems was comparable to the total run time of the main analyses.

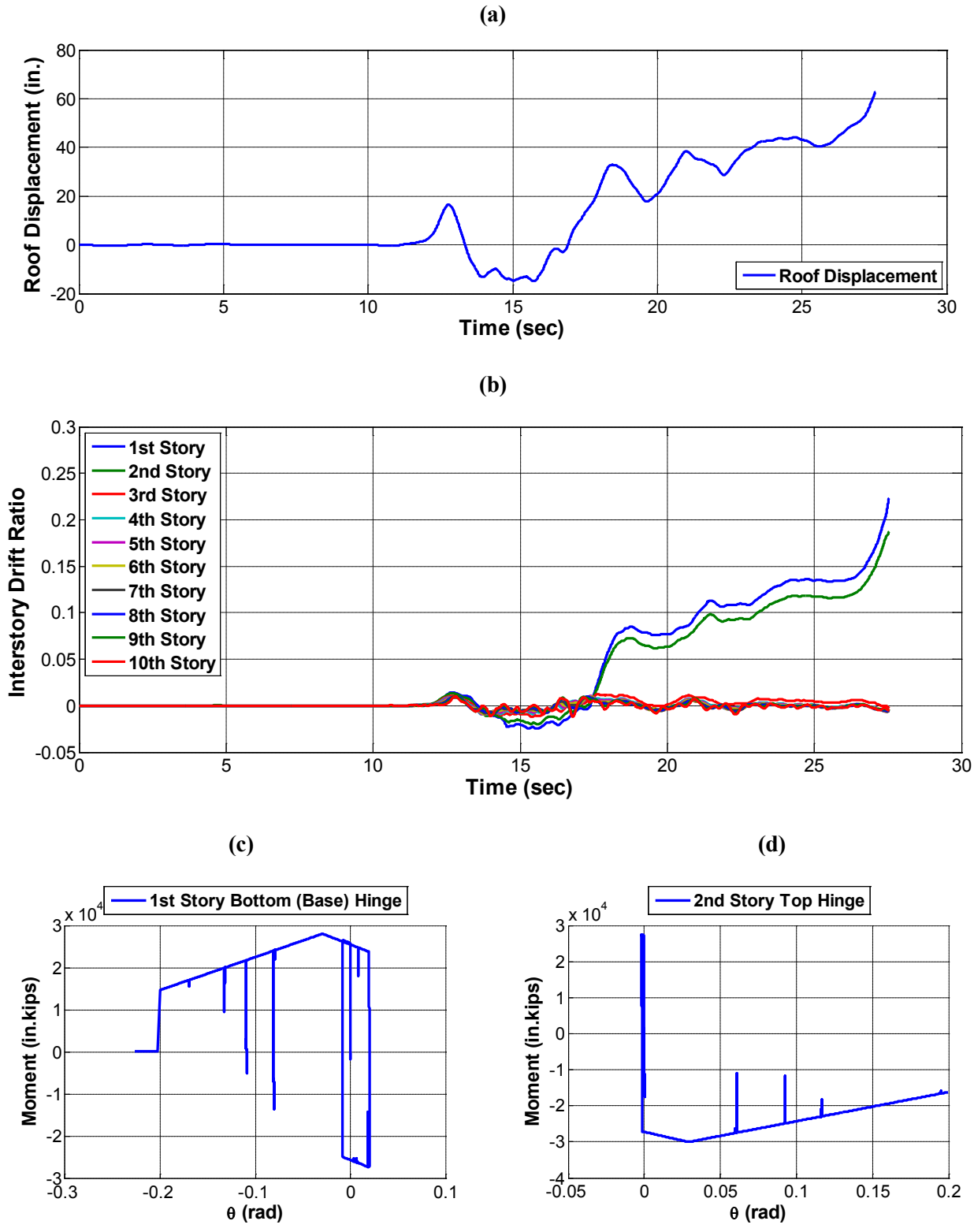

Figure 5-12. Collapse Example for a 10 Story Moment Frame (a) Roof Displacement Response History, (b) Interstory Drift Ratio Histories, (c) Moment-Rotation for the 1st story Exterior Column (Bottom Hinge), (d) Moment-Rotation for the 2nd Story Exterior Column (Top Hinge)

5.7. Hybrid Moment Frame Results

The discussion in this section is made for the hybrid frame model that has been discussed in this chapter (10 story frame with W14 columns and SC/WB of 1.0). When hybrid and regular frame performance is investigated, the comparison is made on four frames. In addition to the regular frame, two hybrid frames with the same column types (W14 or W24) and the same SC/WB ratios as the regular frame are used in the comparison. In order to evaluate the efficiency of the hybrid idea on moment frames, another regular frame with the same column type, however with a higher SC/WB was also added to the comparison. As explained earlier in this chapter, only the girder sections were changed for hybrid frames while the columns were kept the same, and as a result the cost of the frame in terms of the structural weight and doubler plates increased about 5-10%. The idea of adding the 4th frame into the comparison was to check if this increase in cost could be spent in a better place inside the moment frame, which is the column in this example. Table 5-4 tabulates the frames used for comparison in this section.

Table 5-4. 10 Moment Frames used for Hybrid Frame Comparison in this Section

Archetype ID	Weight (lbs)			Doubler Plate Vert. Edge (in^2)	T_1 (sec)
	Column	Girder	Total		
1-10St-Dmax-W14-SC/WB=1.0-REG	222176	188550	410726	3050 (58)	2.46
2-10St-Dmax-W14-SC/WB=1.0-HYB1	222716	210000	432716	3391 (52)	2.48
3-10St-Dmax-W14-SC/WB=1.0-HYB2	222716	208230	430946	3555 (50)	2.50
4-10St-Dmax-W14-SC/WB=1.5-REG	267396	171750	439146	631 (34)	2.50

5.7.1. Static Pushover Analysis

Figure 5-13 shows the pushover curves for the 10 story regular and hybrid frames shown in Table 5-4. The yielding sequence of the girder and column hinges for these analyses are tabulated in Table 5-5. In Table 5-5, the tabulated values are the roof drift ratios up to 3%. The values in the table should be divided by 1,000 to find the roof drift ratio of the hinge yielding. For example, the tabulated value of 2,000 means 2% roof drift ratio. In the table, yellow highlighted cells show yielding. The girder hinges are shown for the bottom 7 levels, and the column hinges are shown for the bottom 5 stories. There was no yielding observed at the higher levels.

As displayed in Figure 5-4, there are two hinges at the ends of beam-column elements. In the pushover analyses, the frame was pushed to the right side. Since the gravity and lateral load moments accumulate at the right end of the girders in the same sign, the hinges at the right end of the girders form first. Although the early yielding of the hybrid frames is not observed in the pushover curves, it is seen in Table 5-5 that the hinges at the right ends of the 1st, 3rd, and 5th bays form earlier than the regular frames, and the hinges

at the 2nd and 4th bays of the hybrid frames yield slightly later than the regular frame hinges. The roof drift ratio difference of early yielding is about 0.1% to 0.2%. Model IDs 1, 2, and 3 should be compared in Table 5-5 to see the difference.

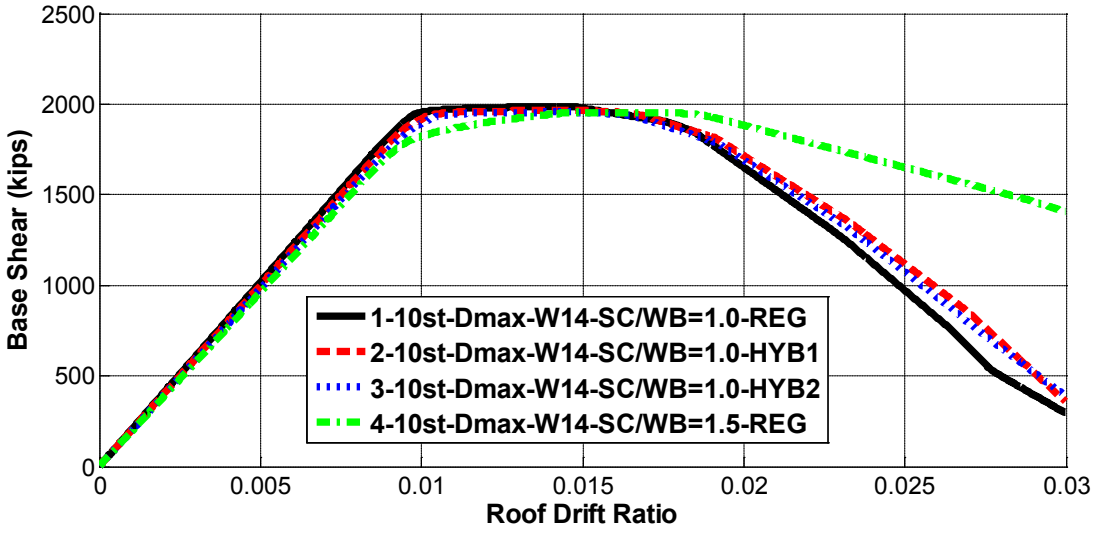

Figure 5-13. Pushover Curves for 10 Story Regular and Hybrid Frames

As may be seen in Figure 5-13, the real change in the pushover curves was obtained with the 4th model, which is a regular frame design with higher SC/WB ratio (1.5 instead of 1.0). The main difference observed in the 4th model pushover curve is the high post-yield stiffness. The reason of this benefit is clearly observed in Table 5-5. A multi-level story mechanism (at the bottom two stories) forms about 1.8% roof drift ratio for the 1st, 2nd and 3rd models. This story mechanism results in strength loss in the pushover curve. However, there is no story mechanism in the 4th model up to 3% roof drift ratio. Only the bottom level hinges form in columns of the 4th model and there are more girder hinges yielding. This is a desired yield mechanism for moment frames. Although the yielding sequence changed slightly with the hybrid frames, and the story mechanism formation is delayed about 0.1% roof drift ratio, the benefits are definitely not as good as the 4th model, which is a regular design with higher SC/WB ratio.

As a result of pushover analyses, it can be concluded that hybrid systems worked slightly better, however the real benefit occurred with the higher SC/WB ratio regular frame design. When the costs of these frames are compared in Table 5-4, the weight of the 4th model is slightly bigger than the hybrid systems (2 and 3), however there is a significant reduction in the doubler plates of the 4th model. This is due to the use of bigger column sizes. Thus, hybrid frame method does not work efficiently when compared with a higher SC/WB ratio design.

Table 5-5. Plastic Hinge Yield Sequence Comparison of 10 Story Model ID=1, 2, 3, and 4

Level	Bay	Left/ Right	Girder Plastic Hinges Pushover Roof Drift Ratio ID for 10 story Model				Story	Pier	Bottom/ Top	Column Plastic Hinges Pushover Roof Drift Ratio ID for 10 story Model			
			1	2	3	4				1	2	3	4
2	1	L	892	825	817	913	1	1	B	985	1014	1034	1483
2	1	R	852	786	778	854	1	2	B	975	955	947	1466
2	2	L	927	953	979	949	1	3	B	976	960	959	1470
2	2	R	861	932	952	867	1	4	B	976	956	956	1470
2	3	L	928	938	972	950	1	5	B	974	959	953	1465
2	3	R	861	803	805	867	1	6	B	986	1015	1035	1489
2	4	L	928	949	968	950	1	1	T	3000	3000	3000	3000
2	4	R	860	935	961	866	1	2	T	3000	3000	3000	3000
2	5	L	932	946	983	955	1	3	T	3000	3000	3000	3000
2	5	R	846	752	722	852	1	4	T	3000	3000	3000	3000
3	1	L	1003	936	907	951	1	5	T	3000	3000	3000	3000
3	1	R	966	876	845	914	1	6	T	3000	3000	3000	3000
3	2	L	1017	1048	1066	974	2	1	B	3000	3000	3000	3000
3	2	R	955	1049	1066	913	2	2	B	3000	3000	3000	3000
3	3	L	1018	1016	1009	977	2	3	B	3000	3000	3000	3000
3	3	R	955	890	857	913	2	4	B	3000	3000	3000	3000
3	4	L	1018	1063	1078	977	2	5	B	3000	3000	3000	3000
3	4	R	953	1036	1057	911	2	6	B	3000	3000	3000	3000
3	5	L	1030	1014	1017	984	2	1	T	1848	1916	1922	3000
3	5	R	962	858	816	908	2	2	T	1773	1680	1628	3000
4	1	L	1101	982	970	938	2	3	T	1774	1687	1643	3000
4	1	R	1000	885	882	868	2	4	T	1775	1679	1637	3000
4	2	L	1089	1137	1184	937	2	5	T	1773	1687	1638	3000
4	2	R	958	1136	1137	853	2	6	T	1844	1914	1919	3000
4	3	L	1087	1083	1053	937	3	1	B	3000	3000	3000	3000
4	3	R	958	885	842	853	3	2	B	3000	3000	3000	3000
4	4	L	1089	1165	1162	938	3	3	B	3000	3000	3000	3000
4	4	R	953	1114	1160	850	3	4	B	3000	3000	3000	3000
4	5	L	1122	1109	1175	953	3	5	B	3000	3000	3000	3000
4	5	R	1006	877	854	874	3	6	B	3000	3000	3000	3000
5	1	L	1417	1192	1105	1052	3	1	T	3000	3000	3000	3000
5	1	R	1264	940	926	976	3	2	T	3000	3000	1897	3000
5	2	L	1385	1502	1570	1047	3	3	T	3000	3000	3000	3000
5	2	R	1132	1498	1477	946	3	4	T	3000	3000	3000	3000
5	3	L	1382	1316	1207	1047	3	5	T	3000	3000	1903	3000
5	3	R	1135	918	861	946	3	6	T	3000	3000	3000	3000
5	4	L	1385	1554	1531	1048	4	1	B	3000	3000	3000	3000
5	4	R	1108	1459	1527	941	4	2	B	3000	3000	3000	3000
5	5	L	1461	1417	1524	1072	4	3	B	3000	3000	3000	3000
5	5	R	1257	929	899	978	4	4	B	3000	3000	3000	3000
6	1	L	3000	3000	3000	1216	4	5	B	3000	3000	3000	3000
6	1	R	3000	1010	950	1094	4	6	B	3000	3000	3000	3000
6	2	L	3000	3000	3000	1189	4	1	T	3000	3000	3000	2986
6	2	R	3000	3000	3000	1024	4	2	T	3000	3000	3000	3000
6	3	L	3000	3000	3000	1190	4	3	T	3000	3000	3000	3000
6	3	R	3000	904	872	1027	4	4	T	3000	3000	3000	3000
6	4	L	3000	3000	3000	1191	4	5	T	3000	3000	3000	3000
6	4	R	3000	3000	3000	1014	4	6	T	3000	3000	3000	2976
6	5	L	3000	3000	3000	1231	5	1	B	3000	3000	3000	3000
6	5	R	3000	997	923	1107	5	2	B	3000	3000	3000	3000
7	1	L	3000	3000	3000	1400	5	3	B	3000	3000	3000	3000
7	1	R	3000	1408	1056	1218	5	4	B	3000	3000	3000	3000
7	2	L	3000	3000	3000	1356	5	5	B	3000	3000	3000	3000
7	2	R	3000	3000	3000	1097	5	6	B	3000	3000	3000	3000
7	3	L	3000	3000	3000	1356	5	1	T	3000	3000	3000	3000
7	3	R	3000	916	905	1102	5	2	T	3000	3000	3000	3000
7	4	L	3000	3000	3000	1357	5	3	T	3000	3000	3000	3000
7	4	R	3000	3000	3000	1082	5	4	T	3000	3000	3000	3000
7	5	L	3000	3000	3000	1416	5	5	T	3000	3000	3000	3000
7	5	R	3000	1097	1013	1236	5	6	T	3000	3000	3000	3000

5.7.2. Nonlinear Response History Analysis

Figure 5-14 through Figure 5-16 display the maximum interstory residual drift comparison of the discussed hybrid moment frame group (see Table 5-4) under DBE, MCE and 1.5xMCE levels. The response of all frames under the Far-Field ground motion set is shown in the line charts. When the regular and hybrid frames with SC/WB ratio of 1.0 (model IDs 1, 2, and 3) are compared, it may be concluded that hybrid systems performed somewhat better than the regular system. The results are mostly very similar for most of the ground motions though. Similar to the pushover results, the best performance was achieved with the 4th frame which is a regular SMF with SC/WB ratio of 1.5 instead of 1.0.

Figure 5-17 through Figure 5-21 display similar comparison for maximum interstory drifts under 0.1xMCE, 0.2xMCE, DBE, MCE and 1.5xMCE levels. At low intensities (0.1xMCE and 0.2MCE), the performance is better for the model IDs 1, 2, and 3 than model ID 4. This is due to early yielding of the first three models. Especially, hybrid systems (model IDs 2 and 3) yield earlier than the 4th model. At high intensities, 4th frame performed the best as expected.

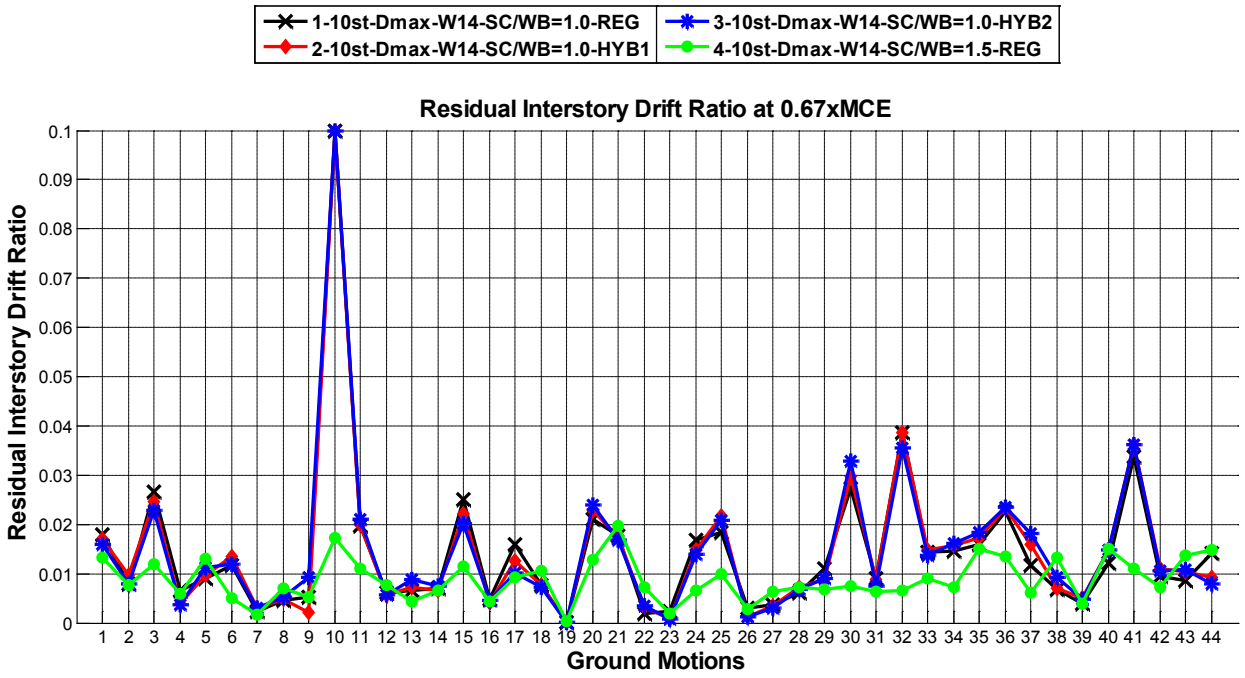

Figure 5-14. Hybrid Moment Frame Residual Displacement Performance Comparison at DBE Level

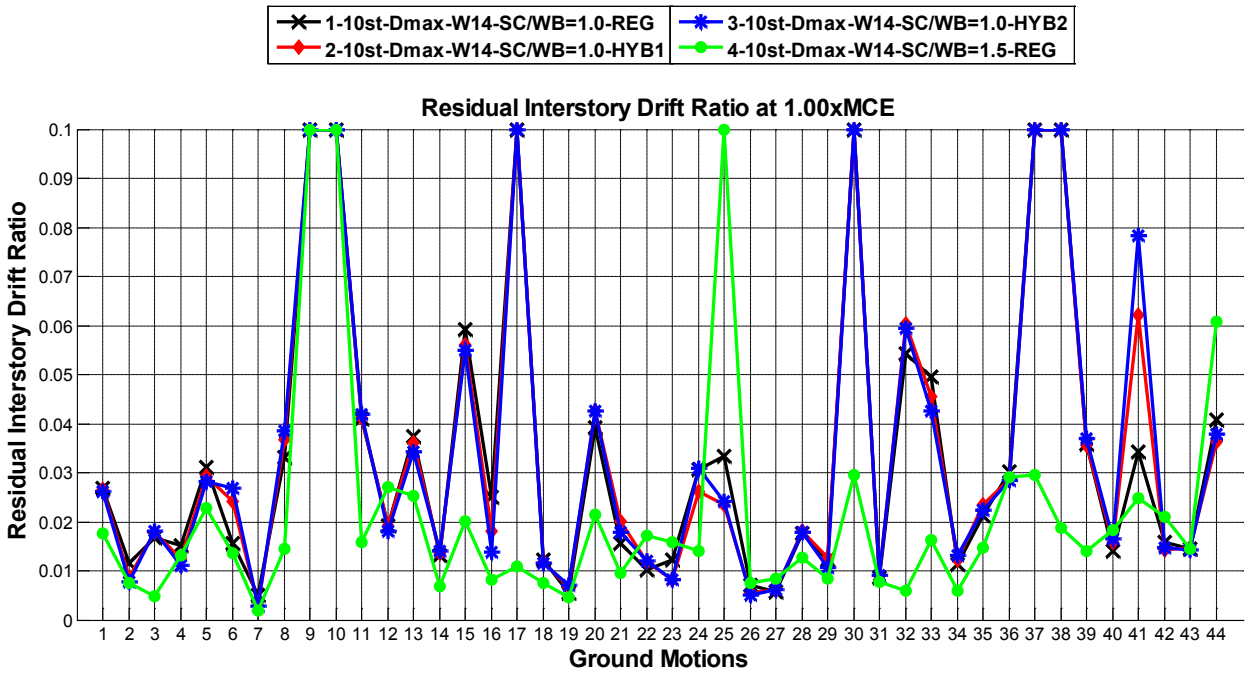

Figure 5-15. Hybrid Moment Frame Residual Displacement Performance Comparison at MCE Level

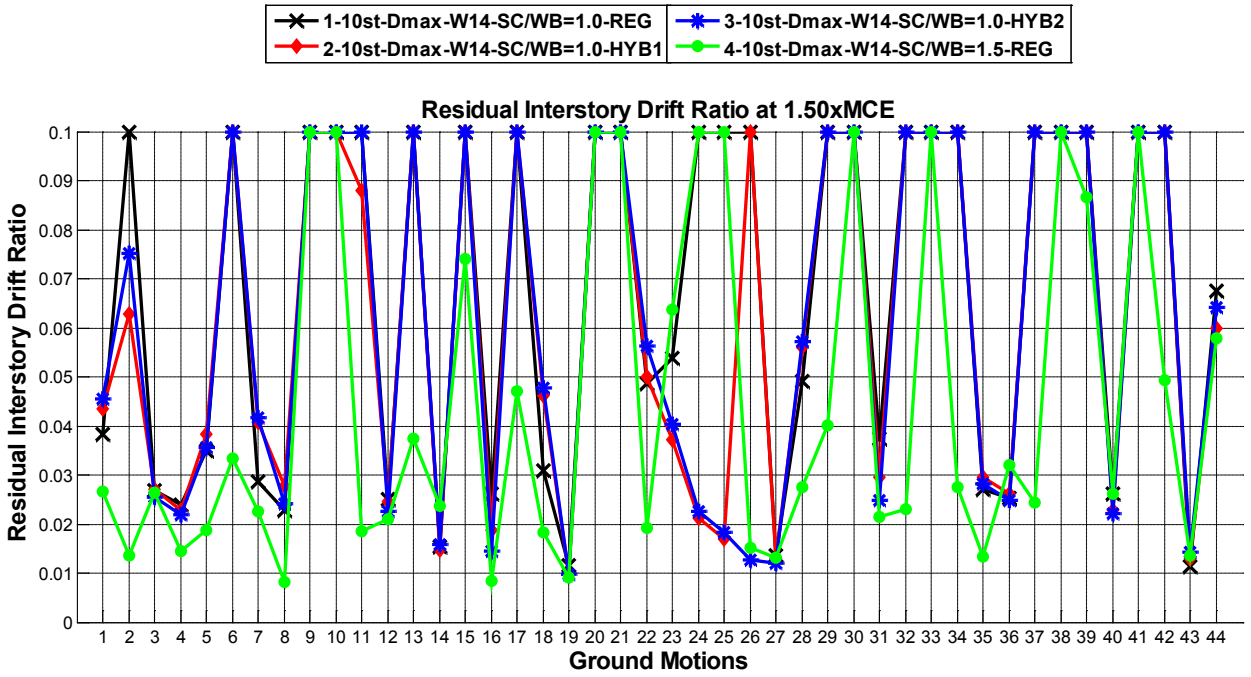

Figure 5-16. Hybrid Moment Frame Residual Displacement Performance Comparison at 1.5xMCE Level

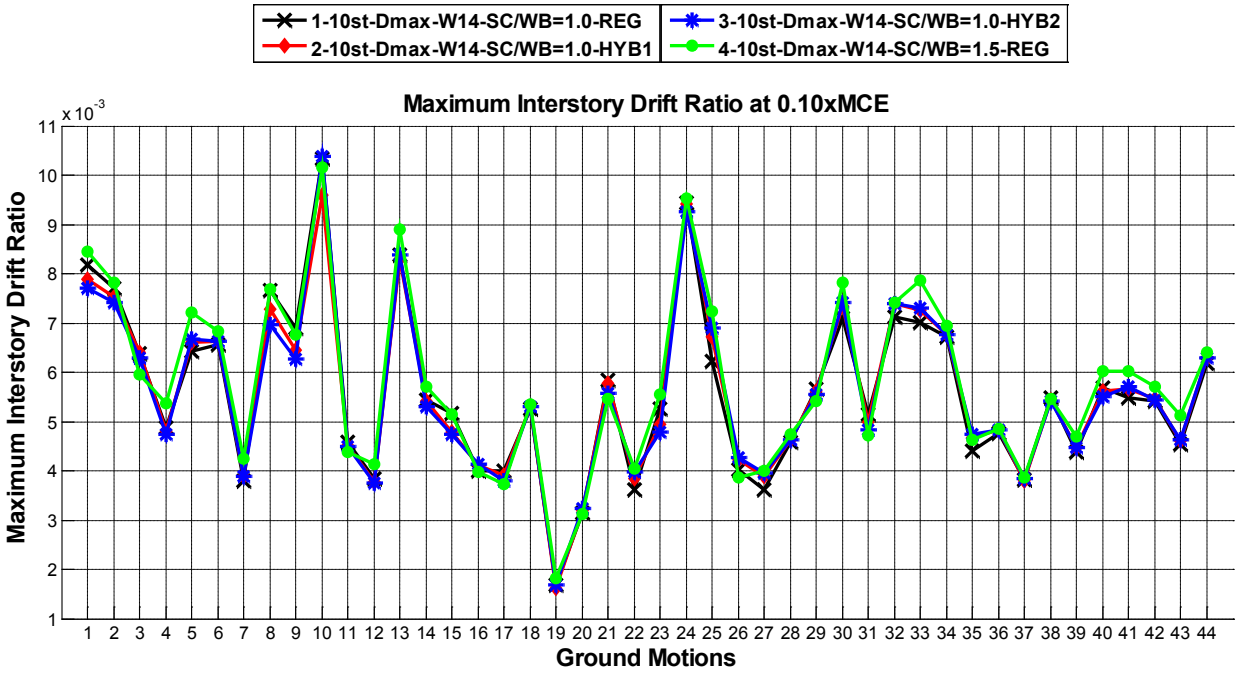

Figure 5-17. Hybrid Moment Frame Maximum Displacement Performance Comparison at 0.1xMCE Level

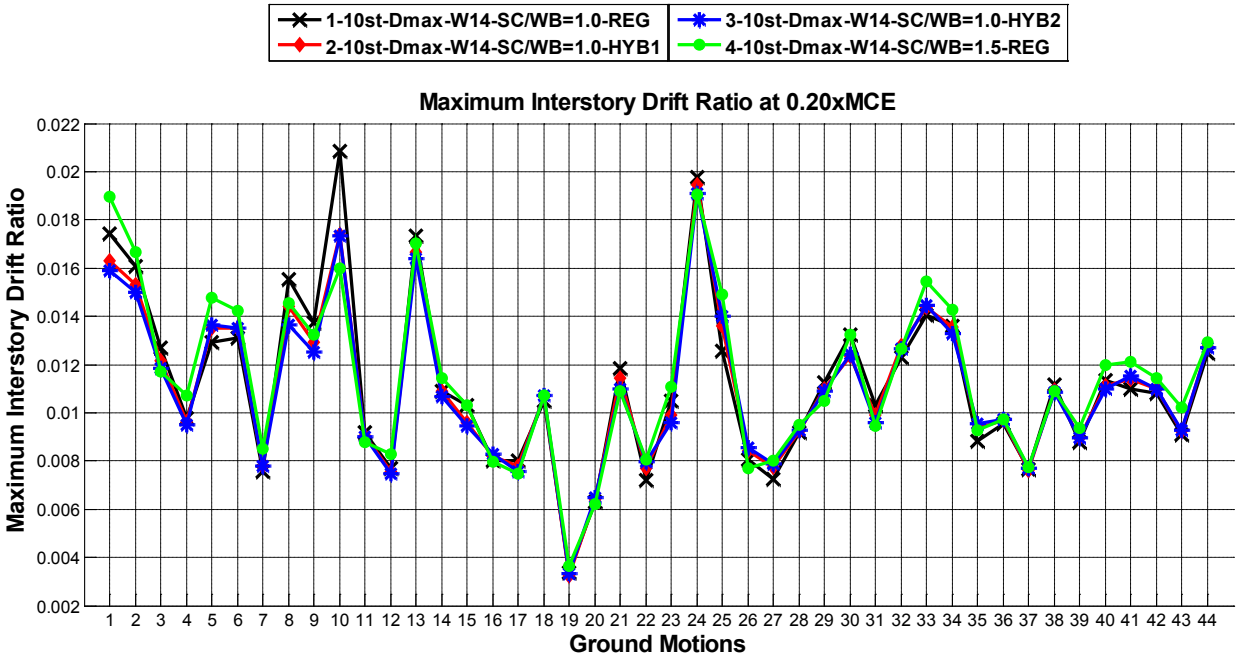

Figure 5-18. Hybrid Moment Frame Maximum Displacement Performance Comparison at 0.2xMCE Level

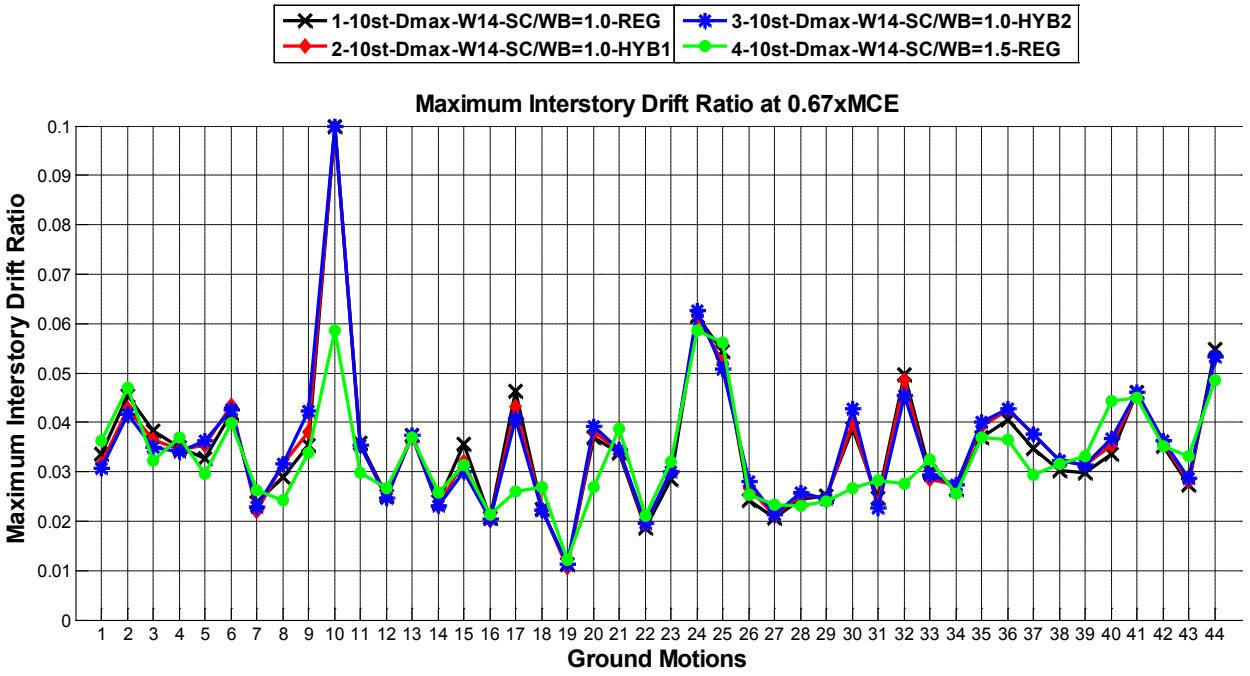

Figure 5-19. Hybrid Moment Frame Maximum Displacement Performance Comparison at DBE Level

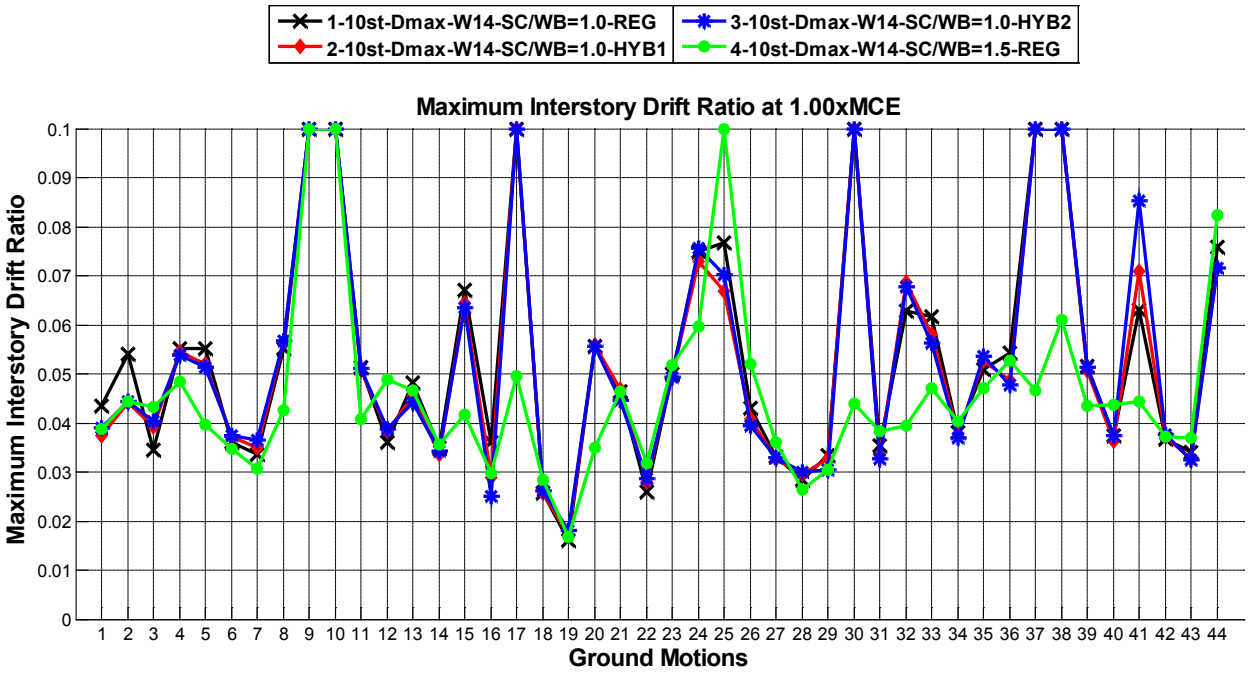

Figure 5-20. Hybrid Moment Frame Maximum Displacement Performance Comparison at MCE Level

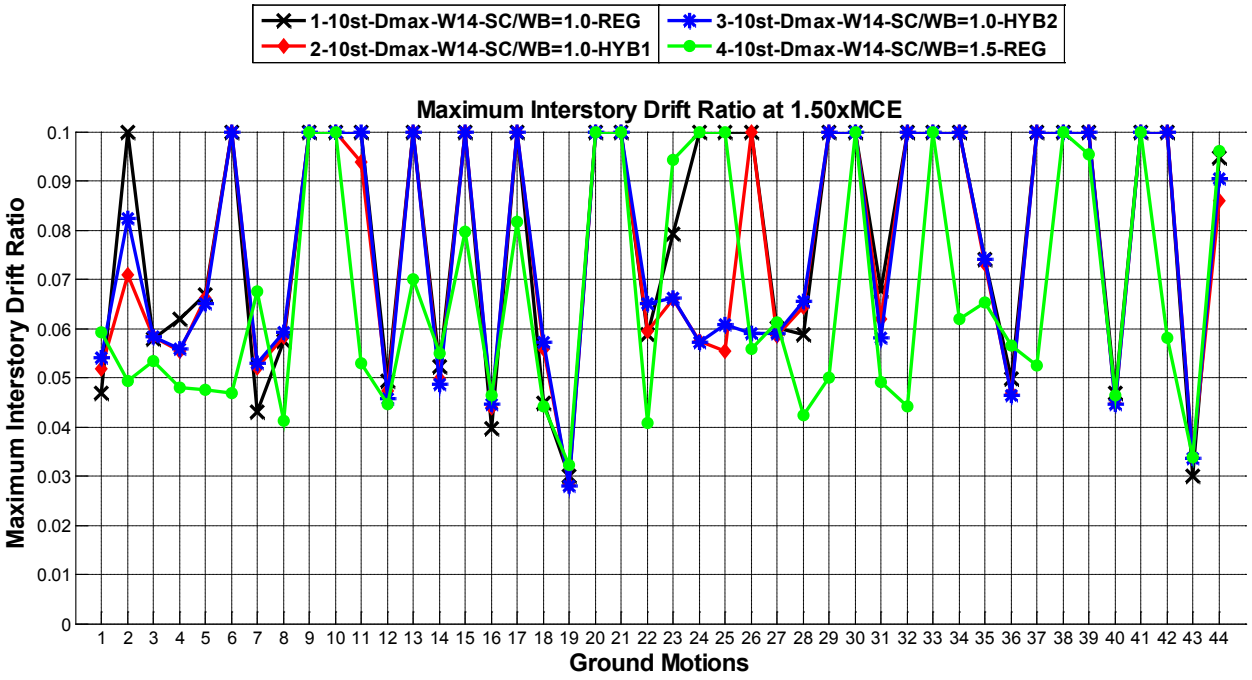

Figure 5-21. Hybrid Moment Frame Maximum Displacement Performance Comparison at 1.5xMCE Level

Table 5-6 shows the number of collapses obtained for this performance group. As may be seen, the numbers of collapses at the DBE and MCE levels are the same for the first three models. At 1.5xMCE level, the number of collapses dropped from 23 to 19 for the hybrid systems. The number of collapses decreased significantly at all three intensities with the 4th model. Figure 5-22 show the fragility curves for the models tabulated in Table 5-6.

Table 5-6. Number of Collapses for the 1st 10 Story Performance Group

Archetype ID	Number of Collapses		
	DBE	MCE	1.5xMCE
1-10St-Dmax-W14-SC/WB=1.0-REG	1	6	23
2-10St-Dmax-W14-SC/WB=1.0-HYB1	1	6	19
3-10St-Dmax-W14-SC/WB=1.0-HYB2	1	6	19
4-10St-Dmax-W14-SC/WB=1.5-REG	-	3	10

The performance comparisons in terms of maximum and residual drifts are shown in Figure 5-23. Comparisons are made for the median and 84th percentile of the 44 Far-Field ground motion results. While the performances of the first three models are similar, the performance improved with the 4th model.

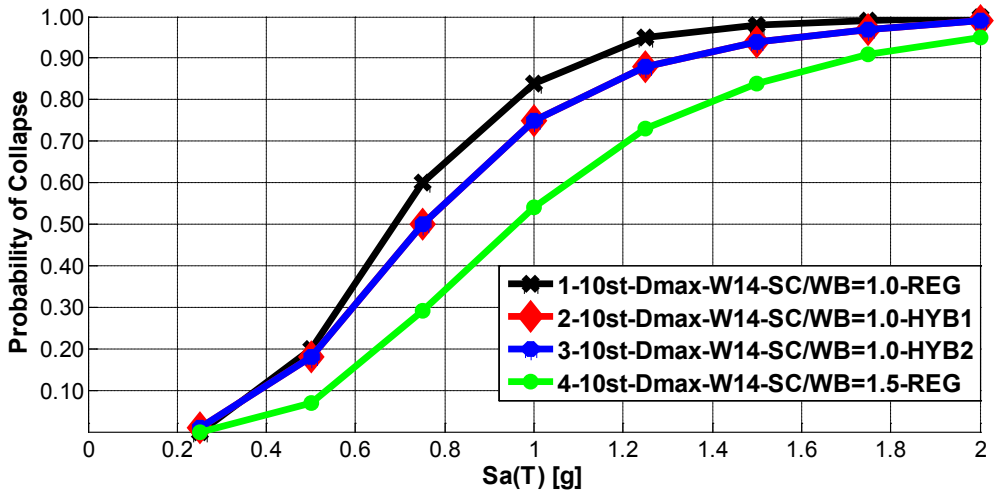

Figure 5-22. Fragility Curves for 10 Story Regular and Hybrid Frames

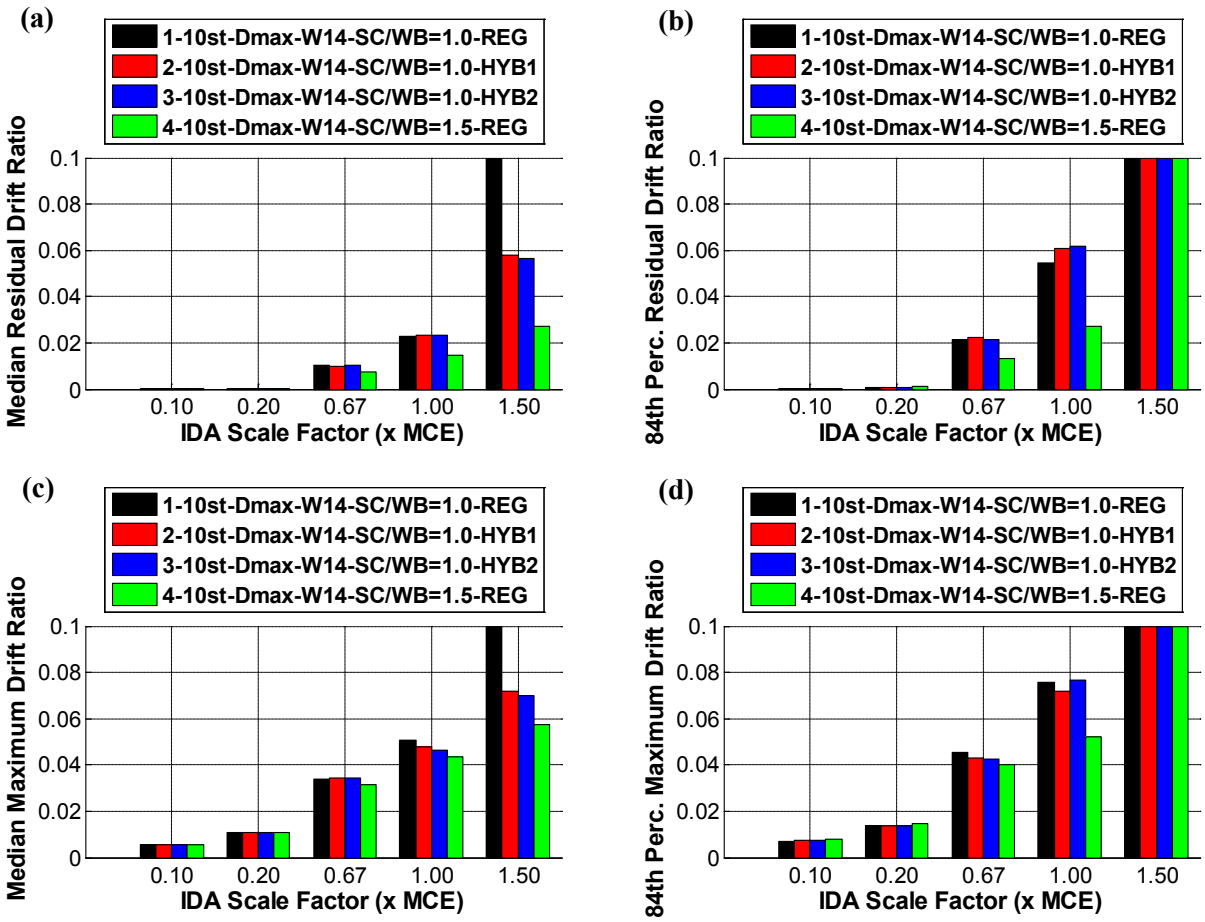

Figure 5-23. Comparison of Regular and Hybrid Frames for 10 Story SMF Designed at Dmax SDC with W14 columns and SC/WB Ratio of 1.0 (a) Median Residual Drift Ratios, (b) 84th Percentile Residual Drift Ratios, (c) Median Maximum Drift Ratios, (d)84th Percentile Maximum Drift Ratios

Figure 5-24 through Figure 5-35 summarize the results of all the archetypes tabulated in Table 5-1. Note that these figures only compare the effect of hybrid idea on the regular frames. The performance comparison of different column depth and SC/WB ratio designs are made in Appendix B.

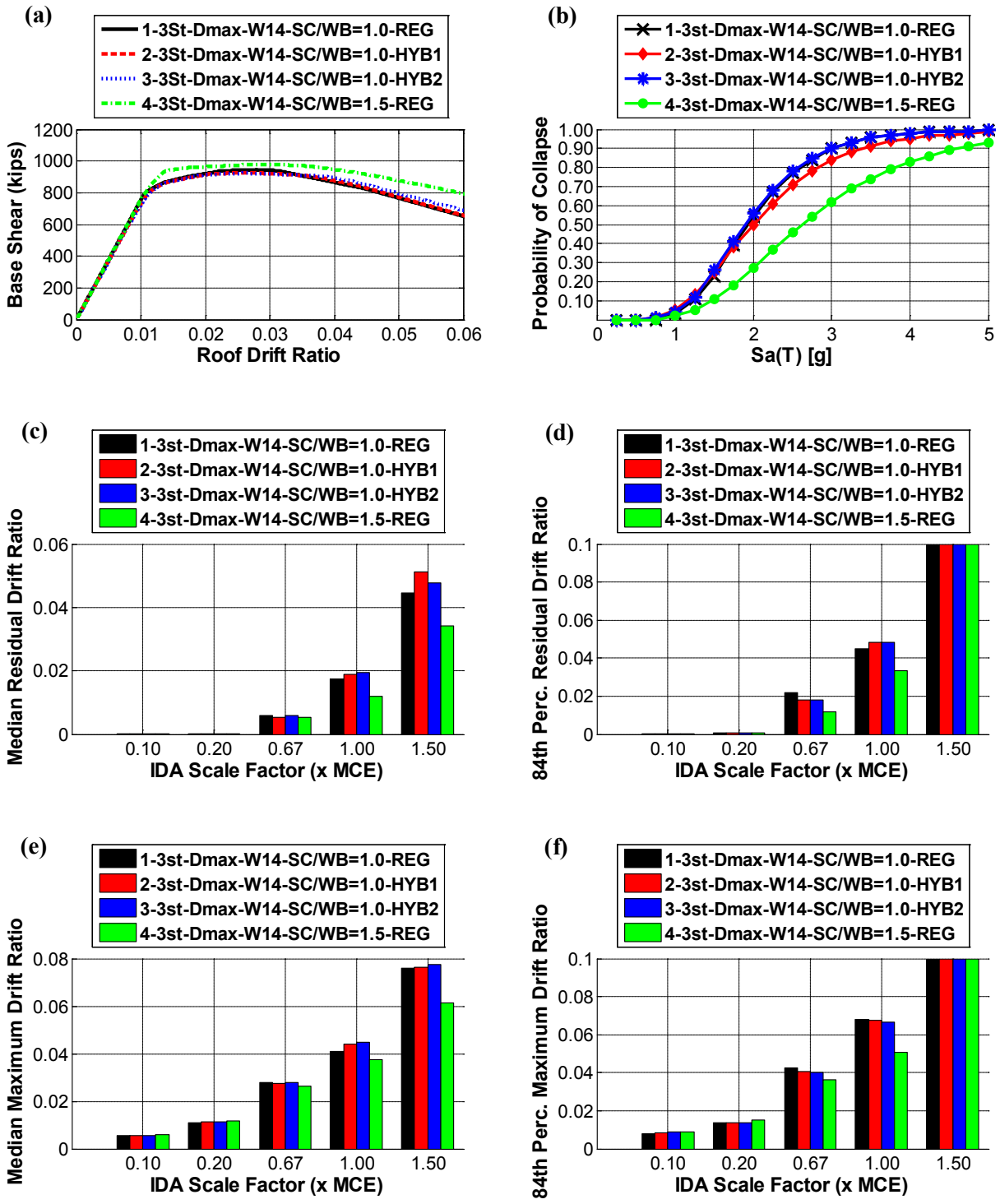

Figure 5-24. Comparison of Regular and Hybrid Frames for 3 Story SMF Designed at Dmax SDC with W14 Columns and SC/WB Ratio of 1.0 (a) Pushover Curves, (b) Fragility Curves, (c) Median Residual Drift Ratios, (d) 84th Percentile Residual Drift Ratios, (e) Median Maximum Drift Ratios, (f) 84th Percentile Maximum Drift Ratios

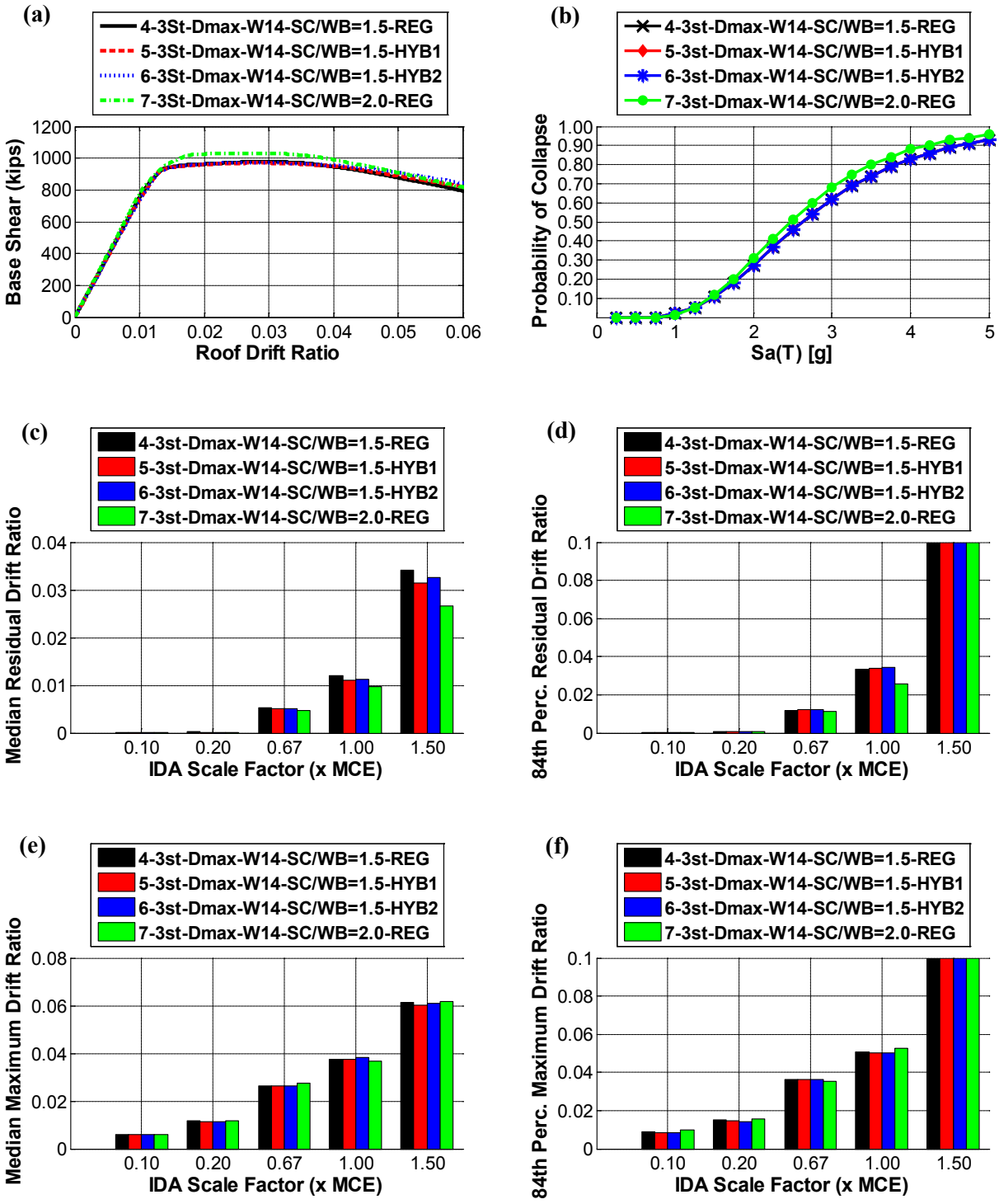

Figure 5-25. Comparison of Regular and Hybrid Frames for 3 Story SMF Designed at Dmax SDC with W14 Columns and SC/WB Ratio of 1.5 (a) Pushover Curves, (b) Fragility Curves, (c) Median Residual Drift Ratios, (d) 84th Percentile Residual Drift Ratios, (e) Median Maximum Drift Ratios, (f) 84th Percentile Maximum Drift Ratios

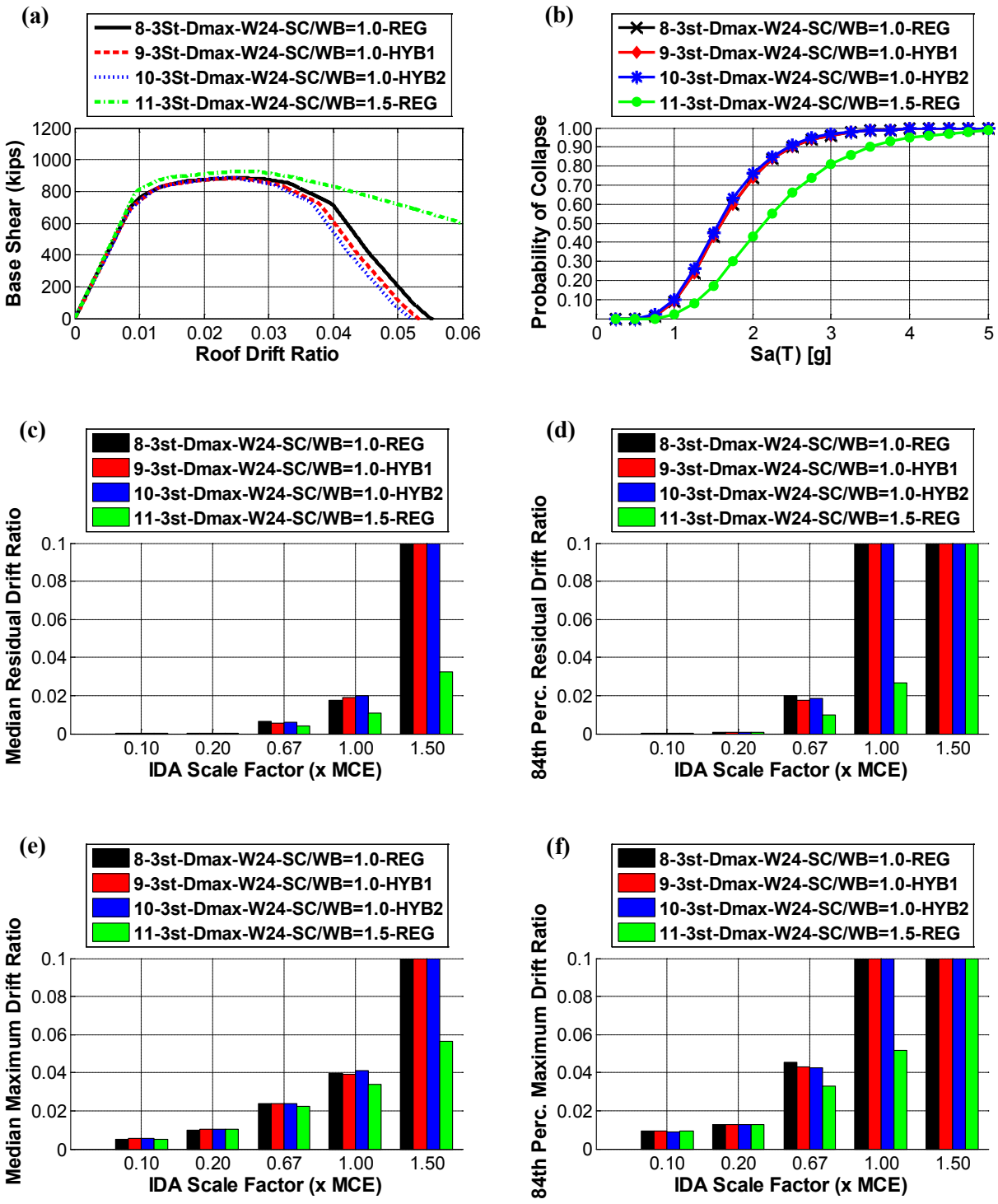

Figure 5-26. Comparison of Regular and Hybrid Frames for 3 Story SMF Designed at Dmax SDC with W24 Columns and SC/WB Ratio of 1.0 (a) Pushover Curves, (b) Fragility Curves, (c) Median Residual Drift Ratios, (d) 84th Percentile Residual Drift Ratios, (e) Median Maximum Drift Ratios, (f) 84th Percentile Maximum Drift Ratios

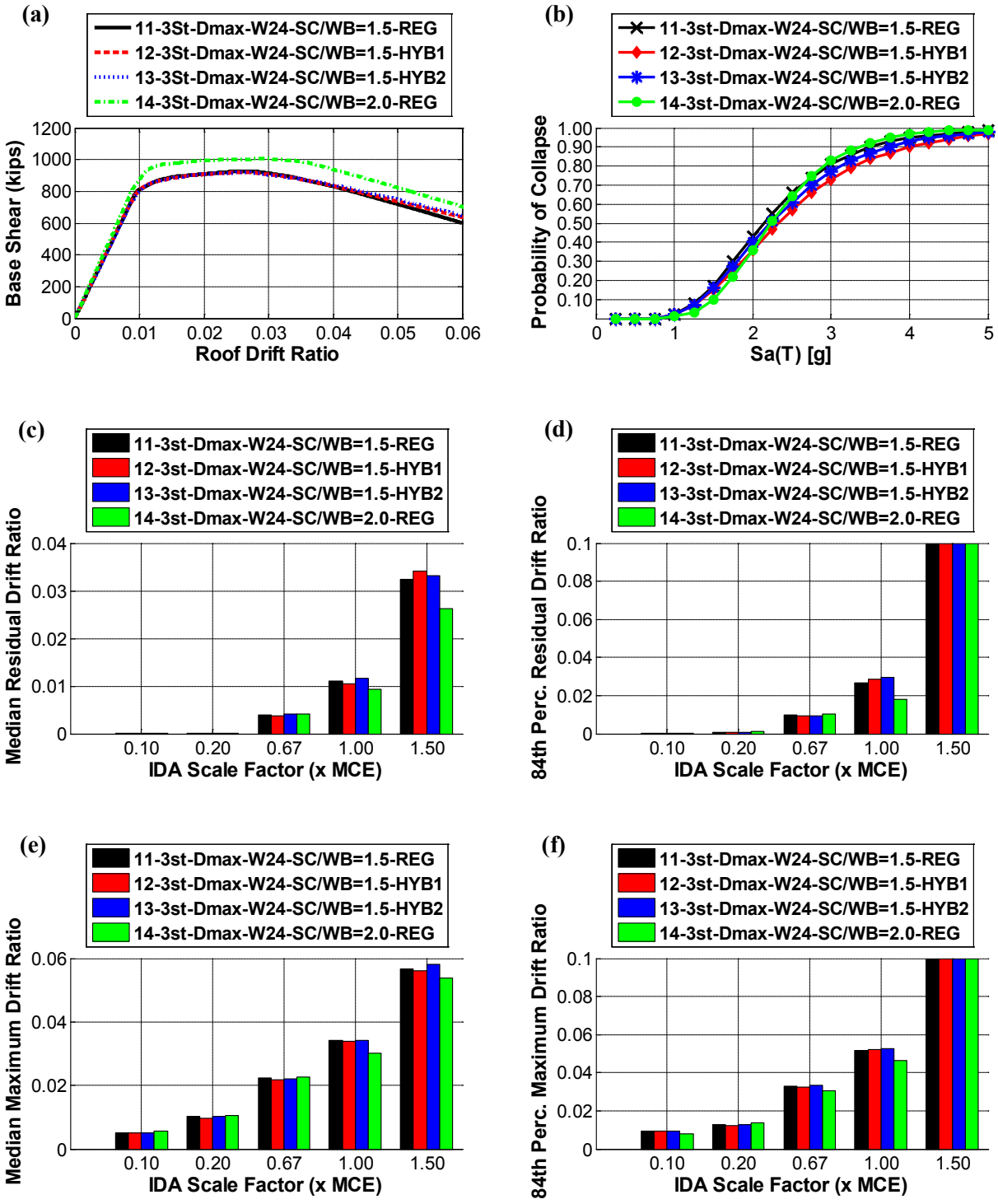

Figure 5-27. Comparison of Regular and Hybrid Frames for 3 Story SMF Designed at Dmax SDC with W24 Columns and SC/WB Ratio of 1.5 (a) Pushover Curves, (b) Fragility Curves, (c) Median Residual Drift Ratios, (d) 84th Percentile Residual Drift Ratios, (e) Median Maximum Drift Ratios, (f) 84th Percentile Maximum Drift Ratios

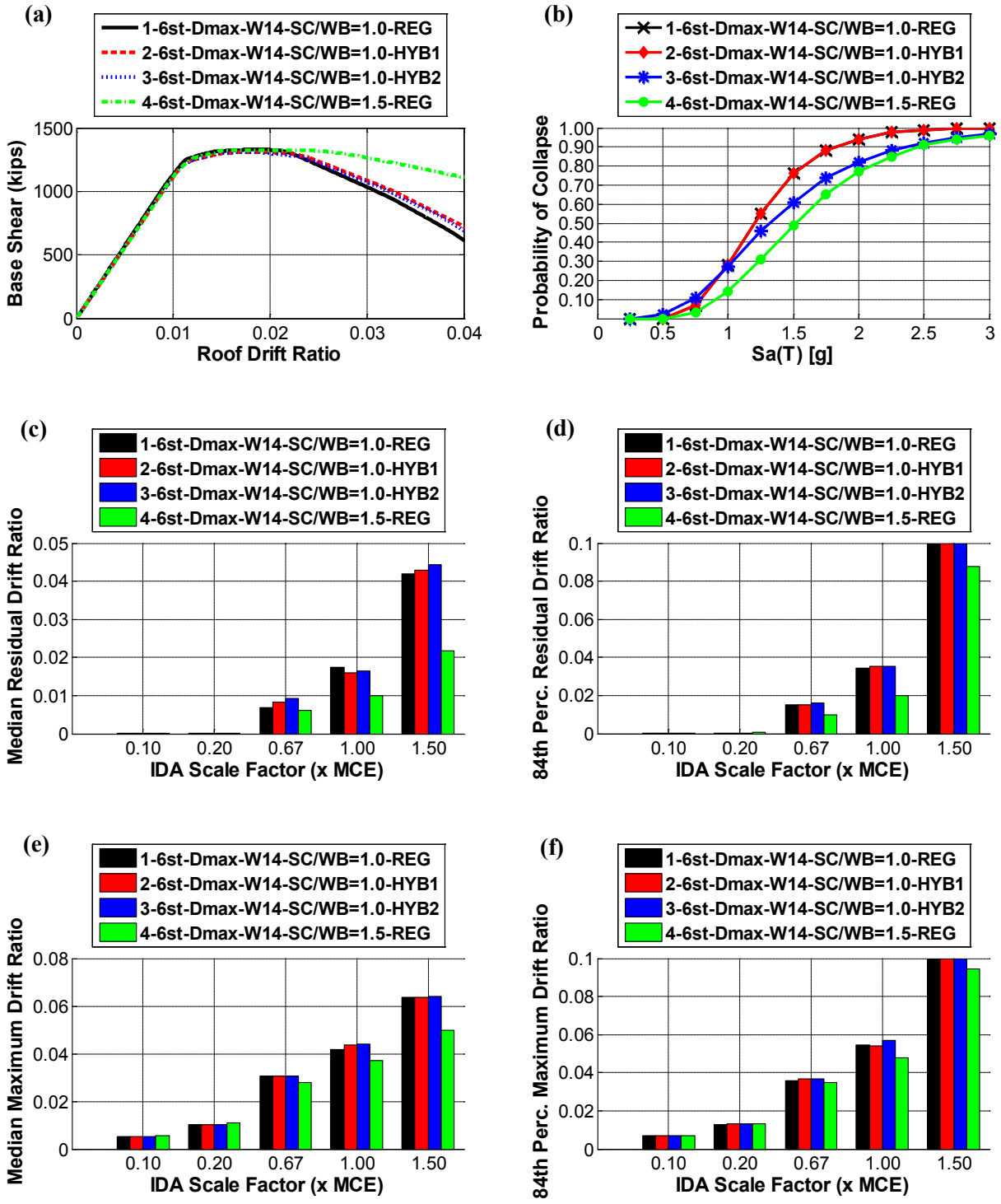

Figure 5-28. Comparison of Regular and Hybrid Frames for 6 Story SMF Designed at Dmax SDC with W14 Columns and SC/WB Ratio of 1.0 (a) Pushover Curves, (b) Fragility Curves, (c) Median Residual Drift Ratios, (d) 84th Percentile Residual Drift Ratios, (e) Median Maximum Drift Ratios, (f) 84th Percentile Maximum Drift Ratios

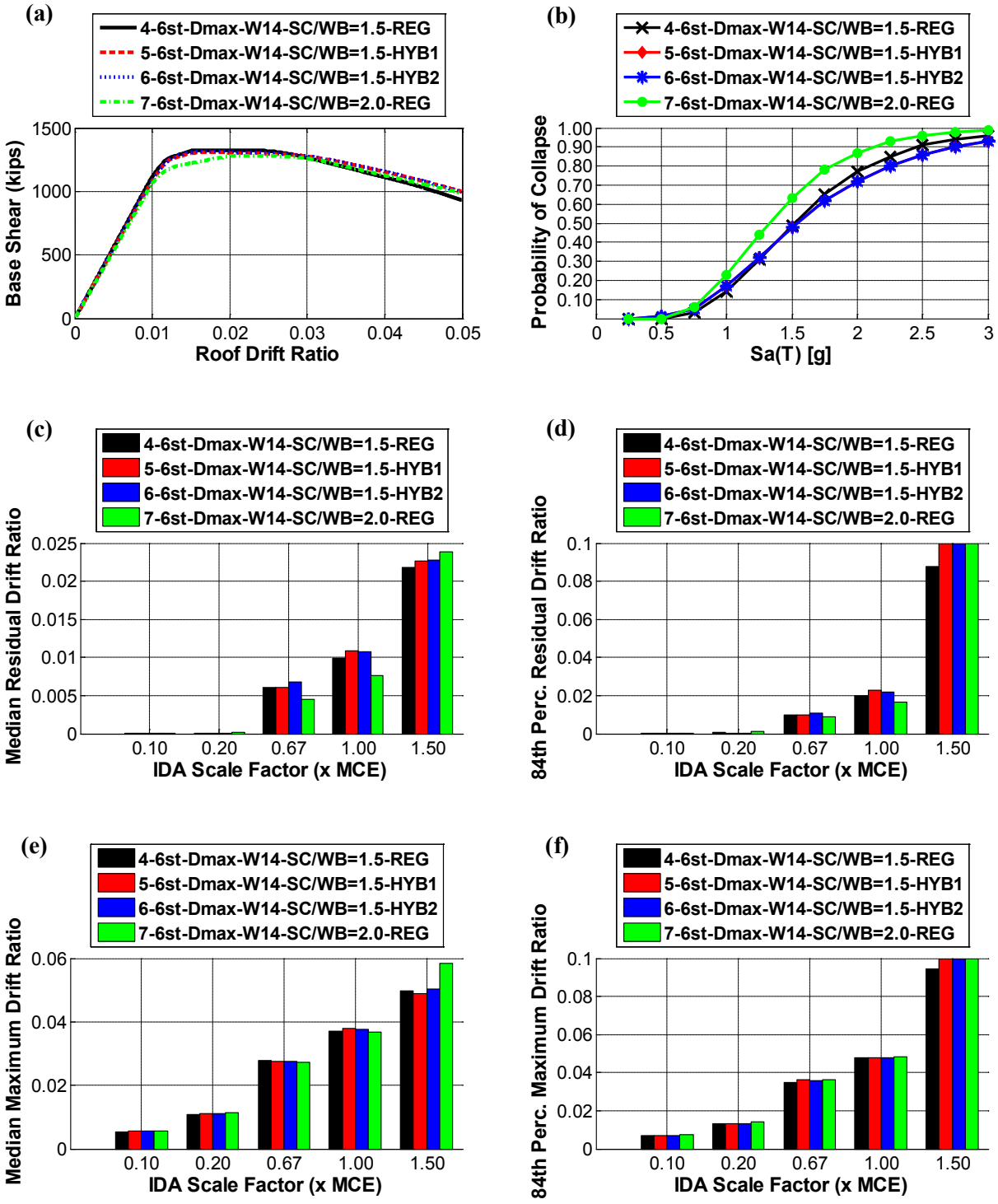

Figure 5-29. Comparison of Regular and Hybrid Frames for 6 Story SMF Designed at Dmax SDC with W14 Columns and SC/WB Ratio of 1.5 (a) Pushover Curves, (b) Fragility Curves, (c) Median Residual Drift Ratios, (d) 84th Percentile Residual Drift Ratios, (e) Median Maximum Drift Ratios, (f) 84th Percentile Maximum Drift Ratios

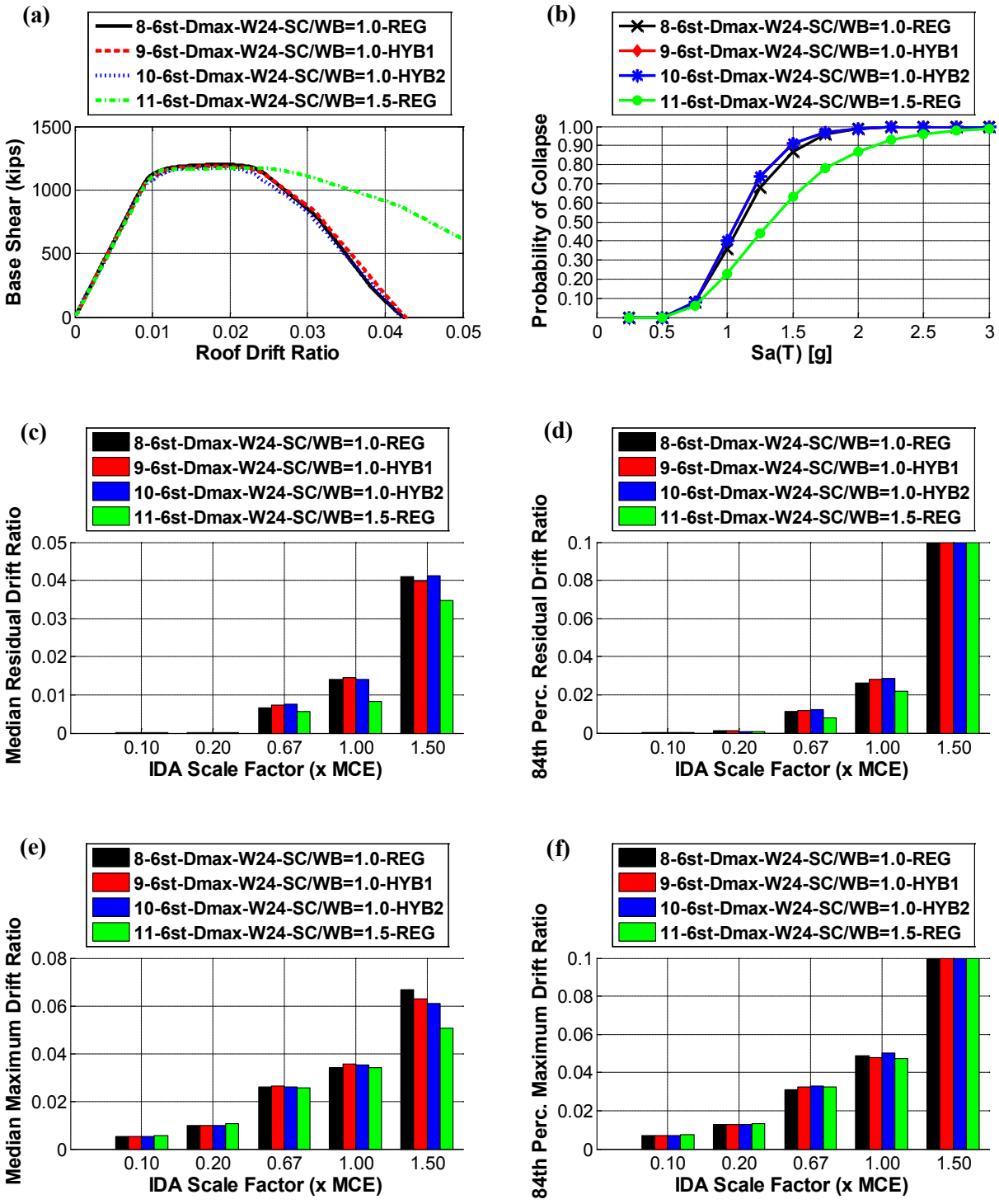

Figure 5-30. Comparison of Regular and Hybrid Frames for 6 Story SMF Designed at Dmax SDC with W24 Columns and SC/WB Ratio of 1.0 (a) Pushover Curves, (b) Fragility Curves, (c) Median Residual Drift Ratios, (d) 84th Percentile Residual Drift Ratios, (e) Median Maximum Drift Ratios, (f) 84th Percentile Maximum Drift Ratios

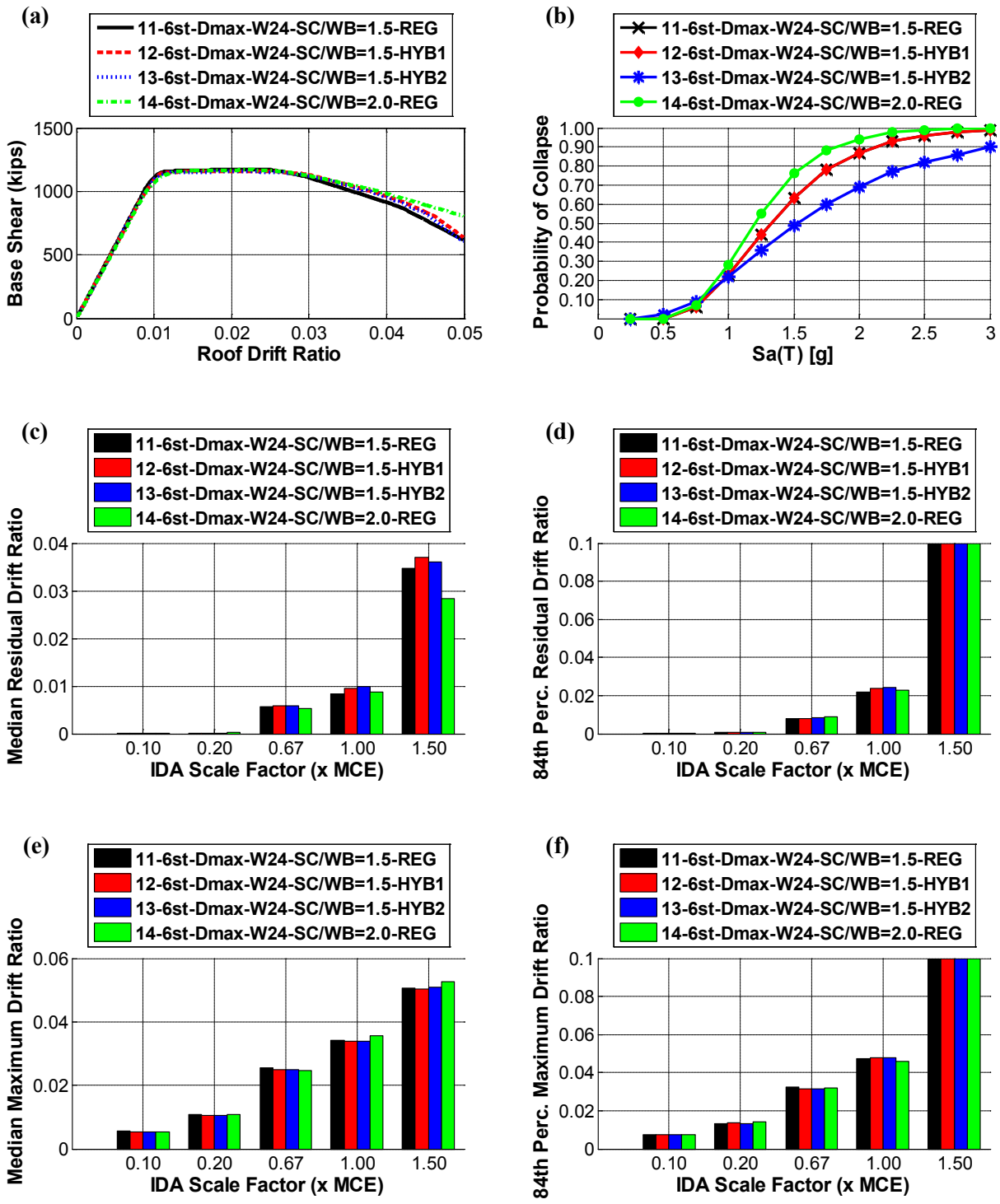

Figure 5-31. Comparison of Regular and Hybrid Frames for 6 Story SMF Designed at Dmax SDC with W24 Columns and SC/WB Ratio of 1.5 (a) Pushover Curves, (b) Fragility Curves, (c) Median Residual Drift Ratios, (d) 84th Percentile Residual Drift Ratios, (e) Median Maximum Drift Ratios, (f) 84th Percentile Maximum Drift Ratios

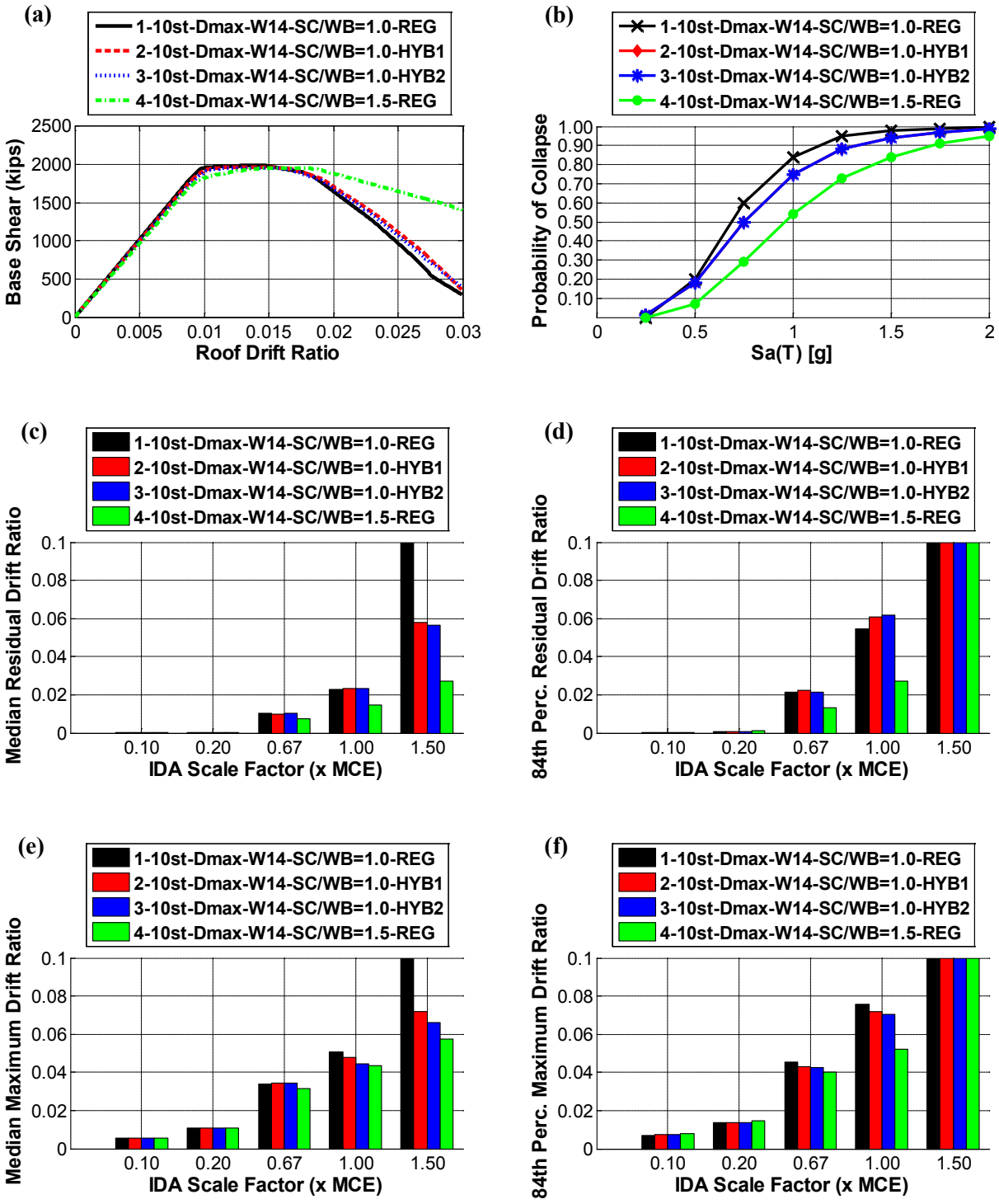

Figure 5-32. Comparison of Regular and Hybrid Frames for 10 Story SMF Designed at Dmax SDC with W14 Columns and SC/WB Ratio of 1.0 (a) Pushover Curves, (b) Fragility Curves, (c) Median Residual Drift Ratios, (d) 84th Percentile Residual Drift Ratios, (e) Median Maximum Drift Ratios, (f) 84th Percentile Maximum Drift Ratios

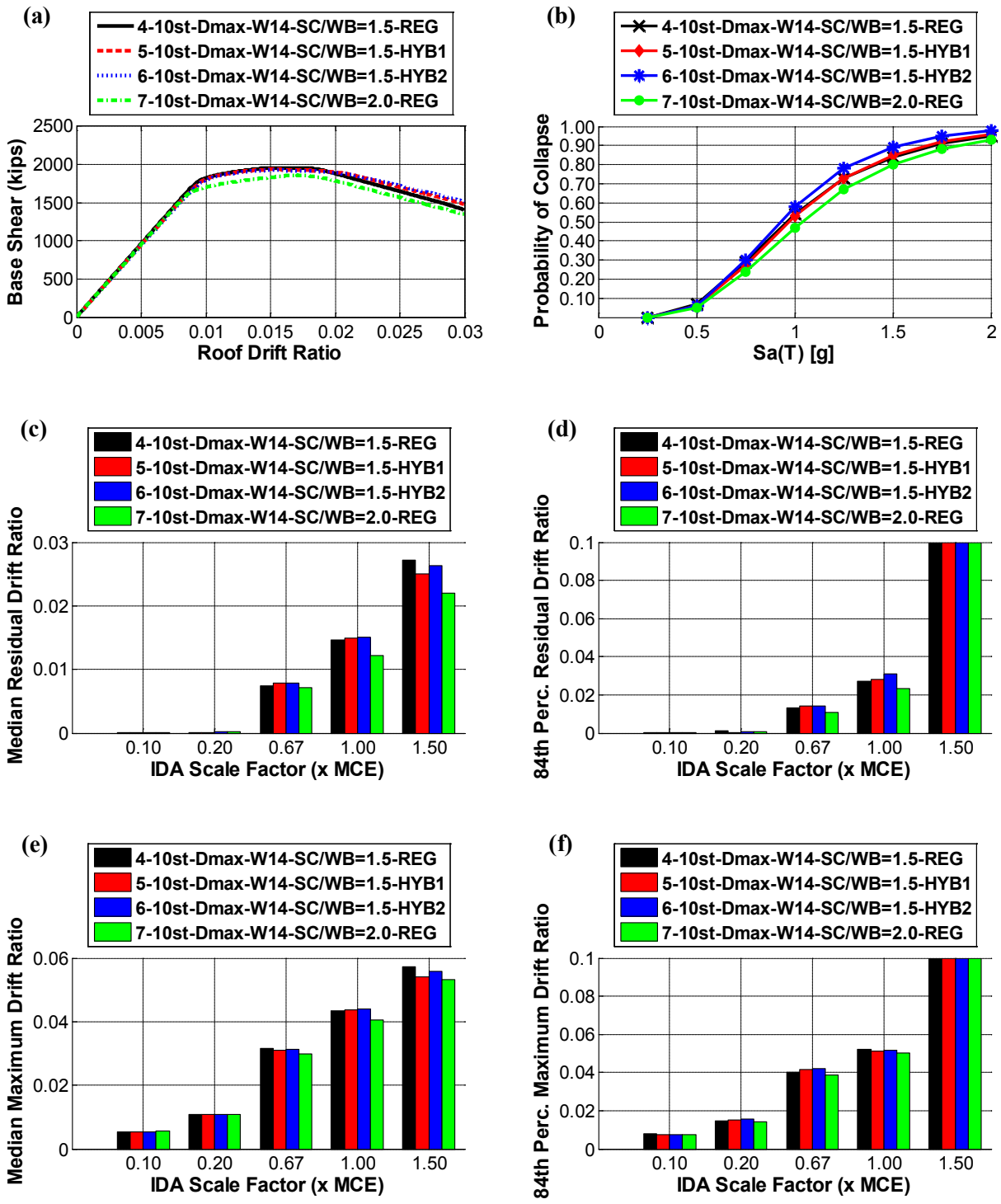

Figure 5-33. Comparison of Regular and Hybrid Frames for 10 Story SMF Designed at Dmax SDC with W14 Columns and SC/WB Ratio of 1.5 (a) Pushover Curves, (b) Fragility Curves, (c) Median Residual Drift Ratios, (d) 84th Percentile Residual Drift Ratios, (e) Median Maximum Drift Ratios, (f) 84th Percentile Maximum Drift Ratios

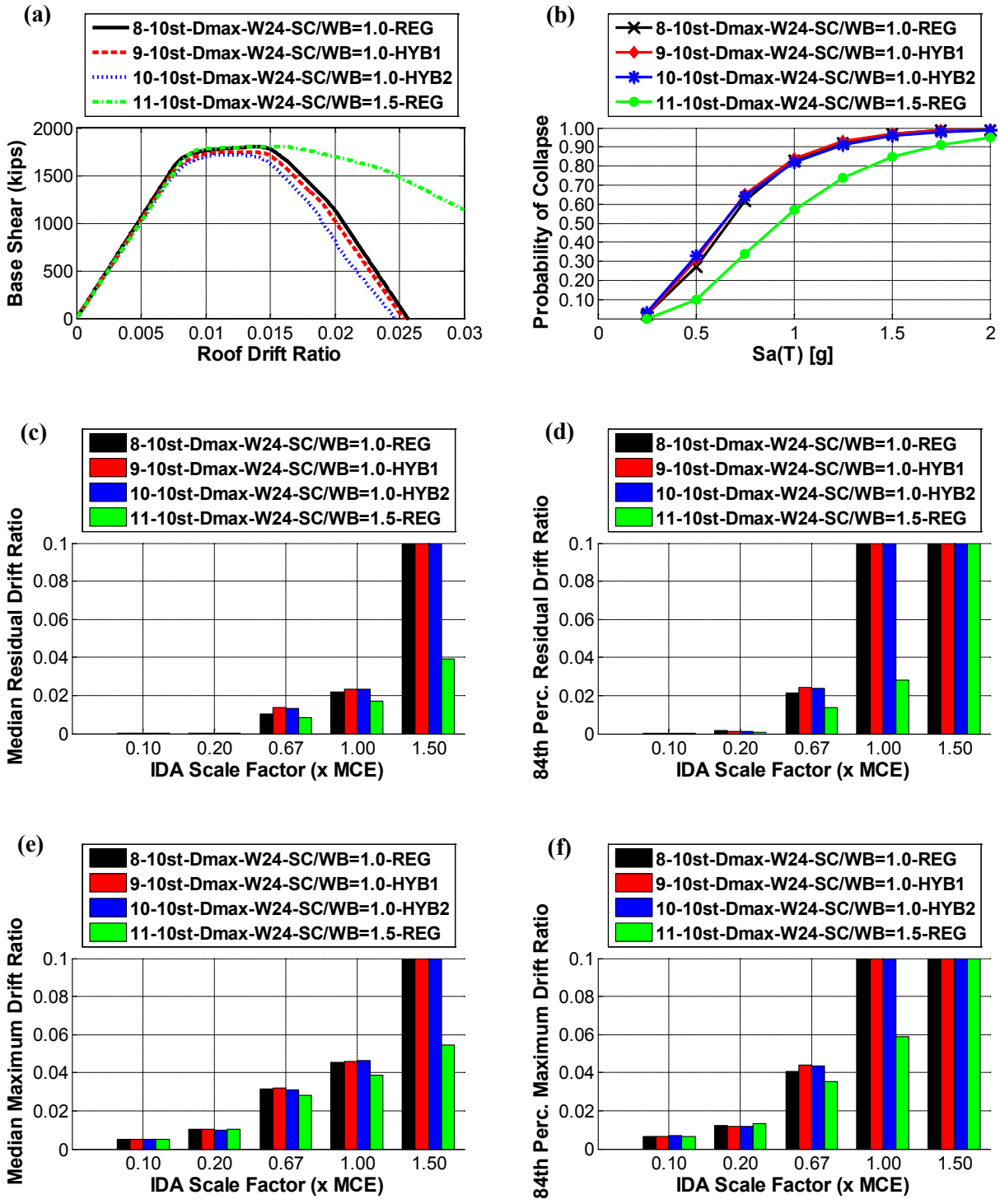

Figure 5-34. Comparison of Regular and Hybrid Frames for 10 Story SMF Designed at Dmax SDC with W24 Columns and SC/WB Ratio of 1.0 (a) Pushover Curves, (b) Fragility Curves, (c) Median Residual Drift Ratios, (d) 84th Percentile Residual Drift Ratios, (e) Median Maximum Drift Ratios, (f) 84th Percentile Maximum Drift Ratios

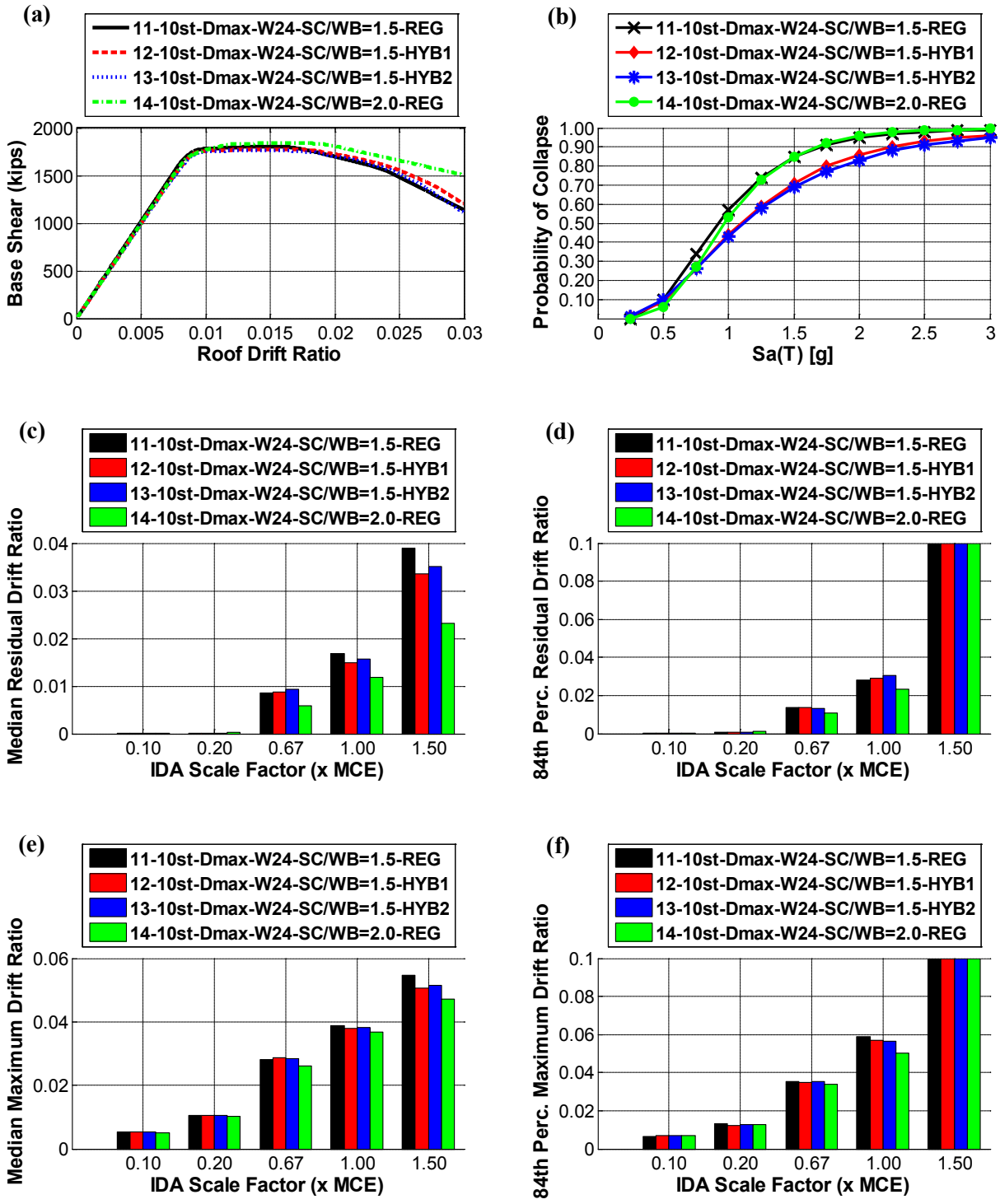

Figure 5-35. Comparison of Regular and Hybrid Frames for 10 Story SMF Designed at Dmax SDC with W24 Columns and SC/WB Ratio of 1.5 (a) Pushover Curves, (b) Fragility Curves, (c) Median Residual Drift Ratios, (d) 84th Percentile Residual Drift Ratios, (e) Median Maximum Drift Ratios, (f) 84th Percentile Maximum Drift Ratios

5.8. Effect of Change in Depth of Girders on Hybrid Behavior

A different way of implementing hybridity into the moment frames might be to use girders with different depths, but with same plastic capacities. At the same curvatures, the deep girders reach higher strain levels (at top and bottom fibers) and are expected to yield earlier than shallow girders. Note that this idea is actually used indirectly in the previous sections of this chapter. The depths of the girders were reduced to increase the capacity and delay the yielding. This was mainly done to keep the stiffness to the hybrid moment frame the same as standard moment frame while changing the girder capacities throughout the story.

The effect of different depth girders is briefly studied on component basis in this section. As an example, the possibility of replacing W27x114 girder with W30x108 and W24x131 sections is studied. All of these girders have RBS connections. They have different depths but they have the same plastic capacities. Figure 5-36 shows the difference in plastic section modulus, inertia, depth to thickness ratio of the beam web, and Ibarra-Krawinkler deterioration parameters of these sections. As may be seen in the figure, moment of inertias increase with deep girders, and the deterioration parameters decrease which results in a reduction in energy dissipation capacities of deep girders.

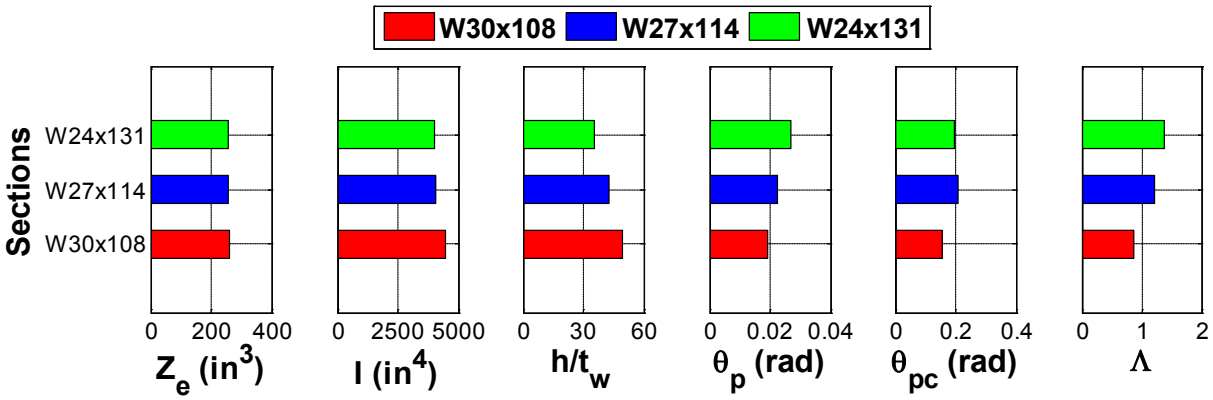

Figure 5-36. Comparison of Girder Sections with Same Plastic Capacities but with Different Depths

Figure 5-37(a) shows the moment curvature diagrams of these three sections with different depths but with same plastic capacities. As may be seen, the deeper girder yields earlier. Figure 5-37(b) shows how a regular and a hybrid frame total moment curvature relationship would look like if a story made of three W27x114 girders were replaced with W30x108, W27x114, and W24x131 sections. As may be seen in the figure, hybrid frame with different depth girders provides somewhat early yielding with the help of deep section (W30). The change in the yielding sequence could be increased if different steel materials with different yield strengths were used in these sections.

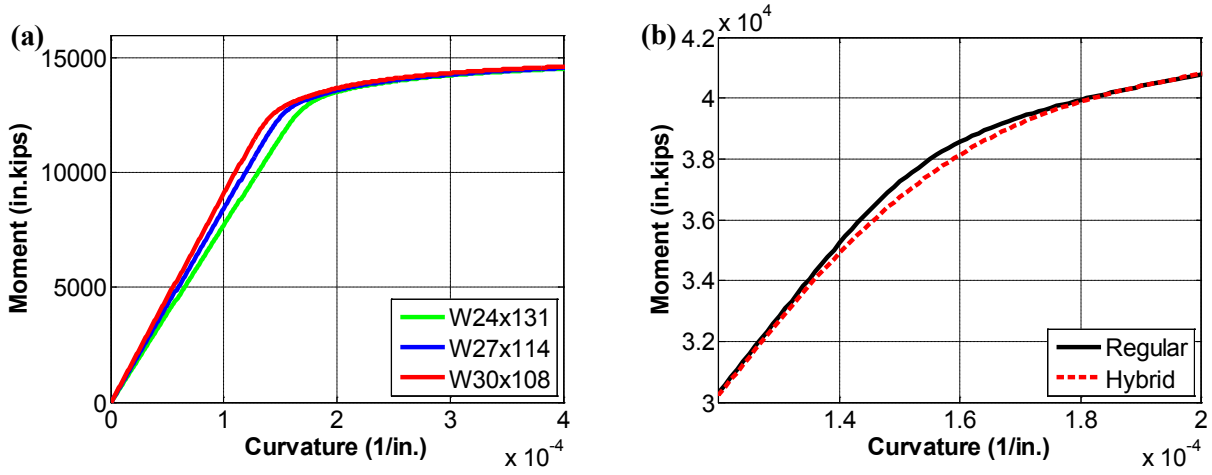

Figure 5-37. (a) Moment curvature relationship (at the center of RBS) of different depth girders with the same plastic capacities (b) Total moment curvature relationship for a regular moment frame (with three W27x114 girders) and hybrid moment frame (with W24x131, W27x114, and W30x108)

Figure 5-38(a) shows the effect of different depth girders with RBS on moment rotation backbone curves created with modified Ibarra-Krawinkler deterioration model. As may be seen, pre-capping and post-capping rotation capacities dropped for the deep W30x108 girder. This is mainly due to the increase in the web depth to thickness ratio of this deep girder. Figure 5-38 (b) and (c) show the hysteresis of 20 ft long W27x114 and W30x108 girders when they are loaded with AISC cyclic load test protocol (up to 4% drift ratio). Figure 5-38 (d) shows the change in the hysteresis for W27x114 and W30x108 girder sections. In addition to the reduction in the plastic capacities (see the monotonic backbone curves), the cyclic deterioration is also more critical for the deep W30 section. The reduction in the Λ value of W30 girder (see Figure 5-36) explains the reason of this behavior.

Although varying girder depths can be used to change the plastification of the system (provide early yielding), the deterioration parameters get worse with the deeper sections which results in a reduction in the energy dissipation capacities. In addition, it is sometimes not possible to increase the depth of the section but keep the plastic capacity the same. This is because of the limitation on the web and flange slenderness limits for highly ductile members.

This preliminary study on the possibility of using deep sections is within the limitations of the RBS beam column connection type and the modified Ibarra-Krawinkler deterioration model with which the deterioration parameters were calculated. Further investigation on the effect of deep girders is necessary investigating different beam-column connection types.

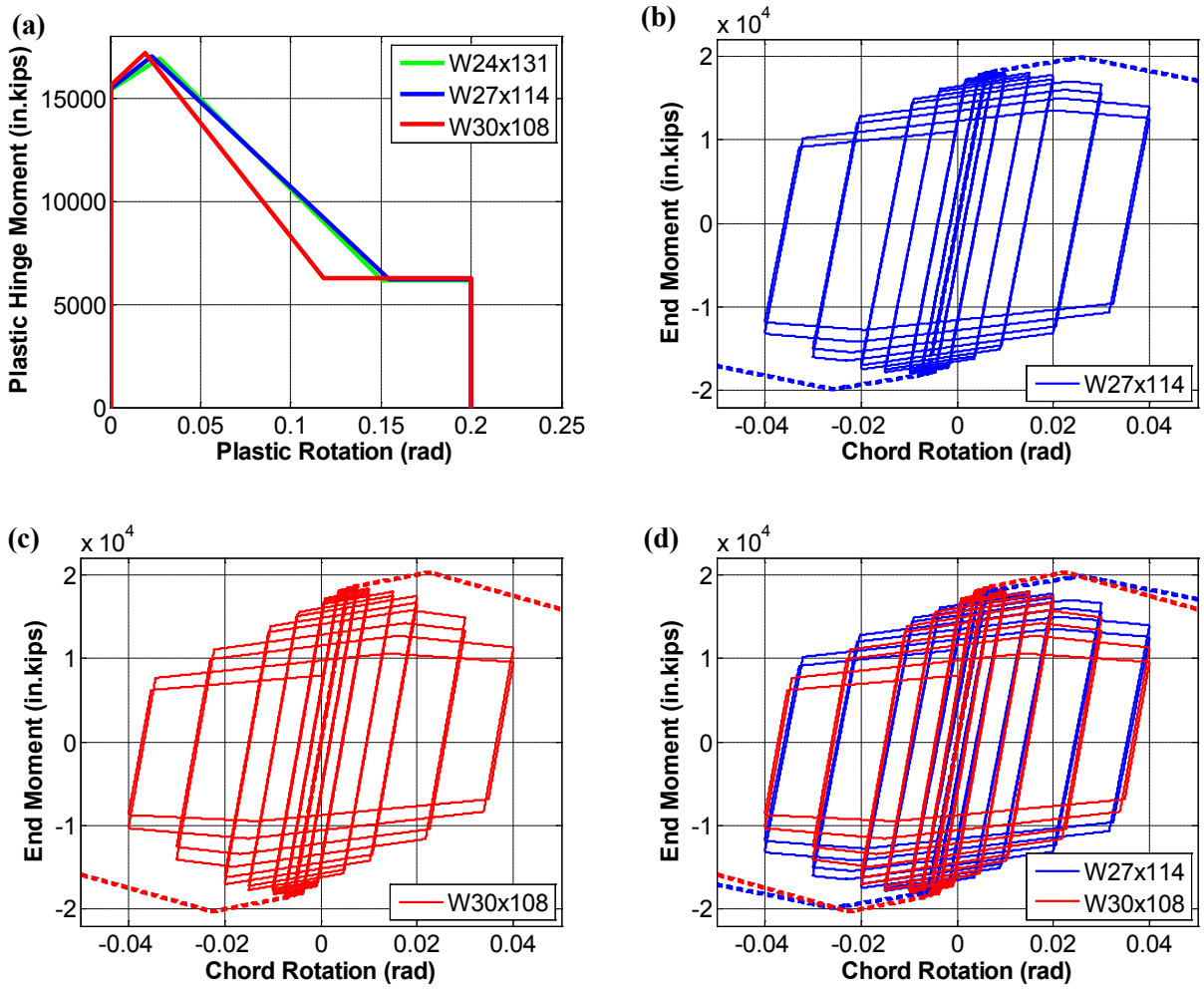

Figure 5-38. (a) Effect of Different Depth Girders with RBS on Moment Rotation Backbone Curves (b) Hysteresis of W27x114 (RBS) with AISC 341 Cyclic Load Test (c) Hysteresis of W30x108 (RBS) with AISC 341 Cyclic Load Test (d) Change in Hysteresis for Different Depth Girders

5.9. Challenges with Hybrid Moment Frames

Unlike Hybrid BRBFs, the performance of the regular systems could not be improved with the Hybrid moment frames. The performance of Hybrid moment frames was sometimes better and sometimes worse than the regular moment frames. The reasons for this can be summarized as follows:

- Changing the yield sequence of the moment frames is much more difficult than the braced frames.

- The modification made for Hybrid moment frames was only on the girder sections. While, this could provide a little bit of early yielding, the post-yield behavior could not be improved. This is

because moment frame collapse mechanisms form in the columns and this is what governs the post-yield behavior.

- The degradation of the moment frame connections affects the performance negatively. While providing early yielding, the cut of RBS was increased and the girder sizes were decreased. Most of the time, this change reduces the energy dissipation capacity of the connection.

- While modifying the girder sections, the total plastic capacity and stiffness of the story was kept the same. These two constraints resulted in an increase in the cost. Better performance could be achieved when this additional expense was used on columns by increasing the SC/WB ratios of the regular moment frames.

CHAPTER 6: ALTERNATIVE HYBRID MOMENT FRAMES

To provide adequate ductility in the reduced capacity bays with special detailing, alternative hybrid moment frame connections adapting the use of low strength steel were also considered. Two different approaches have been studied and are presented herein. Because low strength steel is available in plates, the connection types where yielding is occurring in the plates are studied. Note that the models and analyses in this section are preliminary and the use of low strength steel in moment frame connections should be investigated further.

6.1. Alternative Hybrid Moment Frame Strategy-1

Alternative hybrid strategy was implemented on a four story model building taken from NIST (2010). This building was designed according to Dmax seismic design category. Figure 6-1 shows the plan and elevation views of the model. Analyses were performed on a 2-D model using OpenSees. P-Delta effects were included thorough a leaning column. Displacement based beam-column elements were used to model distributed plasticity of fiber sections. Krawinkler type panel zones were used. Deterioration was neglected for both the plastic hinges and panel zones. Fundamental period of the model was calculated as 1.21 sec.

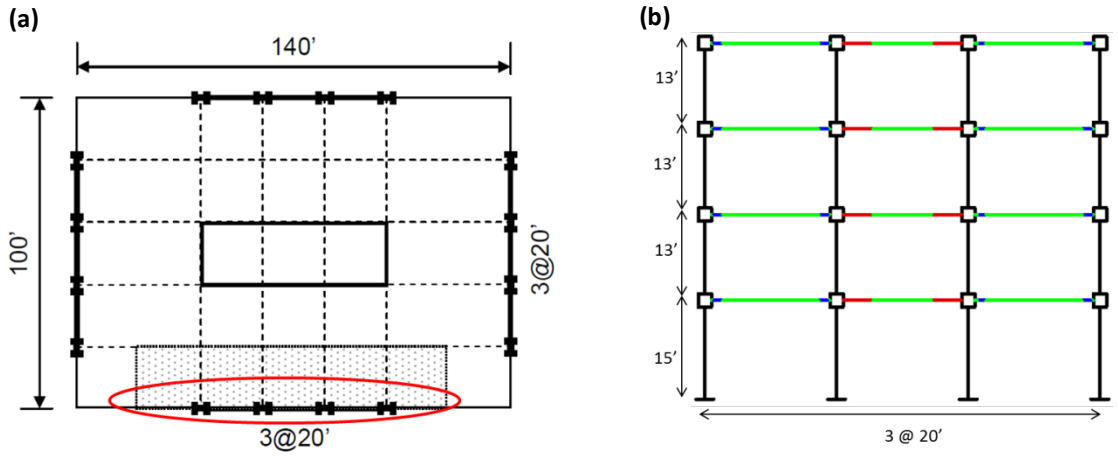

Figure 6-1. (a) Plan and (b) Elevation Views of Moment Frame Used in Analyses

To provide hybridity into the system, the capacity of the middle bay was increased by 100%, and the capacities of the 1st and the 3rd bays decreased by 50%, keeping the total plastic strength of the frame the same. Figure 6-2 (a) and (b) show the methods used to increase and decrease the capacities of the girders.

Capacity decrease was provided by cutting the flange and adding a low strength steel instead. Highly ductile low strength steel will start dissipating energy early and will help to minimize the response under low intensity earthquakes. Although it is not shown in Figure 6-2, there should be a buckling restraint plate placed on top of the yielding plate to prevent the buckling of the yielding plate. Capacity increase was provided by adding a cover plate. This will help to move the plastic hinge location away from the column face and the capacity will be increased depending on the length and thickness of the reinforcement plate. A bigger wide flange section can also be used to increase the girder capacity instead of reinforcement addition.

Figure 6-3 shows the girder modification (with fiber sections) and the moment-curvatures of the first story girder, W24x103. Figure 6-4 displays the pushover curves for the regular and hybrid four story SMF. Unlike Hybrid BRBFs, the strength of the regular frame could not be achieved in Hybrid moment frame. Early yielding can be observed in the zoomed pushover plot. While regular SMF reached negative stiffness at 2% roof drift, Hybrid SMF has positive stiffness up to 4% roof drift. Note that the neglect of the possible deterioration might have contributed in achieving higher post-yield stiffness of the Hybrid system. This proposed connection should be tested before modeling the deterioration parameters of the connection.

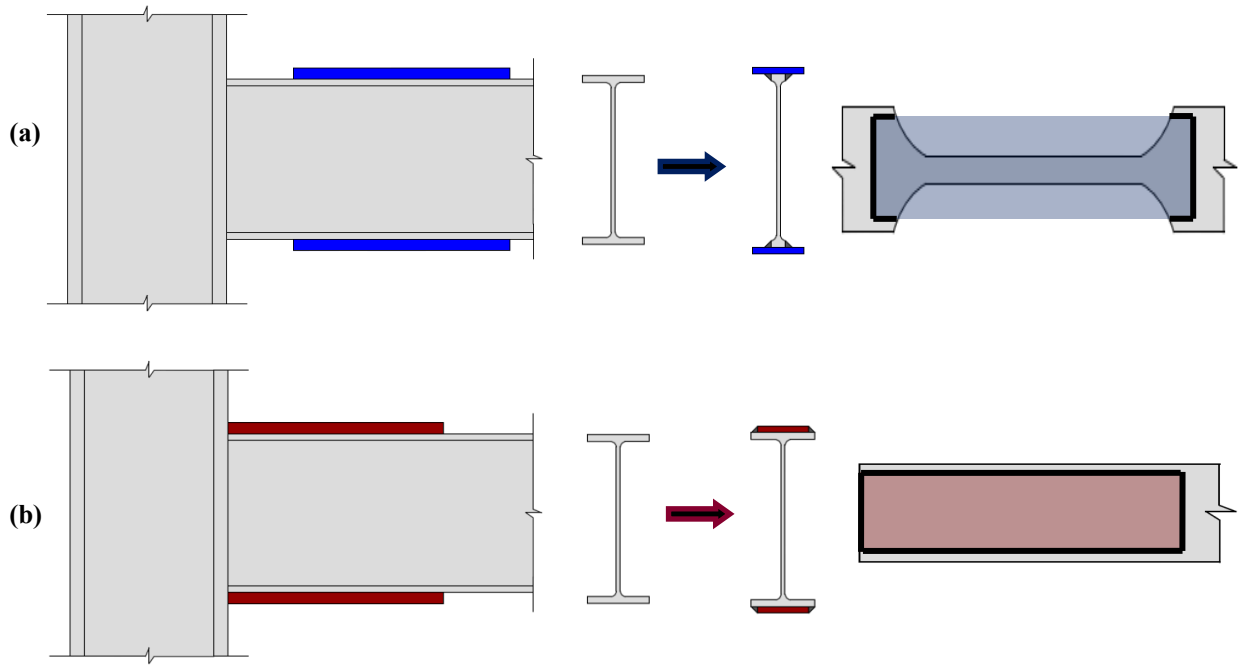

Figure 6-2. Hybrid Frame Connection (a) Capacity Decrease (b) Capacity Increase

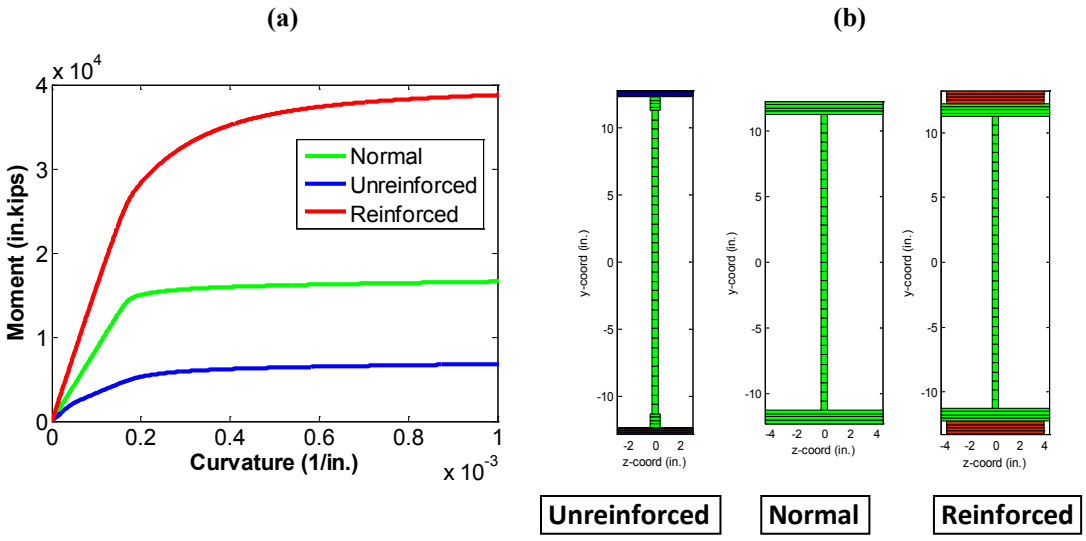

Figure 6-3. (a) Moment Curvature of W24x103 Sections (b) Girder Modification

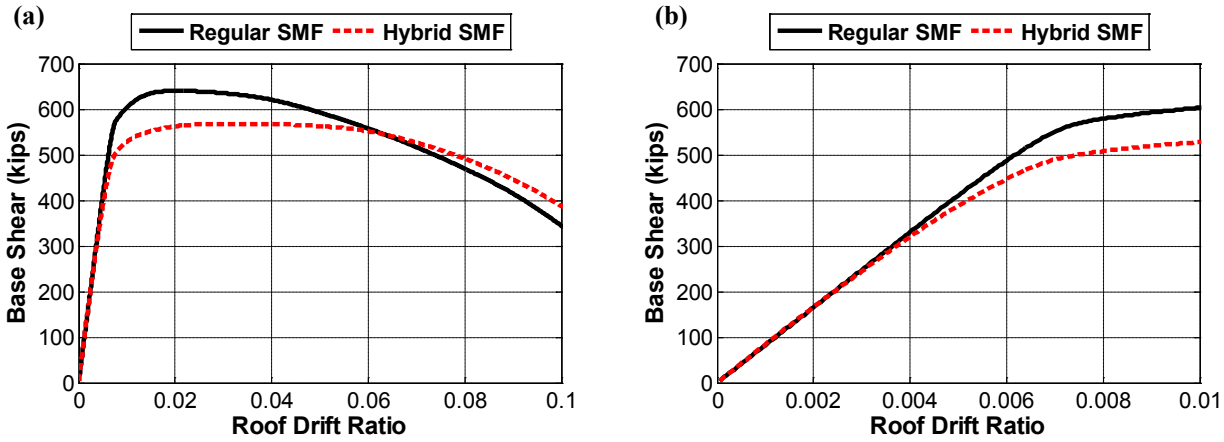

Figure 6-4. Pushover Curves for Regular and Hybrid SMF (2nd Plot Zooms in Low Drift Levels)

Figure 6-5 and Figure 6-6 compare the maximum story drift ratios for the regular and Hybrid moment frames under Far-Field ground motion set at DBE and MCE levels. Figure 6-7 shows median maximum interstory drift ratios calculated from the response of 44 earthquakes for regular and Hybrid SMFs.

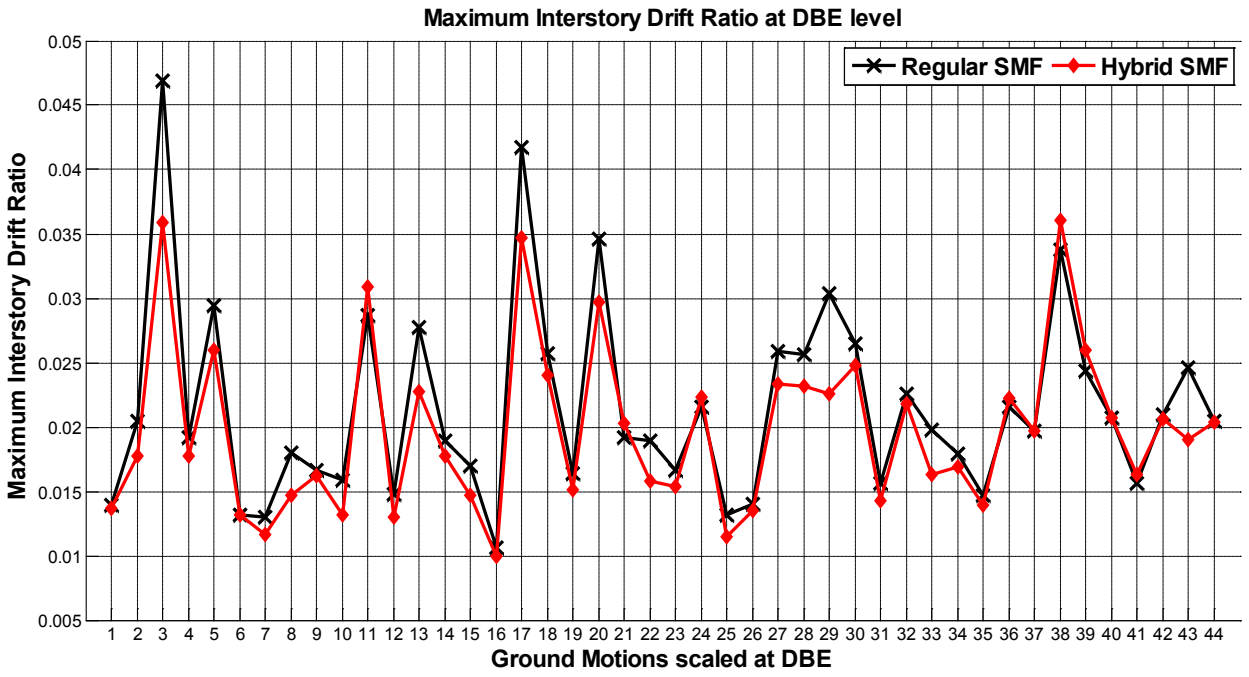

Figure 6-5. Hybrid Moment Frame Maximum IDR Performance Comparison at DBE Level

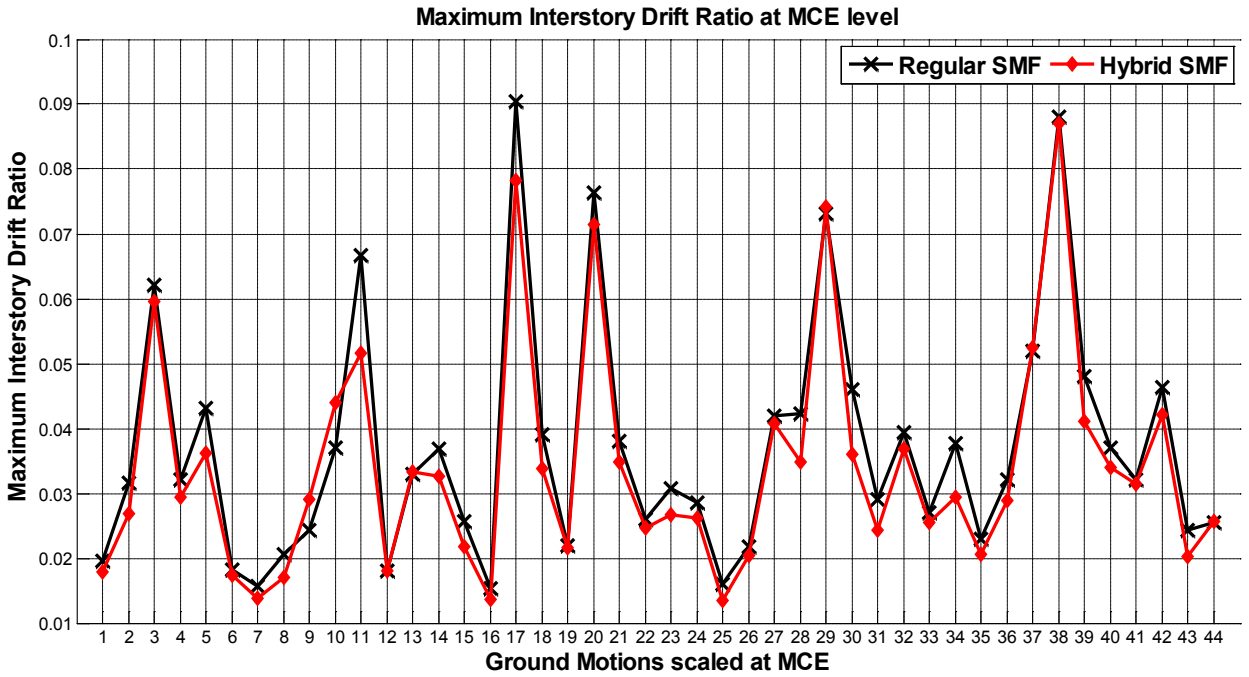

Figure 6-6. Hybrid Moment Frame Maximum IDR Performance Comparison at MCE Level

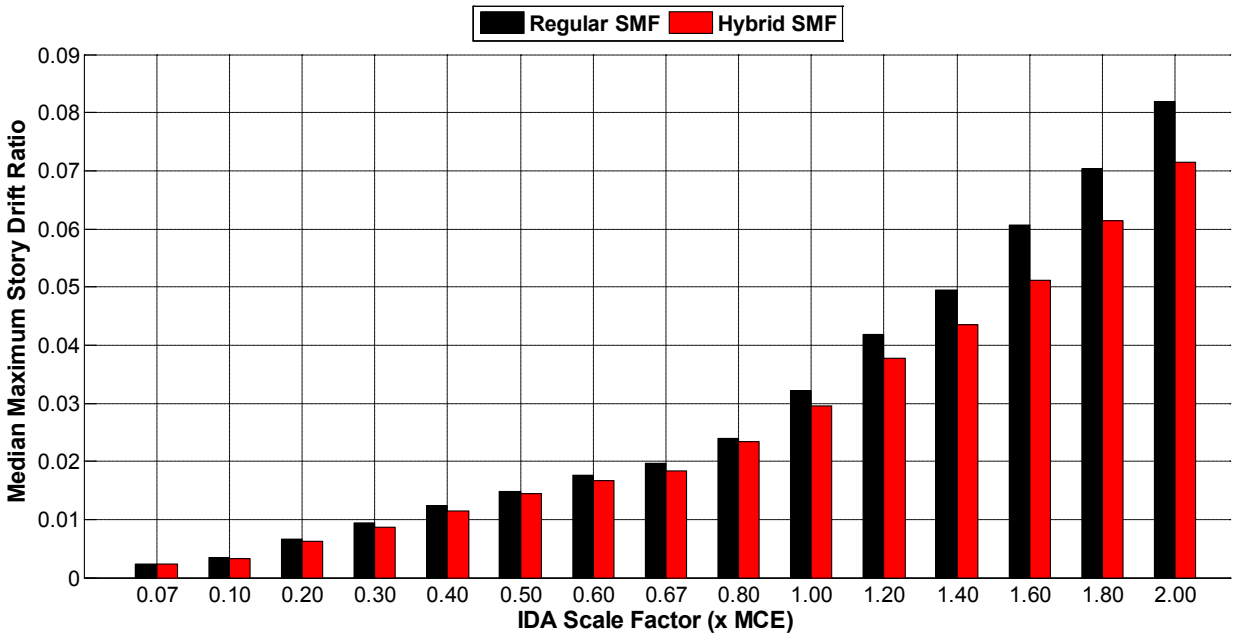

Figure 6-7. Median Maximum Interstory Drift Ratio for Regular and Hybrid SMFs

6.2. Alternative Hybrid Moment Frame Strategy-2

As the second alternative of Hybrid moment frames, a new type of special moment frame connection patented by Simpson Strong-Tie (SST) was tried (Simpson Strong-Tie, 2011). The connection system features a pair of buckling restrained T-shaped yield links that provide a moment resisting connection between the beam and the column (See Figure 6-8(a)). The stem of the yield link has a central portion of reduced width such that all the yielding in the connection is constrained within this central portion while providing the required ductility in the frame to resist lateral forces from seismic events (See Figure 6-8(b)). The yield link stem is connected to the yield link flange with a set of double sided fillet welds. The restraint against buckling is provided by means of a cover plate which is bolted to the beam flange. Spacers are provided between the buckling restraint cover plate and the beam flange such that the required gap is provided for Poisson's expansion of the links while in compression. The yield link stem is connected to the beam flange through fully pretensioned ASTM A490 bolts. The yield link T-flanges connect to the column flanges through pairs of snug-tight ASTM A325 bolts. The shear transfer between the beam and column is made via a standard bolted shear tab connection using a combination of holes and slots, with slots perpendicular to the line of shear force (Simpson Strong-Tie, 2011). The advantages of this connection are that it is easy to repair after an event as all the damage is localized in the link element, and since the demands on the beam are small, the lateral bracing requirements of the beams are reduced.

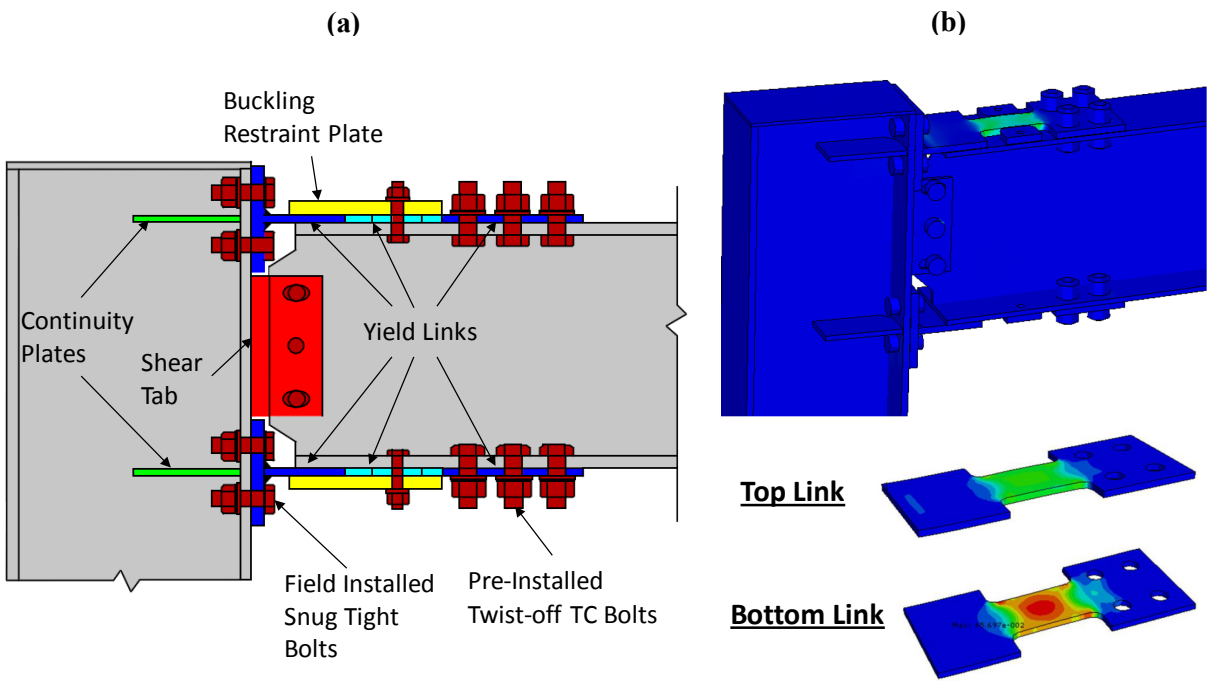

Figure 6-8. (a) Simpson Strong-Connection (b) Plastic Strains in the Yield Links as a Result of FEA (Simpson Strong-Tie, 2011: Used with Permission)

This connection was studied on a one story SMF taken from *ATC-76-1* project (NIST, 2010). The plan of the building is the same as shown in Figure 6-1(a). In the model; columns were pinned at the base, Krawinkler type panel zones were used and beam-column elements were modeled using distributed plasticity elements with fiber sections. Deterioration in the properties of panel zone and yield link was not considered. Since the yield link is working like a BRB, the deterioration for this connection is limited and less than RBS connection. In order to model reduced beam sections (RBS) with fiber sections, RBS was divided into eight pieces with different flange widths assigned for each piece (See Figure 6-9). The fundamental period of the frame was calculated as 0.78 sec.

Hybridity was implemented to the frame with some certain assumptions. As may be seen in Figure 6-10, the regular SMF has RBS at all three bays. It was decided to increase the capacity of the middle girder while decreasing the capacities of the exterior girders. Capacity increase was implemented by not using a RBS at the middle bay. In order to decrease the capacities of the edge girders, RBS connections were replaced by SST connection with LYP steel. Two different sections were tried for the yield link of the SST connection (See Figure 6-10). The only difference between the sections is the width of the top portion of the yield link stem. In Hybrid-1 model, yield link top portion was assumed to be equal to the

flange width of the beam, and in Hybrid-2 model, it was assumed as 80% of the beam flange width. Yield links were modeled with fiber section elements.

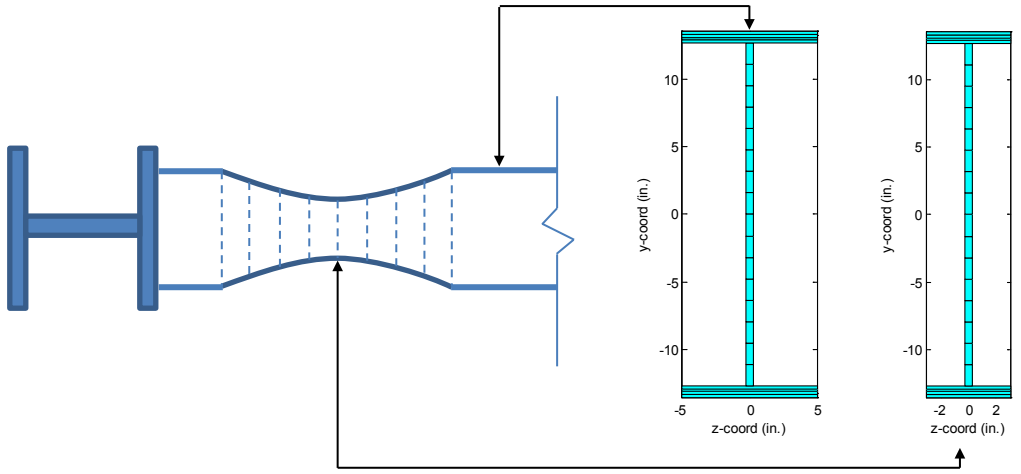

Figure 6-9. Reduced Beam Section (RBS) Modeling Using Fiber Section Elements

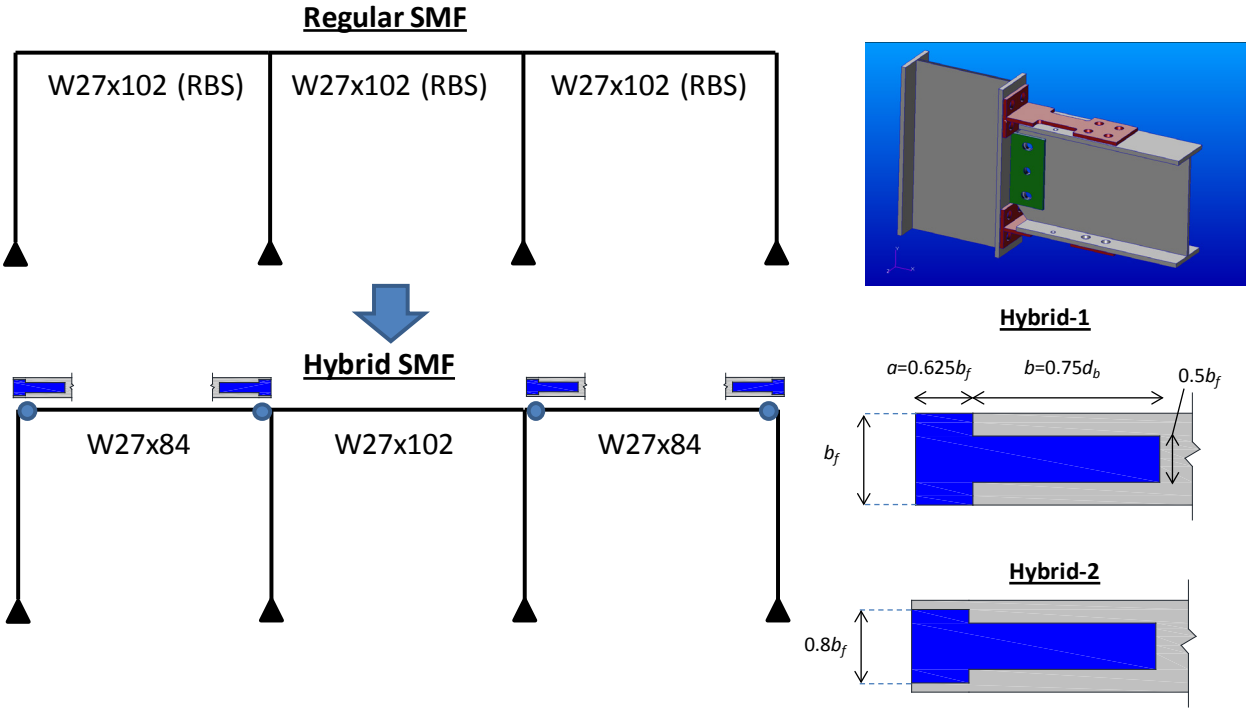

Figure 6-10. Implementing Hybridity into the System for SST Moment Connection

Figure 6-11 shows the pushover curves of regular SMF and hybrid SMFs with SST connection. As may be seen, initial stiffnesses of the frames are identical and due to reduced width of Hybrid-2 connection,

Hybrid-2 frame yields earlier than Hybrid-1. Unlike the 1st moment frame strategy (See Figure 6-4), the strength of the regular SMF could be achieved with SST connection (See Figure 6-11).

The post-yield stiffness of the hybrid frames found to be slightly larger than the regular frame stiffness.

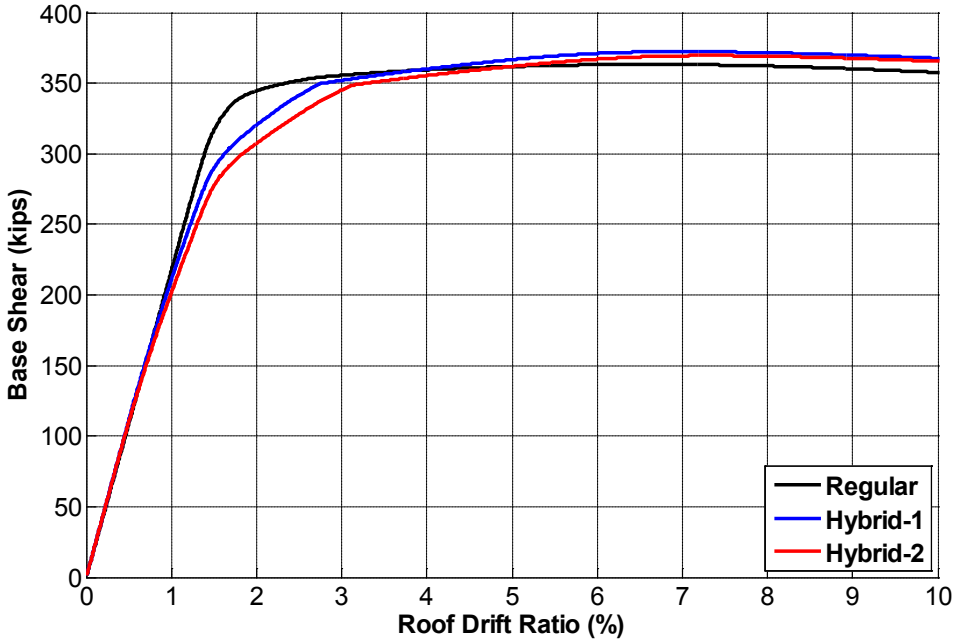

Figure 6-11. Pushover Curves for SST Moment Connection

Dynamic analyses were run using *FEMA P-695* methodology. Analyses were run up to MCE level in twenty increments. Figure 6-12 and Figure 6-13 show the median performance improvement of hybrid frames for maximum story acceleration and maximum interstory drifts respectively. On average, performance improvement is about 4% for the story acceleration and about 8% for the maximum interstory drifts. Since deterioration was neglected in the analyses, residual displacements were very small for both systems.

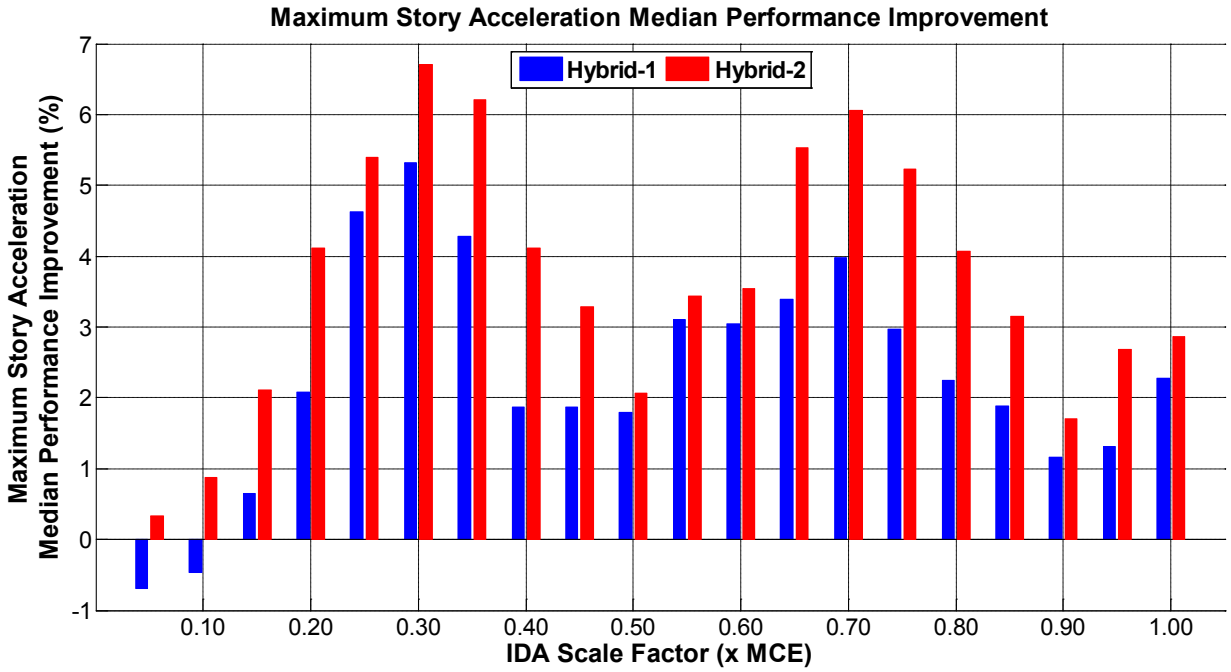

Figure 6-12. Maximum Story Acceleration Median Performance Improvement for Hybrid Frames with SST Connection

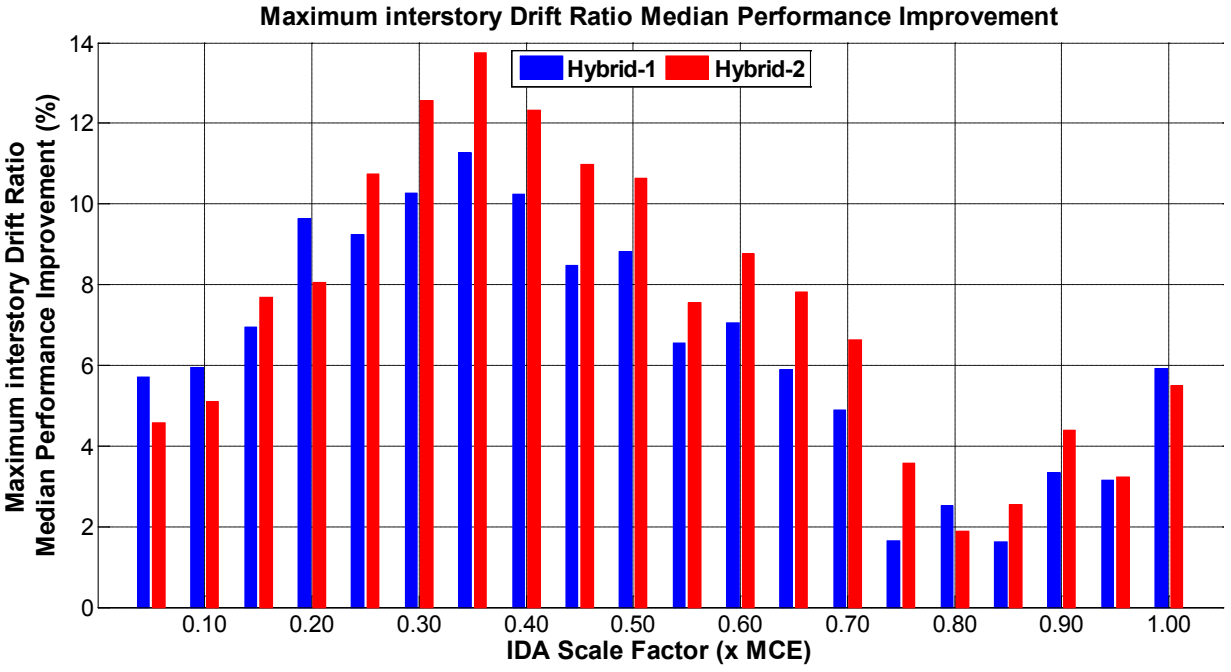

Figure 6-13. Maximum Interstory Drift Ratio Median Performance Improvement for Hybrid Frames with SST Connection

6.3. Chapter Summary

Two new moment resisting connections were tried as alternative ways to implement hybridity into the moment frames. What makes these connection types special is that the yielding is occurring in the plates for both of these connections. This is important for the implementation of LYP steel into the moment frame connections as LYP steel is only available in plates. Preliminary pushover and dynamic analyses were conducted on short story moment resisting buildings.

When the pushover curves shown in Figure 6-4 and Figure 6-11 are compared with the pushover curves discussed in Chapter 5, it may be concluded that it is much easier to obtain early yielding and change the plastic hinge forming sequence when different steel material like LYP100 is used at the moment frame connections.

When the maximum interstory drift ratios of alternative hybrid moment frames are compared with regular (non-hybrid) frames, a reduction of 5% to 10% was achieved with hybrid frames. The degradation in these moment frame connections were not implemented in the analytical models. However, because the yielding plates are acting like BRBs, the degradation of these connections is expected to be less severe than the regular moment frame connections like RBS connections. The first alternative connection type is introduced as a new connection idea, and lab tests need to be conducted before evaluating the degradation of the connection. Simpson Strong-Tie (SST) connection was tested in the lab, and it could easily pass the Seismic provisions criterion. Out of three lab tests conducted on SST connection, only one of them showed limited pinching at about 5% drift ratio, while the other tests showed very stable hysteresis up to 5% drift ratio (Simpson Strong-Tie, 2011). SST is interested in incorporating low strength steel in their patented connection.

As a result of preliminary analyses performed on alternative hybrid moment frame connections with LYP steel yield plates, encouraging results were obtained. The story accelerations and maximum story drifts of hybrid frames were smaller than the regular systems under all ground motion intensities. However, the change in the performance (5-10% reduction in story acceleration and drifts) was minor. These connection types should further be investigated on a design space thorough *FEMA P-695* evaluation and lab tests incorporating the use of low strength steel as the steel yield plate should be conducted.

CHAPTER 7: SUMMARY and CONCLUSION

7.1. Research Summary

This research introduces two new structural steel systems: hybrid Buckling Restrained Braced Frames (BRBF) and hybrid steel Moment Frames (MF). In this study, the hybrid term for the BRBFs comes from the use of different steel material including carbon steel (A36), high-performance steel (HPS) and low yield point (LYP) steel. The hybridity of the moment frames is related to the changes in the plastification of the systems which is provided by using weaker and stronger girder sections. Alternative moment frame connections incorporating the use of LYP steel plates were also investigated.

A hybrid BRBF was developed by modifying regular (non-hybrid) various BRBFs. The possibility of an independent multi-core brace was discussed and the available options in practice were presented. The hybrid BRBF approach was tested on seventeen regular frames with different story heights, seismic design categories and building plans. Varying the steel areas and materials in the BRB cores, three hybrid BRBFs were developed for each regular frame and their behavior was compared against each other through pushover and incremental dynamic analyses. The benefits of the hybridity were presented using different damage measures such as story accelerations, interstory drifts, and residual displacements. Collapse performance evaluation was also provided.

The performance of hybrid moment frames was investigated on a design space including forty-two moment frame archetypes. Two different hybrid combinations were implemented on the designs with different column sections and different SC/WB ratios. The efficiency of the hybrid moment frame idea in which only the girder sizes were changed to control the plastification was compared with regular moment frame designs with higher SC/WB ratios. As side studies, the effect of shallow and deep column sections and SC/WB ratios on the moment frame behavior were also investigated.

To provide adequate ductility in the reduced capacity bays with special detailing, alternative hybrid moment frame connections adapting the use of low strength steel were also considered. Preliminary analyses were conducted on two hybrid moment frame approaches. The first option provided a capacity decrease by removing a portion of the original beam flange and replacing it with a low strength steel cover plate. Moment capacity increase was provided by adding a cover plate or by using a bigger wide flange section. The second option involved a new type of special moment frame connection patented by Simpson Strong-Tie. This connection offers a T-shaped buckling restrained yield link which has a central portion with reduced width. Hybridity was added thorough the use of LYP steel in these yield links.

Preliminary pushover and dynamic analyses were conducted on hybrid moment frames with LYP steel plate connections.

7.2. Conclusions

The following conclusions can be made as a result of the research studied on hybrid BRBFs:

- The use of low strength steel results in early yielding while providing high ductility capacity.

- Hybrid BRBFs gave very encouraging results in terms of overall seismic performance. The median maximum interstory reduced up to 10% at all ground motion levels up to collapse. Performance improvement in story accelerations was not significant. *The most significant improvement was that the residual displacements decreased about 30% to 40% at all intensities.*

- In hybrid BRBFs, while enhancing the system performance, the cost of the system stays very close to that of regular non-hybrid systems. The only cost increase is due to the very slight increase in the total brace core area and due to use of low strength steel and high strength steel instead of carbon steel. This minimum economic impact makes hybrid BRBFs more attractive.

- Collapse margin ratios increased and probability of collapse decreased for hybrid BRBFs. As an example, at individual archetype collapse evaluation intensity, 7 (out of 44) earthquakes caused collapse on regular BRBFs, while 3 collapses occurred for hybrid BRBFs in the 1st case study, BOB model.

- The increased collapse margin ratios or reduced collapse probabilities of hybrid BRBFs indicate that a higher response modification factor (R) than 8, which is used for non-hybrid BRBFs, could be used for hybrid BRBF systems. The increase in the R factor of hybrid BRBFs will make the hybrid BRBFs perform similar to non-hybrid BRBFs, but will result in a cheaper system than the regular BRBFs. If the same R factor of regular BRBFs, which is 8, is also used for hybrid BRBFs, then the cost will be similar but the performance will be enhanced.

- Hybrid BRBFs counteracts the negative post-yield stiffness that occurs due to P-Delta effects. Thus, their use is more beneficial on buildings where P-Delta effects are more critical. The effect of P-Delta is more on tall buildings, buildings with high gravity loads, and buildings that are not designed at very high seismic design categories.

- The benefits of hybrid BRBFs were minimized on short period (1-2 story) buildings designed at high seismic categories.

- The repair costs of the buildings with hybrid BRBFs will be less than that of the regular buildings due to lower residual drifts.

- Hybrid BRBFs resulted in smaller dispersion than the regular systems as a result of incremental dynamic analyses. This means that the reliability of hybrid BRBFs is more than the regular BRBFs.

- Because the initial stiffness and the strength of the hybrid BRBs are kept the same as the regular BRBs, hybrid BRBs automatically complies with the capacity design principles. Thus, additional work is not necessary in terms of creating code-based design rules for hybrid BRBFs.

- As the hybridity of the frames increases, the response gets better. The Hybrid-3 frame almost always gave the best results.

The following conclusions can be made as a result of the research studied on hybrid moment frames:

- Unlike hybrid BRBFs, the performance of the regular systems could not be improved with the hybrid moment frames significantly. The performance of hybrid moment frames was sometimes better and sometimes worse than the regular moment frames. A consistent improvement under most of the ground motions could not be obtained with hybrid moment frames.

- While implementing hybridity into the moment frames, story wise flexural strength, and stiffness were kept the same as regular frames. These two constraints resulted in about 10% cost increase for hybrid moment frames. Better performance could be achieved when this additional expense was used on columns by increasing the SC/WB ratios of the regular moment frames.

- Changing the yield sequence of the moment frames is much more difficult than for the braced frames.

- The modification made for hybrid moment frames was only on the girder sections. While, this could provide limited early yielding, the post-yield behavior could not be improved. This is because moment frame collapse mechanisms form in the columns and the post-yield behavior is governed by these mechanisms.

- The degradation of the moment frame connections affects the performance negatively. While providing early yielding, the cut of RBS was increased and the girder sizes were decreased. Most of the time, this change reduces the energy dissipation capacity of the connection. Although this was not found critical, it might affect the hybrid frame behavior under certain cases.

- Two alternative hybrid moment frame connections adapting the use of low strength steel (LYP100) were studied. Since LYP100 is only available in plates, the studied connection types were limited to the ones where inelasticity occurs in the plates.

- The early yielding could be achieved and plastic hinging sequence could be changed much more easily when low strength steel was used in the moment frame connections.

- The Simpson Strong-Tie (SST) connection, which is in prequalification process, is a practical way to use low-strength steel in the connections. According to the results of preliminary analyses, story drifts decreased about 8% on average for all ground motions up to MCE level. Story accelerations decreased about 4%. An enhanced performance can be achieved with an optimization study on SST connection with LYP steel yield links.

In addition to the hybrid frames, the effect of different depth columns (W14 and W24 sections) on moment frame designs was also investigated. Lower W24 column deterioration parameters did not affect the dynamic analyses results significantly. This should be because the deterioration is more important in the girders as they yield earlier than the columns, and attract more damage. Also, although W24 columns have worse deterioration parameters than W14 columns, they should still be good enough for reasonable performance. Note that this study is within the limitations of column hinge modeling which is discussed in Chapter 5 and Appendix B.

Another side study was made to see the effect of different SC/WB ratios (1.0, 1.5 and 2.0) on moment frames. The performance of moment frames increased significantly for higher SC/WB ratio designs. This is related with the prevention of story mechanisms with bigger column sizes. The main increase in the performance was obtained when SC/WB was increased from 1.0 to 1.5. Further increase in SC/WB (from 1.5 to 2.0) did not provide much benefit.

7.3. Future Work

The recommendations for future work of hybrid steel frames are outlined as follows:

- A set of lab tests should be conducted on hybrid BRBs. The use of LYP100 steel with HPS100W in a hybrid brace is encouraged. Alternative low-strength but highly ductile steels with high strain hardening can also be used instead of LYP100. Stainless steel is a good alternative for LYP100. Although the unit cost of stainless steel is more than LYP100, it is much easier to obtain.

- The effect of yield plate eccentricity on the BRB behavior should be investigated through lab tests and finite element analyses.

- The proposed hybrid brace design method, which is actually the same as the regular brace, should be reevaluated as a result of the lab tests. A more conservative approach than the regular brace design might be necessary to design the casing of the hybrid brace.

- In addition to the LYP steel plate connections for the moment frames, stainless steel (SS) is an attractive material for use. This is because of the availability of SS as wide flange beams and its similar material behavior as LYP steels.

- The effect of deep girder sections to achieve early yielding in hybrid moment frames should be investigated further.

REFERENCES

Aiken, I.D., Mahin, S.A., and Uriz P. (2002). Large-scale testing of BRBFs. *Proceedings of Japan passive control symposium*, Tokyo Institute of Technology, Yokohoma, Japan.

Aki, K. and Richards, P.G. (2009). *Quantitative Seismology*. 2nd edition, University Science Books, Sausalito, California.

AISC. (2010a). *Seismic Provisions for Structural Steel Buildings, (AISC 341-10)*. American Institute of Steel Construction, Chicago (IL).

AISC. (2010b). *Prequalified Connections for Special and Intermediate Steel Moment Frames for Seismic Applications, (AISC 358-10)*. American Institute of Steel Construction, Chicago (IL).

AISC. (2010c). *Specification for Structural Steel Buildings, (AISC 360-10)*. American Institute of Steel Construction, Chicago (IL).

ArcelorMittal. (2011). *Plate Specification Guide 2011-2012*. HPS100W: High Strength Steel for Bridges Brochure.

Ariyaratana C., and Fahnestock, L.A. (2011). Evaluation of buckling-restrained brace frame seismic performance considering reserve strength. *Engineering Structures* **33**: 77-89.

ASCE. (2006a). *Minimum Design Loads for Buildings and Other Structures (ASCE 7-05)*. American Society of Civil Engineers, Reston, VA.

ASCE. (2006b). *Seismic Rehabilitation of Existing Buildings (ASCE 41-06)*. American Society of Civil Engineers, Reston, VA.

ASCE. (2010). *Minimum Design Loads for Buildings and Other Structures (ASCE 7-10)*. American Society of Civil Engineers, Reston, VA.

ASTM (2009). *ASTM Standards in Building Codes*. Volume 1, ASTM International, West Conshohocken, PA.

Atlayan, O. (2008). *Effect of Viscous Fluid Dampers on Steel Moment Frames Designed for Strength, and Hybrid Steel Moment Frame Design*. M.S. Thesis. Department of Civil and Environmental Engineering, Virginia Tech, Blacksburg, VA.

Baker, J.W. (2007). Quantitative Classification of Near-Fault Ground Motions Using Wavelet Analysis. *Bulletin of the Seismological Society of America* **97:5** 1486-1501.

Baker, J.W. (2011). Fitting Fragility Functions to Structural Analysis Data using Maximum Likelihood Estimation; accessible via the world wide web at: http://www.stanford.edu/~bakerjw/fragility_old.html .

Bruneau, M., Uang, C.M., and Sabelli R. (2011). *Ductile Design of Steel Structures*. 2nd edition, McGraw-Hill, New York.

Charney, F.A. (1991). The Use of Displacement Participation Factors in the Optimization of Drift Sensitive Buildings. *Proceedings of the Second Conference on Tall Buildings in Seismic Regions*. Los Angeles, pp:780-783.

Charney, F.A. (1993). Economy of Steel Frame Buildings through Identification of Structural Behavior. *Proceedings of the Spring 1993 AISC Steel Construction Conference*. Orlando, pp:21-1 to 21-33.

Charney, F.A., and Atlayan, O. (2011). Hybrid Moment-Resisting Steel Frames. *AISC Engineering Journal* **48:3** 169-182.

Charney, F.A. and Marshall, J.D. (2006). A comparison of the Krawinkler and Scissor Models for Including Beam-Column Joint Deformations in the Analysis of Steel Frames. *AISC Engineering Journal* **43:1** 31-48.

Charney F.A., Tola A. and Atlayan O. (2010). Structural Analysis. *FEMA P-751: NEHRP Recommended Provisions: Design Examples*. Chapter 4: Structural Analysis.

Chen, C.C., Chen, S.Y., and Liaw, J.J. (2001). Application of low yield strength steel on controlled plastification ductile concentrically braced frames. *Canadian Journal of Civil Engineering* **28:** 823-836.

Chi, W.M., Deierlein, G.G., and Ingraffea, A.R. (1997). *Finite Element Fracture Mechanics Investigation of Welded Beam-column Connections*. Report No: SAC/BD-97/05. SAC Joint Venture.

Chou, C.C. and Tsai, K.C. (2002). Plasticity-fibre model for steel triangular plate energy dissipating devices. *Earthquake Engineering and Structural Dynamics* **31**: 1643-1655.

Christopulos, A.S. (2005). *Improved Seismic Performance of BRBFs*. M.S. Thesis. Department of Civil and Environmental Engineering, University of Washington, WA.

Coffin, L.F. (1954). A study of the effects of Cyclic Thermal Stresses on a Ductile Metal. *Trans. ASME* **76**: 931-950.

Coons, R.G. (1999). *Seismic Design and Database of End Plate and T-stub Connections*. M.S. Thesis. Department of Civil and Environmental Engineering, University of Washington, WA.

CSI. (2006). *Perform-3D User's Guide*. Nonlinear analysis and performance assessment of structures. Computers and Structures Inc., Berkeley CA.

CSI (2012). *Static and Dynamic Finite Element Analysis of Structures*. SAP2000 Version 15. Computers and Structures Inc., Berkeley CA.

De Matteis, G., Landolfo, R., and Mazzolani, F. (2003). Seismic response of MR steel frames with low-yield steel shear panels. *Engineering Structures* **25:** 155-168.

Di Sarno, L., Elnashai, A.S., and Nethercot, D.A. (2006). Seismic retrofitting of framed structures with stainless steel. *Journal of Constructional Steel Research* **62:** 93-104.

Di Sarno, L., Elnashai, A.S., and Nethercot, D.A. (2008). Seismic response of stainless steel braced frames. *Journal of Constructional Steel Research* **64**: 914-925.

Dusicka, P., Itani, A.M., and Buckle, I.G. (2007). Cyclic response of plate steels under large inelastic strains. *Journal of Constructional Steel Research* **63:2** 156-164.

El-Tawil, S., Mikesell, T., Vidarsson, E., and Kunnath S.K. (1998). *Strength and Ductility of FR-Bolted Connections*. Report No: SAC/BD-98/01. SAC Joint Venture.

Engelhardt, M.D. (2007). Design of Seismic-Resistant Steel Building Structures: Buckling Restrained Braced Frames. *AISC Teaching Aids*; accessible via the world wide web at: http://www.aisc.org/UploadedContent/TeachingAids/AISC_Seismic_Design-Module5-Buckling_Restrained_Braced_Frames.ppt .

European Commision (2001). *Development of the use of stainless steel in construction*. Final Report, Direcrorate-General for Research. European Commision, Technical Steel Research EUR 20030- EN.

Fahnestock L.A., Ricles J.M., and Sause R. (2007). Experimental evaluation of large-scale BRBF. *Journal of Structural Engineering* **133(9)**:1205-1214.

FEMA. (2000a). *State of the Art Report on Systems Performance, (FEMA 355-C)*. Federal Emergency Management Agency, Washington D.C.

FEMA. (2000b). *State of the Art Report on Connection Performance, (FEMA 355-D)*. Federal Emergency Management Agency, Washington D.C.

FEMA. (2004a). *NEHRP Recommended Provisions for Seismic Regulations for New Buildings and Other Structures*, (*FEMA 450-1*/2003). Part 1: Provisions, Federal Emergency Management Agency, Washington D.C.

FEMA. (2004b). *NEHRP Recommended Provisions for Seismic Regulations for New Buildings and Other Structures*, (*FEMA 450-2*/2003). Part 2: Commentary, Federal Emergency Management Agency, Washington D.C.

FEMA. (2009). *Quantification of Building Seismic Performance Factors, (FEMA P-695)*. Prepared by Applied Technology Council for the Federal Emergency Management Agency, Washington D.C.

Gardner, L. (2005). The use of stainless steel in structures. *Progress in Structural Engineering and Materials* **7:** 45-55.

Gardner, L., Cruise R.B., Sok, C.P., Krishnan, K., and Dos Santos J.M. (2007). Life-cycle costing of metallic structures. *Proceedings of the Institution of Civil Engineers, Engineering Sustainability* **160(4):**167-177.

Hewitt, C., Sabelli, R., and Bray J. (2009). Economy of steel-framed buildings for seismic loading. *Steel Tips*, Structural Steel Education Council.

Kanvinde A.M. and Deierlein G.G. (2007). Cyclic Void Growth Model to Assess Ductile Fracture Initiation in Structural Steels due to Ultra Low Cycle Fatigue. *Journal of Engineering Mechanics* **133:6** 701-712.

Kiggins, S., and Uang, C.M. (2006). Reducing residual drift of buckling-restrained braced frames as a dual-system. *Engineering Structures* **28:** 1525-1532.

Kaufmann E.J., Metrovich B., and Pense A.W. (2001). Characterization of Cyclic Inelastic Strain Behavior on Properties of A572 Gr. 50 and A913 Gr. 50 Rolled Sections. *ATLSS Report No.01-13*, Lehigh University.

Krawinkler, H. (1978). Shear design of steel frame joints. *AISC Engineering Journal* **15:3** 82-91.

Kuroda, M. (2001). Extremely low cycle fatigue life prediction based on a new cumulative fatigue damage model. *International Journal of Fatigue* **24**: 699-703.

Lignos, D.G. and Krawinkler, H. (2011). Deterioration Modeling of Steel Components in Support of Collapse Prediction of Steel Moment Frames under Earthquake Loading. *Journal of Structural Engineering* **137:11** 1291-1302.

Manson S.S.(1953). Behavior of Materials Under Conditions of Thermal Stress. *Heat Transfer Symposium*, University of Michigan, university of Michigan Press pp:9-76.

Mazzoni, S., McKenna, F., Scott, M.H., and Fenves, G.L. (2006). *Open System for Earthquake Engineering Simulation (OpenSeeS) User Command Language Manual*.

Merritt, S., Uang, C.M., and Benzoni, G. (2003). *Subassemblage Testing of Star Seismic Buckling Restrained Braces*, in report No. TR-2003/04. University of California, San Diego, La Jolla.

Nair, R.S., Malley, J.O and Hooper J.D. (2011). Design of Steel Buildings for Earthquake and Stability by Application of ASCE 7 and AISC 360. *AISC Engineering Journal* **48:3** 199-204.

Nakamura H., Maeda Y., Sasaki T., Wada A., Takeuchi T., Nakata Y., and Iwata M. (2000). Fatigue Properties of Practical-Scale Unbonded Braces. *Nippon Steel Technical Report* **No.82:** 51-57; accessible via the world wide web at: http://www.nssmc.com/en/tech/report/nsc/pdf/8207.pdf .

Nakashima, M., Iwai, S., Iwata, M., Takeuchi, T., Konomi, S., and Akazawa, T. (1994). Energy dissipation behaviour of shear panels made of low yield steel. *Earthquake Engineering and Structural Dynamics* **23:12**, 1299-1313.

Newell J.D, and Uang C.M.(2008). Cyclic Behavior of Steel Wide-Flange Columns Subjected to Large Drift. *Journal of Structural Engineering* **134:8** 1334-1342.

Nippon Steel (2009). *Steel Plates*. On the leading edge:Nippon Steel, N.S. Corporation.

NIST. (2010). *Evaluation of the FEMA P-695 Methodology for Quantification of Building Seismic Performance Factors*. *ATC-76-1* report (NIST GCR 10-917-8). Gaithersburg, Maryland.

NIST. (2011). *Research Plan for the Study of Seismic Behavior and Design of Deep, Slender Wide Flange Structural Steel Beam-Column Members*. NIST GCR 11-917-13. Gaithersburg, Maryland.

PEER/ATC. (2010). *Modeling and Acceptance Criteria for Seismic Design and Analysis of Tall Buildings*. *PEER/ATC 72-1* report prepared by ATC for the PEER Center, Redwood City, California.

Romero, P., Reavaley L.D., Miller P., and Okahashi, T. (2007). *Full Scale Testing of WC Series Buckling-Restrained Braces Final Report*. The University of Utah Department of Civil& Environmental Engineering.

Saeki, E., Sugisawa, M., Yamaguchi, T., and Wada A. (1998). Mechanical properties of low yield point steels. *Journal of Materials in Civil Engineering* **10(3):** 143-152.

Sabelli, R. (2001). Research on improving the design and analysis of earthquake-resistant steel braced frames. *The 2000 NEHRP Professional Fellowship Report*, EERI, Oakland, California.

Sabelli, R., Mahin, S.A., and Chang, C. (2003). Seismic demands on steel braced-frame buildings with buckling-restrained braces. *Engineering Structures* **25:5** 655-666.

SEAOC Seismology Committee (2008). Buckling Restrained Braced Frames. March 2008, *The SEAOC Blue Book: Seismic design recommendations*. Structural Engineers Association of California, Sacramento, CA; accessible via the world wide web at: http://www.seaoc.org/bluebook/index.html .

Shirsat, P.S. (2011). *Preliminary Analysis of Doubler Plate Attachment Details for Steel Moment Resisting Frames*. M.S. Thesis. The University of Texas at Austin, TX.

Shuttleworth E.P. (1989). *Structural applications for stainless steel offshore*. Report to the Nickel Development Institute, Report No. SCI-RT-030. The Steel Construction Institute.

Simpson Strong-Tie. (2011). *Simpson Strong-Tie special moment frame connection*. Simpson Strong-Tie AC129 Report. Pleasanton, CA.

Sugisawa, M., Nakamura, H., Ichikawa, Y., Hokari, M., Saeki, E., Hirabayashi, R., and Ueki, M. (1995). Development of earthquake-resistant, vibration Control, and base isolation technology for building structures. *Nippon Steel Technical Report* **No.66:** 37-46; accessible via the world wide web at: http://www.nssmc.com/en/tech/report/nsc/pdf/6605.pdf .

Tsai, K.C, Hsiao, B.C., Lai, J.W., Chen, C.H., Lin, M.L., and Weng, Y.T. (2003). Pseudo-dynamic experimental response of a full-scale CFT/BRB composite frame. *Proceedings, joint NCREE/JRC workshop*.

Tremblay, R., Lacerte M., and Christopoulos C. (2008). Seismic response of multistory buildings with self-centering energy dissipative steel braces. *Journal of Structural Engineering* **134:1** 108-120.

Uang, C.M., and Nakashima, M. (2003). Steel Buckling-Restrained Braced Frames. Chapter 16 in *Earthquake Engineering: Recent Advances and Applications*, CRC Press, Boca Raton, FL.

Uang, C.M., Nakashima, M., and Tsai K. (2004). Research and Application of Buckling Restrained Braced Frames. *Steel Structures* **4:** 301-313.

Uriz, P., and Mahin, S.A. (2008). *Toward earthquake-resistant design of concentrically braced steel-frame structures*. PEER report 2008/08. Berkeley: University of California.

Vian, D., and Bruneau, M. (2004). Testing of special LYS steel plate shear walls. *Proceedings of 13th World Conference on Earthquake Engineering*. Vancouver, Canada.

Watanabe, A., Hitomi, Y., Yaeki, E., Wada A., and Fujimoto, M. (1988). Properties of brace encased in buckling-restraining concrete and steel tube. *Proceedings, 9th World Conference on Earthquake Engineering*. Tokyo-Kyoto, Japan, IV, 719-724.

Wigle V.R., and Fahnestock L.A. (2010). Buckling-restrained braced frame connection performance. *Journal of Constructional Steel Research* **66:** 65-74.

Xue, L. (2008). A unified expression for low cycle fatigue and extremely low cycle fatigue and its implication for monotonic loading. *International Journal of Fatigue* **30**: 1691-1698.

Yamaguchi, T., Takeuchi, T., Nagao, T., Suzuki, T., Nakata, Y., Ikebe, T., and Minami, A. (1998). Seismic control devices using low-yield-point steel. *Nippon Steel Technical Report* **No.77:** 65-72; accessible via the world wide web at: http://www.nssmc.com/en/tech/report/nsc/pdf/7709.pdf .

APPENDIX A: *ATC-76-1* PROJECT BUCKLING RESTRAINED BRACED FRAME ARCHETYPES PERFORMANCE EVALUATION

The *ATC-76-1* project report, *Evaluation of the P-695 Methodology for Quantification of Building Seismic Performance Factors* (NIST, 2010), provides a design space for BRBFs in Chapter 7. This appendix compares the performance of the regular BRBF archetypes in *ATC-76-1* project with the hybrid frames. All the modeling assumptions and hybrid brace properties that are explained in Chapter 4 are also used for the models discussed in this appendix. Note that deflection amplification factor, C_d, of 8 which is equal to response modification factor, R, was used in the designs of all archetypes discussed in this appendix.

A.1. Supplemental Case Study-1 for Hybrid Buckling Restrained Braced Frames: Long Period Performance Group at SDC Dmax

This case study investigates the performance comparison between Hybrid and regular frames on long period performance group (PG-10) at seismic design category Dmax. Table A-1 shows the design properties of five archetypes that are included in this performance group, PG-10. Note that an archetype notation similar to "4S-LB-15B-Dmax" is used in the table and throughout the text. This notation stands for a 4 story BRBF with diagonal (Lighting Bolt) brace configuration with 15ft Bay widths designed at seismic design category Dmax.

Table A-1. *ATC-76-1* Project Performance Group PG-10 Archetype Design Properties

Arch. Design ID No.	No. of Stories	Key Archetype Design Parameters						
		Analysis Method	Seismic Design Criteria					$S_{MT}(T)$ (g)
			SDC	R	T (sec)	T_1 (sec)	V/W (g)	
Performance Group PG-10. SDC Dmax / Long-Period Archetypes								
4S-LB-15B-Dmax	4	RSA	Dmax	8	0.81	1.16	0.078	1.11
6S-LB-15B-Dmax	6	RSA	Dmax	8	1.10	1.66	0.058	0.816
9S-LB-15B-Dmax	9	RSA	Dmax	8	1.49	2.34	0.047	0.602
12S-LB-15B-Dmax	12	RSA	Dmax	8	1.85	3.36	0.037	0.485
18S-LB-15B-Dmax	18	RSA	Dmax	8	2.51	4.83	0.037	0.358

Figure A-1 shows the plan and elevation view of the four story archetype model. Archetypes in this performance group have uniform bay widths and heights of 15ft and 13ft respectively.

A.1.1. Nonlinear Model Details and Pushover Analysis

Similar modeling assumptions were used as discussed in Chapter 4. Non-moment resisting beam-column connections were used in the frames. Computed periods from eigenvalue analyses are tabulated in Table A-1. Figure A-2 through Figure A-6 display the pushover curves of four, six, nine, twelve and eighteen story models. General trends of hybrid systems which are early yielding and higher post-yield stiffness are observed in all the pushover curves studied.

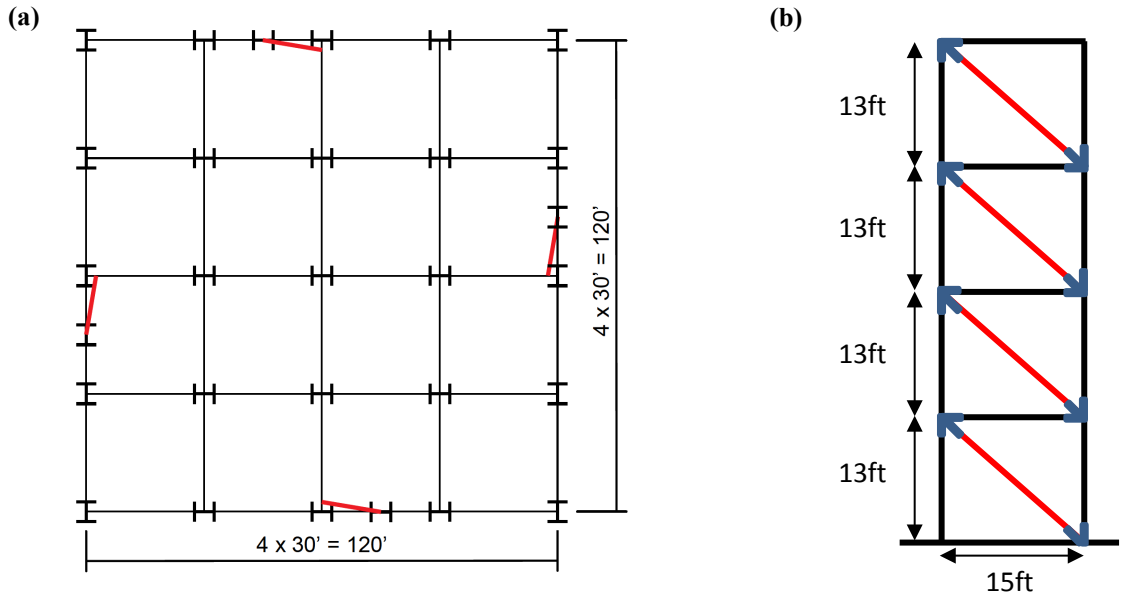

Figure A-1. PG-10 Performance Group Archetype Models (a) Plan View for all Models (b) Elevation of 4 Story Archetype (only Story Number Changes for the Other Archetypes)

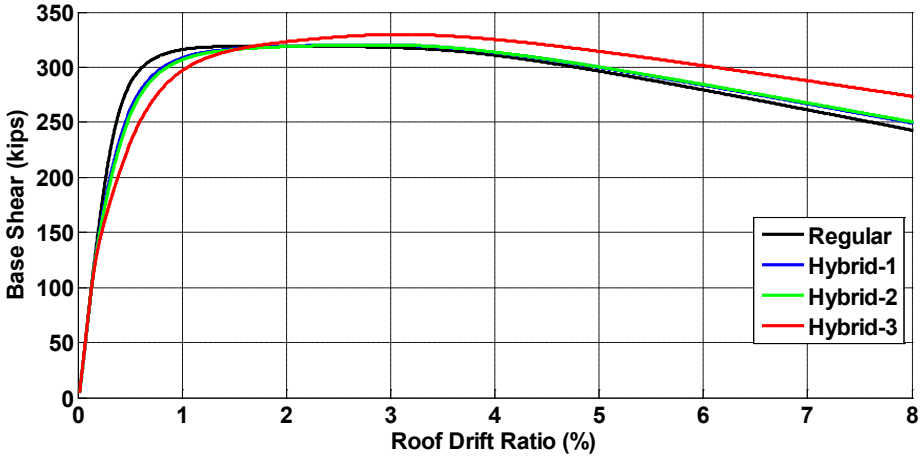

Figure A-2. Pushover Curve for PG10-4S-LB-15B-Dmax Model

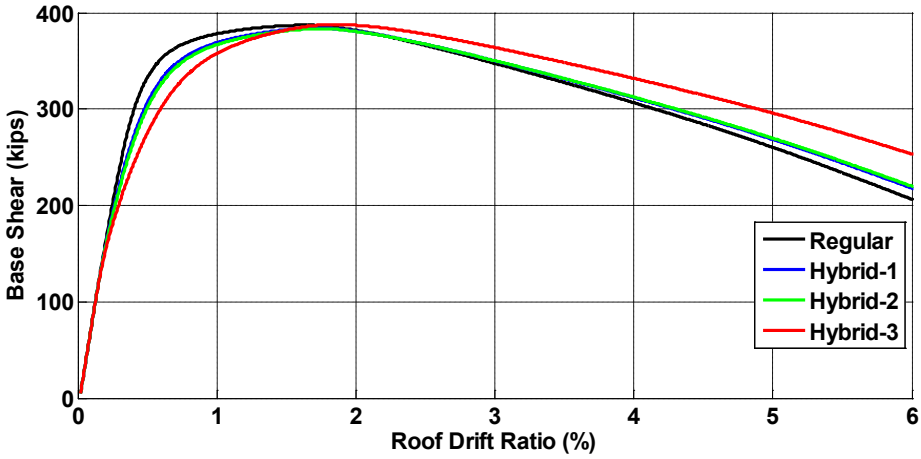

Figure A-3. Pushover Curve for PG10-6S-LB-15B-Dmax Model

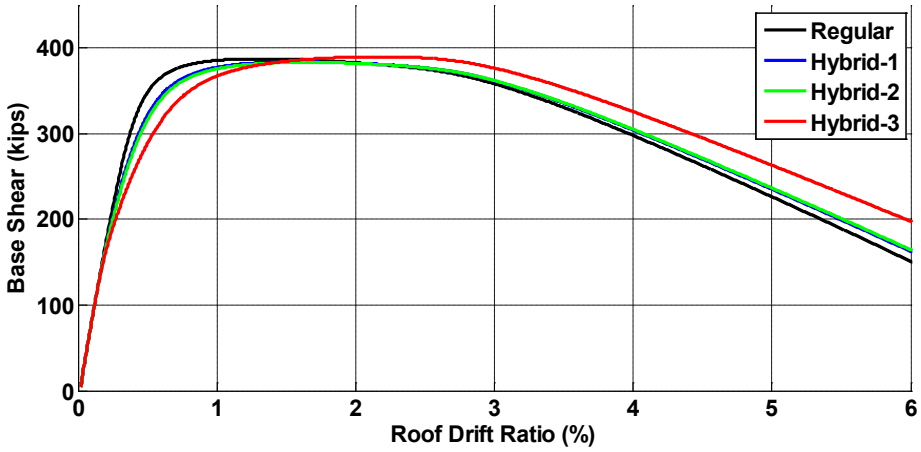

Figure A-4. Pushover Curve for PG10-9S-LB-15B-Dmax Model

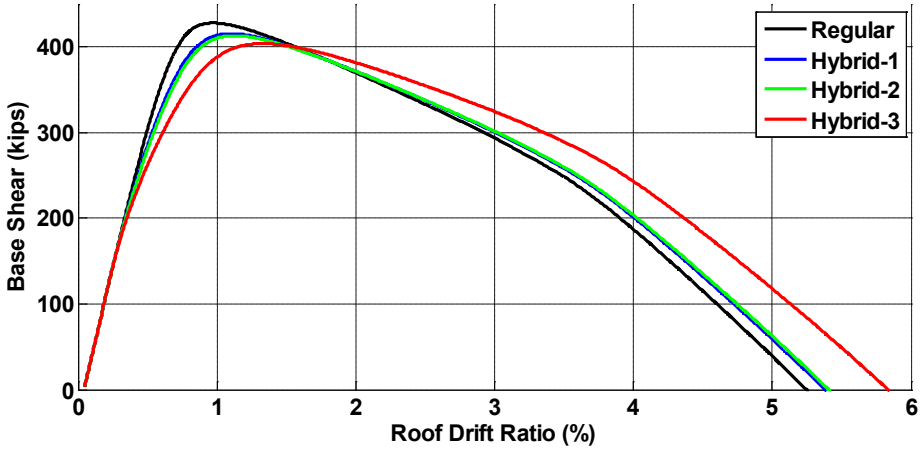

Figure A-5. Pushover Curve for PG10-12S-LB-15B-Dmax Model

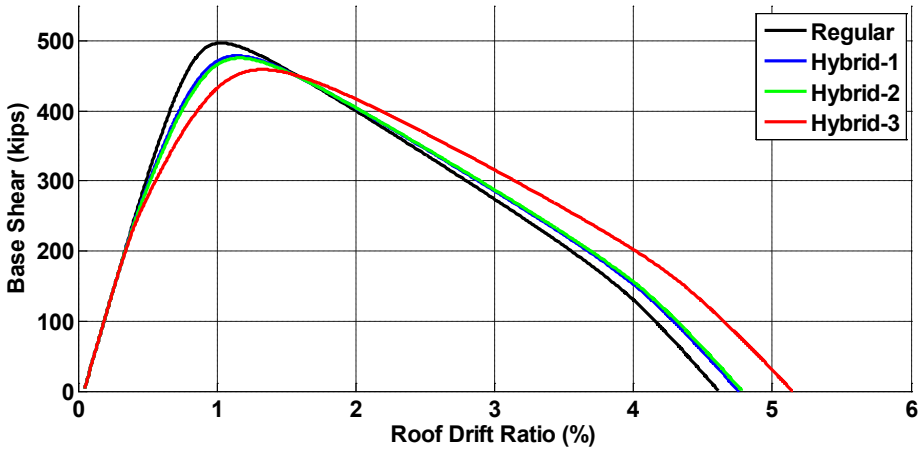

Figure A-6. Pushover Curve for PG10-18S-LB-15B-Dmax Model

A.1.2. Incremental Dynamic Analysis

Bar charts showing the performance improvement of regular frames with hybrid frames are displayed from Figure A-7 through Figure A-11. Figures are for four, six, nine, twelve and eighteen story models respectively. Twenty increments were used up to MCE level. As may be seen in the figures, hybrid frames performed better than the regular frames, with the Hybrid-3 frame performing the best. The real benefit was obtained in the residual displacements. Superior performance improvement was obtained for taller BRBFs.

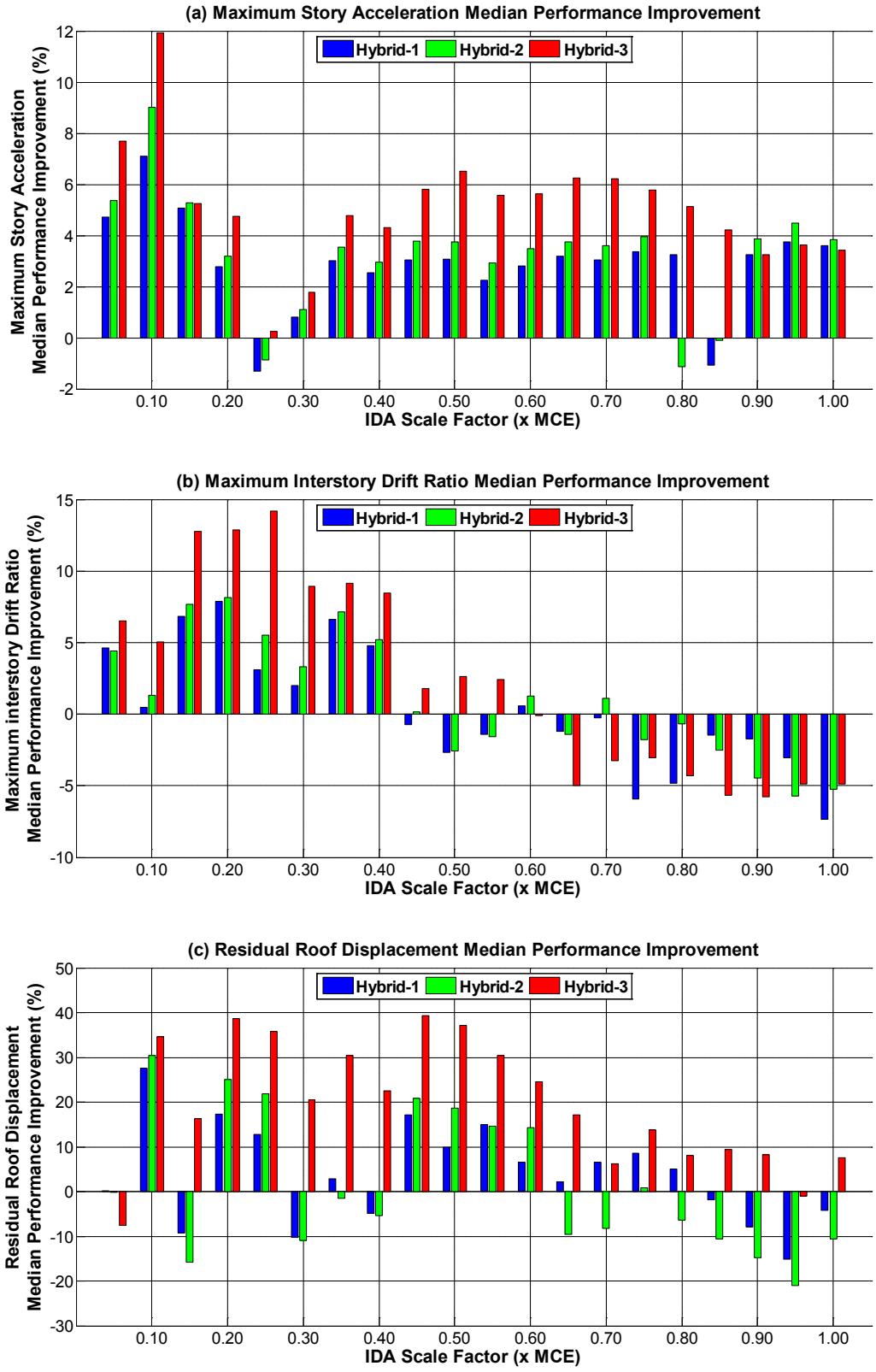

Figure A-7. PG10-4S-LB-15B-Dmax Model Median Performance Improvements for (a) Maximum Story Acceleration (b) Maximum Interstory Drift Ratios (c) Residual Roof Displacement

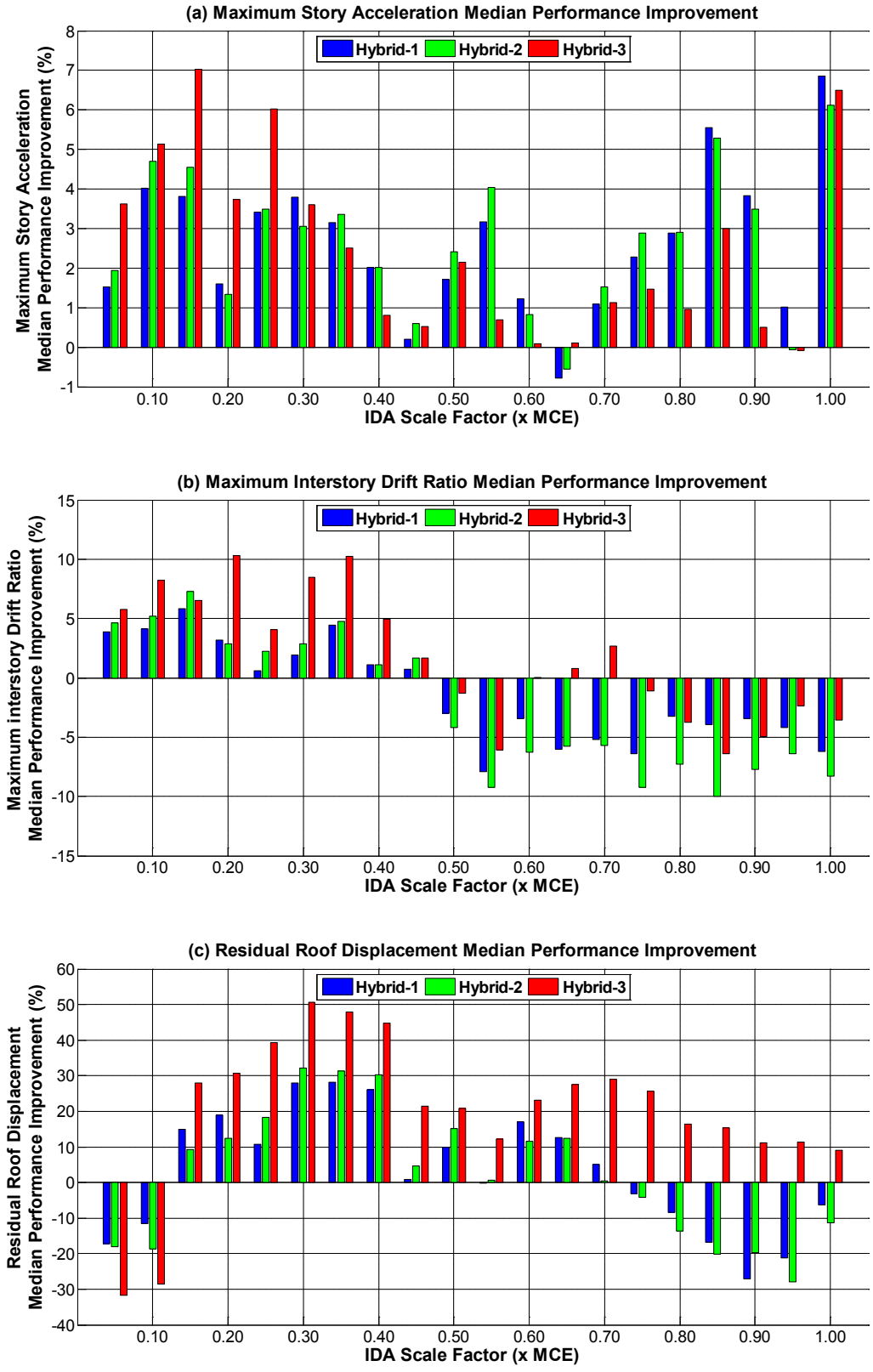

Figure A-8. PG10-6S-LB-15B-Dmax Model Median Performance Improvements for (a) Maximum Story Acceleration (b) Maximum Interstory Drift Ratios (c) Residual Roof Displacement

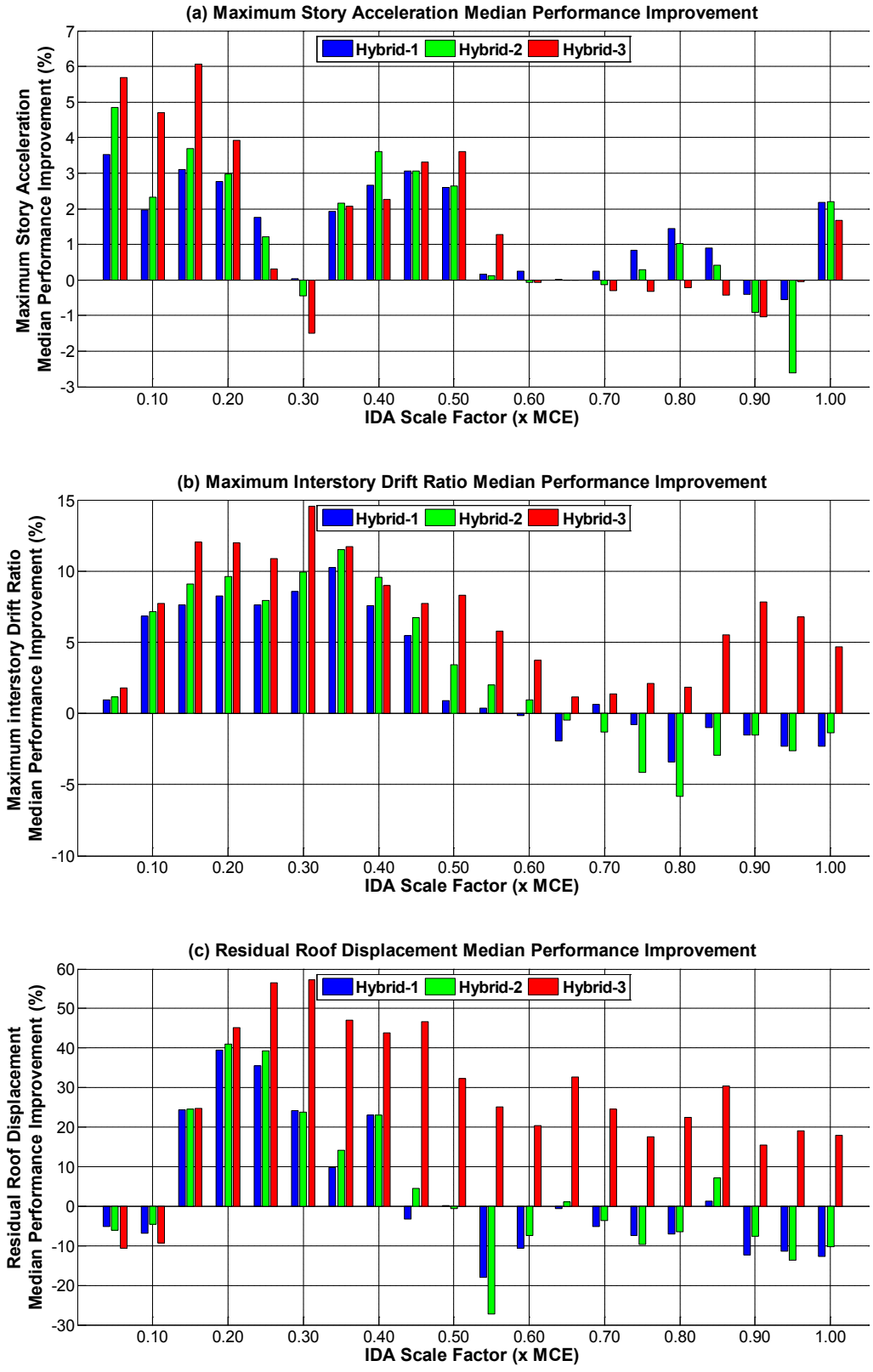

Figure A-9. PG10-9S-LB-15B-Dmax Model Median Performance Improvements for (a) Maximum Story Acceleration (b) Maximum Interstory Drift Ratios (c) Residual Roof Displacement

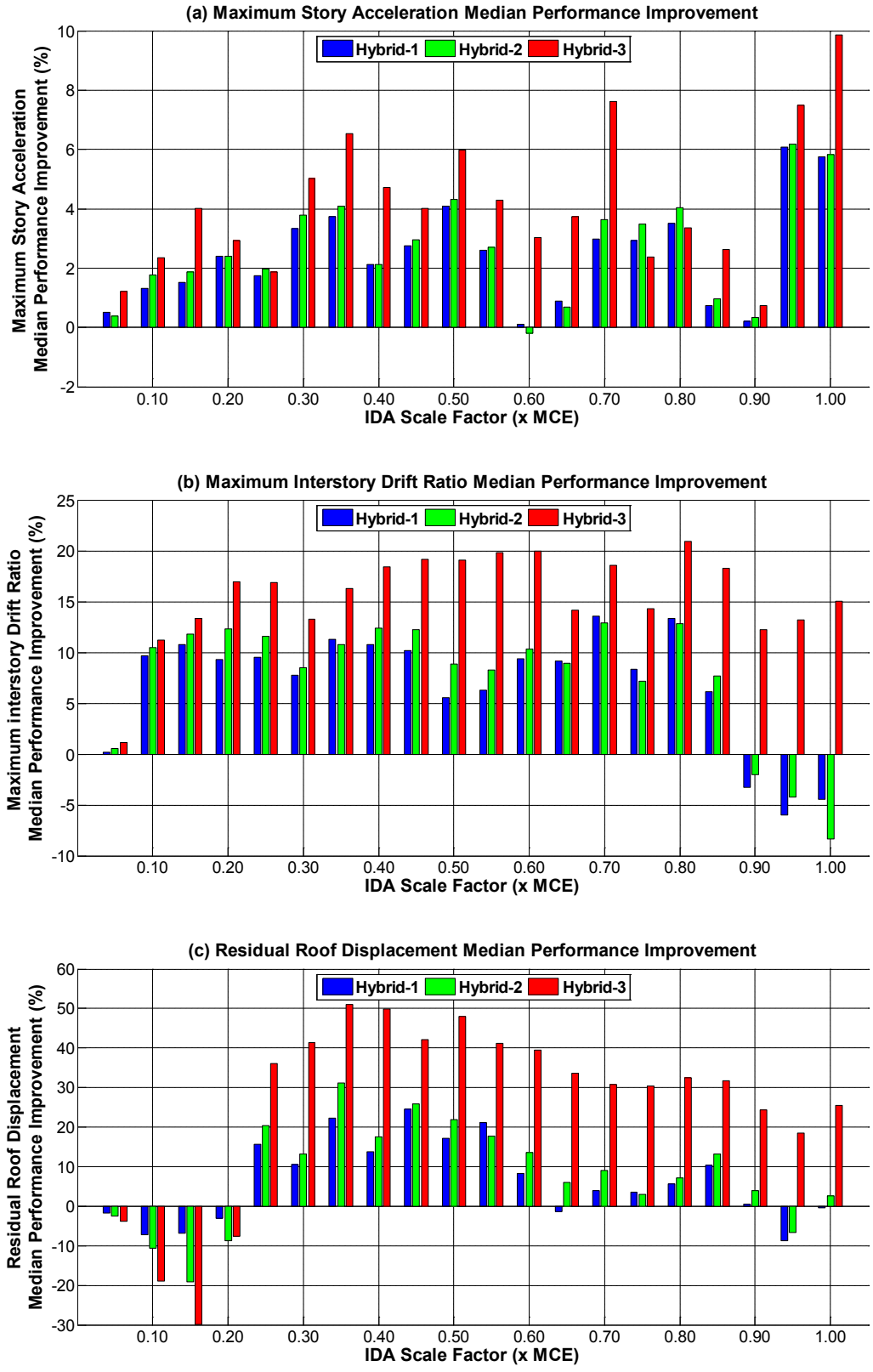

Figure A-10. PG10-12S-LB-15B-Dmax Model Median Performance Improvements for (a) Maximum Story Acceleration (b) Maximum Interstory Drift Ratios (c) Residual Roof Displacement

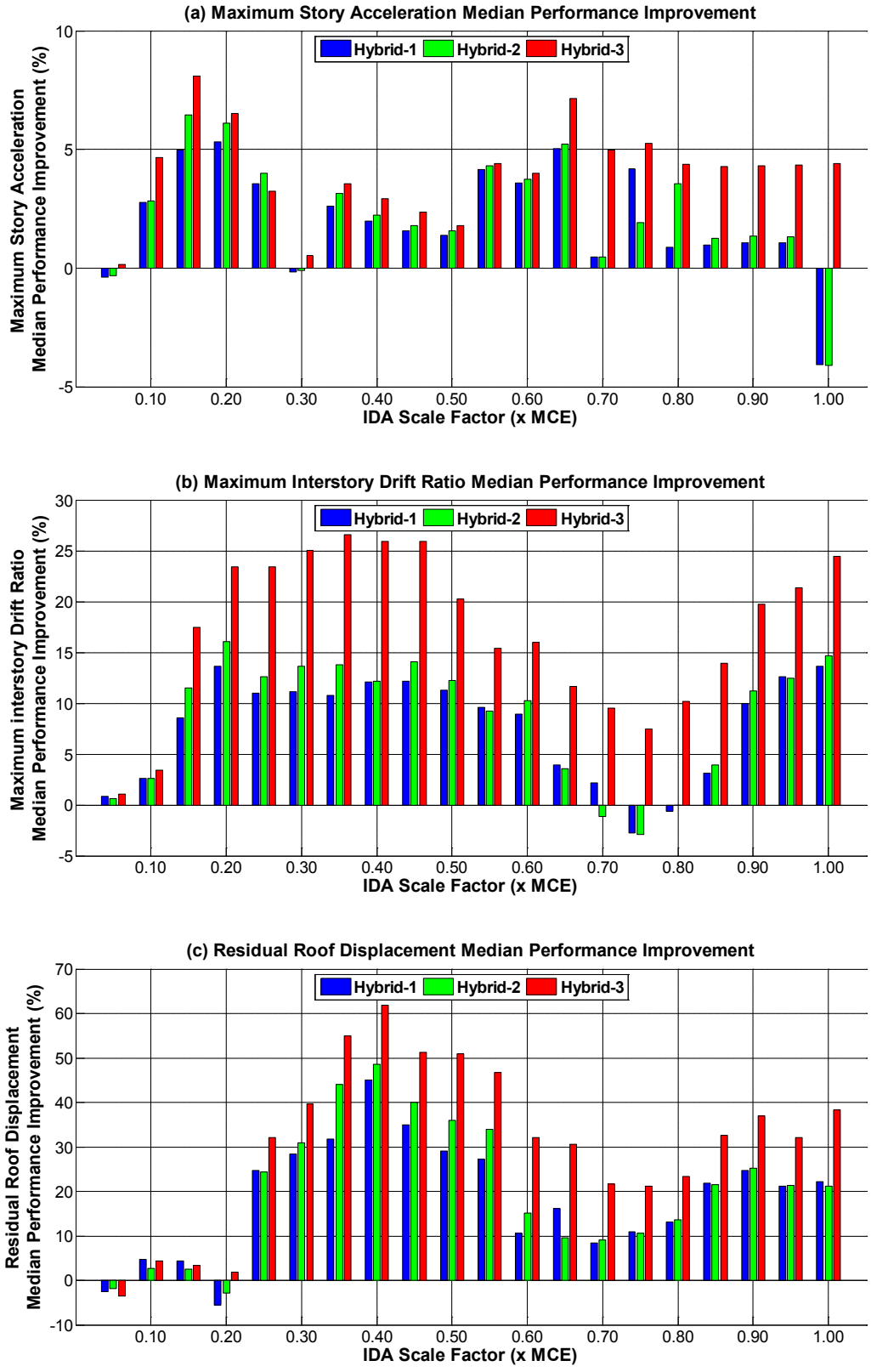

Figure A-11. PG10-18S-LB-15B-Dmax Model Median Performance Improvements for (a) Maximum Story Acceleration (b) Maximum Interstory Drift Ratios (c) Residual Roof Displacement

A.1.3. *FEMA P-695* Performance Evaluation

Table A-2 shows *FEMA P-695* performance evaluation for PG-10. Collapse probabilities of six, nine, twelve, and eighteen story archetypes reduced almost by half with Hybrid-3 model. Regular BRBF performed better than the hybrid frames only on the 4 story model. However, even for the 4 story model, the collapse probability of the regular frame (6.8%) and Hybrid-3 frame (7.2%) are very close. The mean performance group collapse probabilities dropped from 6.8% to 3.8 with Hybrid-3 frame.

Table A-2. *ATC-76-1* Project Performance Group PG-10 SDC Dmax/ Long-Period Archetypes Collapse Performance Evaluation Using 10% Interstory Drift + Low Cycle Fatigue Failure of Braces as Collapse Criteria

Arch. Design ID No.	BRBF Model	Computed Overstrength and Collapse Margin Parameters					Acceptance Check		
		Static Ω	*CMR*	μ_T	*SSF*	*ACMR*	Accept. *ACMR*	Pass / Fail	Collapse Probability (%)
4S-LB-15B-Dmax	Regular	1.25	1.55	26.5	1.41	2.19	1.56	Pass	6.8
	Hybrid-1	1.25	1.41	27.5	1.41	1.99	1.56	Pass	9.5
	Hybrid-2	1.25	1.40	27.7	1.41	1.97	1.56	Pass	9.8
	Hybrid-3	1.29	1.53	30.4	1.41	2.16	1.56	Pass	7.2
6S-LB-15B-Dmax	Regular	1.36	1.39	12.6	1.49	2.07	1.56	Pass	8.3
	Hybrid-1	1.35	1.37	13.3	1.49	2.04	1.56	Pass	8.7
	Hybrid-2	1.34	1.37	13.4	1.49	2.04	1.56	Pass	8.7
	Hybrid-3	1.36	1.62	14.8	1.49	2.41	1.56	Pass	4.7
9S-LB-15B-Dmax	Regular	1.12	1.67	13.6	1.61	2.69	1.56	Pass	3.0
	Hybrid-1	1.11	1.70	14.1	1.61	2.74	1.56	Pass	2.8
	Hybrid-2	1.11	1.68	14.2	1.61	2.70	1.56	Pass	2.9
	Hybrid-3	1.12	1.87	14.9	1.61	3.01	1.56	Pass	1.8
12S-LB-15B-Dmax	Regular	1.18	1.25	6.3	1.53	1.91	1.56	Pass	11.0
	Hybrid-1	1.14	1.34	7.0	1.56	2.09	1.56	Pass	8.0
	Hybrid-2	1.14	1.36	7.2	1.57	2.14	1.56	Pass	7.4
	Hybrid-3	1.11	1.50	8.5	1.61	2.42	1.56	Pass	4.7
18S-LB-15B-Dmax	Regular	0.91	1.43	4.9	1.45	2.07	1.56	Pass	8.3
	Hybrid-1	0.88	1.49	5.6	1.49	2.22	1.56	Pass	6.5
	Hybrid-2	0.87	1.51	5.7	1.49	2.26	1.56	Pass	6.1
	Hybrid-3	0.84	1.72	6.7	1.55	2.66	1.56	Pass	3.1
Mean of Performance Group	Regular	1.16				2.18	1.96	Pass	6.8
	Hybrid-1	1.15				2.21	1.96	Pass	6.5
	Hybrid-2	1.14				2.22	1.96	Pass	6.4
	Hybrid-3	1.15				2.53	1.96	Pass	3.8

A.1.4. Frame Sections for Performance Group 10

Beam-column member sizes and brace areas for PG-10 archetypes are summarized in the following tables.

Table A-3. Sections for Archetype ID = 4S-LB-15B-Dmax

Level / story	Brace Area (in.^{2})	Beams	Columns
Roof	-	W21x50	-
4	5.0	W21x62	W14x74
3	7.0	W21x73	W14x82
2	9.0	W21x73	W14x132
Ground	10.0	-	W14x145

Table A-4. Sections for Archetype ID = 6S-LB-15B-Dmax

Level / story	Brace Area (in.^{2})	Beams	Columns
Roof	-	W21x73	-
6	8.0	W21x73	W14x132
5	9.0	W24x76	W14x159
4	10.0	W24x76	W14x159
3	10.0	W27x94	W14x193
2	11.0	W27x94	W14x211
Ground	11.0	-	W14x233

Table A-5. Sections for Archetype ID = 9S-LB-15B-Dmax

Level / story	Brace Area (in.^{2})	Beams	Columns
Roof	-	W21x62	-
9	9.0	W24x76	W14x370
8	9.0	W24x76	W14x370
7	10.0	W24x76	W14x370
6	10.0	W27x94	W14x398
5	11.0	W27x94	W14x398
4	11.0	W27x94	W14x455
3	11.0	W27x94	W14x455
2	12.0	W27x94	W14x500
Ground	12.0	-	W14x500

Table A-6. Sections for Archetype ID = 12S-LB-15B-Dmax (2 Bays of Bracing Per Side)

Level / story	Brace Area (in.^{2})	Beams	Columns
Roof	-	W21x50	-
12	3.0	W21x50	W14x145
11	4.0	W21x62	W14x145
10	5.0	W21x62	W14x145
9	6.0	W21x62	W14x145
8	6.0	W21x62	W14x211
7	6.0	W21x62	W14x211
6	7.0	W21x62	W14x211
5	7.0	W21x62	W14x211
4	8.0	W21x73	W14x257
3	8.0	W21x73	W14x257
2	9.0	W21x73	W14x283
Ground	9.0	-	W14x283

Table A-7. Sections for Archetype ID = 18S-LB-15B-Dmax (2 Bays of Bracing Per Side)

Level / story	Brace Area (in.^{2})	Beams	Columns
Roof	-	W21x50	-
18	4.0	W21x62	W14x176
17	5.0	W21x62	W14x176
16	5.0	W21x62	W14x342
15	5.0	W21x62	W14x342
14	6.0	W21x62	W14x342
13	6.0	W21x62	W14x342
12	8.0	W24x76	W14x426
11	8.0	W24x76	W14x426
10	8.0	W24x76	W14x426
9	8.0	W24x76	W14x426
8	8.0	W24x76	W14x500
7	10.0	W24x76	W14x500
6	10.0	W24x76	W14x500
5	10.0	W24x76	W14x500
4	10.0	W24x94	W14x605
3	12.0	W24x94	W14x605
2	12.0	W24x94	W14x605
Ground	12.0	-	W14x605

A.2. Supplemental Case Study-2 for Hybrid Buckling Restrained Braced Frames: Long Period Performance Group at SDC Dmin

The same building model of section A.1 was used for this performance group models. The only difference is in the seismic design category, which changed from Dmax to Dmin. This performance group is called as PG-12 in chapter 7 of *ATC-76-1* project (NIST, 2010). Table A-8 shows the archetypes of this performance group with their design properties.

Table A-8. *ATC-76-1* Project Performance Group PG-12 Archetype Design Properties

Arch. Design ID No.	No. of Stories	Key Archetype Design Parameters						
		Analysis Method	Seismic Design Criteria					$S_{MT}(T)$ (g)
			SDC	R	T (sec)	T_1 (sec)	V/W (g)	
Performance Group PG-12. SDC Dmin / Long-Period Archetypes								
2S-LB-15B-Dmin	2	RSA	Dmin	8	0.52	0.92	0.063	0.579
3S-LB-15B-Dmin	3	RSA	Dmin	8	0.70	1.33	0.063	0.427
4S-LB-15B-Dmin	4	RSA	Dmin	8	0.87	1.78	0.063	0.344
6S-LB-15B-Dmin	6	RSA	Dmin	8	1.18	2.69	0.019	0.254
9S-LB-15B-Dmin	9	RSA	Dmin	8	1.60	3.90	0.019	0.187
12S-LB-15B-Dmin	12	RSA	Dmin	8	1.99	5.34	0.019	0.151
18S-LB-15B-Dmin	18	RSA	Dmin	8	2.69	8.65	0.019	0.111

A.2.1. Nonlinear Model Details and Pushover Analysis

Similar modeling techniques as explained in Chapter 4 were used in the analytical models. Figure A-12 through Figure A-18 show the pushover curves of this performance group. The figures are for two, three, four, six, nine, twelve, and eighteen story archetypes respectively.

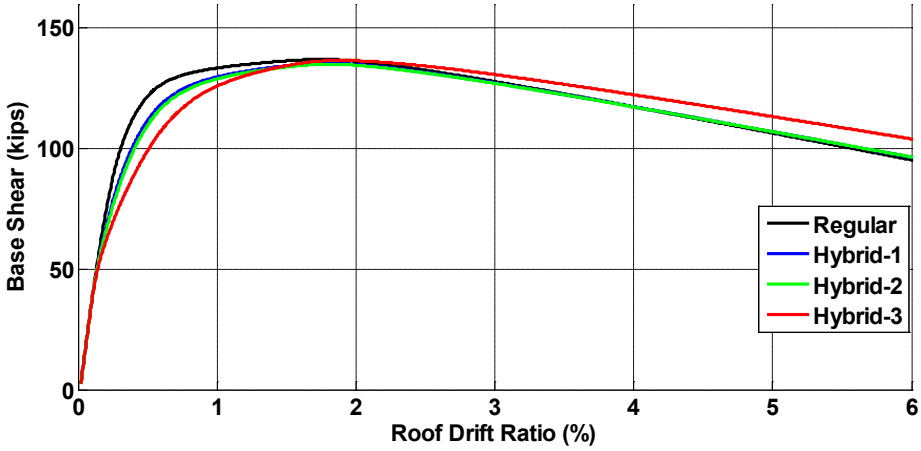

Figure A-12. Pushover Curve for PG12-2S-LB-15B-Dmin Model

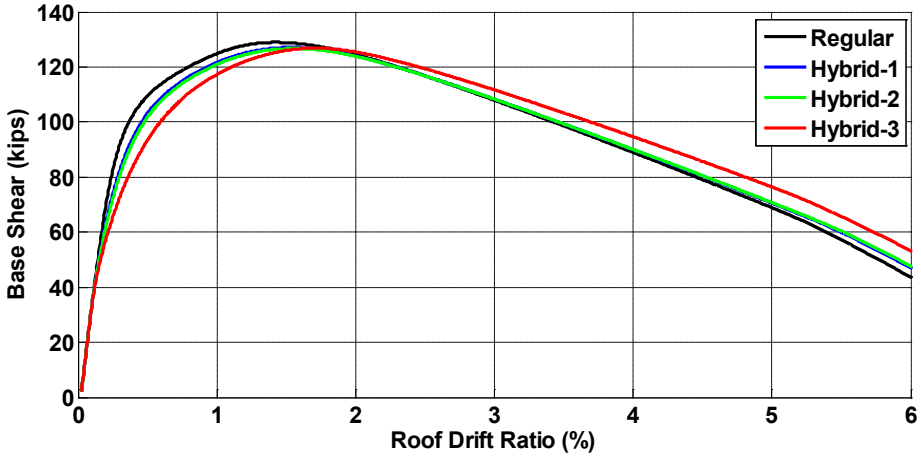

Figure A-13. Pushover Curve for PG12-3S-LB-15B-Dmin Model

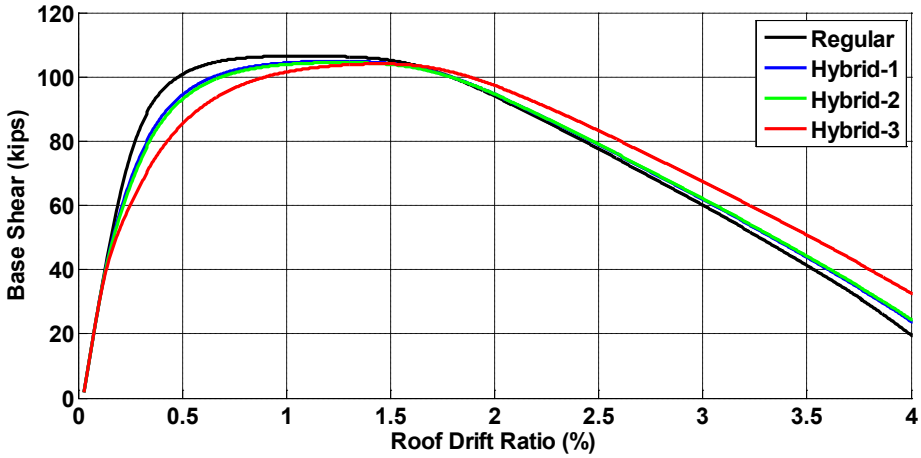

Figure A-14. Pushover Curve for PG12-4S-LB-15B-Dmin Model

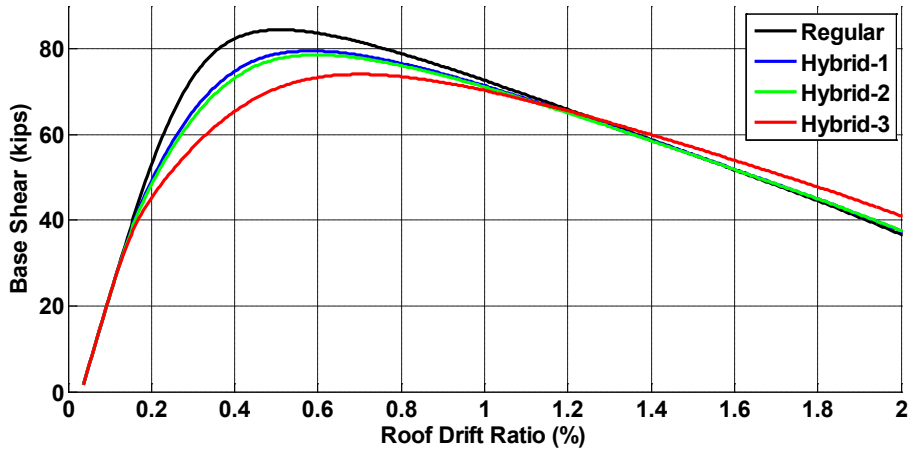

Figure A-15. Pushover Curve for PG12-6S-LB-15B-Dmin Model

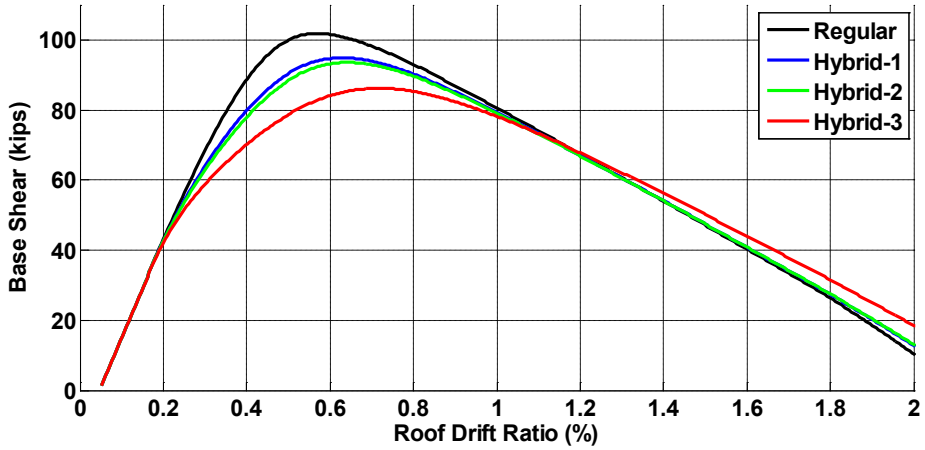

Figure A-16. Pushover Curve for PG12-9S-LB-15B-Dmin Model

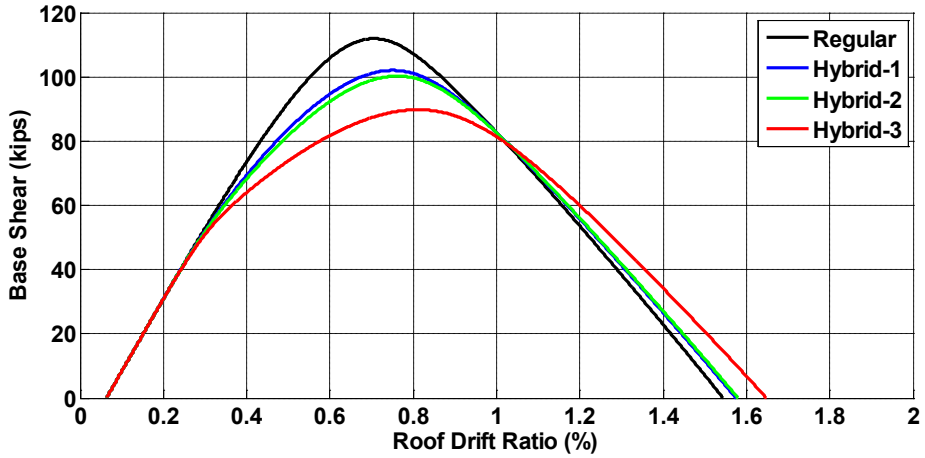

Figure A-17. Pushover Curve for PG12-12S-LB-15B-Dmin Model

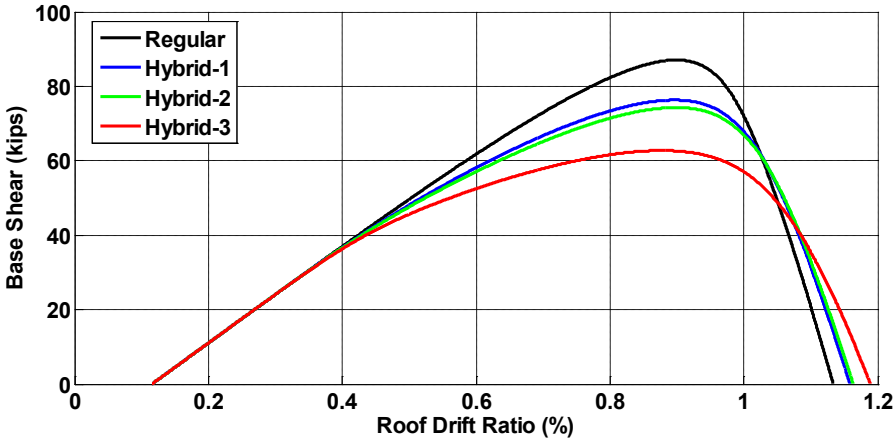

Figure A-18. Pushover Curve for PG12-18S-LB-15B-Dmax Model

A.2.2. Incremental Dynamic Analysis

When the bar plots in Figure A-19 through Figure A-25 are studied, it can be concluded that the benefit of Hybrid systems is more for the taller structures with longer periods. Note that for twelve and eighteen story structures (Figure A-24 and Figure A-25) at IDA scale factors of 0.95 and 1.0, the plots show that there is 100% improvement in the performance. This is because the regular frame had a very low *CMR,* i.e., regular frame reached its median collapse capacity at a lower scale than MCE.

The reason of this behavior is the very low overstrength values of this performance group. This performance group was originally designed with moment-resisting beam-column connections; however, since hybrid systems and also BRBs work better with non-moment resisting beam-column connections, Non-MR connections were used in the numerical models. The reduction of overstrength is not significant for the Dmax performance groups, however, the significant drop of overstrength affected the performance for Dmin archetypes. Note that for braced frames, it is possible to have overstrength values less than 1.0. This generally happens when the damage concentrates at the mid-height to top stories of the frame. However, the main reason for the small overstrength values is the beam-column connections. With moment resisting beam-column connections the overstrength of the performance group doubled up.

A.2.3. *FEMA P-695* Performance Evaluation

As discussed in the previous section, this performance group gave very small overstrength values (about 0.7 for the performance group average). In order to satisfy the *FEMA P-695* methodology with his low overstrength, the ductility reduction factor which is related to energy dissipation capacity of the system should be very high. It is surprising that even with this low overstrength values, Hybrid-3 frame could still satisfy the performance group acceptance criteria with less than 10% collapse probability. This shows the excellent energy dissipation capacity of this hybrid BRBF.

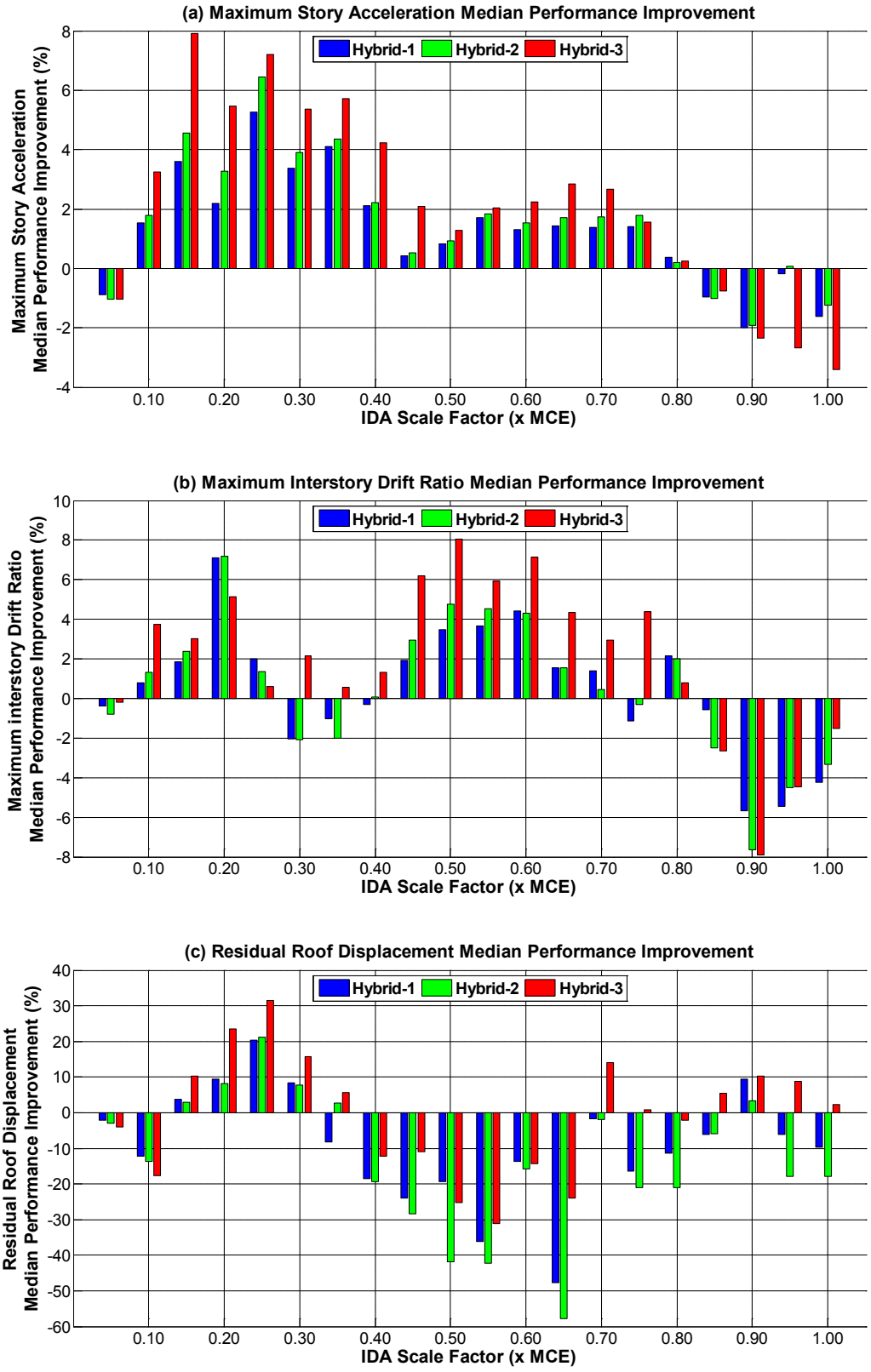

Figure A-19. PG12-2S-LB-15B-Dmin Model Median Performance Improvements for (a) Maximum Story Acceleration (b) Maximum Interstory Drift Ratios (c) Residual Roof Displacement

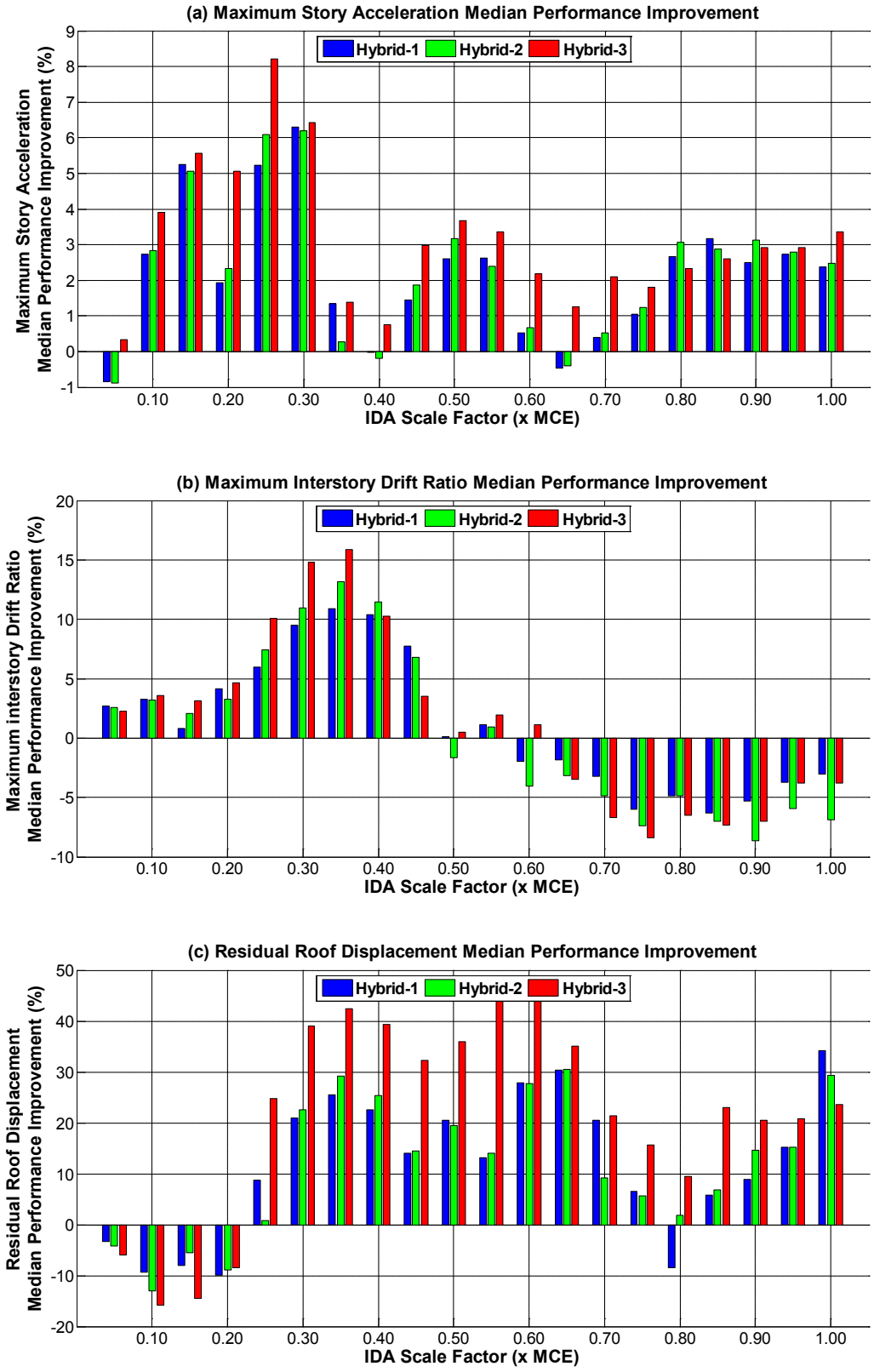

Figure A-20. PG12-3S-LB-15B-Dmin Model Median Performance Improvements for (a) Maximum Story Acceleration (b) Maximum Interstory Drift Ratios (c) Residual Roof Displacement

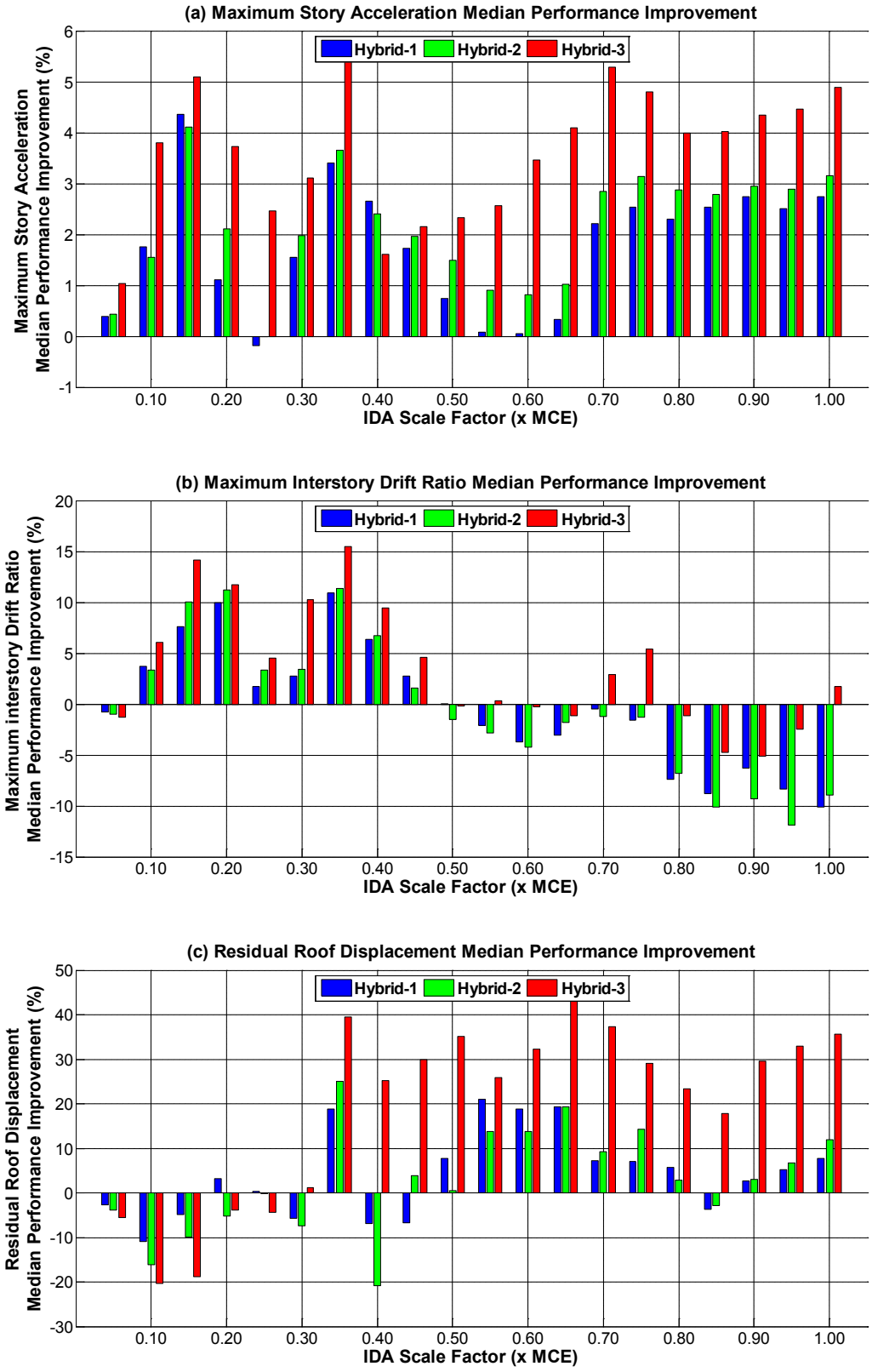

Figure A-21. PG12-4S-LB-15B-Dmin Model Median Performance Improvements for (a) Maximum Story Acceleration (b) Maximum Interstory Drift Ratios (c) Residual Roof Displacement

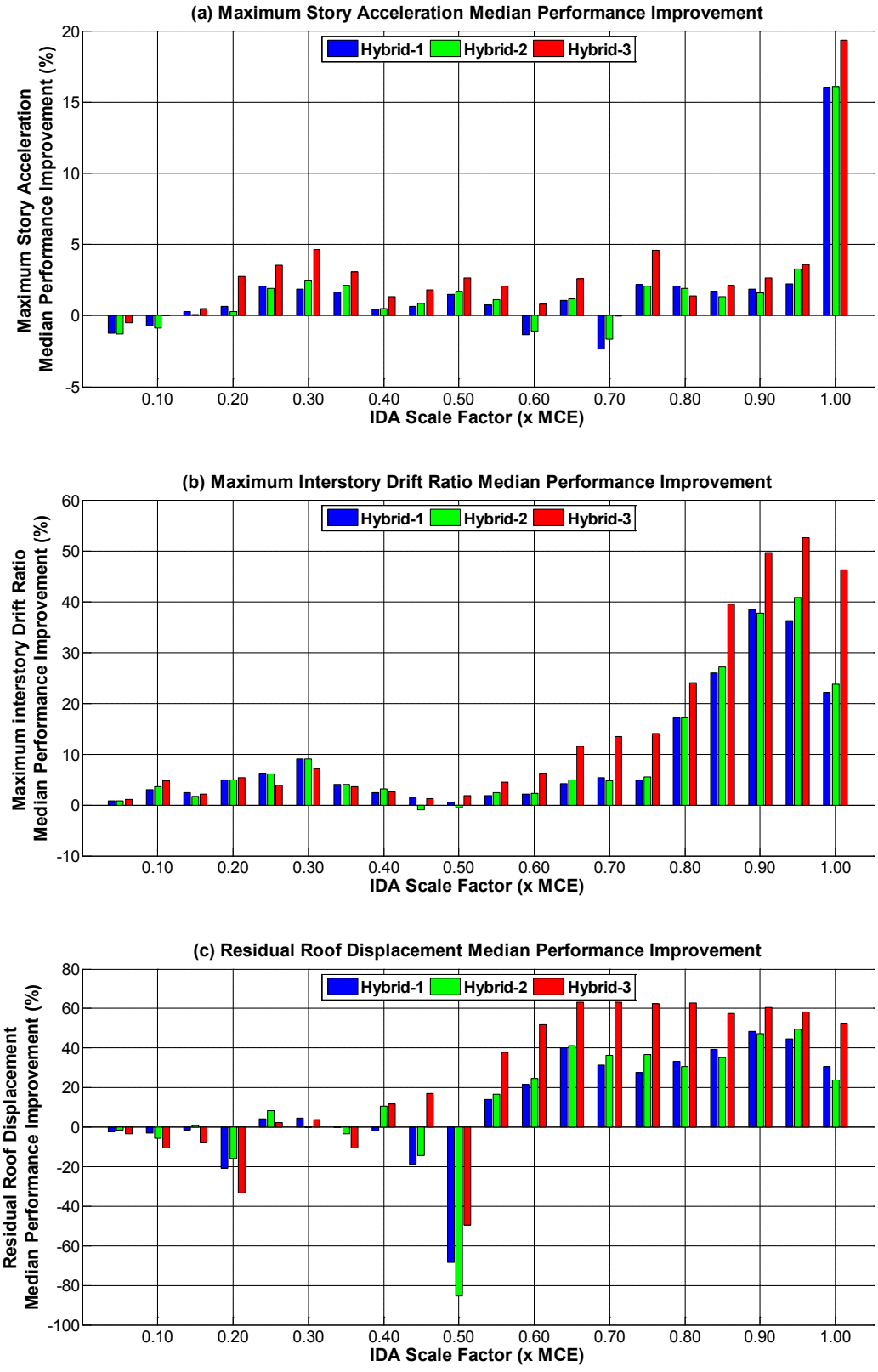

Figure A-22. PG12-6S-LB-15B-Dmin Model Median Performance Improvements for (a) Maximum Story Acceleration (b) Maximum Interstory Drift Ratios (c) Residual Roof Displacement

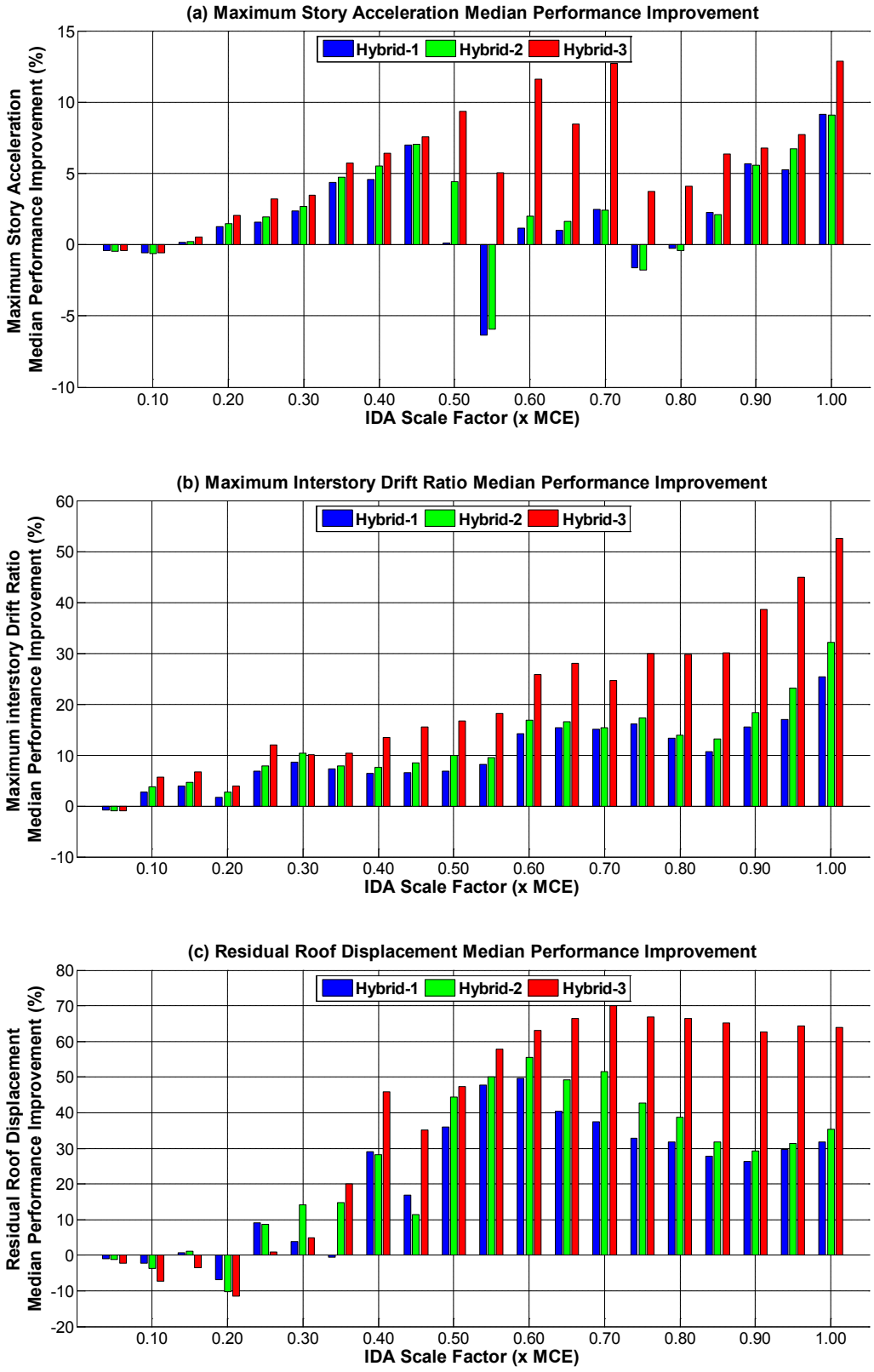

Figure A-23. PG12-9S-LB-15B-Dmin Model Median Performance Improvements for (a) Maximum Story Acceleration (b) Maximum Interstory Drift Ratios (c) Residual Roof Displacement

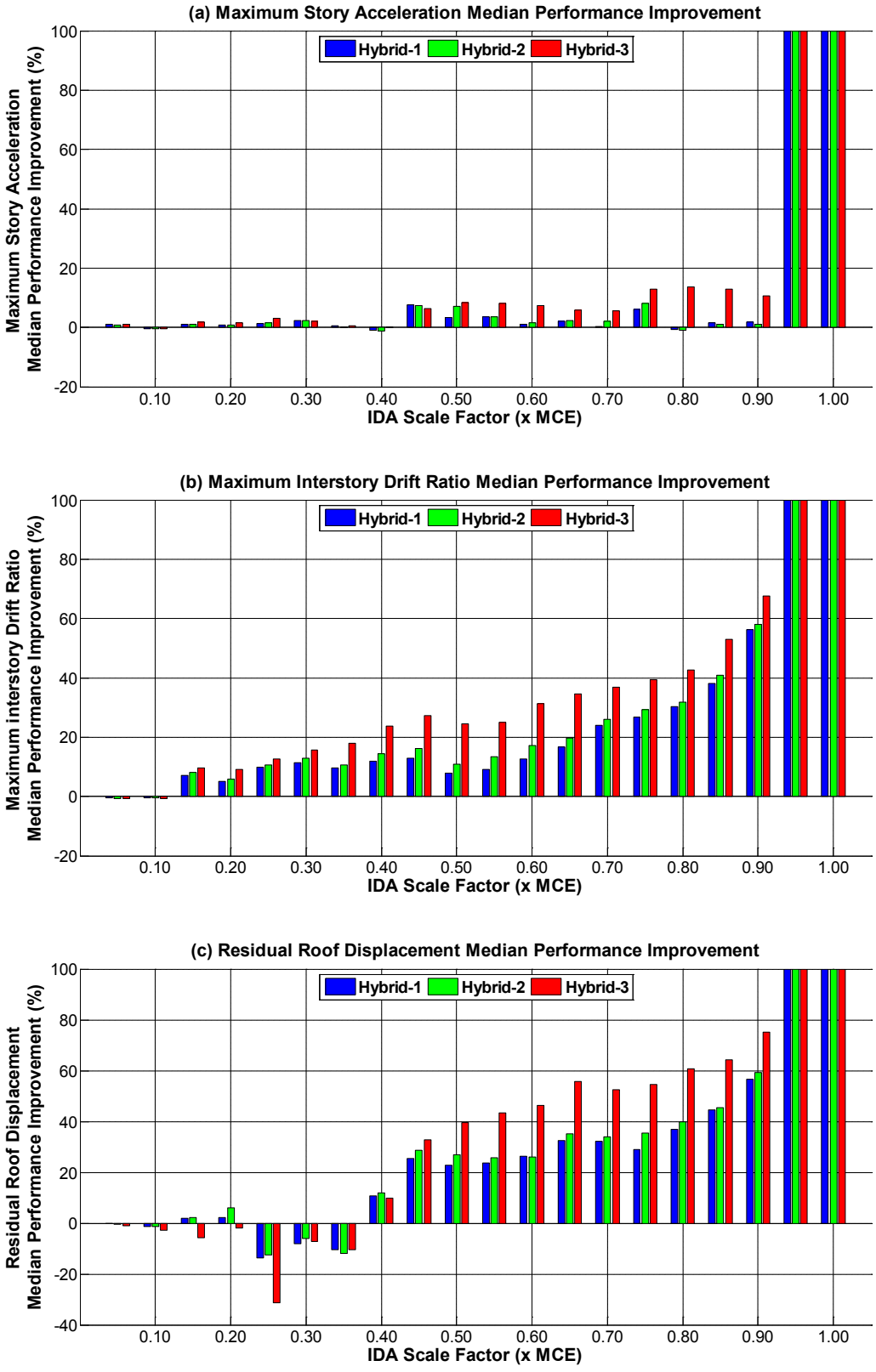

Figure A-24. PG12-12S-LB-15B-Dmin Model Median Performance Improvements for (a) Maximum Story Acceleration (b) Maximum Interstory Drift Ratios (c) Residual Roof Displacement

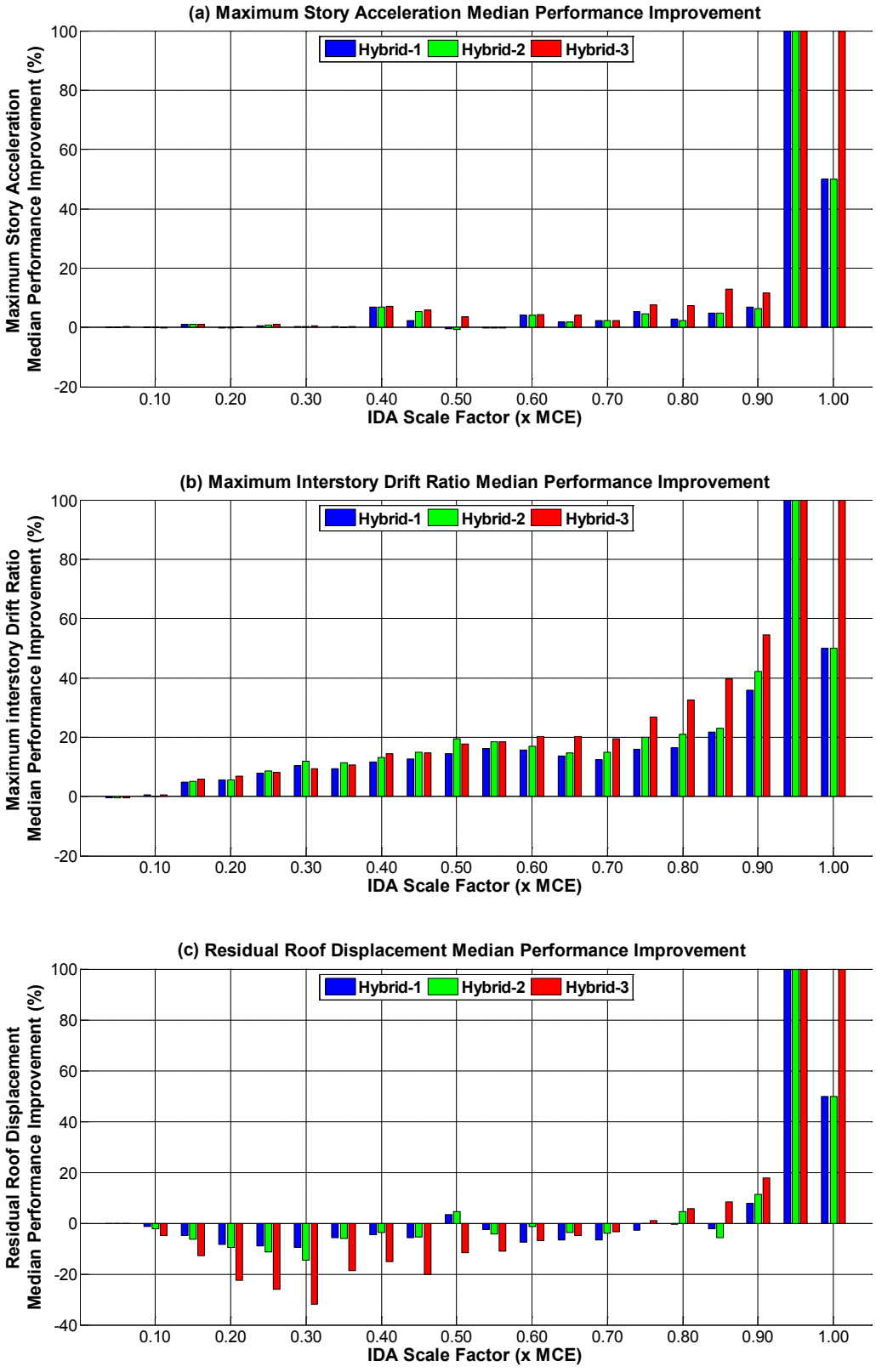

Figure A-25. PG12-18S-LB-15B-Dmin Model Median Performance Improvements for (a) Maximum Story Acceleration (b) Maximum Interstory Drift Ratios (c) Residual Roof Displacement

Table A-9. *ATC-76-1* Project Performance Group PG-12 SDC Dmin/ Long-Period Archetypes Collapse Performance Evaluation Using 10% Interstory Drift + Low Cycle Fatigue Failure of Braces as Collapse Criteria

Arch. Design ID No.	BRBF Model	Computed Overstrength and Collapse Margin Parameters					Acceptance Check		
		Static Ω	*CMR*	μ_T	*SSF*	*ACMR*	Accept. *ACMR*	Pass / Fail	Collapse Probability (%)
2S-LB-15B-Dmin	Regular	1.33	2.70	17.5	1.14	3.08	1.56	Pass	1.6
	Hybrid-1	1.32	2.67	18.3	1.14	3.04	1.56	Pass	1.7
	Hybrid-2	1.31	2.64	18.5	1.14	3.01	1.56	Pass	1.8
	Hybrid-3	1.33	2.77	20.3	1.14	3.16	1.56	Pass	1.4
3S-LB-15B-Dmin	Regular	0.83	2.00	13.3	1.18	2.36	1.56	Pass	5.1
	Hybrid-1	0.82	2.13	13.9	1.18	2.51	1.56	Pass	4.0
	Hybrid-2	0.82	2.14	14.1	1.18	2.53	1.56	Pass	3.9
	Hybrid-3	0.82	2.26	14.9	1.18	2.67	1.56	Pass	3.1
4S-LB-15B-Dmin	Regular	0.52	1.62	10.8	1.22	1.98	1.56	Pass	9.7
	Hybrid-1	0.51	1.71	11.3	1.22	2.09	1.56	Pass	8.1
	Hybrid-2	0.51	1.70	11.5	1.22	2.07	1.56	Pass	8.2
	Hybrid-3	0.50	1.93	12.2	1.22	2.35	1.56	Pass	5.1
6S-LB-15B-Dmin	Regular	0.90	1.10	6.5	1.26	1.38	1.56	Fail	26.8
	Hybrid-1	0.85	1.18	7.6	1.28	1.52	1.56	Fail	21.4
	Hybrid-2	0.84	1.18	7.8	1.29	1.52	1.56	Fail	21.2
	Hybrid-3	0.79	1.30	9.2	1.29	1.68	1.56	Pass	16.1
9S-LB-15B-Dmin	Regular	0.73	1.03	4.7	1.27	1.31	1.56	Fail	30.2
	Hybrid-1	0.68	1.14	5.5	1.30	1.48	1.56	Fail	22.6
	Hybrid-2	0.67	1.16	5.6	1.31	1.51	1.56	Fail	21.4
	Hybrid-3	0.61	1.45	6.7	1.34	1.94	1.56	Pass	10.4
12S-LB-15B-Dmin	Regular	0.60	0.92	3.8	1.24	1.14	1.56	Fail	40.0
	Hybrid-1	0.55	1.07	4.4	1.26	1.35	1.56	Fail	28.3
	Hybrid-2	0.54	1.10	4.6	1.27	1.40	1.56	Fail	26.2
	Hybrid-3	0.48	1.26	5.5	1.30	1.64	1.56	Pass	17.3
18S-LB-15B-Dmin	Regular	0.31	0.92	4.3	1.26	1.16	1.56	Fail	38.9
	Hybrid-1	0.27	0.98	5.1	1.29	1.26	1.56	Fail	32.8
	Hybrid-2	0.26	1.00	5.2	1.29	1.29	1.56	Fail	31.3
	Hybrid-3	0.22	1.13	6.2	1.33	1.50	1.56	Fail	22.1
Mean of Performance Group	Regular	0.75				1.77	1.96	Fail	13.8
	Hybrid-1	0.71				1.89	1.96	Fail	11.2
	Hybrid-2	0.71				1.91	1.96	Fail	11.0
	Hybrid-3	0.68				2.13	1.96	Pass	7.4

A.2.4. Frame Sections for Performance Group 12

Table A-10. Sections for Archetype ID = 2S-LB-15B-Dmin

Level / story	Brace Area (in.^{2})	Beams	Columns
Roof	-	W18x35	-
2	3.0	W21x50	W14x38
Ground	3.0	-	W14x53

Table A-11. Sections for Archetype ID = 3S-LB-15B-Dmin

Level / story	Brace Area (in.^{2})	Beams	Columns
Roof	-	W18x35	-
3	3.0	W21x50	W14x38
2	3.0	W21x50	W14x53
Ground	3.0	-	W14x74

Table A-12. Sections for Archetype ID = 4S-LB-15B-Dmin

Level / story	Brace Area (in.^{2})	Beams	Columns
Roof	-	W18x35	-
4	3.0	W21x50	W14x74
3	3.0	W21x50	W14x74
2	3.0	W21x50	W14x74
Ground	3.0	-	W14x82

Table A-13. Sections for Archetype ID = 6S-LB-15B-Dmin

Level / story	Brace Area (in.^{2})	Beams	Columns
Roof	-	W18x35	-
6	3.0	W21x50	W14x74
5	3.0	W21x50	W14x74
4	3.0	W21x50	W14x74
3	3.0	W21x50	W14x82
2	3.0	W21x50	W14x132
Ground	3.0	-	W14x132

Table A-14. Sections for Archetype ID = 9S-LB-15B-Dmin

Level / story	Brace Area (in.^{2})	Beams	Columns
Roof	-	W18x35	-
9	3.0	W21x50	W14x74
8	3.0	W21x50	W14x74
7	3.0	W21x50	W14x74
6	3.0	W21x50	W14x132
5	4.0	W21x62	W14x132
4	4.0	W21x62	W14x132
3	6.0	W21x62	W14x159
2	6.0	W21x62	W14x159
Ground	6.0	-	W14x176

Table A-15. Sections for Archetype ID = 12S-LB-15B-Dmin

Level / story	Brace Area (in.^{2})	Beams	Columns
Roof	-	W18x35	-
12	3.0	W21x50	W14x82
11	3.0	W21x50	W14x82
10	3.0	W21x62	W14x132
9	4.0	W21x62	W14x132
8	4.0	W21x62	W14x132
7	5.0	W21x62	W14x132
6	5.0	W21x62	W14x159
5	5.0	W21x62	W14x159
4	6.0	W21x62	W14x193
3	7.0	W21x62	W14x193
2	7.0	W21x62	W14x257
Ground	7.0	-	W14x257

Table A-16. Sections for Archetype ID = 18S-LB-15B-Dmin

Level / story	Brace Area (in.^{2})	Beams	Columns
Roof	-	W18x35	-
18	3.0	W21x62	W14x132
17	4.0	W21x62	W14x132
16	4.0	W21x62	W14x132
15	5.0	W21x62	W14x132
14	5.0	W21x62	W14x132
13	5.0	W21x62	W14x132
12	5.0	W21x62	W14x211
11	6.0	W21x62	W14x211
10	6.0	W21x62	W14x211
9	6.0	W21x62	W14x211
8	6.0	W21x62	W14x257
7	7.0	W21x73	W14x257
6	8.0	W21x73	W14x283
5	8.0	W21x73	W14x283
4	9.0	W24x76	W14x342
3	10.0	W24x94	W14x342
2	11.0	W24x94	W14x398
Ground	11.0	-	W14x398

A.3. Supplemental Case Study-3 for Hybrid Buckling Restrained Braced Frames: Short Period Performance Group at SDC Dmax

This case study investigates the performance comparison between hybrid and regular frames on short period performance group (PG-13) at seismic design category Dmax. See Table A-17 for the design properties of the performance group.

Table A-17. *ATC-76-1* Project Performance Group PG-13 Archetype Design Properties

Arch. Design ID No.	No. of Stories	Key Archetype Design Parameters						
		Analysis Method	Seismic Design Criteria					$S_{MT}(T)$ (g)
			SDC	R	T (sec)	T_1 (sec)	V/W (g)	
Performance Group PG-13. SDC Dmax / Short-Period Archetypes								
1S-LB-25B-Dmax	1	RSA	Dmax	8	0.29	0.50	0.125	1.50
2S-LB-25B-Dmax	2	RSA	Dmax	8	0.48	0.60	0.112	1.50
3S-LB-25B-Dmax	3	RSA	Dmax	8	0.66	0.91	0.097	1.37

Figure A-26 displays the plan and elevation views of PG-13 archetypes used in this section.

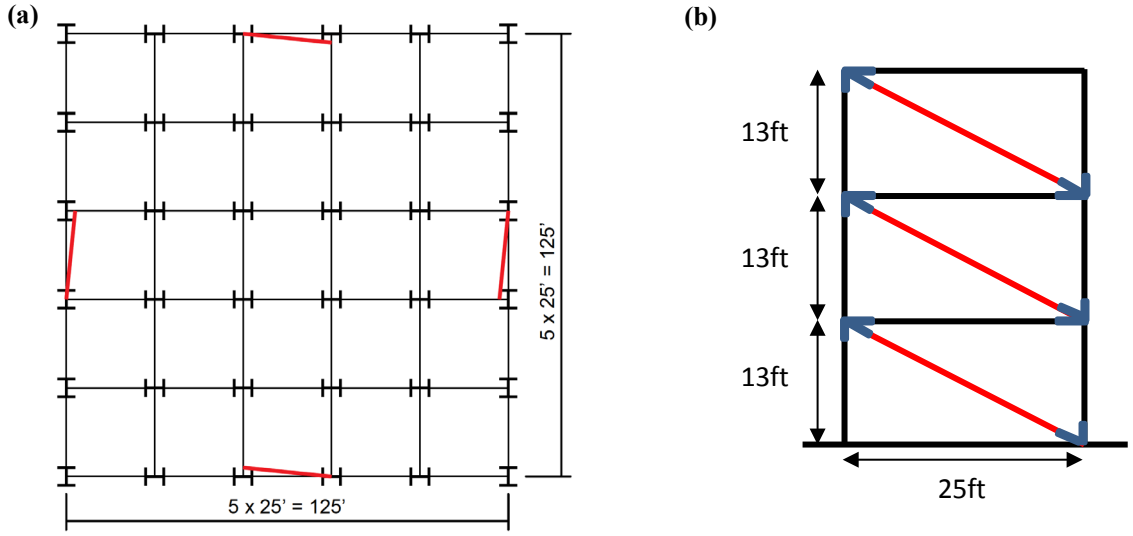

Figure A-26. (a) Plan View for all Models (b) Elevation of 3 Story Archetype (Only Number of Stories Changes for the Other Archetypes)

A.3.1. Nonlinear Model Details and Pushover Analysis

The same modeling techniques discussed before were also used for this performance group models.

Figure A-27 through Figure A-29 display the pushover curves for one, two and three story archetype models.

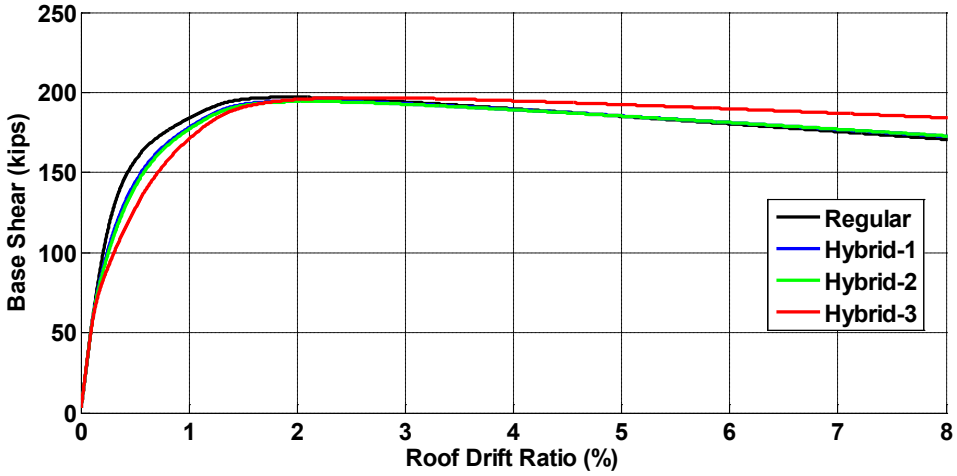

Figure A-27. Pushover Curve for PG13-1S-LB-25B-Dmax Model

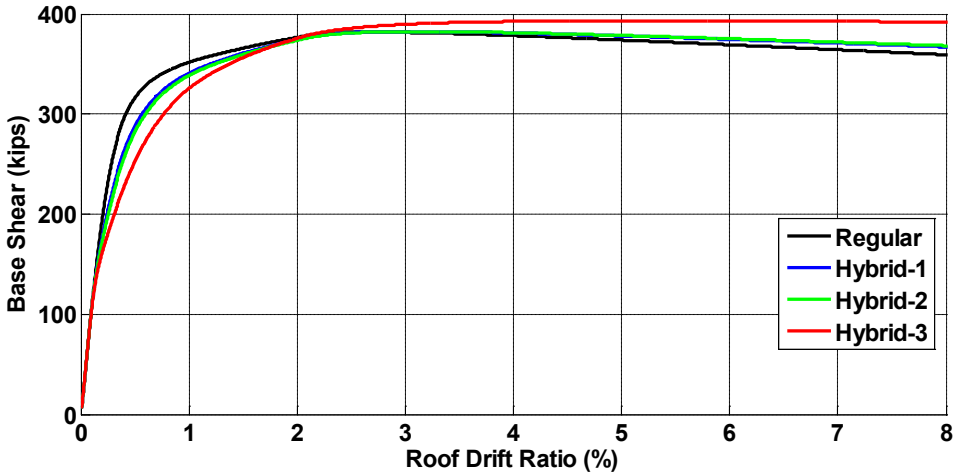

Figure A-28. Pushover Curve for PG13-2S-LB-25B-Dmax Model

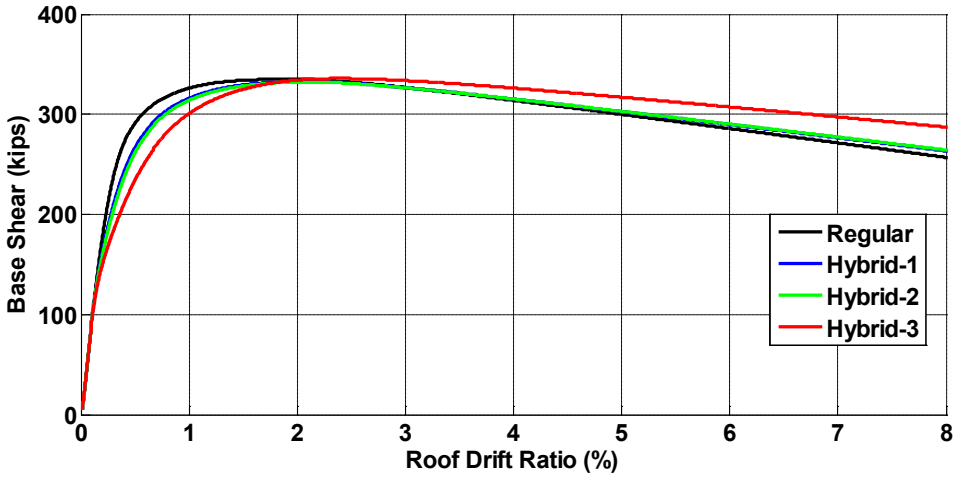

Figure A-29. Pushover Curve for PG13-3S-LB-25B-Dmax Model

A.3.2. Incremental Dynamic Analysis

When the bar charts in Figure A-30 through Figure A-32 are analyzed, it can be concluded that hybrid BRBFs do not increase the performance of very short period buildings (See Figure A-30 for one story archetype results). The performance drops at and after DBE level. Two and three story archetypes of this performance group performed much better than the one story archetype.

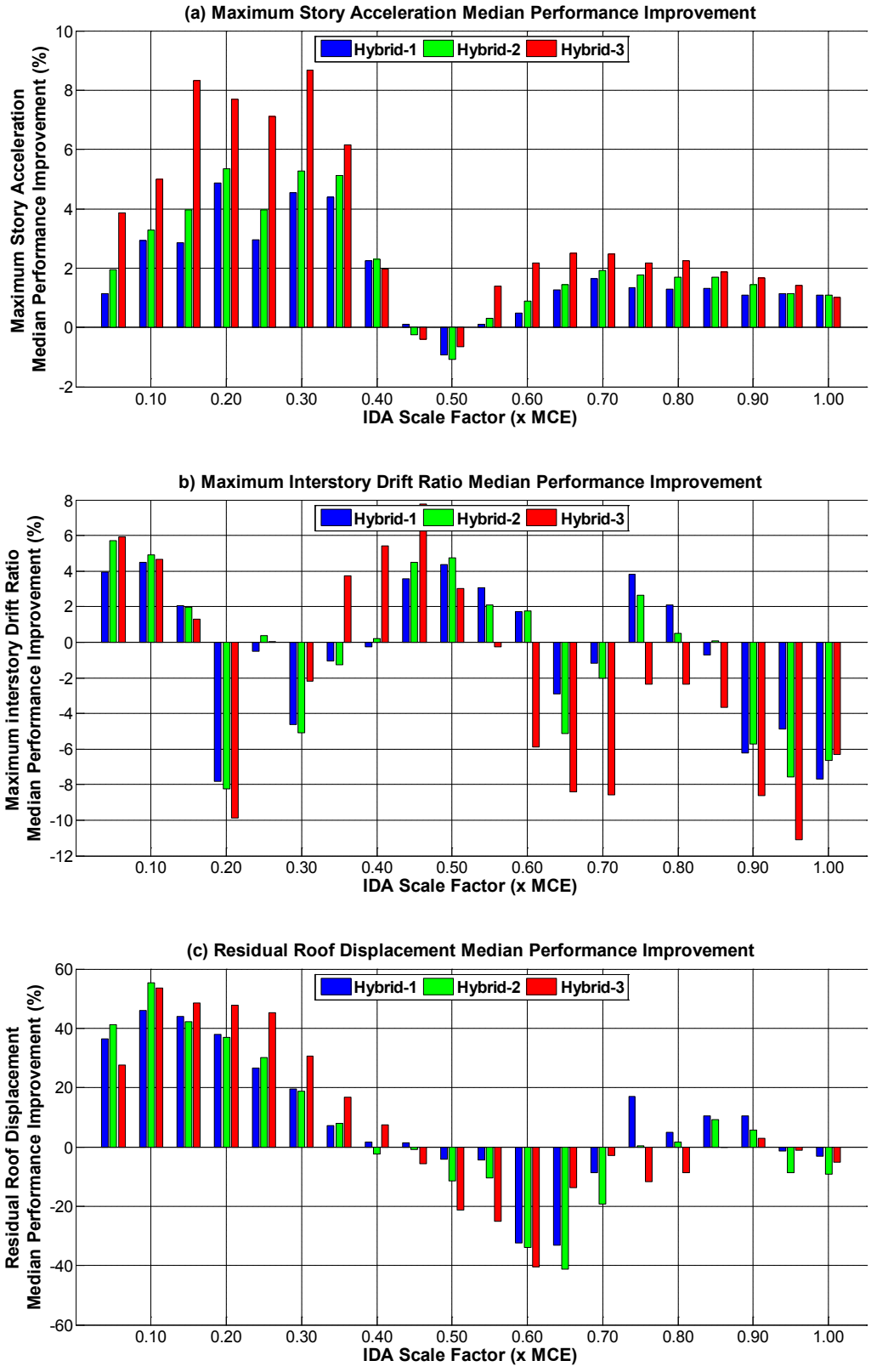

Figure A-30. PG13-1S-LB-25B-Dmin Model Median Performance Improvements for (a) Maximum Story Acceleration (b) Maximum Interstory Drift Ratios (c) Residual Roof Displacement

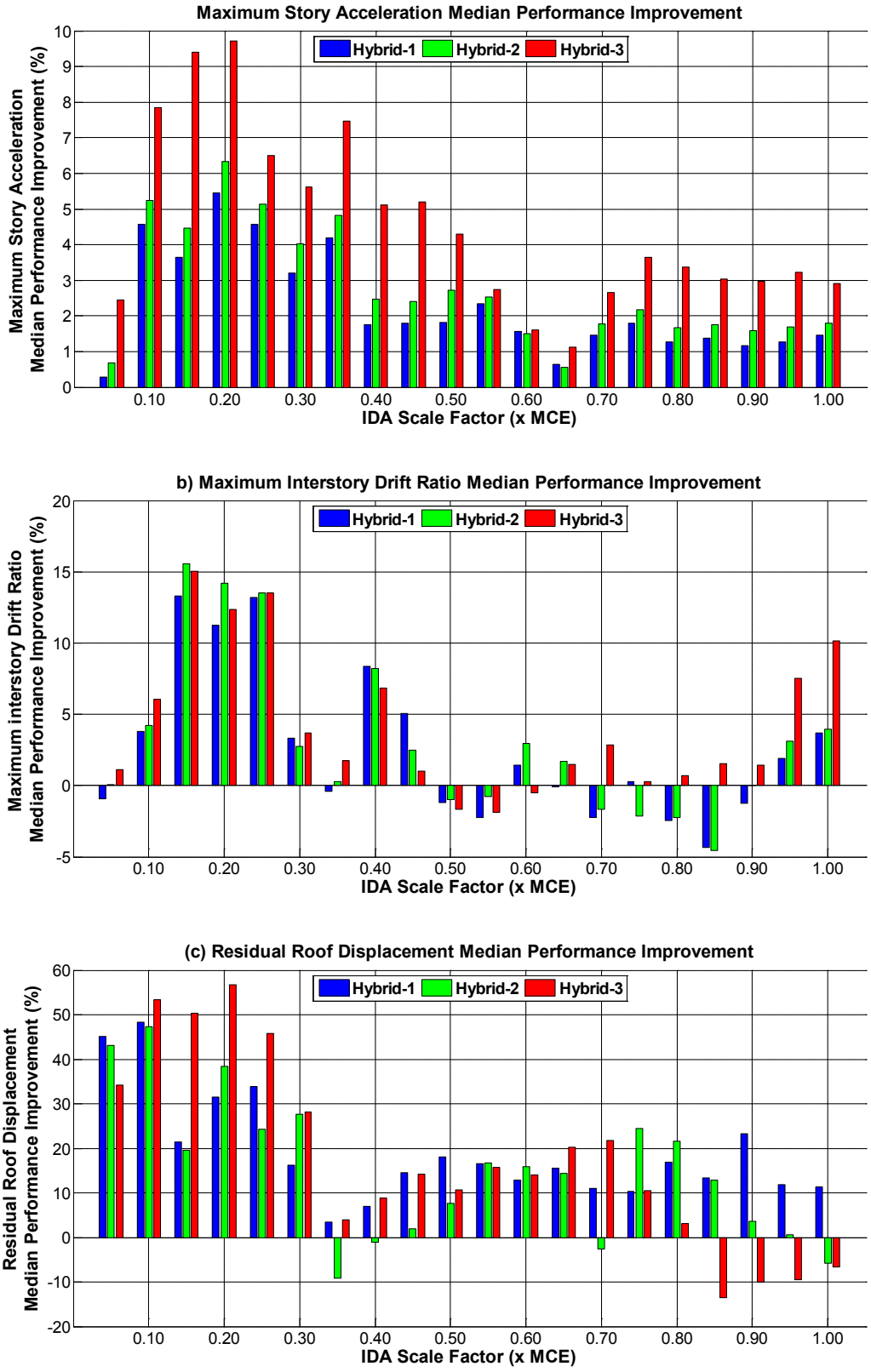

Figure A-31. PG13-2S-LB-25B-Dmin Model Median Performance Improvements for (a) Maximum Story Acceleration (b) Maximum Interstory Drift Ratios (c) Residual Roof Displacement

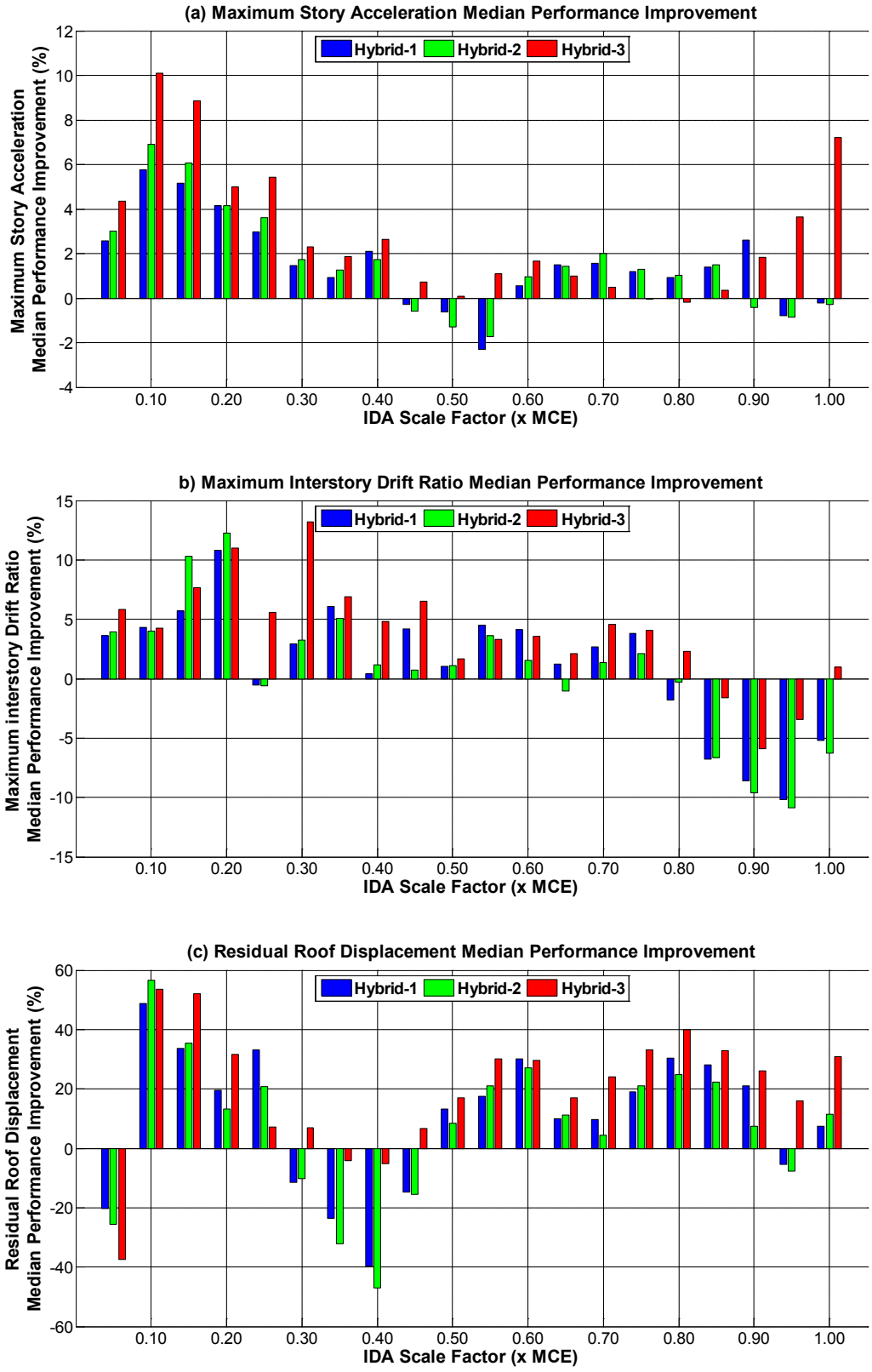

Figure A-32. PG13-3S-LB-25B-Dmin Model Median Performance Improvements for (a) Maximum Story Acceleration (b) Maximum Interstory Drift Ratios (c) Residual Roof Displacement

A.3.3. *FEMA P-695* Performance Evaluation

Table A-18 tabulates the performance evaluation of the short period performance group, PG-13. Hybrid-3 frame performed slightly better than the regular frame; however the benefit of hybridity is not as significant as the one in long period frames discussed earlier in this appendix.

Table A-18. *ATC-76-1* Performance Group PG-13 SDC Dmax/ Long-Period Archetypes Collapse Performance Evaluation Using 10% Interstory Drift + Low Cycle Fatigue Failure of Braces as Collapse Criteria

Arch. Design ID No.	BRBF Model	Computed Overstrength and Collapse Margin Parameters					Acceptance Check		
		Static Ω	*CMR*	μ_T	*SSF*	*ACMR*	Accept. *ACMR*	Pass / Fail	Collapse Probability (%)
1S-LB-25B-Dmax	Regular	1.78	1.98	28.6	1.33	2.63	1.56	Pass	3.3
	Hybrid-1	1.76	1.91	28.9	1.33	2.54	1.56	Pass	3.8
	Hybrid-2	1.76	1.87	28.9	1.33	2.49	1.56	Pass	4.1
	Hybrid-3	1.78	2.04	28.6	1.33	2.71	1.56	Pass	2.9
2S-LB-25B-Dmax	Regular	1.93	2.38	29.5	1.33	3.17	1.56	Pass	1.4
	Hybrid-1	1.94	2.26	29.4	1.33	3.01	1.56	Pass	1.8
	Hybrid-2	1.94	2.30	29.4	1.33	3.06	1.56	Pass	1.7
	Hybrid-3	1.99	2.40	28.7	1.33	3.19	1.56	Pass	1.4
3S-LB-25B-Dmax	Regular	1.30	1.47	26.0	1.37	2.02	1.56	Pass	9.1
	Hybrid-1	1.30	1.46	28.2	1.37	2.00	1.56	Pass	9.3
	Hybrid-2	1.29	1.48	28.6	1.37	2.03	1.56	Pass	8.9
	Hybrid-3	1.31	1.61	31.2	1.37	2.21	1.56	Pass	6.6
Mean of Performance Group	Regular	1.67				2.61	1.96	Pass	3.4
	Hybrid-1	1.66				2.52	1.96	Pass	3.9
	Hybrid-2	1.66				2.53	1.96	Pass	3.9
	Hybrid-3	1.69				2.70	1.96	Pass	2.9

A.3.4. Frame Sections for Performance Group 13

Table A-19. Sections for Archetype ID = 1S-LB-25B-Dmax

Level / story	Brace Area (in.^{2})	Beams	Columns
Roof	-	W21x62	-
Ground	4.0	-	W14x38

Table A-20. Sections for Archetype ID = 2S-LB-25B-Dmax

Level / story	Brace Area (in.^{2})	Beams	Columns
Roof	-	W21x50	-
2	6.0	W21x73	W14x82
Ground	9.0	-	W14x82

Table A-21. Sections for Archetype ID = 3S-LB-25B-Dmax

Level / story	Brace Area (in.^{2})	Beams	Columns
Roof	-	W21x62	-
3	5.0	W21x73	W14x38
2	7.0	W24x76	W14x74
Ground	8.0	-	W14x82

APPENDIX B: MOMENT FRAME DESIGN DETAILS AND SECTIONS

This appendix investigates the effect of column depth and SC/WB on the moment frame archetypes discussed in Chapter 5. Two different column depths (W14 and W24), and SC/WB ratios of 1.0, 1.5, and 2.0 were used in the design space. The effect of these two design decisions are discussed here. Note that only the regular (non-hybrid) archetypes are discussed in here concentrating on the effects of column depth and SC/WB ratio.

B.1. Effect of Column Depth on Moment Frames

In modified Ibarra-Krawinkler deterioration model, the main contributor of the deterioration parameters (θ_p, θ_{pc}, and Λ) is beam web depth to thickness ratio (h/t_w). Flange width to thickness ratio ($b_f/2t_f$), beam depth (d), and shear span to beam depth ratio (L/d) also has an effect on the regression equations with which the deterioration parameters are found. Figure B-1 shows the variation of h/t_w and $b_f/2t_f$ for W14 and W24 columns.

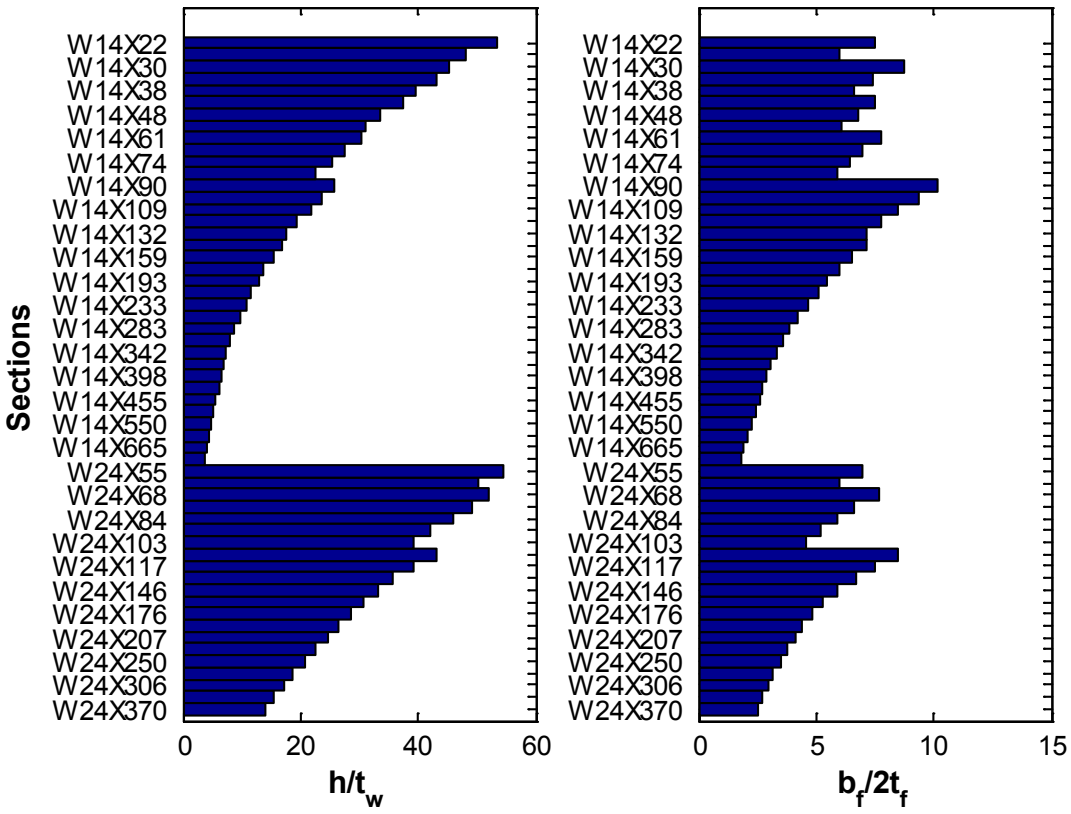

Figure B-1. Change in Web Depth to Thickness Ratio (h / t_w) and Flange Width to Thickness Ratio (b_f/ $2t_f$) for W14 and W24 Wide Flange Sections

As explained in Chapter 5, the steel database that was used to develop the regression equations for deterioration models includes mostly beams. Newell and Uang (2008) tested nine full-scale heavy W14 columns (up to W14x370) under different levels of axial load and demonstrated that the plastic rotation capacity of heavy W14 columns is large. The columns began to lose capacity after 7% to 9% interstory drift ratio under cyclic lateral and axial loads. These tests were limited to heavy W14 columns and there is not enough experimental data to calibrate the deterioration of light W14 and deep column sections. A current ATC project, *NIST GCR 11-917-13*, (NIST, 2011) is investigating the behavior of deep column sections under cyclic loading at different axial load levels. Due to the lack of experimental data for columns, the regression equations for "other than RBS" beams, proposed by Lignos and Krawinkler (2011), were used in modeling the stiffness and strength deterioration of the columns. The same modeling approach was also used in *ATC-76-1* project. The discussion in this appendix is within these modeling limitations.

Figure B-2 shows deterioration parameters of W14 and W24 columns. In addition to the section properties, expected yield strength, F_{ye}, of 55ksi, shear span length, L, of 65 in., and unbraced length, L_b, of 130 in. were used in the "other than RBS" regression equations to find the values in Figure B-2.

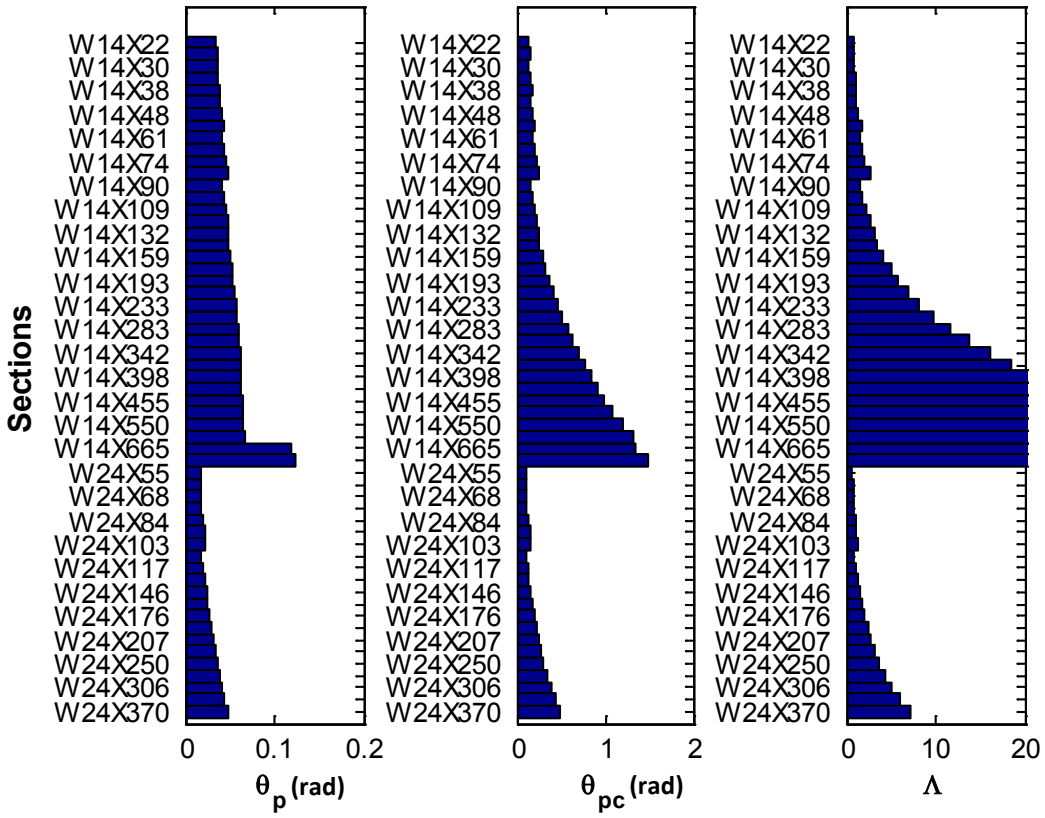

Figure B-2. Change in Plastic Rotation Capacity (θ_p), Post-Capping Rotation Capacity (θ_{pc}) and Strength-Stiffness Deterioration (Λ) Parameters for W14 and W24 Wide Flange Sections

As may be seen in Figure B-2, the deterioration parameters of W14 columns are much better than W24 columns. The effects of these parameters are investigated in details on 6 story designs. Table B-1 shows the sections of six story W14 and W24 column designs with SC/WB ratio of 1.0. W14 column design has heavier columns and girders than the W24 column design. Note that both of these designs are drift controlled.

Table B-1. Sections for 6 story W14 and W24 Designs with SC/WB of 1.0

Level / story	1-6St-Dmax-W14-SC/WB=1.0-REG			8-6St-Dmax-W24-SC/WB=1.0-REG		
	Columns		Girders	Columns		Girders
	Exterior	Interior		Exterior	Interior	
Roof	-	-	W21x44	-	-	W21x44
6	W14x82	W14x145	W24x84	W24X55	W24x94	W24x76
5	W14x82	W14x145	W27x94	W24X55	W24x94	W24x84
4	W14x132	W14x233	W27x114	W24X84	W24x146	W27x102
3	W14x132	W14x233	W27x146	W24X84	W24x146	W27x129
2	W14x176	W14x283	W27x102	W24X131	W24x176	W27x84
Ground	W14x176	W14x283	-	W24X131	W24x176	-

Figure B-3 shows the column deterioration parameters of the sections tabulated in Table B-1. In Figure B-3, the notations of the "y" axis labels show the column level and position. For instance "1-E" stands for the exterior columns of story 1 and 2, while "3-I" stands for the interior columns story 5 and 6. As mentioned in Chapter 5, column splices were placed at every two stories in the designs. As may be seen in Figure B-3, W14 columns have better deterioration parameters than W24 columns and the difference is the most in reference cumulative plastic rotation, Λ.

Figure B-4 shows the girder deterioration parameters of the sections tabulated in Table B-4. While the difference is significant in column deterioration parameters, girder parameters are comparable and they are sometimes better for W24 column design sections.

The pushover and fragility curves of these two designs are displayed in Figure B-5. As may be seen, W14 column design has higher strength and lower collapse probability than the W24 column design. Since these designs are both drift controlled, their initial stiffness are period are very close, and the W24 design has slightly higher initial stiffness. It is also worth noting that W24 column design reaches negative stiffness at higher drift values than W14 column design.

When the residual and maximum drifts of these two designs are compared in Figure B-5, it is seen that the W24 column design actually performed better than W14 design at DBE and MCE levels. At higher intensities, W14 column design gives less collapses though as may be seen in the fragility curves.

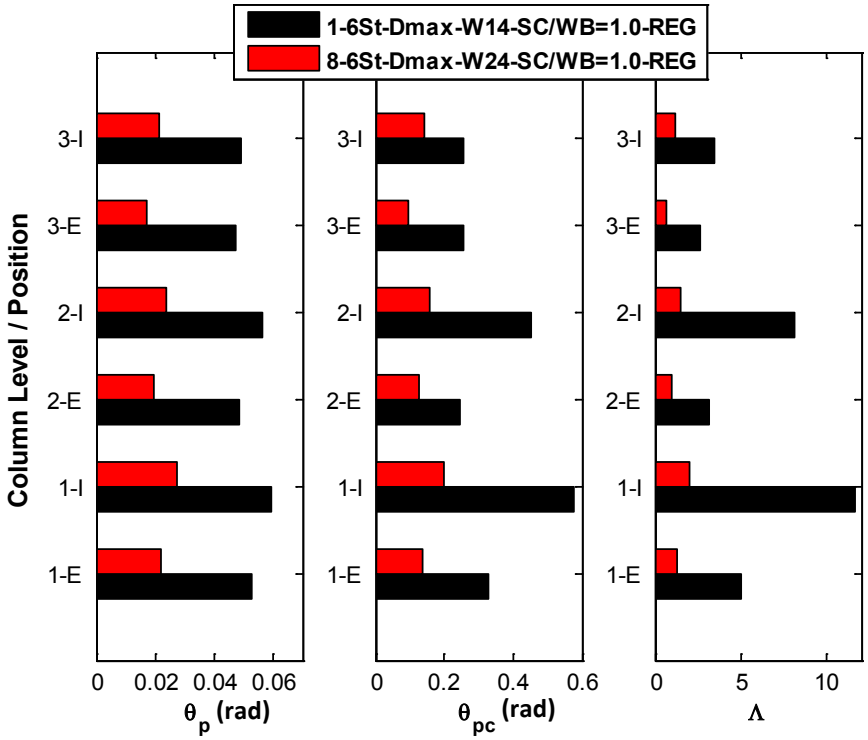

Figure B-3. Change in θ_p, θ_{pc} and Λ Deterioration Parameters for the Columns of 6 Story Moment Frames: ID=1-6St-Dmax-W14-SC/WB=1.0-REG and 8-6St-Dmax-W24-SC/WB=1.0-REG

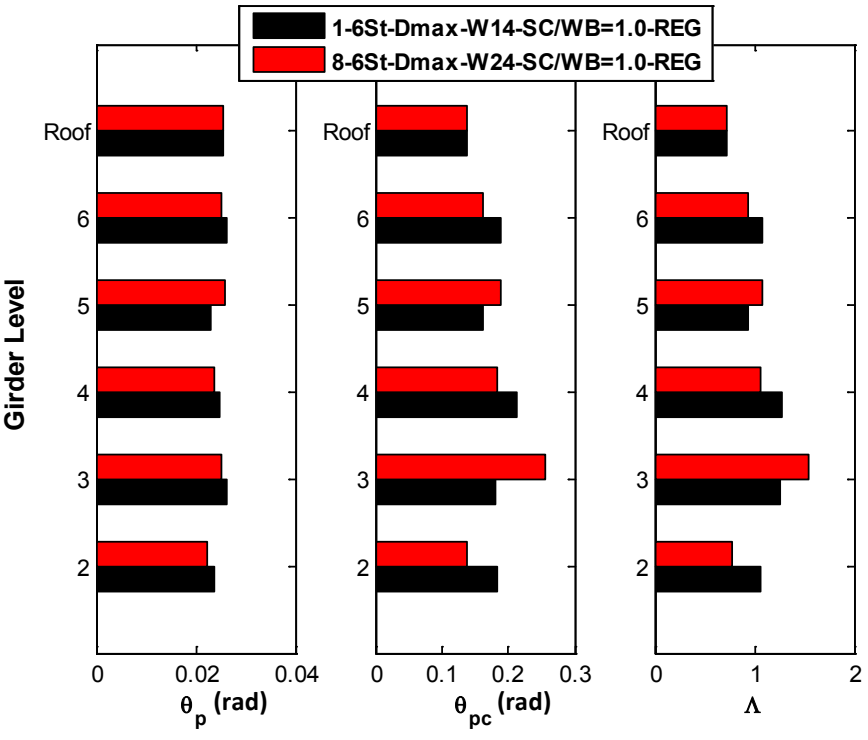

Figure B-4. Change in θ_p, θ_{pc} and Λ Deterioration Parameters for the Girders of 6 Story Moment Frames: ID=1-6St-Dmax-W14-SC/WB=1.0-REG and 8-6St-Dmax-W24-SC/WB=1.0-REG

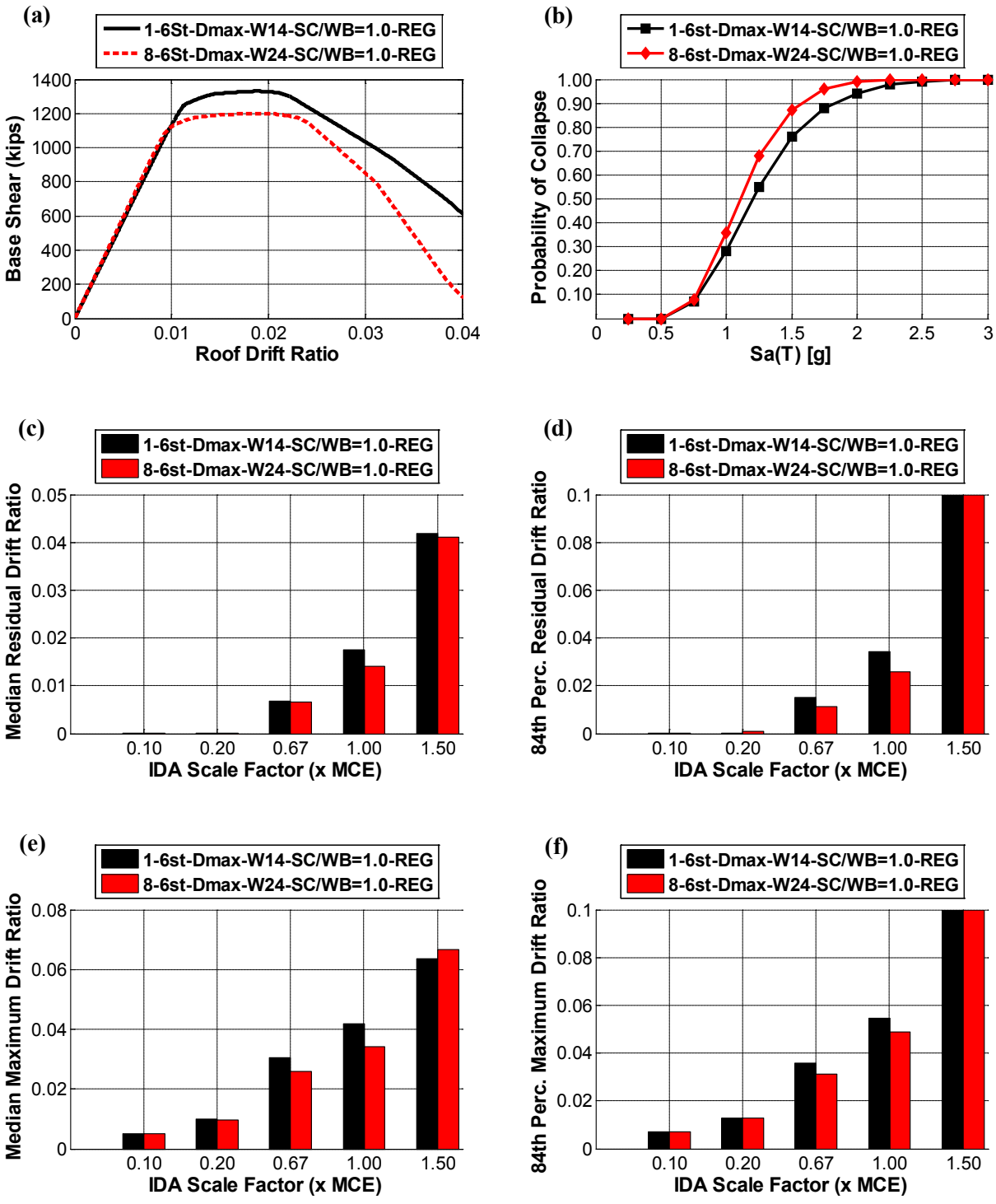

Figure B-5. Comparison between W14 and W24 Column Designs for 6 Story SMF Designed at Dmax SDC with SC/WB Ratio of 1.0 (a) Pushover Curves, (b) Fragility Curves, (c) Median Residual Drift Ratios, (d) 84th Percentile Residual Drift Ratios, (e) Median Maximum Drift Ratios, (f) 84th Percentile Maximum Drift Ratios

Figure B-6 through Figure B-13 illustrate the difference between W14 and W24 column designs for all the archetypes tabulated in Table B-2. When the designs with different column depths but same building heights and SC/WB ratios are compared, shallow depth (W14) column designs are about 30% heavier than deep column depth (W24) designs. Doubler plate requirements for W14 and W24 column designs depend on the SC/WB ratios. When the SC/WB ratio is high, W14 columns have generally less doubler plate vertical edge areas due to their thick webs. When doubler plates are used on W14 and W24 columns, their effect is more on W24s as the increase in panel zone shear strength is directly related to the column depth. The number of joints that needed doubler plates is also shown in parenthesis in Table B-2. As may be seen, the number of doubler plate requirement in terms of joint numbers are always less for W14 column designs no matter what SC/WB ratio is.

Higher strengths are achieved in pushover curves with the use of W14 columns. The initial stiffness of the pushover curves is slightly higher for W24 column designs. This can also be observed from the computed periods tabulated in Table B-2.

Regarding nonlinear response history analyses results, residual and maximum drifts are mostly better for W24 columns at DBE and MCE levels. This should be due to the higher initial stiffnesses of W24 column designs and similar post-yield stiffnesses. For the 3 story designs with SC/WB of 1.0 (see Figure B-6), however, the post yield stiffness is much lower for the W24 column design, as a result, the residual and maximum drifts (especially at high intensities) are much better for W14 column design. At 1.5xMCE ground motion intensity, W14 column designs gave generally better performance. This is reflected in the fragility curves. W14 column designs gave better lower probabilities than W24 column designs for three and six story models. Fragility curves of ten story, different column depth designs were very close to each other.

It can be concluded that lower W24 column deterioration parameters (see Figure B-2 and Figure B-3) did not affect the dynamic analyses results significantly. This should be because the deterioration is more important in the girders as they yield earlier than the columns, and attract more damage. Also, although W24 columns have worse deterioration parameters than W14 columns, they should still be good enough for reasonable performance. Note that the effect of axial load on deterioration parameters is neglected as the modified Ibarra-Krawinkler model is actually calibrated for beams. Thus, the results presented in this Appendix are within this column modeling limitation.

Table B-2. Summary of Archetypes for W14 and W24 Column Designs with Various SC/WB Ratios

Archetype ID	Weight (lbs)			Doubler Plate Vert. Edge (in^2) and # of joints	T_1 (sec)
	Column	Girder	Total		
1-3St-Dmax-W14-SC/WB=1.0-REG	36900	32700	69600	656 (16)	1.32
8-3St-Dmax-W24-SC/WB=1.0-REG	23124	30300	53424	332 (18)	1.23
4-3St-Dmax-W14-SC/WB=1.5-REG	45428	31500	76928	349 (12)	1.29
11-3St-Dmax-W24-SC/WB=1.5-REG	27716	29100	56816	240 (18)	1.20
7-3St-Dmax-W14-SC/WB=2.0-REG	55186	30300	85486	117 (10)	1.25
14-3St-Dmax-W24-SC/WB=2.0-REG	34276	29100	63376	156 (12)	1.15
1-6St-Dmax-W14-SC/WB=1.0-REG	91992	87600	179592	1748 (36)	2.00
8-6St-Dmax-W24-SC/WB=1.0-REG	59236	77850	137086	973 (36)	1.94
4-6St-Dmax-W14-SC/WB=1.5-REG	112052	80850	192902	843 (30)	2.00
11-6St-Dmax-W24-SC/WB=1.5-REG	67892	72900	140792	705 (36)	1.95
7-6St-Dmax-W14-SC/WB=2.0-REG	132748	74400	207148	65 (8)	2.03
14-6St-Dmax-W24-SC/WB=2.0-REG	82028	70200	152228	350 (30)	1.97
1-10St-Dmax-W14-SC/WB=1.0-REG	222176	188550	410726	3050 (58)	2.46
8-10St-Dmax-W24-SC/WB=1.0-REG	135472	174600	310072	2646 (60)	2.40
4-10St-Dmax-W14-SC/WB=1.5-REG	267396	171750	439146	631 (34)	2.50
11-10St-Dmax-W24-SC/WB=1.5-REG	178864	164400	343264	1110 (52)	2.42
7-10St-Dmax-W14-SC/WB=2.0-REG	307056	159450	466506	64 (6)	2.51
14-10St-Dmax-W24-SC/WB=2.0-REG	211440	161400	372840	359 (36)	2.44

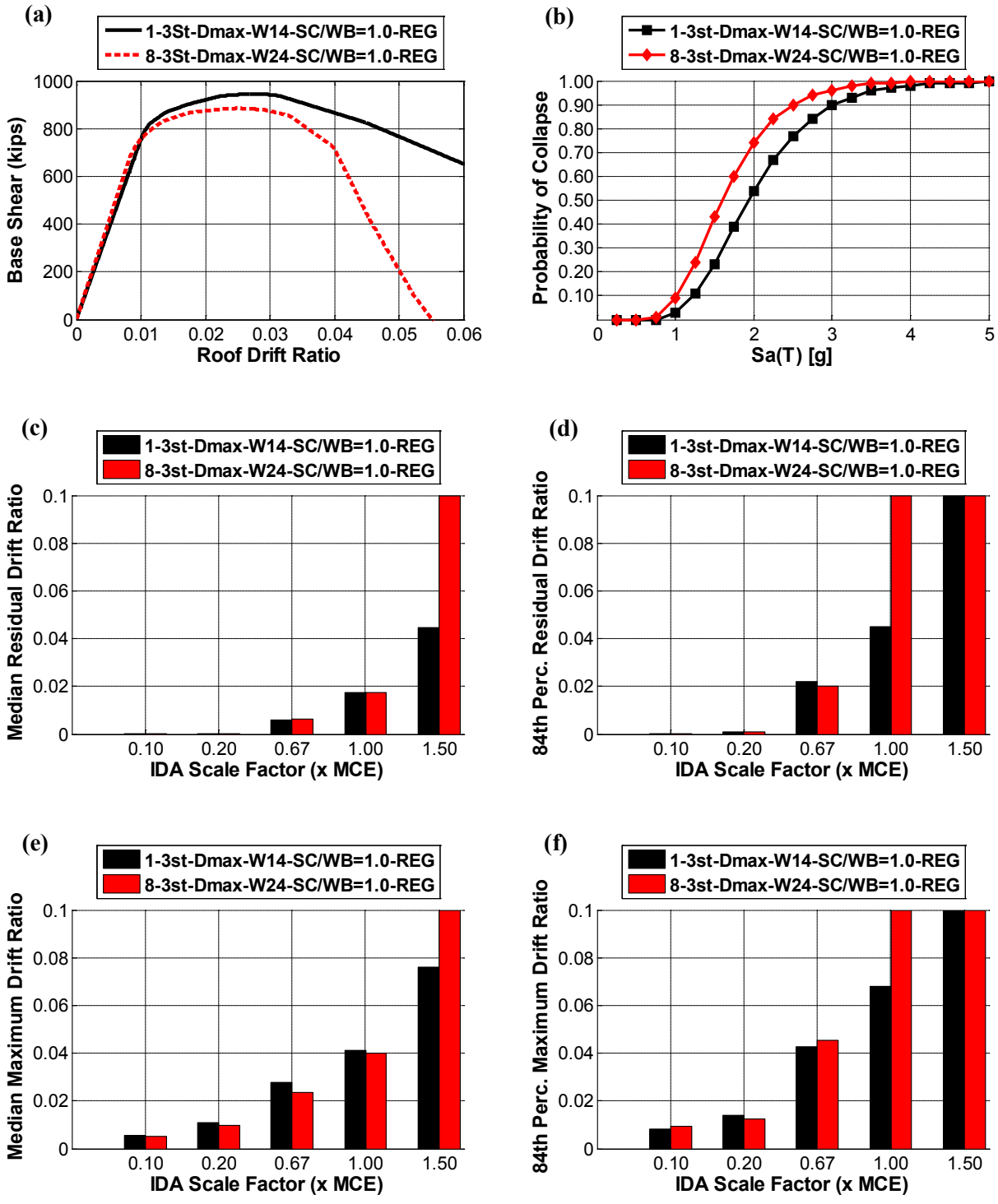

Figure B-6. Comparison between W14 and W24 Column Designs for 3 Story SMF Designed at Dmax SDC with SC/WB Ratio of 1.0 (a) Pushover Curves, (b) Fragility Curves, (c) Median Residual Drift Ratios, (d) 84th Percentile Residual Drift Ratios, (e) Median Maximum Drift Ratios, (f) 84th Percentile Maximum Drift Ratios

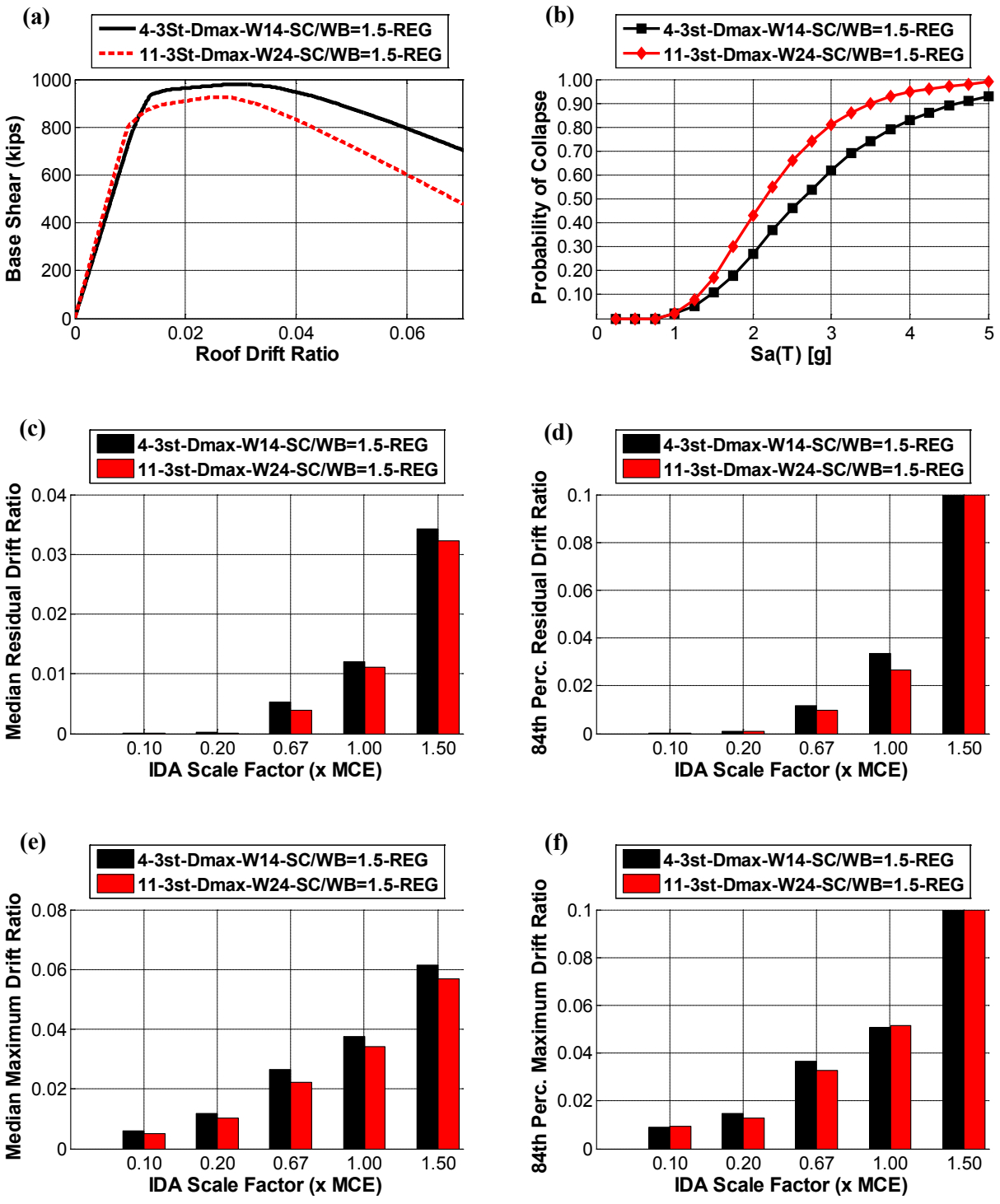

Figure B-7. Comparison between W14 and W24 Column Designs for 3 story SMF Designed at Dmax SDC with SC/WB Ratio of 1.5 (a) Pushover Curves, (b) Fragility Curves, (c) Median Residual Drift Ratios, (d) 84th Percentile Residual Drift Ratios, (e) Median Maximum Drift Ratios, (f) 84th Percentile Maximum Drift Ratios

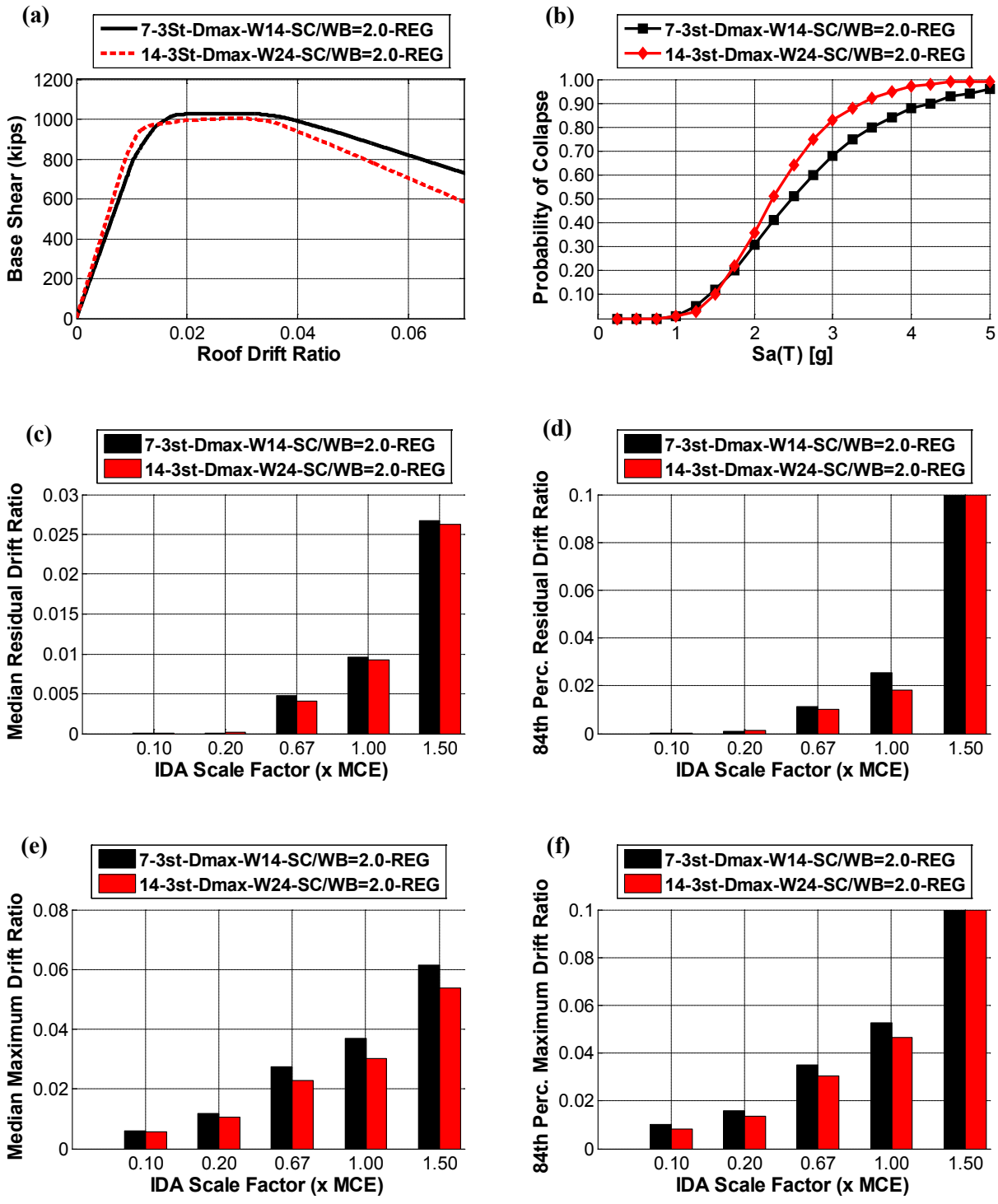

Figure B-8. Comparison between W14 and W24 Column Designs for 3 Story SMF Designed at Dmax SDC with SC/WB Ratio of 2.0 (a) Pushover Curves, (b) Fragility Curves, (c) Median Residual Drift Ratios, (d) 84th Percentile Residual Drift Ratios, (e) Median Maximum Drift Ratios, (f) 84th Percentile Maximum Drift Ratios

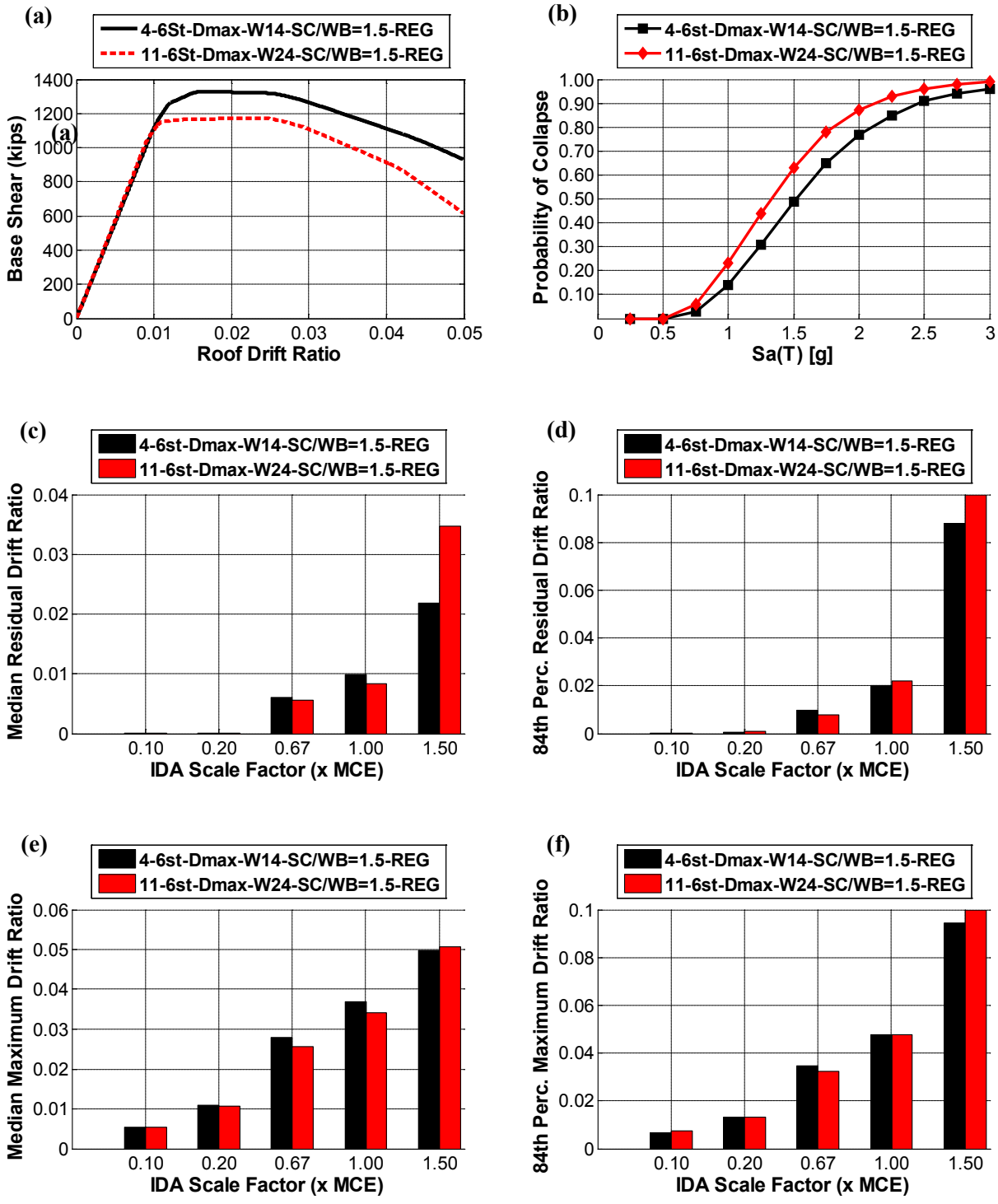

Figure B-9. Comparison between W14 and W24 Column Designs for 6 Story SMF Designed at Dmax SDC with SC/WB Ratio of 1.5 (a) Pushover Curves, (b) Fragility Curves, (c) Median Residual Drift Ratios, (d) 84th Percentile Residual Drift Ratios, (e) Median Maximum Drift Ratios, (f) 84th Percentile Maximum Drift Ratios

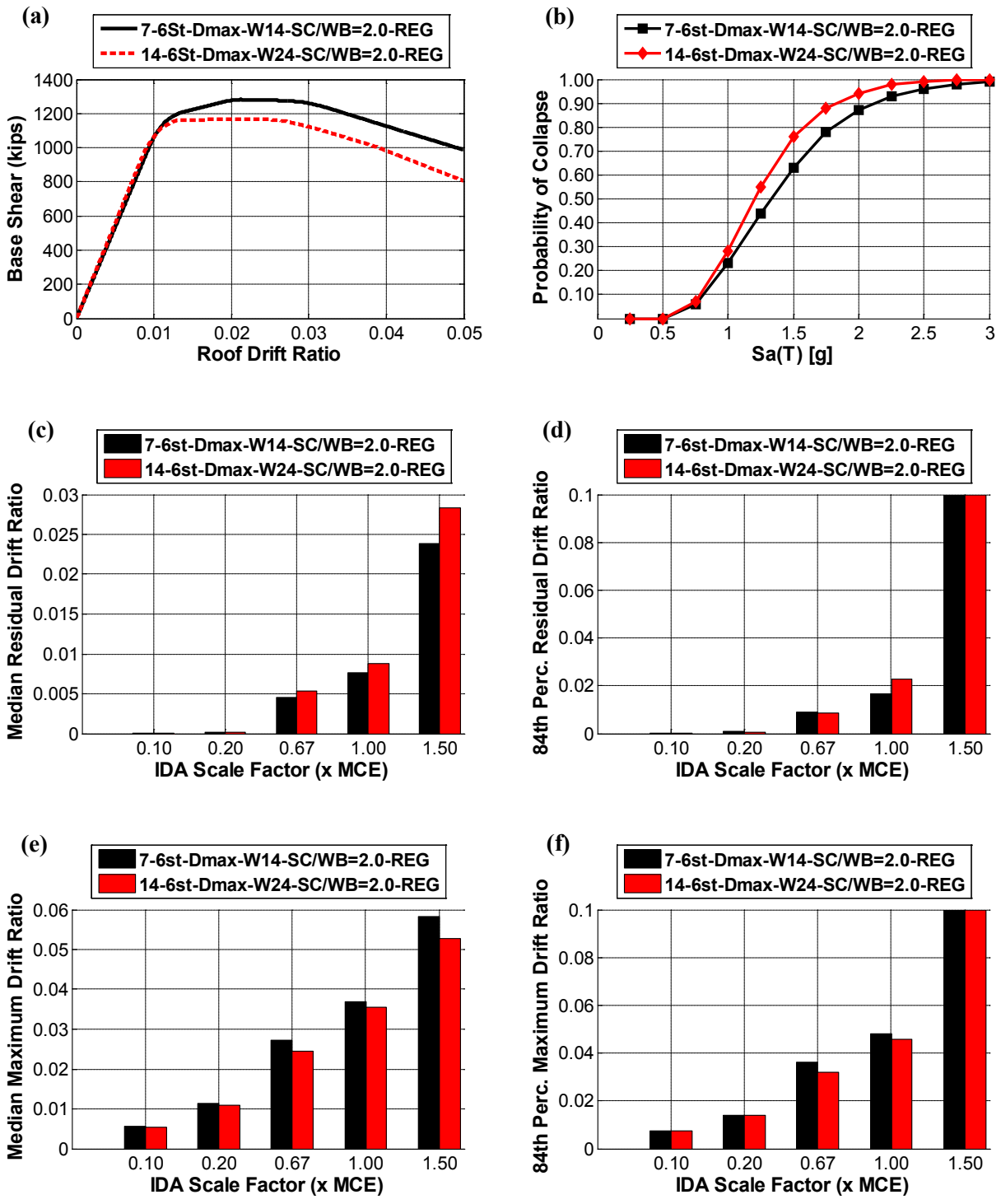

Figure B-10. Comparison between W14 and W24 Column Designs for 6 Story SMF Designed at Dmax SDC with SC/WB Ratio of 2.0 (a) Pushover Curves, (b) Fragility Curves, (c) Median Residual Drift Ratios, (d) 84th Percentile Residual Drift Ratios, (e) Median Maximum Drift Ratios, (f) 84th Percentile Maximum Drift Ratios

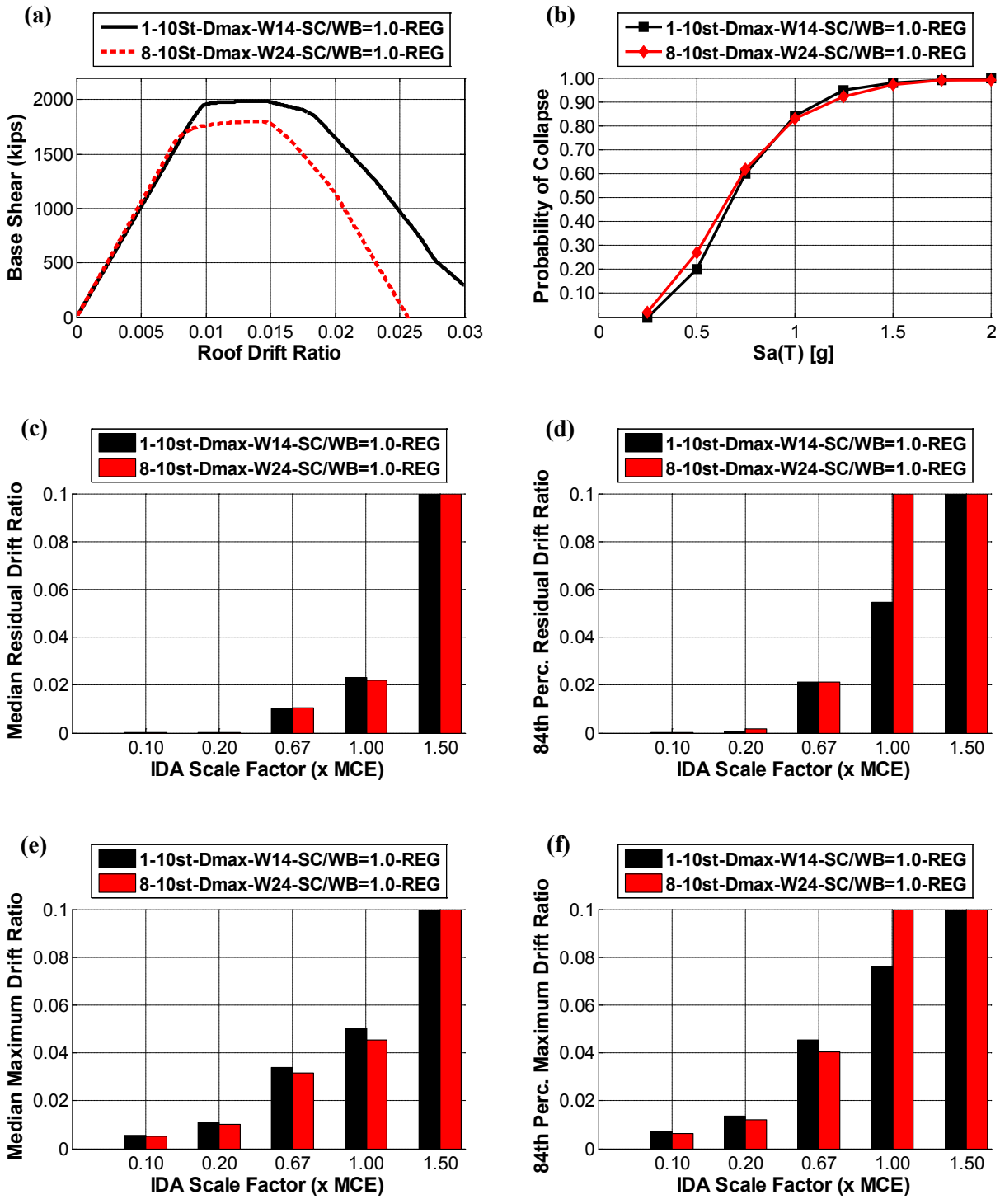

Figure B-11. Comparison between W14 and W24 Column Designs for 10 Story SMF Designed at Dmax SDC with SC/WB Ratio of 1.0 (a) Pushover Curves, (b) Fragility Curves, (c) Median Residual Drift Ratios, (d) 84th Percentile Residual Drift Ratios, (e) Median Maximum Drift Ratios, (f) 84th Percentile Maximum Drift Ratios

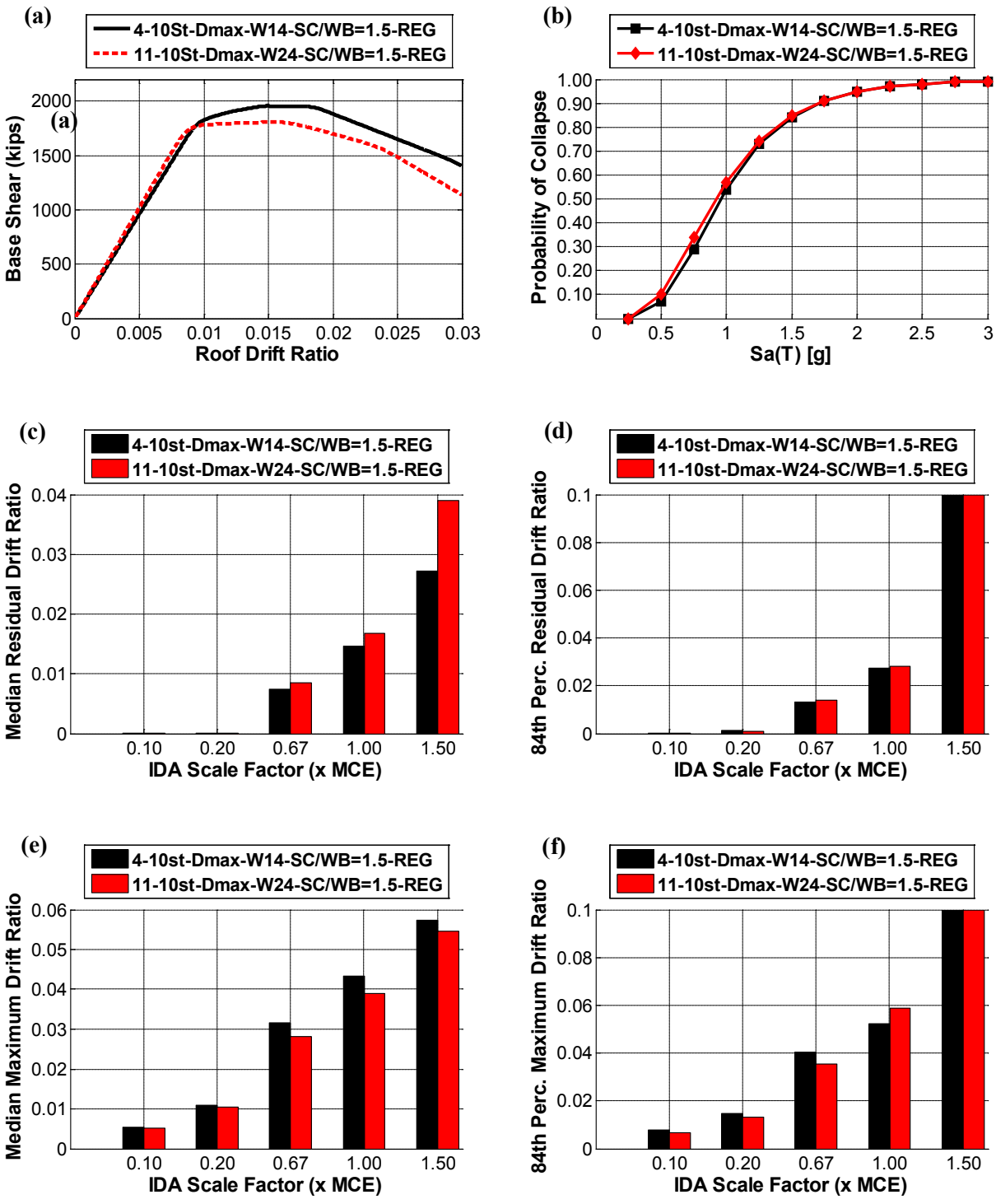

Figure B-12. Comparison between W14 and W24 Column Designs for 10 Story SMF Designed at Dmax SDC with SC/WB Ratio of 1.5 (a) Pushover Curves, (b) Fragility Curves, (c) Median Residual Drift Ratios, (d) 84th Percentile Residual Drift Ratios, (e) Median Maximum Drift Ratios, (f) 84th Percentile Maximum Drift Ratios

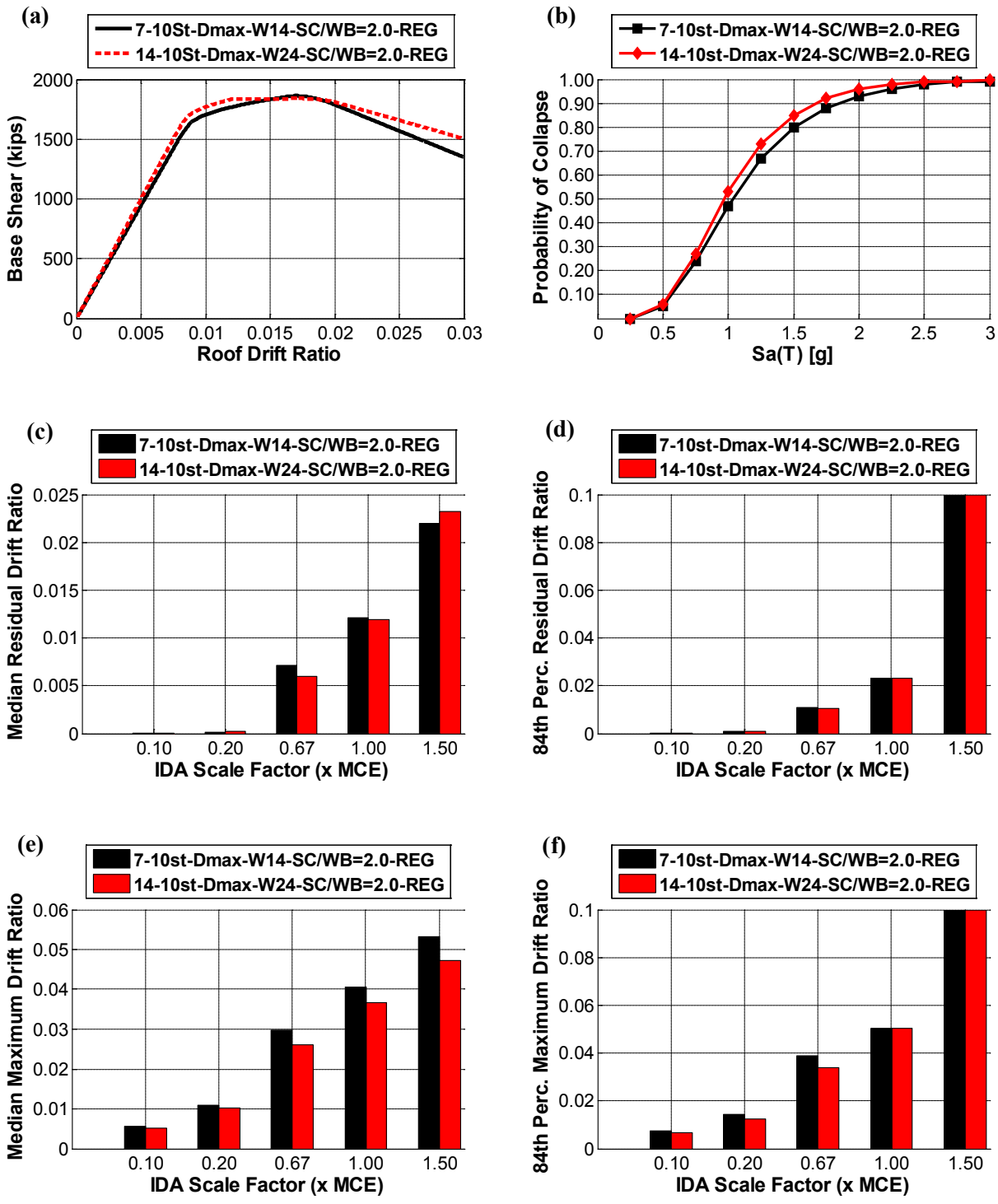

Figure B-13. Comparison between W14 and W24 Column Designs for 10 Story SMF Designed at Dmax SDC with SC/WB Ratio of 2.0 (a) Pushover Curves, (b) Fragility Curves, (c) Median Residual Drift Ratios, (d) 84th Percentile Residual Drift Ratios, (e) Median Maximum Drift Ratios, (f) 84th Percentile Maximum Drift Ratios

B.2. Effect of Strong Column Weak Beam Ratio (SC/WB) on Moment Frames

This section investigates the effect of SC/WB ratio on designs with different building heights (three, six and ten story models) and different column depths (W14 and W24). As mentioned in Chapter 5, when SC/WB was increased from 1.0 to 1.5 or 2.0, a complete new design was made. Thus, the girder sections of the higher SC/WB ratio designs are actually smaller than the lower SC/WB ratio designs when the designs are drift-controlled.

Table B-3 shows the archetype groups focusing on the SC/WB ratio difference. As may be seen in Table B-3, the weights of the frames increase as the SC/WB ratios increase. However, the doubler plate vertical edge areas and the number of joints that requires doubler plates decrease significantly as the SC/WB ratio increases. The stiffness of the strength controlled designs (three story models) increase as the SC/WB ratio increases. The stiffness of the drift-controlled designs remains similar or decreases slightly as the SC/WB ratio increases (see the period values in Table B-3). The change in the stiffness of drift controlled designs is controlled by the change in the sizes of both columns and girders. Figure B-14 through Figure B-19 illustrate the performance of the archetypes tabulated in Table B-3.

When the pushover curves are compared, it is seen that six and ten story models with different SC/WB ratios have the same strength, while the strength increased with higher SC/WB ratio for the three story design. This is because the three story design is strength-controlled, i.e. the girder sections were governed by strength and thus higher SC/WB ratio designs have bigger column sections and the same girder sections as the lower SC/WB ratio designs. As a result, strength increased for three story high SC/WB ratio designs. The more important change in the pushover curves is the higher post-yield stiffnesses obtained with higher SC/WB ratio designs. The difference in the post-yield stiffnesses is especially huge between SC/WB ratio of 1.0 and SC/WB ratio of 1.5 designs. This is because the story mechanisms were already prevented when the SC/WB ratio was increased from 1.0 to 1.5, thus the effect of increasing the SC/WB ratio further (from 1.5 to 2.0) did not help much.

Designs with SC/WB ratio of 1.5 and 2.0 gave much less collapse probabilities than the SC/WB ratio of 1.0 design as expected (see the fragility curves of Figure B-14 through Figure B-19). Similarly the residual and maximum story drifts decreased substantially for the higher SC/WB ratio designs.

In conclusion, the performance increased significantly for higher SC/WB ratio designs. This is related with the prevention of story mechanisms with bigger column sizes. The performance of SC/WB ratio of 1.5 designs was sometimes slightly better than SC/WB ratio of 2.0 designs. This is possible for the drift-controlled designs due to the different girder sizes used.

Table B-3. Summary of Archetypes Used to Investigate the Effect of Different SC/WB Ratios

Archetype ID	Weight (lbs)			Panel Zone Vert. Edge (in^2) and # of joints	T_1 (sec)
	Column	Girder	Total		
1-3St-Dmax-W14-SC/WB=1.0-REG	36900	32700	69600	656 (16)	1.32
4-3St-Dmax-W14-SC/WB=1.5-REG	45428	31500	76928	349 (12)	1.29
7-3St-Dmax-W14-SC/WB=2.0-REG	55186	30300	85486	117 (10)	1.25
8-3St-Dmax-W24-SC/WB=1.0-REG	23124	30300	53424	332 (18)	1.23
11-3St-Dmax-W24-SC/WB=1.5-REG	27716	29100	56816	240 (18)	1.20
14-3St-Dmax-W24-SC/WB=2.0-REG	34276	29100	63376	156 (12)	1.15
1-6St-Dmax-W14-SC/WB=1.0-REG	91992	87600	179592	1748 (36)	2.00
4-6St-Dmax-W14-SC/WB=1.5-REG	112052	80850	192902	843 (30)	2.00
7-6St-Dmax-W14-SC/WB=2.0-REG	132748	74400	207148	65 (8)	2.03
8-6St-Dmax-W24-SC/WB=1.0-REG	59236	77850	137086	973 (36)	1.94
11-6St-Dmax-W24-SC/WB=1.5-REG	67892	72900	140792	705 (36)	1.95
14-6St-Dmax-W24-SC/WB=2.0-REG	82028	70200	152228	350 (30)	1.97
1-10St-Dmax-W14-SC/WB=1.0-REG	222176	188550	410726	3050 (58)	2.46
4-10St-Dmax-W14-SC/WB=1.5-REG	267396	171750	439146	631 (34)	2.50
7-10St-Dmax-W14-SC/WB=2.0-REG	307056	159450	466506	64 (6)	2.51
8-10St-Dmax-W24-SC/WB=1.0-REG	135472	174600	310072	2646 (60)	2.40
11-10St-Dmax-W24-SC/WB=1.5-REG	178864	164400	343264	1110 (52)	2.42
14-10St-Dmax-W24-SC/WB=2.0-REG	211440	161400	372840	359 (36)	2.44

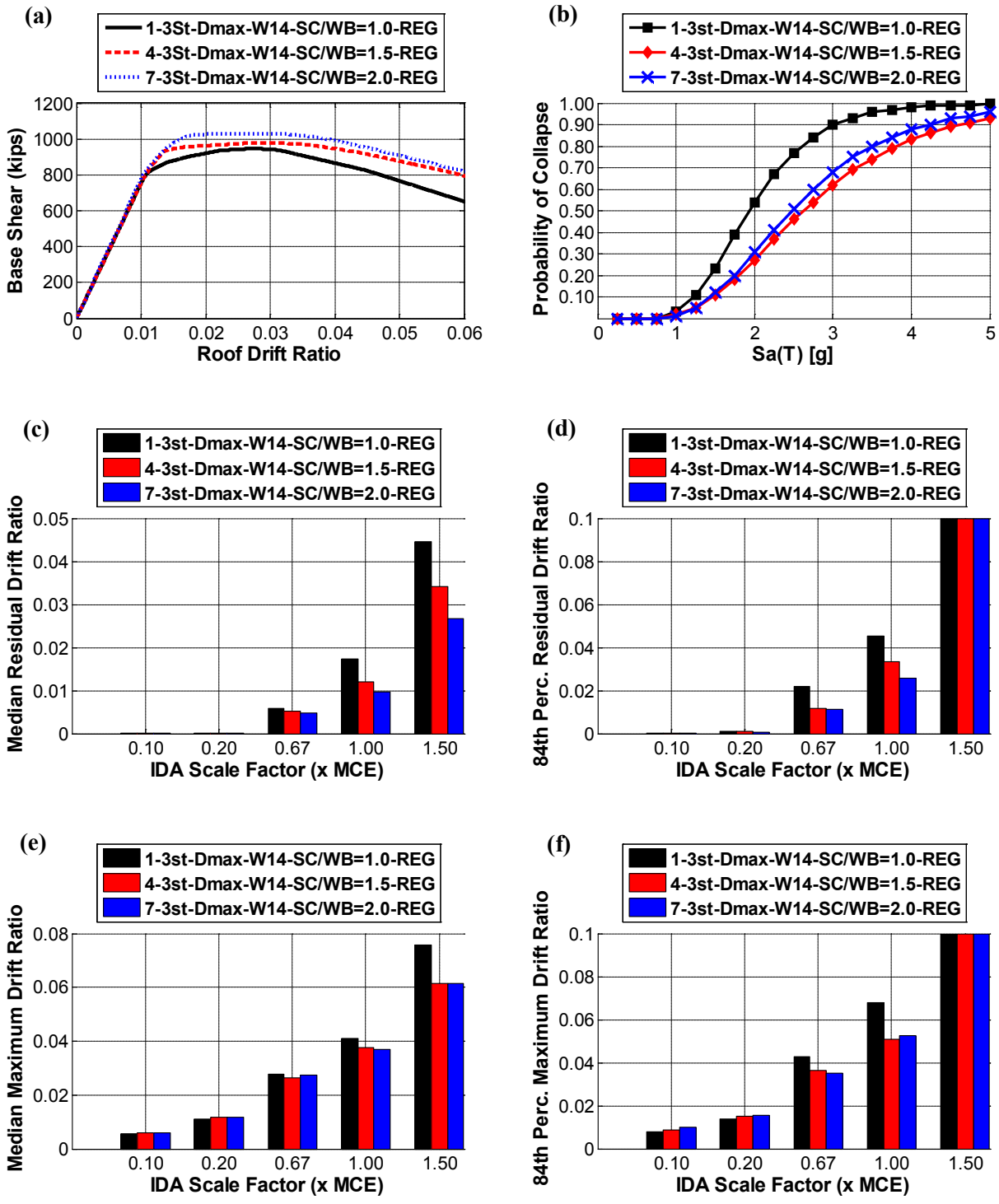

Figure B-14. Comparison among SC/WB=1.0, SC/WB=1.5 and SC/WB=2.0 Designs for 3 Story SMF Designed at Dmax SDC with W14 Columns (a) Pushover Curves, (b) Fragility Curves, (c) Median Residual Drift Ratios, (d) 84th Percentile Residual Drift Ratios, (e) Median Maximum Drift Ratios, (f) 84th Percentile Maximum Drift Ratios

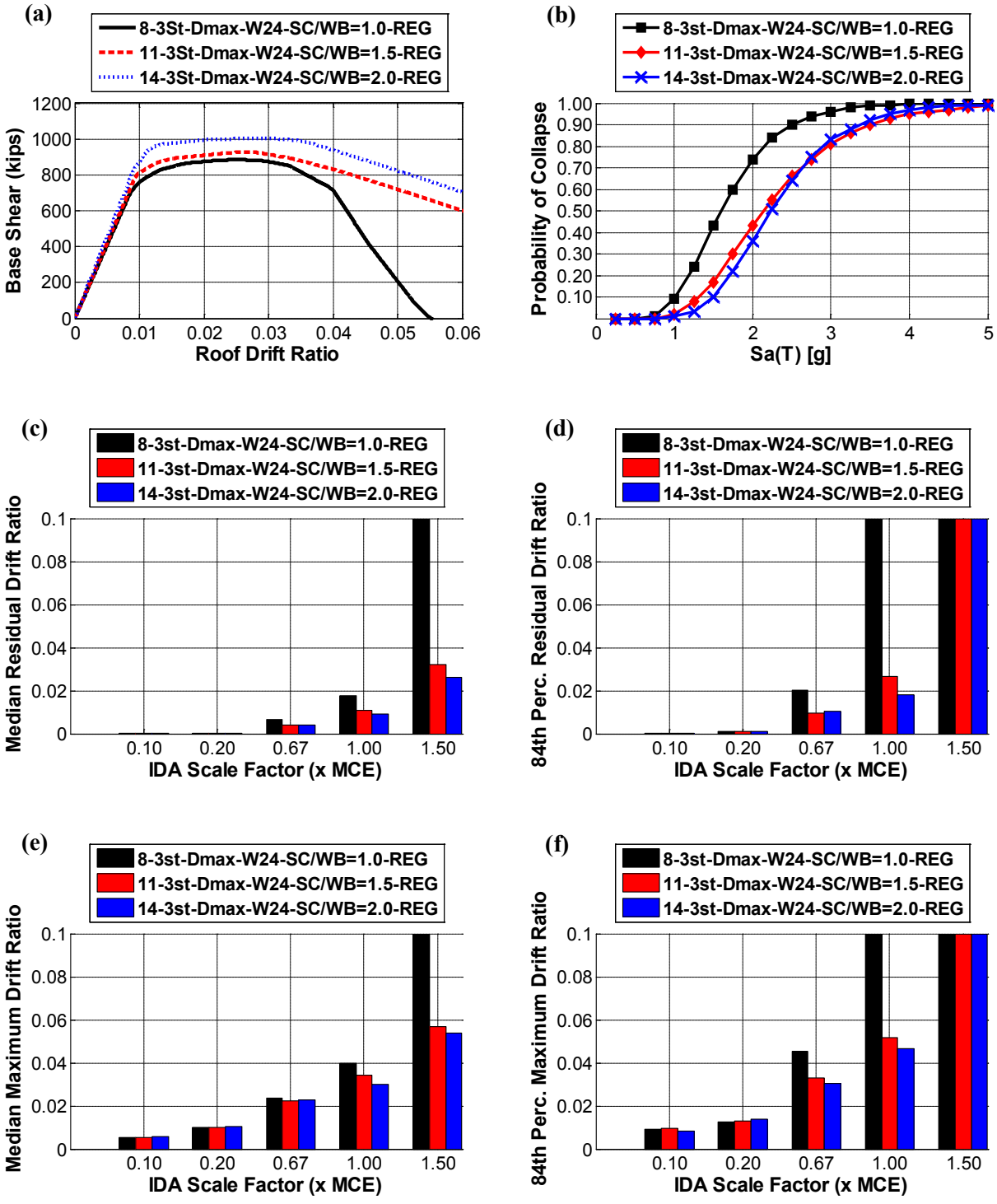

Figure B-15. Comparison among SC/WB=1.0, SC/WB=1.5 and SC/WB=2.0 Designs for 3 Story SMF Designed at Dmax SDC with W24 Columns (a) Pushover Curves, (b) Fragility Curves, (c) Median Residual Drift Ratios, (d) 84th Percentile Residual Drift Ratios, (e) Median Maximum Drift Ratios, (f) 84th Percentile Maximum Drift Ratios

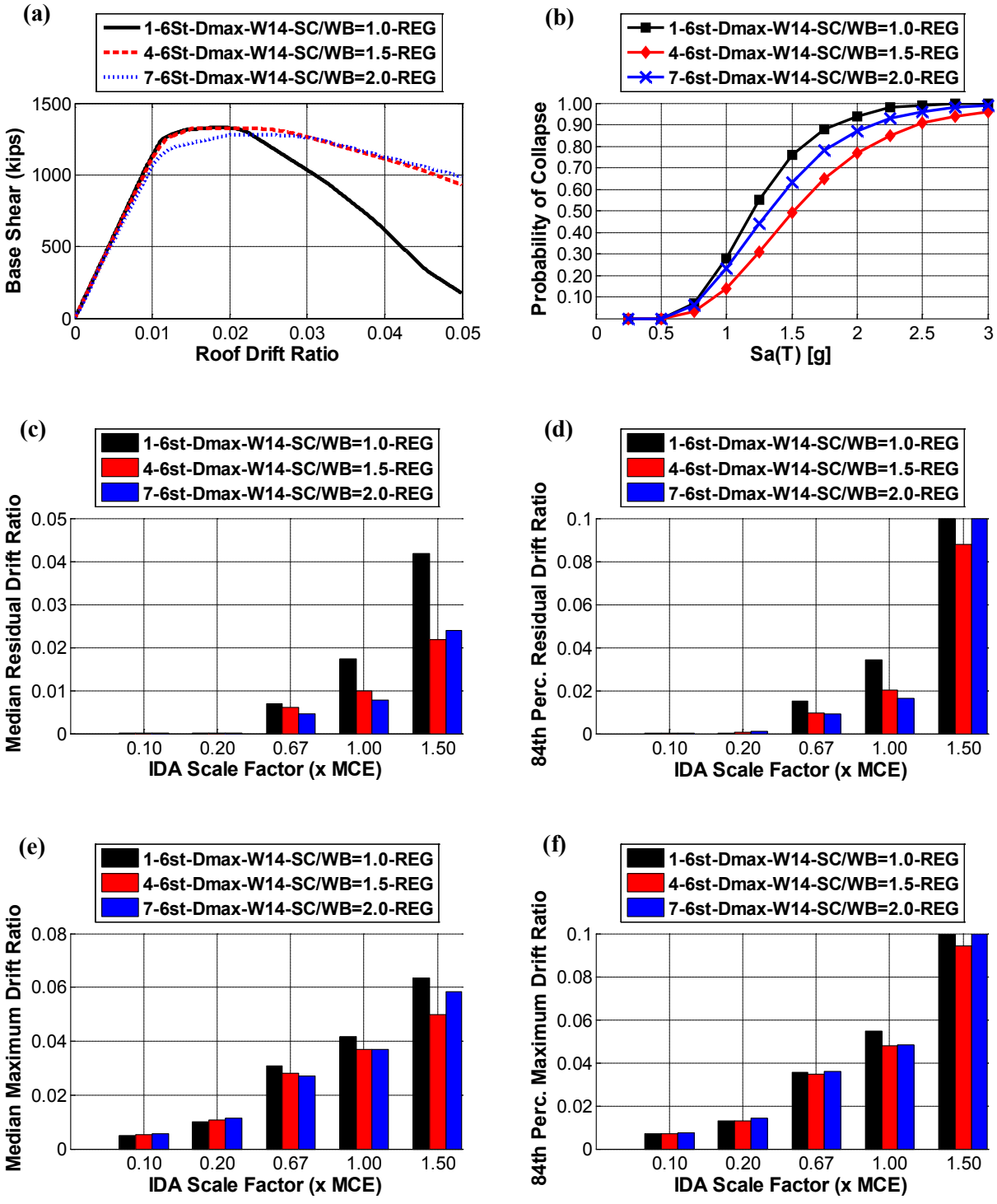

Figure B-16. Comparison among SC/WB=1.0, SC/WB=1.5 and SC/WB=2.0 Designs for 6 Story SMF Designed at Dmax SDC with W14 Columns (a) Pushover Curves, (b) Fragility Curves, (c) Median Residual Drift Ratios, (d) 84th Percentile Residual Drift Ratios, (e) Median Maximum Drift Ratios, (f) 84th Percentile Maximum Drift Ratios

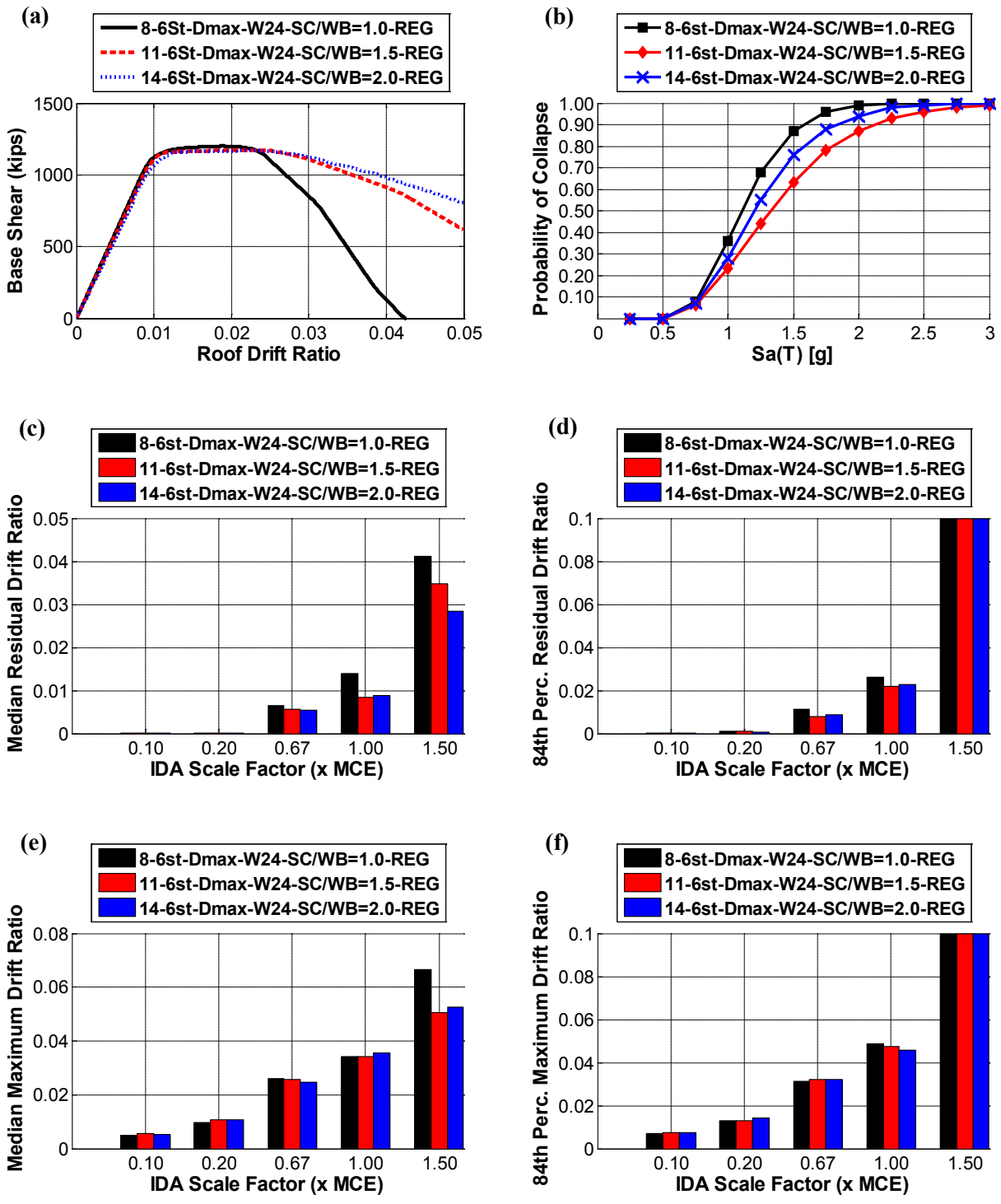

Figure B-17. Comparison among SC/WB=1.0, SC/WB=1.5 and SC/WB=2.0 Designs for 6 Story SMF Designed at Dmax SDC with W24 Columns (a) Pushover Curves, (b) Fragility Curves, (c) Median Residual Drift Ratios, (d) 84th Percentile Residual Drift Ratios, (e) Median Maximum Drift Ratios, (f) 84th Percentile Maximum Drift Ratios

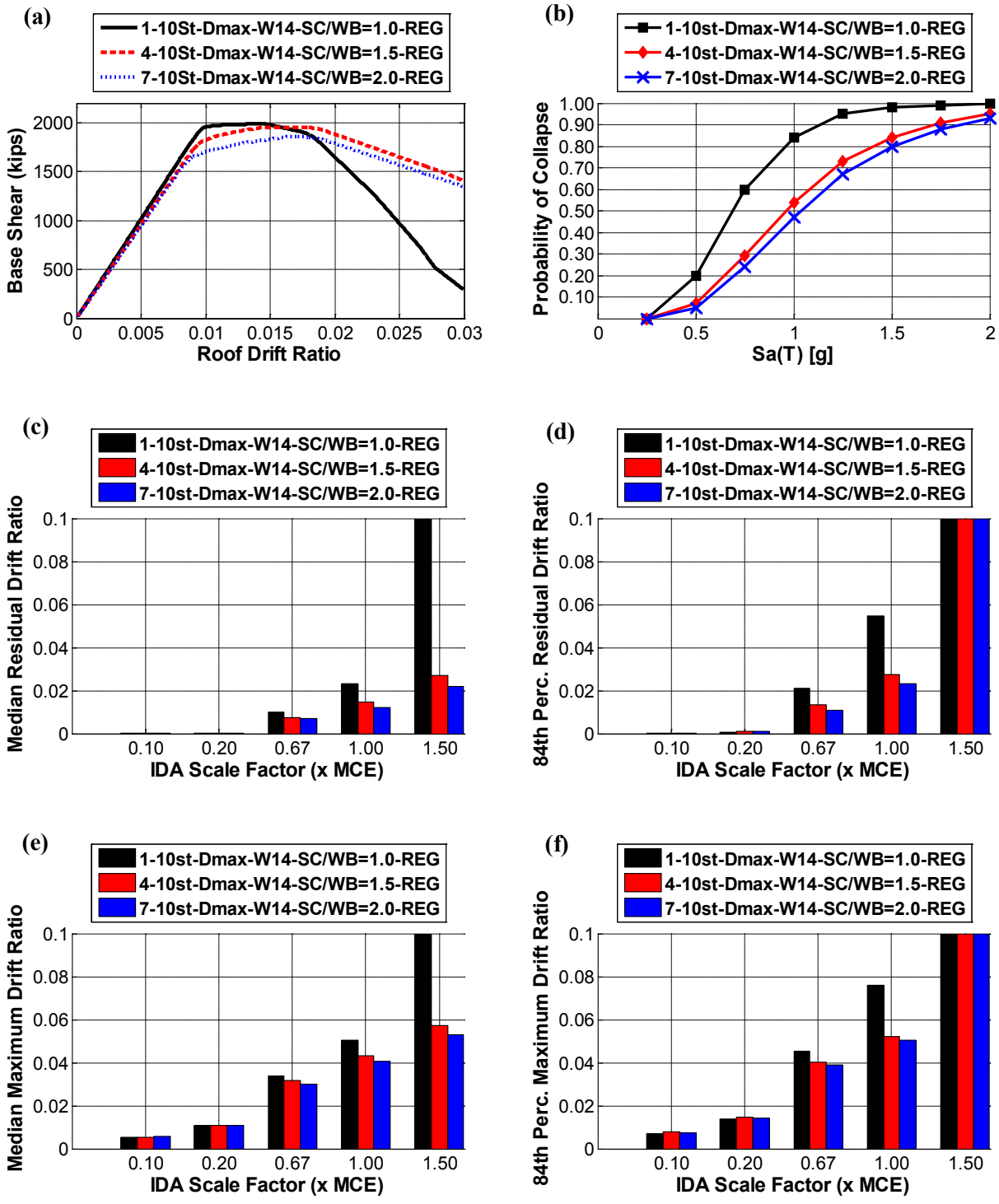

Figure B-18. Comparison among SC/WB=1.0, SC/WB=1.5 and SC/WB=2.0 Designs for 10 Story SMF Designed at Dmax SDC with W14 Columns (a) Pushover Curves, (b) Fragility Curves, (c) Median Residual Drift Ratios, (d) 84th Percentile Residual Drift Ratios, (e) Median Maximum Drift Ratios, (f) 84th Percentile Maximum Drift Ratios

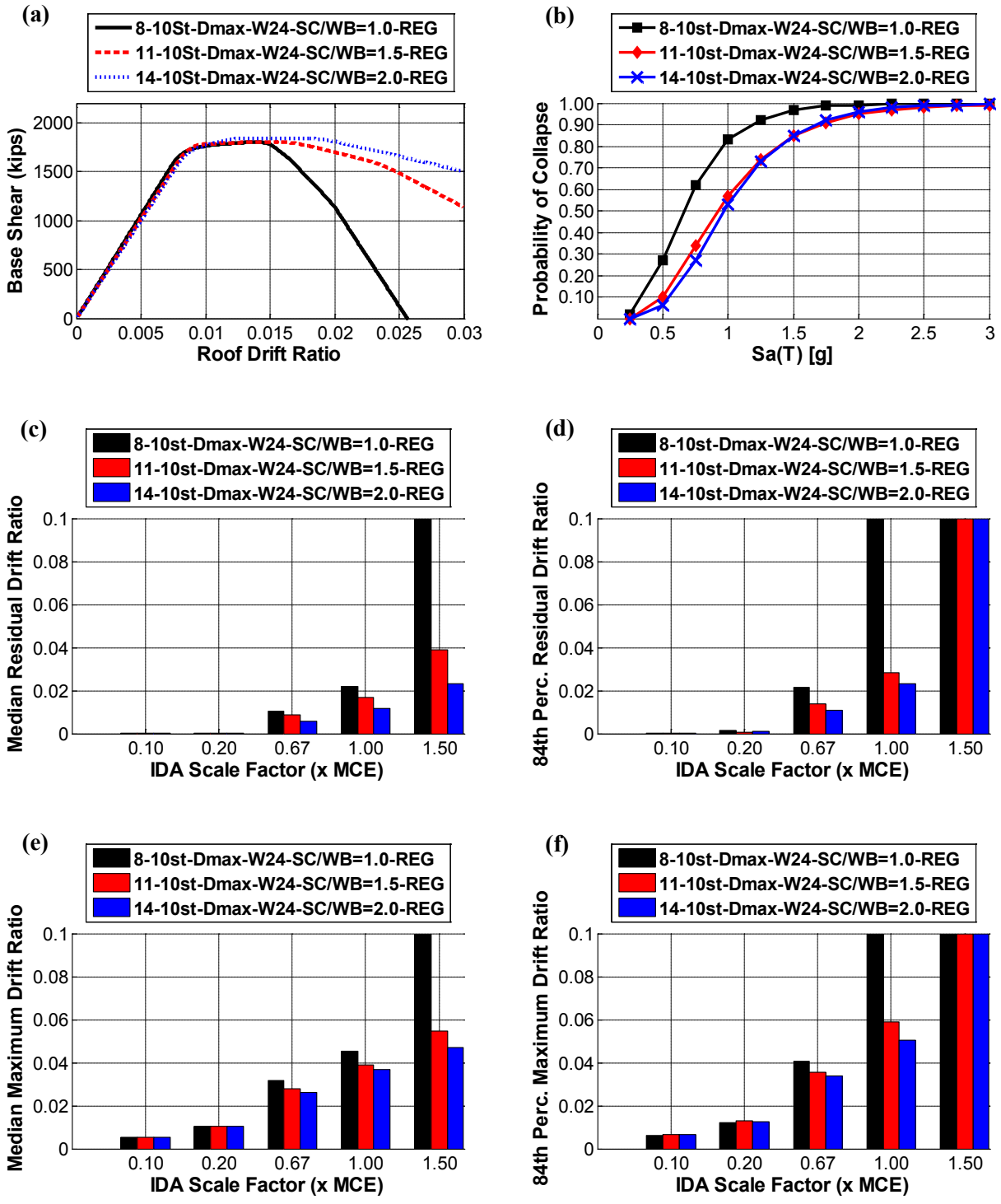

Figure B-19. Comparison among SC/WB=1.0, SC/WB=1.5 and SC/WB=2.0 Designs for 10 Story SMF Designed at Dmax SDC with W24 Columns (a) Pushover Curves, (b) Fragility Curves, (c) Median Residual Drift Ratios, (d) 84th Percentile Residual Drift Ratios, (e) Median Maximum Drift Ratios, (f) 84th Percentile Maximum Drift Ratios

B.3. Moment Frame Archetype Sections

B.2.1. 3 Story Model Sections

Table B-4. Sections for Archetype ID = 1-3St-Dmax-W14-SC/WB=1.0-REG

Level / story	Columns		Beams with RBS flange cut		Doubler Plate Sizes (in.)		
	Exterior	Interior	Bays 1-3-5	Bay 2-4	Ext. Col.	Middle Col.	Int. Col.
Roof	-	-	W21x50 (38%)	W21x50 (38%)	-	5/16	5/16
3	W14x132	W14x159	W27x84 (35%)	W27x84 (35%)	7/16	1-5/16	1-5/16
2	W14x132	W14x159	W24x84 (35%)	W24x84 (35%)	7/16	1-5/16	1-5/16
Ground	W14x132	W14x159	-	-	-	-	-

Table B-5. Sections for Archetype ID = 2-3St-Dmax-W14-SC/WB=1.0-HYB1

Level / story	Columns		Beams with RBS flange cut		Doubler Plate Sizes (in.)		
	Exterior	Interior	Bays 1-3-5	Bay 2-4	Ext. Col.	Middle Col.	Int. Col.
Roof	-	-	W18x46 (50%)	W18x76 (32%)	-	9/16	10/16
3	W14x132	W14x159	W24x76 (48%)	W27x114 (31%)	3/16	1-7/16	1-12/16
2	W14x132	W14x159	W24x68 (50%)	W21x132 (33%)	1/16	1-12/16	1-8/16
Ground	W14x132	W14x159	-	-	-	-	-

Table B-6. Sections for Archetype ID = 3-3St-Dmax-W14-SC/WB=1.0-HYB2

Level / story	Columns		Beams with RBS flange cut		Doubler Plate Sizes (in.)		
	Exterior	Interior	Bays 1-3-5	Bay 2-4	Ext. Col.	Middle Col.	Int. Col.
Roof	-	-	W18x40 (50%)	W18x86 (35%)	-	10/16	11/16
3	W14x132	W14x159	W24x62 (44%)	W27x129 (33%)	-	1-8/16	1-14/16
2	W14x132	W14x159	W24x62 (50%)	W21x147 (35%)	-	1-13/16	1-10/16
Ground	W14x132	W14x159	-	-	-	-	-

Table B-7. Sections for Archetype ID = 4-3St-Dmax-W14-SC/WB=1.5-REG

Level / story	Columns		Beams with RBS flange cut		Doubler Plate Sizes (in.)		
	Exterior	Interior	Bays 1-3-5	Bay 2-4	Ext. Col.	Middle Col.	Int. Col.
Roof	-	-	W21x50 (38%)	W21x50 (38%)	-	-	-
3	W14x132	W14x211	W24x76 (35%)	W24x76 (35%)	5/16	10/16	10/16
2	W14x132	W14x211	W24x84 (35%)	W24x84 (35%)	7/16	14/16	14/16
Ground	W14x132	W14x211	-	-	-	-	-

Table B-8. Sections for Archetype ID = 5-3St-Dmax-W14-SC/WB=1.5-HYB1

Level / story	Columns		Beams with RBS flange cut		Doubler Plate Sizes (in.)		
	Exterior	Interior	Bays 1-3-5	Bay 2-4	Ext. Col.	Middle Col.	Int. Col.
Roof	-	-	W18x46 (50%)	W18x76 (32%)	-	2/16	2/16
3	W14x132	W14x211	W24x62 (50%)	W24x103 (30%)	-	12/16	13/16
2	W14x132	W14x211	W24x68 (50%)	W21x132 (33%)	1/16	1-4/16	1-1/16
Ground	W14x132	W14x211	-	-	-	-	-

Table B-9. Sections for Archetype ID = 6-3St-Dmax-W14-SC/WB=1.5-HYB2

Level / story	Columns		Beams with RBS flange cut		Doubler Plate Sizes (in.)		
	Exterior	Interior	Bays 1-3-5	Bay 2-4	Ext. Col.	Middle Col.	Int. Col.
Roof	-	-	W18x40 (50%)	W18x86 (35%)	-	3/16	3/16
3	W14x132	W14x211	W24x55 (50%)	W24x132 (36%)	-	1-1/16	14/16
2	W14x132	W14x211	W24x62 (50%)	W21x147 (35%)	-	1-5/16	1-2/16
Ground	W14x132	W14x211	-	-	-	-	-

Table B-10. Sections for Archetype ID = 7-3St-Dmax-W14-SC/WB=2.0-REG

Level / story	Columns		Beams with RBS flange cut		Doubler Plate Sizes (in.)		
	Exterior	Interior	Bays 1-3-5	Bay 2-4	Ext. Col.	Middle Col.	Int. Col.
Roof	-	-	W21x50 (38%)	W21x50 (38%)	-	-	-
3	W14x159	W14x257	W24x68 (35%)	W24x68 (35%)	-	1/16	1/16
2	W14x159	W14x257	W24x84 (35%)	W24x84 (35%)	4/16	7/16	7/16
Ground	W14x159	W14x257	-	-	-	-	-

Table B-11. Sections for Archetype ID = 8-3St-Dmax-W24-SC/WB=1.0-REG

Level / story	Columns		Beams with RBS flange cut		Doubler Plate Sizes (in.)		
	Exterior	Interior	Bays 1-3-5	Bay 2-4	Ext. Col.	Middle Col.	Int. Col.
Roof	-	-	W21x50 (38%)	W21x50 (38%)	1/16	3/16	3/16
3	W24x76	W24x103	W24x68 (35%)	W24x68 (35%)	2/16	9/16	9/16
2	W24x76	W24x103	W24x84 (35%)	W24x84 (35%)	5/16	13/16	13/16
Ground	W24x76	W24x103	-	-	-	-	-

Table B-12. Sections for Archetype ID = 9-3St-Dmax-W24-SC/WB=1.0-HYB1

Level / story	Columns		Beams with RBS flange cut		Doubler Plate Sizes (in.)		
	Exterior	Interior	Bays 1-3-5	Bay 2-4	Ext. Col.	Middle Col.	Int. Col.
Roof	-	-	W18x46 (50%)	W18x76 (32%)	-	6/16	6/16
3	W24x76	W24x103	W24x55 (48%)	W24x94 (32%)	1/16	9/16	10/16
2	W24x76	W24x103	W24x68 (50%)	W21x132 (33%)	1/16	1-1/16	15/16
Ground	W24x76	W24x103	-	-	-	-	-

Table B-13. Sections for Archetype ID = 10-6St-Dmax-W24-SC/WB=1.0-HYB2

Level / story	Columns		Beams with RBS flange cut		Doubler Plate Sizes (in.)		
	Exterior	Interior	Bays 1-3-5	Bay 2-4	Ext. Col.	Middle Col.	Int. Col.
Roof	-	-	W18x40 (50%)	W18x86 (35%)	-	6/16	7/16
3	W24x76	W24x103	W21x55 (50%)	W24x103 (31%)	1/16	10/16	13/16
2	W24x76	W24x103	W24x62 (50%)	W21x147 (35%)	1/16	1-2/16	1
Ground	W24x76	W24x103	-	-	-	-	-

Table B-14. Sections for Archetype ID = 11-3St-Dmax-W24-SC/WB=1.5-REG

Level / story	Columns		Beams with RBS flange cut		Doubler Plate Sizes (in.)		
	Exterior	Interior	Bays 1-3-5	Bay 2-4	Ext. Col.	Middle Col.	Int. Col.
Roof	-	-	W21x50 (38%)	W21x50 (38%)	1/16	2/16	2/16
3	W24x76	W24x131	W24x68 (35%)	W24x68 (35%)	2/16	7/16	7/16
2	W24x76	W24x131	W24x76 (35%)	W24x76 (35%)	3/16	9/16	9/16
Ground	W24x76	W24x131	-	-	-	-	-

Table B-15. Sections for Archetype ID = 12-3St-Dmax-W24-SC/WB=1.5-HYB1

Level / story	Columns		Beams with RBS flange cut		Doubler Plate Sizes (in.)		
	Exterior	Interior	Bays 1-3-5	Bay 2-4	Ext. Col.	Middle Col.	Int. Col.
Roof	-	-	W18x46 (50%)	W18x76 (32%)	-	5/16	5/16
3	W24x76	W24x131	W24x55 (48%)	W24x94 (32%)	1/16	8/16	9/16
2	W24x76	W24x131	W24x62 (50%)	W24x103 (30%)	1/16	10/16	11/16
Ground	W24x76	W24x131	-	-	-	-	-

Table B-16. Sections for Archetype ID = 13-3St-Dmax-W24-SC/WB=1.5-HYB2

Level / story	Columns		Beams with RBS flange cut		Doubler Plate Sizes (in.)		
	Exterior	Interior	Bays 1-3-5	Bay 2-4	Ext. Col.	Middle Col.	Int. Col.
Roof	-	-	W18x40 (50%)	W18x86 (35%)	-	5/16	5/16
3	W24x76	W24x131	W21x55 (50%)	W24x103 (31%)	1/16	9/16	12/16
2	W24x76	W24x131	W24x55 (50%)	W21x132 (36%)	1/16	14/16	12/16
Ground	W24x76	W24x131	-	-	-	-	-

Table B-17. Sections for Archetype ID = 14-6St-Dmax-W24-SC/WB=2.0-REG

Level / story	Columns		Beams with RBS flange cut		Doubler Plate Sizes (in.)		
	Exterior	Interior	Bays 1-3-5	Bay 2-4	Ext. Col.	Middle Col.	Int. Col.
Roof	-	-	W21x50 (38%)	W21x50 (38%)	-	-	-
3	W24x94	W24x162	W24x68 (35%)	W24x68 (35%)	1/16	5/16	5/16
2	W24x94	W24x162	W24x76 (35%)	W24x76 (35%)	2/16	7/16	7/16
Ground	W24x94	W24x162	-	-	-	-	-

B.2.2. 6 Story Model Sections

Table B-18. Sections for Archetype ID = 1-6St-Dmax-W14-SC/WB=1.0-REG

Level / story	Columns		Beams with RBS flange cut		Doubler Plate Sizes (in.)		
	Exterior	Interior	Bays 1-3-5	Bay 2-4	Ext. Col.	Middle Col.	Int. Col.
Roof	-	-	W21x44 (38%)	W21x44 (38%)	1/16	4/16	4/16
6	W14x82	W14x145	W24x84 (35%)	W24x84 (35%)	10/16	23/16	23/16
5	W14x82	W14x145	W27x94 (35%)	W27x94 (35%)	9/16	15/16	1
4	W14x132	W14x233	W27x114 (35%)	W27x114 (35%)	14/16	1-8/16	1-8/16
3	W14x132	W14x233	W27x146 (35%)	W27x146 (35%)	1-1/16	1-15/16	1-15/16
2	W14x176	W14x283	W27x102 (35%)	W27x102 (35%)	6/16	11/16	11/16
Ground	W14x176	W14x283	-	-	-	-	-

Table B-19. Sections for Archetype ID = 2-6St-Dmax-W14-SC/WB=1.0-HYB1

Level / story	Columns		Beams with RBS flange cut		Doubler Plate Sizes (in.)		
	Exterior	Interior	Bays 1-3-5	Bay 2-4	Ext. Col.	Middle Col.	Int. Col.
Roof	-	-	W18x40 (50%)	W18x71 (36%)	-	8/16	9/16
6	W14x82	W14x145	W21x83 (46%)	W24x104 (30%)	8/16	1-9/16	1-14/16
5	W14x82	W14x145	W24x84 (48%)	W24x146 (34%)	5/16	1-6/16	1-7/16
4	W14x132	W14x233	W24x103 (48%)	W24x176 (34%)	8/16	1-15/16	2-1/16
3	W14x132	W14x233	W27x129 (50%)	W24x207 (28%)	8/16	2-7/16	2-2/16
2	W14x176	W14x283	W24x94 (50%)	W24x162 (36%)	1/16	1-2/16	1-3/16
Ground	W14x176	W14x283	-	-	-	-	-

Table B-20. Sections for Archetype ID = 3-6St-Dmax-W14-SC/WB=1.0-HYB2

Level / story	Columns		Beams with RBS flange cut		Doubler Plate Sizes (in.)		
	Exterior	Interior	Bays 1-3-5	Bay 2-4	Ext. Col.	Middle Col.	Int. Col.
Roof	-	-	W18x35 (50%)	W18x76 (36%)	-	9/16	9/16
6	W14x82	W14x145	W21x68 (50%)	W21x147 (35%)	5/16	1-15/16	2
5	W14x82	W14x145	W24x76 (50%)	W24x162 (36%)	3/16	1/7/16	1-8/16
4	W14x132	W14x233	W24x84 (48%)	W24x207 (38%)	4/16	2	2-2/16
3	W14x132	W14x233	W27x102 (48%)	W27x217 (29%)	3/16	2-4/16	2-5/16
2	W14x176	W14x283	W24x76 (50%)	W24x192 (39%)	-	1-3/16	1-5/16
Ground	W14x176	W14x283	-	-	-	-	-

Table B-21. Sections for Archetype ID = 4-6St-Dmax-W14-SC/WB=1.5-REG

Level / story	Columns		Beams with RBS flange cut		Doubler Plate Sizes (in.)		
	Exterior	Interior	Bays 1-3-5	Bay 2-4	Ext. Col.	Middle Col.	Int. Col.
Roof	-	-	W21x44 (38%)	W21x44 (38%)	-	-	-
6	W14x132	W14x193	W24x76 (35%)	W24x76 (35%)	5/16	13/16	13/16
5	W14x132	W14x193	W27x94 (35%)	W27x94 (35%)	6/16	12/16	12/16
4	W14x159	W14x257	W27x94 (35%)	W27x94 (35%)	6/16	12/16	12/16
3	W14x159	W14x257	W27x129 (35%)	W27x129 (35%)	7/16	13/16	13/16
2	W14x211	W14x342	W27x102 (35%)	W27x102 (35%)	2/16	3/16	3/16
Ground	W14x211	W14x342	-	-	-	-	-

Table B-22. Sections for Archetype ID = 5-6St-Dmax-W14-SC/WB=1.5-HYB1

Level / story	Columns		Beams with RBS flange cut		Doubler Plate Sizes (in.)		
	Exterior	Interior	Bays 1-3-5	Bay 2-4	Ext. Col.	Middle Col.	Int. Col.
Roof	-	-	W18x40 (50%)	W18x71 (36%)	-	1/16	2/16
6	W14x132	W14x193	W21x68 (50%)	W21x122 (34%)	1/16	1-3/16	1-4/16
5	W14x132	W14x193	W24x84 (48%)	W24x146 (36%)	2/16	1-1/16	1-2/16
4	W14x159	W14x257	W24x84 (48%)	W24x146 (36%)	2/16	1-1/16	1-2/16
3	W14x159	W14x257	W24x117 (48%)	W24x207 (37%)	1/16	1-5/16	1-6/16
2	W14x211	W14x342	W24x94 (50%)	W24x162 (36%)	-	9/16	10/16
Ground	W14x211	W14x342	-	-	-	-	-

Table B-23. Sections for Archetype ID = 6-6St-Dmax-W14-SC/WB=1.5-HYB2

Level / story	Columns		Beams with RBS flange cut		Doubler Plate Sizes (in.)		
	Exterior	Interior	Bays 1-3-5	Bay 2-4	Ext. Col.	Middle Col.	Int. Col.
Roof	-	-	W18x35 (50%)	W18x76 (36%)	-	2/16	3/16
6	W14x132	W14x193	W21x62 (50%)	W21x132 (35%)	-	1-3/16	1-5/16
5	W14x132	W14x193	W24x76 (50%)	W24x162 (36%)	-	1-3/16	1-4/16
4	W14x159	W14x257	W24x76 (50%)	W24x162 (36%)	-	1-3/16	1-4/16
3	W14x159	W14x257	W27x94 (50%)	W24x207 (28%)	-	1-7/16	1-3/16
2	W14x211	W14x342	W24x76 (50%)	W24x192 (39%)	-	10/16	12/16
Ground	W14x211	W14x342	-	-	-	-	-

Table B-24. Sections for Archetype ID = 7-6St-Dmax-W14-SC/WB=2.0-REG

Level / story	Columns		Beams with RBS flange cut		Doubler Plate Sizes (in.)		
	Exterior	Interior	Bays 1-3-5	Bay 2-4	Ext. Col.	Middle Col.	Int. Col.
Roof	-	-	W21x44 (39%)	W21x44 (39%)	-	-	-
6	W14x132	W14x211	W24x62 (37%)	W24x62 (37%)	1/16	4/16	4/16
5	W14x132	W14x211	W27x84 (35%)	W27x84 (35%)	-	-	-
4	W14x211	W14x370	W27x102 (35%)	W27x102 (35%)	2/16	-	-
3	W14x211	W14x370	W27x102 (35%)	W27x102 (35%)	-	-	-
2	W14x233	W14x370	W27x102 (35%)	W27x102 (35%)	-	-	-
Ground	W14x233	W14x370	-	-	-	-	-

Table B-25. Sections for Archetype ID = 8-6St-Dmax-W24-SC/WB=1.0-REG

Level / story	Columns		Beams with RBS flange cut		Doubler Plate Sizes (in.)		
	Exterior	Interior	Bays 1-3-5	Bay 2-4	Ext. Col.	Middle Col.	Int. Col.
Roof	-	-	W21x44 (38%)	W21x44 (38%)	2/16	2/16	2/16
6	W24X55	W24x94	W24x76 (35%)	W24x76 (35%)	5/16	11/16	11/16
5	W24X55	W24x94	W24x84 (35%)	W24x84 (35%)	4/16	10/16	10/16
4	W24X84	W24x146	W27x102 (35%)	W27x102 (35%)	6/16	1-3/16	1-3/16
3	W24X84	W24x146	W27x129 (35%)	W27x129 (35%)	7/16	1-4/16	1-4/16
2	W24X131	W24x176	W27x84 (38%)	W27x84 (38%)	1/16	7/16	7/16
Ground	W24X131	W24x176	-	-	-	-	-

Table B-26. Sections for Archetype ID = 9-6St-Dmax-W24-SC/WB=1.0-HYB1

Level / story	Columns		Beams with RBS flange cut		Doubler Plate Sizes (in.)		
	Exterior	Interior	Bays 1-3-5	Bay 2-4	Ext. Col.	Middle Col.	Int. Col.
Roof	-	-	W18x40 (50%)	W18x71 (36%)	1/16	5/16	5/16
6	W24x55	W24x94	W21x68 (50%)	W24x104 (30%)	2/16	13/16	1
5	W24x55	W24x94	W21x73 (46%)	W24x117 (32%)	1/16	12/16	1-3/16
4	W24x84	W24x146	W24x94 (50%)	W24x162 (36%)	3/16	1-4/16	1-5/16
3	W24x84	W24x146	W24x117 (48%)	W24x207 (37%)	4/16	1-10/16	1-11/16
2	W24x131	W24x176	W24x76 (50%)	W24x131 (38%)	-	11/16	12/16
Ground	W24x131	W24x176	-	-	-	-	-

Table B-27. Sections for Archetype ID = 10-6St-Dmax-W24-SC/WB=1.0-HYB2

Level / story	Columns		Beams with RBS flange cut		Doubler Plate Sizes (in.)		
	Exterior	Interior	Bays 1-3-5	Bay 2-4	Ext. Col.	Middle Col.	Int. Col.
Roof	-	-	W18x35 (50%)	W18x76 (36%)	1/16	5/16	6/16
6	W24x55	W24x94	W21x55 (42%)	W24x117 (33%)	2/16	13/16	1-1/16
5	W24x55	W24x94	W21x62 (44%)	W24x131 (33%)	1/16	13/16	1
4	W24x84	W24x146	W24x76 (50%)	W24x192 (39%)	1/16	1-5/16	1-6/16
3	W24x84	W24x146	W24x103 (50%)	W24x229 (37%)	2/16	1-10/16	1-12/16
2	W24x131	W24x176	W24x62 (48%)	W27x129 (36%)	-	9/16	12/16
Ground	W24x131	W24x176	-	-	-	-	-

Table B-28. Sections for Archetype ID = 11-6St-Dmax-W24-SC/WB=1.5-REG

Level / story	Columns		Beams with RBS flange cut		Doubler Plate Sizes (in.)		
	Exterior	Interior	Bays 1-3-5	Bay 2-4	Ext. Col.	Middle Col.	Int. Col.
Roof	-	-	W21x44 (38%)	W21x44 (38%)	1/16	2/16	2/16
6	W24x62	W24x103	W21x68 (35%)	W21x68 (35%)	3/16	8/16	8/16
5	W24x62	W24x103	W27x84 (38%)	W27x84 (38%)	1/16	8/16	8/16
4	W24x131	W24x176	W27x94 (35%)	W27x94 (35%)	3/16	11/16	11/16
3	W24x131	W24x176	W27x102 (35%)	W27x102 (35%)	4/16	11/16	11/16
2	W24x131	W24x192	W27x94 (35%)	W27x94 (35%)	3/16	9/16	9/16
Ground	W24x131	W24x192	-	-	-	-	-

Table B-29. Sections for Archetype ID = 12-6St-Dmax-W24-SC/WB=1.5-HYB1

Level / story	Columns		Beams with RBS flange cut		Doubler Plate Sizes (in.)		
	Exterior	Interior	Bays 1-3-5	Bay 2-4	Ext. Col.	Middle Col.	Int. Col.
Roof	-	-	W18x40 (50%)	W18x71 (36%)	1/16	4/16	4/16
6	W24x62	W24x103	W21x55 (50%)	W21x93 (29%)	1/16	9/16	10/16
5	W24x62	W24x103	W24x76 (50%)	W24x131 (38%)	-	11/16	12/16
4	W24x131	W24x176	W24x84 (48%)	W24x146 (34%)	-	15/16	1
3	W24x131	W24x176	W24x94 (50%)	W24x162 (36%)	1/16	1	1
2	W24x131	W24x192	W24x84 (48%)	W24x146 (34%)	-	13/16	14/16
Ground	W24x131	W24x192	-	-	-	-	-

Table B-30. Sections for Archetype ID = 13-6St-Dmax-W24-SC/WB=1.5-HYB2

Level / story	Columns		Beams with RBS flange cut		Doubler Plate Sizes (in.)		
	Exterior	Interior	Bays 1-3-5	Bay 2-4	Ext. Col.	Middle Col.	Int. Col.
Roof	-	-	W18x35 (50%)	W18x76 (36%)	1/16	4/16	5/16
6	W24x62	W24x103	W21x48 (50%)	W21x101 (30%)	1/16	10/16	11/16
5	W24x62	W24x103	W24x62 (48%)	W27129 (36%)	-	9/16	12/16
4	W24x131	W24x176	W24x76 (50%)	W24x162 (36%)	-	15/16	1
3	W24x131	W24x176	W24x84 (50%)	W24x176 (37%)	-	1	1-1/16
2	W24x131	W24x192	W24x76 (50%)	W24x162 (36%)	-	14/16	15/16
Ground	W24x131	W24x192	-	-	-	-	-

Table B-31. Sections for Archetype ID = 14-6St-Dmax-W24-SC/WB=2.0-REG

Level / story	Columns		Beams with RBS flange cut		Doubler Plate Sizes (in.)		
	Exterior	Interior	Bays 1-3-5	Bay 2-4	Ext. Col.	Middle Col.	Int. Col.
Roof	-	-	W21x44 (38%)	W21x44 (38%)	1/16	-	-
6	W24x76	W24x131	W21x68 (35%)	W21x68 (35%)	2/16	7/16	7/16
5	W24x76	W24x131	W24x84 (35%)	W24x84 (35%)	1/16	3/16	3/16
4	W24x131	W24x229	W27x94 (35%)	W27x94 (35%)	3/16	6/16	6/16
3	W24x131	W24x229	W27x94 (35%)	W27x94 (35%)	1/16	6/16	6/16
2	W24x146	W24x229	W27x84 (36%)	W27x84 (36%)	-	3/16	3/16
Ground	W24x146	W24x229	-	-	-	-	-

B.2.3. 10 Story Model Sections

Table B-32. Sections for Archetype ID = 1-10St-Dmax-W14-SC/WB=1.0-REG

Level / story	Columns		Beams with RBS flange cut		Doubler Plate Sizes (in.)		
	Exterior	Interior	Bays 1-3-5	Bay 2-4	Ext. Col.	Middle Col.	Int. Col.
Roof	-	-	W21x44 (38%)	W21x44 (38%)	-	3/16	3/16
10	W14x132	W14x159	W24x94 (35%)	W24x94 (35%)	9/16	1-9/16	1-9/16
9	W14x132	W14x159	W30x116 (35%)	W30x116 (35%)	11/16	1-2/16	1-2/16
8	W14x159	W14x283	W33x118 (38%)	W33x118 (38%)	12/16	1-2/16	1-2/16
7	W14x159	W14x283	W33x130 (37%)	W33x130 (37%)	5/16	11/16	11/16
6	W14x233	W14x370	W33x141 (36%)	W33x141 (36%)	8/16	15/16	15/16
5	W14x233	W14x370	W33x152 (35%)	W33x152 (35%)	10/16	1-4/16	1-4/16
4	W14x233	W14x370	W33x152 (35%)	W33x152 (35%)	10/16	1-4/16	1-4/16
3	W14x233	W14x370	W33x169 (35%)	W33x169 (35%)	7/16	1-6/16	1-6/16
2	W14x283	W14x398	W33x141 (36%)	W33x141 (36%)	2/16	11/16	11/16
Ground	W14x283	W14x398	-	-	-	-	-

Table B-33. Sections for Archetype ID = 2-10St-Dmax-W14-SC/WB=1.0-HYB1

Level / story	Columns		Beams with RBS flange cut		Doubler Plate Sizes (in.)		
	Exterior	Interior	Bays 1-3-5	Bay 2-4	Ext. Col.	Middle Col.	Int. Col.
Roof	-	-	W18x40 (50%)	W18x71 (36%)	-	6/16	7/16
10	W14x132	W14x159	W24x76 (48%)	W21x147 (32%)	3/16	2-1/16	1-13/16
9	W14x132	W14x159	W27x102 (48%)	W27x178 (34%)	6/16	1-9/16	1-10/16
8	W14x159	W14x283	W30x108 (47%)	W33x152 (34%)	7/16	1-4/16	1-9/16
7	W14x159	W14x283	W30x116 (50%)	W30x191 (32%)	-	1-2/16	1-3/16
6	W14x233	W14x370	W30x132 (50%)	W30x211 (36%)	2/16	1-7/16	1-8/16
5	W14x233	W14x370	W33x118 (45%)	W30x235 (35%)	1/16	1-13/16	1-9/16
4	W14x233	W14x370	W33x118 (45%)	W30x235 (35%)	1/16	1-13/16	1-9/16
3	W14x233	W14x370	W33x130 (45%)	W30x261 (35%)	-	1-15/16	1-11/16
2	W14x283	W14x398	W30x132 (50%)	W30x211 (36%)	-	1-2/16	1-3/16
Ground	W14x283	W14x398	-	-	-	-	-

Table B-34. Sections for Archetype ID = 3-10St-Dmax-W14-SC/WB=1.0-HYB2

Level / story	Columns		Beams with RBS flange cut		Doubler Plate Sizes (in.)		
	Exterior	Interior	Bays 1-3-5	Bay 2-4	Ext. Col.	Middle Col.	Int. Col.
Roof	-	-	W18x35 (50%)	W18x76 (36%)	-	7/16	7/16
10	W14x132	W14x159	W24x68 (44%)	W24x131 (28%)	2/16	1-13/16	1-15/16
9	W14x132	W14x159	W27x84 (42%)	W30x173 (31%)	3/16	1-6/16	1-12/16
8	W14x159	W14x283	W30x90 (46%)	W33x169 (32%)	4/16	1-5/16	1-11/16
7	W14x159	W14x283	W30x108 (50%)	W30x211 (37%)	-	1-2/16	1-4/16
6	W14x233	W14x370	W30x108 (50%)	W30x235 (34%)	-	1-9/16	1-10/16
5	W14x233	W14x370	W30x116 (49%)	W30x261 (36%)	1/16	1-14/16	2
4	W14x233	W14x370	W30x116 (49%)	W30x261 (36%)	1/16	1-14/16	2
3	W14x233	W14x370	W33x118 (50%)	W30x292 (36%)	-	2-1/16	1-13/16
2	W14x283	W14x398	W30x108 (50%)	W30x235 (34%)	-	1-4/16	1-6/16
Ground	W14x283	W14x398	-	-	-	-	-

Table B-35. Sections for Archetype ID = 4-10St-Dmax-W14-SC/WB=1.5-REG

Level / story	Columns		Beams with RBS flange cut		Doubler Plate Sizes (in.)		
	Exterior	Interior	Bays 1-3-5	Bay 2-4	Ext. Col.	Middle Col.	Int. Col.
Roof	-	-	W21x44 (38%)	W21x44 (38%)	-	-	-
10	W14x132	W14x193	W24x76 (35%)	W24x76 (35%)	5/16	13/16	13/16
9	W14x132	W14x193	W30x108 (36%)	W30x108 (36%)	5/16	6/16	6/16
8	W14x193	W14x342	W30x116 (35%)	W30x116 (35%)	7/16	9/16	9/16
7	W14x193	W14x342	W33x118 (38%)	W33x118 (38%)	-	-	-
6	W14x257	W14x426	W33x130 (37%)	W33x130 (37%)	2/16	3/16	3/16
5	W14x257	W14x426	W33x141 (36%)	W33x141 (36%)	2/16	3/16	3/16
4	W14x283	W14x455	W33x130 (37%)	W33x130 (37%)	-	-	-
3	W14x283	W14x455	W33x152 (35%)	W33x152 (35%)	-	1/16	1/16
2	W14x342	W14x500	W33x130 (37%)	W33x130 (37%)	-	-	-
Ground	W14x342	W14x500	-	-	-	-	-

Table B-36. Sections for Archetype ID = 5-10St-Dmax-W14-SC/WB=1.5-HYB1

Level / story	Columns		Beams with RBS flange cut		Doubler Plate Sizes (in.)		
	Exterior	Interior	Bays 1-3-5	Bay 2-4	Ext. Col.	Middle Col.	Int. Col.
Roof	-	-	W18x40 (50%)	W18x71 (36%)	-	1/16	2/16
10	W14x132	W14x193	W24x62 (50%)	W24x103 (30%)	-	14/16	15/16
9	W14x132	W14x193	W27x94 (48%)	W27x161 (33%)	-	12/16	13/16
8	W14x193	W14x342	W27x102 (48%)	W27x178 (35%)	1/16	1	1-1/16
7	W14x193	W14x342	W33x152 (33%)	W30x108 (48%)	-	-	4/16
6	W14x257	W14x426	W30x116 (50%)	W30x191 (32%)	-	9.16	10/16
5	W14x257	W14x426	W30x132 (50%)	W30x211 (36%)	-	10/16	10/16
4	W14x283	W14x455	W30x116 (50%)	W30x191 (32%)	-	5/16	6/16
3	W14x283	W14x455	W33x118 (45%)	W30x235 (35%)	-	8/16	5/16
2	W14x342	W14x500	W30x116 (50%)	W30x191 (32%)	-	-	-
Ground	W14x342	W14x500	-	-	-	-	-

Table B-37. Sections for Archetype ID = 6-10St-Dmax-W14-SC/WB=1.5-HYB2

Level / story	Columns		Beams with RBS flange cut		Doubler Plate Sizes (in.)		
	Exterior	Interior	Bays 1-3-5	Bay 2-4	Ext. Col.	Middle Col.	Int. Col.
Roof	-	-	W18x35 (50%)	W18x76 (36%)	-	2/16	3/16
10	W14x132	W14x193	W21x62 (50%)	W21x132 (35%)	-	1-3/16	1-5/16
9	W14x132	W14x193	W27x84 (50%)	W27x178 (34%)	-	13/16	14/16
8	W14x193	W14x342	W27x84 (42%)	W30x173 (31%)	-	14/16	1-3/16
7	W14x193	W14x342	W30x90 (46%)	W33x169 (33%)	-	1/16	5/16
6	W14x257	W14x426	W30x108 (50%)	W30x211 (37%)	-	10/16	11/16
5	W14x257	W14x426	W30x108 (50%)	W30x235 (33%)	-	11/16	13/16
4	W14x283	W14x455	W30x108 (50%)	W30x211 (37%)	-	6/16	6/16
3	W14x283	W14x455	W30x116 (50%)	W30x261 (36%)	-	9/16	10/16
2	W14x342	W14x500	W30x108 (50%)	W30x211 (37%)	-	-	-
Ground	W14x342	W14x500	-	-	-	-	-

Table B-38. Sections for Archetype ID = 7-10St-Dmax-W14-SC/WB=2.0-REG

Level / story	Columns		Beams with RBS flange cut		Doubler Plate Sizes (in.)		
	Exterior	Interior	Bays 1-3-5	Bay 2-4	Ext. Col.	Middle Col.	Int. Col.
Roof	-	-	W21x44 (38%)	W21x44 (38%)	-	-	-
10	W14x132	W14x233	W24x68 (35%)	W24x68 (35%)	3/16	4/16	4/16
9	W14x132	W14x233	W30x99 (37%)	W30x99 (37%)	-	-	-
8	W14x233	W14x398	W30x108 (36%)	W30x108 (36%)	-	-	-
7	W14x233	W14x398	W33x118 (38%)	W33x118 (38%)	-	-	-
6	W14x283	W14x500	W33x118 (38%)	W33x118 (38%)	-	-	-
5	W14x283	W14x500	W33x130 (37%)	W33x130 (37%)	-	-	-
4	W14x342	W14x550	W33x130 (37%)	W33x130 (37%)	-	-	-
3	W14x342	W14x550	W33x130 (39%)	W33x130 (39%)	-	-	-
2	W14x342	W14x550	W33x118 (38%)	W33x118 (38%)	-	-	-
Ground	W14x342	W14x550	-	-	-	-	-

Table B-39. Sections for Archetype ID = 8-10St-Dmax-W24-SC/WB=1.0-REG

Level / story	Columns		Beams with RBS flange cut		Doubler Plate Sizes (in.)		
	Exterior	Interior	Bays 1-3-5	Bay 2-4	Ext. Col.	Middle Col.	Int. Col.
Roof	-	-	W21x44 (38%)	W21x44 (38%)	1/16	2/16	2/16
10	W24x62	W24x103	W27x84 (36%)	W27x84 (36%)	5/16	13/16	13/16
9	W24x62	W24x103	W27x102 (35%)	W27x102 (35%)	5/16	14/16	14/16
8	W24x103	W24x162	W30x116 (35%)	W30x116 (35%)	7/16	1-2/16	1-2/16
7	W24x103	W24x162	W33x130 (37%)	W33x130 (37%)	7/16	1-1/16	1-1/16
6	W24x131	W24x207	W33x130 (37%)	W33x130 (37%)	7/16	1-1/16	1-1/16
5	W24x131	W24x207	W33x141 (36%)	W33x141 (36%)	7/16	1-2/16	1-2/16
4	W24x162	W24x229	W33x141 (36%)	W33x141 (36%)	7/16	1-2/16	1-2/16
3	W24x162	W24x229	W33x152 (35%)	W33x152 (35%)	6/16	1-3/16	1-3/16
2	W24x192	W24x250	W30x124 (35%)	W30x124 (35%)	2/16	11/16	11/16
Ground	W24x192	W24x250	-	-	-	-	-

Table B-40. Sections for Archetype ID = 9-10St-Dmax-W24-SC/WB=1.0-HYB1

Level / story	Columns		Beams with RBS flange cut		Doubler Plate Sizes (in.)		
	Exterior	Interior	Bays 1-3-5	Bay 2-4	Ext. Col.	Middle Col.	Int. Col.
Roof	-	-	W18x40 (50%)	W18x71 (36%)	1/16	4/16	4/16
10	W24x62	W24x103	W24x76 (50%)	W24x131 (38%)	2/16	1	1-1/16
9	W24x62	W24x103	W24x94 (50%)	W24x162 (36%)	2/16	1-3/16	1-3/16
8	W24x103	W24x162	W27x102 (48%)	W27x178 (34%)	3/16	1-7/16	1-8/16
7	W24x103	W24x162	W30x116 (50%)	W30x191 (32%)	3/16	1-7/16	1-7/16
6	W24x131	W24x207	W30x116 (50%)	W30x191 (32%)	3/16	1-7/16	1-8/16
5	W24x131	W24x207	W30x132 (50%)	W30x211 (36%)	3/16	1-8/16	1-8/16
4	W24x162	W24x229	W30x132 (50%)	W30x211 (36%)	3/16	1-8/16	1-8/16
3	W24x162	W24x229	W33x118 (45%)	W30x235 (35%)	-	1-9/16	1-7/16
2	W24x192	W24x250	W27x102 (42%)	W27x194 (36%)	-	1	1-1/16
Ground	W24x192	W24x250	-	-	-	-	-

Table B-41. Sections for Archetype ID = 10-10St-Dmax-W24-SC/WB=1.0-HYB2

Level / story	Columns		Beams with RBS flange cut		Doubler Plate Sizes (in.)		
	Exterior	Interior	Bays 1-3-5	Bay 2-4	Ext. Col.	Middle Col.	Int. Col.
Roof	-	-	W18x35 (50%)	W18x76 (36%)	1/16	4/16	5/16
10	W24x62	W24x103	W24x62 (46%)	W27x129 (33%)	2/16	14/16	1-2/16
9	W24x62	W24x103	W24x84 (50%)	W24x176 (37%)	1/16	1-3/16	1-4/16
8	W24x103	W24x162	W27x84 (42%)	W30x173 (31%)	2/16	1-5/16	1-10/16
7	W24x103	W24x162	W30x108 (50%)	W30x211 (37%)	3/16	1-7/16	1-8/16
6	W24x131	W24x207	W30x108 (50%)	W30x211 (37%)	3/16	1-7/16	1-8/16
5	W24x131	W24x207	W30x108 (50%)	W30x235 (33%)	-	1-9/16	1-10/16
4	W24x162	W24x229	W30x108 (50%)	W30x235 (33%)	-	1-9/16	1-10/16
3	W24x162	W24x229	W30x116 (50%)	W30x261 (36%)	-	1-10/16	1-11/16
2	W24x192	W24x250	W30x90 (50%)	W27x194 (30%)	-	1-1/16	15/16
Ground	W24x192	W24x250	-	-	-	-	-

Table B-42. Sections for Archetype ID = 11-10St-Dmax-W24-SC/WB=1.5-REG

Level / story	Columns		Beams with RBS flange cut		Doubler Plate Sizes (in.)		
	Exterior	Interior	Bays 1-3-5	Bay 2-4	Ext. Col.	Middle Col.	Int. Col.
Roof	-	-	W21x44 (38%)	W21x44 (38%)	1/16	-	-
10	W24x76	W24x131	W24x84 (35%)	W24x84 (35%)	5/16	11/16	11/16
9	W24x76	W24x131	W27x84 (36%)	W27x84 (36%)	1/16	3/16	3/16
8	W24x131	W24x229	W30x116 (35%)	W30x116 (35%)	6/16	11/16	11/16
7	W24x131	W24x229	W30x124 (35%)	W30x124 (35%)	3/16	6/16	6/16
6	W24x176	W24x306	W33x130 (37%)	W33x130 (37%)	4/16	7/16	7/16
5	W24x176	W24x306	W33x130 (37%)	W33x130 (37%)	1/16	7/16	7/16
4	W24x207	W24x306	W33x130 (37%)	W33x130 (37%)	1/16	7/16	7/16
3	W24x207	W24x306	W33x130 (37%)	W33x130 (37%)	-	7/16	7/16
2	W24x229	W24x306	W30x124 (35%)	W30x124 (35%)	-	6/16	6/16
Ground	W24x229	W24x306	-	-	-	-	-

Table B-43. Sections for Archetype ID = 12-10St-Dmax-W24-SC/WB=1.5-HYB1

Level / story	Columns		Beams with RBS flange cut		Doubler Plate Sizes (in.)		
	Exterior	Interior	Bays 1-3-5	Bay 2-4	Ext. Col.	Middle Col.	Int. Col.
Roof	-	-	W18x40 (50%)	W18x71 (36%)	-	3/16	3/16
10	W24x76	W24x131	W24x62 (38%)	W24x117 (33%)	1/16	13/16	14/16
9	W24x76	W24x131	W24x76 (50%)	W24x131 (35%)	-	6/16	7/16
8	W24x131	W24x229	W27x102 (48%)	W27x178 (34%)	2/16	1	1-1/16
7	W24x131	W24x229	W27x102 (42%)	W27x194 (36%)	-	10/16	11/16
6	W24x176	W24x306	W30x116 (50%)	W30x191 (32%)	-	12/16	13/16
5	W24x176	W24x306	W30x116 (50%)	W30x191 (32%)	-	12/16	13/16
4	W24x207	W24x306	W30x116 (50%)	W30x191 (32%)	-	12/16	13/16
3	W24x207	W24x306	W30x116 (50%)	W30x191 (32%)	-	12/16	13/16
2	W24x229	W24x306	W27x102 (42%)	W27x194 (36%)	-	10/16	11/16
Ground	W24x229	W24x306	-	-	-	-	-

Table B-44. Sections for Archetype ID = 13-10St-Dmax-W24-SC/WB=1.5-HYB2

Level / story	Columns		Beams with RBS flange cut		Doubler Plate Sizes (in.)		
	Exterior	Interior	Bays 1-3-5	Bay 2-4	Ext. Col.	Middle Col.	Int. Col.
Roof	-	-	W18x35 (50%)	W18x76 (36%)	-	3/16	3/16
10	W24x76	W24x131	W21x68 (50%)	W21x147 (36%)	1/16	1	1-1/16
9	W24x76	W24x131	W24x62 (44%)	W27x129 (35%)	-	4/16	7/16
8	W24x131	W24x229	W27x84 (42%)	W30x173 (32%)	-	14/16	1-2/16
7	W24x131	W24x229	W30x90 (50%)	W27x194 (30%)	-	11/16	9/16
6	W24x176	W24x306	W30x108 (50%)	W30x211 (37%)	-	13/16	13/16
5	W24x176	W24x306	W30x108 (50%)	W30x211 (37%)	-	13/16	13/16
4	W24x207	W24x306	W30x108 (50%)	W30x211 (37%)	-	13/16	13/16
3	W24x207	W24x306	W30x108 (50%)	W30x211 (37%)	-	13/16	13/16
2	W24x229	W24x306	W30x90 (50%)	W27x194 (30%)	-	11/16	9/16
Ground	W24x229	W24x306	-	-	-	-	-

Table B-45. Sections for Archetype ID = 14-10St-Dmax-W24-SC/WB=2.0-REG

Level / story	Columns		Beams with RBS flange cut		Doubler Plate Sizes (in.)		
	Exterior	Interior	Bays 1-3-5	Bay 2-4	Ext. Col.	Middle Col.	Int. Col.
Roof	-	-	W21x44 (38%)	W21x44 (38%)	-	-	-
10	W24x94	W24x162	W24x76 (35%)	W24x76 (35%)	2/16	7/16	7/16
9	W24x94	W24x162	W27x84 (36%)	W27x84 (36%)	-	-	-
8	W24x176	W24x306	W30x116 (35%)	W30x116 (35%)	2/16	4/16	4/16
7	W24x176	W24x306	W30x124 (38%)	W30x124 (38%)	1/16	5/16	5/16
6	W24x192	W24x306	W30x116 (35%)	W30x116 (35%)	1/16	4/16	4/16
5	W24x192	W24x306	W33x130 (37%)	W33x130 (37%)	-	1/16	1/16
4	W24x250	W24x370	W33x130 (37%)	W33x130 (37%)	-	1/16	1/16
3	W24x250	W24x370	W30x132 (35%)	W30x132 (35%)	-	1/16	1/16
2	W24x250	W24x370	W30x124 (35%)	W30x124 (35%)	-	-	-
Ground	W24x250	W24x370	-	-	-	-	-